Singly and Co-Doping of ZnO Thin Films by Spray Pyrolysis

Yiwen Fang
The Queen's College
University of Oxford

Supervisor: Professor Peter P. Edwards FRS, ML
Inorganic Chemistry Laboratory

A thesis submitted for the degree of
Doctor of Philosophy in Inorganic Chemistry
2018

Singly and Co-Doping of ZnO Thin Films by Spray Pyrolysis

Yiwen Fang (The Queen's College)

A thesis submitted for the degree of Doctor of Philosophy in Inorganic Chemistry,

Michaelmas Term 2018

Abstract

Indium-based transparent conducting oxides (TCOs) are widely used in optoelectronic devices. An important goal of this project is to search for TCOs that have reduced In content or indeed no In. The cheap zinc-based TCOs are good candidates to replace expensive indium-based TCOs in applications. A co-doping protocol has been established using both Si and In to obtain films with both good optical and electrical properties. This co-doping strategy can dramatically reduce the cost of the expensive element In while maintaining better optoelectronic performances compared to singly doped ZnO thin films.

The spray pyrolysis technique is used to deposit TCO thin films, which is famous for its lower cost compared with physical deposition methods such as sputtering. I have studied the detailed properties of singly doped (Si or In) ZnO together with co-doped (Si and In together) ZnO thin films. I have also related their optoelectronic performances with structures, elemental compositions, and chemical environment to understand their properties in depth.

It is the first time co-doped ZnO thin films based on Si and In have been successfully synthesised with high optoelectronic performances. Therefore, it is a basis for further development in co-doping and material design. The total chemical composition of elements in the bulk of a TCO material has not been measured previously. Nevertheless, I have studied these to see the limitations or restrictions in doping, thus understanding how doping affects optoelectronic properties including metal-insulator transition. Our ultimate goal is to develop an applicable deposition method and find suitable TCO materials to meet application requirements on both the optoelectronic performance and cost.

Singly and Co-Doping of ZnO Thin Films by Spray Pyrolysis

Yiwen Fang (The Queen's College)

A thesis submitted for the degree of Doctor of Philosophy in Inorganic Chemistry,

Michaelmas Term 2018

Extended Abstract

Indium-based transparent conducting oxides (TCOs) are the key materials in optoelectronic devices. However, due to the cost and global scarcity of In, people have been trying to find alternative TCOs with no or reduced In content to replace indium tin oxide (ITO) and related indium-based TCOs. One of the suitable candidates is inexpensive zinc-based TCOs, which could in principle replace expensive ITOs in wide application areas. The replacement of In by Zn not only significantly reduces the TCO cost but also avoids depleting the limited amounts of In available.

We have used the spray pyrolysis technique in this thesis, which deposits a thin film on a heated substrate by spraying on a precursor solution. The advantages of low equipment costs and high film uniformities make it a valuable technique to be used in industry. Unlike conventional physical deposition methods, spray pyrolysis does not require high vacuum or expensive equipment, which is good news for large-scale manufacturing. What is more, as I will illustrate it is a straightforward process to control easily the film thickness by simply adjusting the precursor solution volume used in spraying.

All the studies are based on singly doped (Si or In) ZnO and co-doped (Si and In together) ZnO thin films. Before the analysis of optoelectronic properties, I have investigated the spraying process from precursor solutions to thin films. The relationship between the film thickness and the precursor solution volume, and the element content in the film and the precursor solution are two key factors in the synthesis of TCO thin films.

A high electrical conductivity and a good visible transparency are two essential properties for TCO thin films. The discussion on the advantages of co-doping over singly doping is based on these. I have understood the behaviour of each dopant Si/In and how the dopants affect the optical and electrical properties. I have also investigated the metal-insulator transition for various TCO materials to explain some fundamental issues in this area.

Common sense tells us that optoelectronic properties of TCO thin films are determined by their crystal and electronic structures. Therefore, I have studied comprehensively the parameters which influence the electrical and optical properties of TCO thin films. The dopant, as well as the film thickness, can significantly affect morphologies, grain sizes, grain growths, and surface structures.

The co-doping mechanism points out the way to achieve an effective co-doping. The contribution to n-type conductivity is primarily related to the defects and 'excess electrons' generated from the occupation of the substitutional Zn sites by the impurities. The substitutional solubility limit in the lattice is the restriction of the electrical performance of TCOs. I also conclude why different dopants (e.g., Si and In) have different behaviours in affecting the optoelectronic performance of TCOs. I have built substitutional doping models together with co-doping design models to enable optimisation of TCOs for manufacturing.

To our knowledge this investigation is the first time co-doped ZnO thin films based on Si and In have been successfully synthesised with both high optical and electrical performances, thus giving a basis for further development in co-doping and material design. It is also the first time that the total chemical composition of elements in the bulk of a TCO material in addition to those of the surface has been thoroughly studied. What is more, I have also found the transfer efficiency for the spray pyrolysis technique, which is one of the key factors in engineering or industry. I have also investigated the variation of the crystal structure growth along the film thickness direction, which is indispensable for the control of the film deposition and growth, the choosing of the substrate, etc. Nevertheless, I have studied these to

understand how the structures affect the optical and electrical properties of TCOs. It has provided a high resolution picture of precisely how doping affects the optoelectronic properties, thus enlightening us to develop an applicable deposition method with suitable TCO materials to satisfy the requirements on both the performance and cost.

The work described in this thesis was carried out in the Inorganic Chemistry Laboratory at the University of Oxford from 2013 until 2018, under the supervision of Professor Peter P. Edwards. All of the work is my own unless otherwise stated, and has not been previously submitted for a degree at this or any other university.

Yiwen Fang

September 2018

Acknowledgments

Many years ago, when I was in primary school, I dreamed of studying at the University of Oxford since I knew Oxford from an Oxford Dictionary, which was a bestseller. It was like a dream if I looked back on the Oxford life in the past few years. I was pleasantly surprised by the Oxford offer years ago, and my dream has been come true eventually.

I would like to express my sincere gratitude to my supervisor, Professor Peter P. Edwards FRS, ML, for providing me with the opportunity to be a DPhil student in Oxford. Besides his aspiring guidance and enlightening me, he also concerned about my personal life, financial situation, and career development. He almost gave me complete freedom to carry out my research and supported me as much as he could. I am so lucky to have Pete as my supervisor, not only the role of a supervisor to be exact.

I am extremely grateful to Professor Jonathan Dilworth, who always gave me good ideas, advice, and academic support, which were invaluable in my life. I really appreciate his weekly research talk and long-period proofreading. He made me understand how to be an excellent chemist. I give my heartfelt thanks to Dr Vladimir Kuznetsov for his profound knowledge and advice on my research. I am also very grateful to Dr Tiancun Xiao for his suggestion both on my research and career development.

I also thank Dr Daniel Slocombe and Dr Michael Jones, who gave me valuable advice on the research when I came to the group years ago. I would like thank my group members, Xiangyu, Shuai, Weisong, Benzhen, Sergio, Andrew, Joshua, Afrah, Bonan, Xian, Nurul, Alex, Nazanin, Zhaoxi, Pirzada, and Himanshu for all the help and support during my DPhil study. I give a special thanks to Ms Linda Webb for her kind help and advice.

I really enjoyed the life with my roommates, Yiding, Bangshan, Jingyi, and Xiao. I also enjoyed the happy days with Peimei, Jingyuan, Xiangwen, Ronghuan, Lun, Tianyi, Jenny,

Kelly, Bingling, Piao, Monica, Guowei, Ying, etc.

I cannot express how grateful I am to my family, especially my parents, who have supported me for my studies. I miss them so much these years. I would like to thank my girlfriend Yunke who can understand, support, and love me.

Finally, I thank all my friends and family members in UK, China, and elsewhere for their support and encouragement in my whole life. Thank you very much.

Abbreviations

AC	Alternating current
AES	Auger electron spectroscopy
AFM	Atomic force microscopy
AIZO (x% Al-y% In)	x% aluminium and y% indium co-doped zinc oxide
ALD	Atomic layer deposition
APCVD	Atmospheric pressure chemical vapor deposition
ARXPS	Angle-resolved XPS
ASF	Atomic sensitivity factors
at%	Atomic percent
ATR	Attenuated total reflectance
AZO (x%)	x% aluminium doped zinc oxide
BF	Bright-field
BM	Burstein-Moss effect
BSE	Backscattered electrons
BSEI	Backscattered electron imaging
CFOM	Cost-based Figure of Merit
CB	Conduction band
c_f	Concentration in the film
c_p	Concentration in the precursor solution
Concentration in the film	[Element] / [Zn] × 100% calculated from ICP-MS data
CSV	Comma-separated value
CVD	Chemical vapor deposition
DC	Direct current
DF	Dark-field
DFT	Density functional theory
EBSD	Electron backscatter diffraction
EC	Electrochromic

EDX	Energy dispersive X-ray spectra
EDXRD	Energy-dispersive X-ray diffraction
EELS	Electron energy loss spectroscopy
EMA	Effective mass approximation
FIB	Focused ion beam
FIB-SEM	Focused ion beam scanning electron microscope
FPD	Flat-panel display
FTO	Fluoride doped tin oxide
FWHM	Full width at half maximum
GZO	Gallium doped zinc oxide
HRTEM	High-resolution transmission electron microscopy
ICDD	International Center for Diffraction Data
ICP-MS	Inductively coupled plasma mass spectrometry
InSiZO (x% In-y% Si)	x% indium and y% silicon co-doped zinc oxide
IRS	Internal reflectance spectroscopy
ITO	Indium tin oxide
IZO (x%)	x% indium doped zinc oxide
JCPDS	Joint Committee on Powder Diffraction Standards
LCVD	Laser chemical vapor deposition
LED	Light emitting diode
LPCVD	Low pressure chemical vapor deposition
MOCVD	Metallorganic chemical vapor deposition
MSE	Mean square error
Nominal concentration	[Element] / [Zn] × 100% calculated from starting materials
NPL	National Physical Laboratory
PCB	Printed circuit board
PDF	Powder Diffraction File
PET	Polyethylene terephthalate
PID	Proportional-integral-derivative

PLD	Pulsed laser deposition
PMT	Photomultiplier
ppt	Parts per trillion
PVD	Physical vapor deposition
RF	Radio frequency
RIR	Reference intensity ratio
RMS	Root mean square
SE	Secondary electrons
SEI	Secondary electron imaging
SEM	Scanning electron microscopy
SiZO (x%)	x% silicon doped zinc oxide
TCO	Transparent conducting oxide
TEM	Transmission electron microscopy
UHV	Ultrahigh vacuum
UHVCVD	Ultrahigh vacuum chemical vapor deposition
UV-Vis-NIR	Ultraviolet-visible-near infrared
v/v	Volume percent
wt%	Weight percent
XPS	X-ray photoelectron spectroscopy
XRD	X-ray diffraction
XRR	X-ray reflectivity
ZnO	Zinc oxide

Contents

List of Figures viii

List of Tables xxiv

1 Introduction 1

1.1 Aim of the Project 2

1.2 Brief Experiment Design 5

1.3 Transparent Conducting Oxides 5

1.4 Applications of Transparent Conducting Oxides 10

1.5 Thin Film Deposition Techniques 12

1.5.1 Physical Deposition Methods 13

1.5.2 Chemical Deposition Methods 17

1.6 ZnO 22

1.7 Precursors for ZnO 24

1.8 Doping of ZnO 25

1.8.1 n-Type Doping 26

1.8.2 p-Type Doping 29

1.8.3 Co-Doping 29

1.9 Structure of ZnO 30

1.10 Optical Properties of ZnO 32

1.11 Electrical Properties of ZnO 34

1.12 Correlation of Optical and Electrical Properties 38

1.13 Defect Models of ZnO 38

1.13.1 Zinc and Oxygen Defect Models 38

1.13.2 Silicon Defect Models 40

1.13.3 Indium Defect Models 42

1.14 Conclusions 43

References 45

2 Experimental Techniques and Data Acquisition 57

2.1 X-Ray Diffraction 58
2.1.1 Introduction 58
2.1.2 Principles of the Technique 59
2.1.3 Applications of XRD 61
2.1.3.1 Phase Identification 61
2.1.3.2 Quantitative Phase Analysis 61
2.1.3.3 Lattice Parameters 63
2.1.3.4 Crystallite Size 64
2.1.4 Instrumentation 65
2.2 Atomic Force Microscopy 65
2.2.1 Introduction 65
2.2.2 Principles of the Technique 66
2.2.3 Applications of AFM 67
2.2.4 Instrumentation 69
2.3 Scanning Electron Microscopy 69
2.3.1 Introduction 69
2.3.2 Principles of the Technique 70
2.3.3 Applications of SEM 72
2.3.4 Instrumentation 73
2.4 Transmission Electron Microscopy 73
2.4.1 Introduction 73
2.4.2 Principles of the Technique 74
2.4.3 Applications of TEM 75
2.4.4 Instrumentation 76
2.5 X-Ray Photoelectron Spectroscopy 79
2.5.1 Introduction 79
2.5.2 Principles of the Technique 79
2.5.3 Applications of XPS 84
2.5.3.1 Qualitative Analysis 84

2.5.3.2 Chemical Analysis 85
2.5.3.3 Energy Loss Features 85
2.5.3.4 Depth of Analysis 86
2.5.3.5 Quantitative Analysis 86
2.5.4 Instrumentation 87
2.6 Inductively Coupled Plasma Mass Spectrometry 88
2.6.1 Introduction 88
2.6.2 Principles of the Technique 88
2.6.3 Applications of ICP-MS 90
2.6.3.1 Semi-Quantitative Analysis 90
2.6.3.2 Quantitative Analysis 91
2.6.3.3 Isotope Ratio 91
2.6.4 Instrumentation 91
2.7 Ultraviolet-Visible-Near-Infrared Absorption Spectroscopy 92
2.7.1 Introduction 92
2.7.2 Principles of the Technique 93
2.7.3 Applications of UV-Vis-NIR Spectroscopy 96
2.7.3.1 Identification of Compounds 96
2.7.3.2 Beer-Lambert Law 96
2.7.3.3 Calculation of Optical Constant 97
2.7.3.4 Calculation of Film Thickness 97
2.7.4 Instrumentation 100
2.8 Reflectance Spectroscopy 100
2.8.1 Introduction 100
2.8.2 Principles of the Technique 101
2.8.3 Applications of Reflectance Spectroscopy 101
2.8.3.1 Internal Reflectance Spectroscopy 101
2.8.3.2 Specular Reflectance Spectroscopy 102
2.8.3.3 Diffuse Reflectance Spectroscopy 103

2.8.4 Instrumentation 103
2.9 Dielectric Modelling 104
2.9.1 Introduction 104
2.9.2 Principles of the Technique 104
2.9.3 Applications of Dielectric Function 105
2.9.4 Instrumentation 105
2.10 Hall Effect Measurement 106
2.10.1 Introduction 106
2.10.2 Principles of the Technique 106
2.10.2.1 Hall Effect 106
2.10.2.2 The van der Pauw Technique 108
2.10.3 Instrumentation 111
References 113
3 From Precursor Solutions to Thin Films 123
3.1 Experimental 124
3.2 Results and Discussion 127
3.2.1 Thickness Control of Thin Films 127
3.2.2 Elemental Analysis of ZnO Thin Films 129
3.2.2.1 Effect of Element Concentration: From Precursor Solutions to Thin Films 129
3.2.2.1.1 Singly Doped Thin Films 129
3.2.2.1.2 Co-Doped Thin Films 133
3.2.2.2 Effect of Film Thickness 135
3.3 Conclusions 136
References 139
4 Electrical Properties 140
4.1 Introduction 141
4.1.1 Singly Doped Thin Films: SiZO 141
4.1.2 Singly Doped Thin Films: IZO 142

4.1.3 Co-Doped Thin Films ... 145

4.2 Experimental ... 148

4.3 Results and Discussion ... 151

4.3.1 Effect of Element Concentration ... 151

4.3.1.1 Singly Doped Thin Films: SiZO ... 151

4.3.1.2 Singly Doped Thin Films: IZO ... 154

4.3.1.3 Co-Doped Thin Films: InSiZO ... 156

4.3.2 Effect of Film Thickness ... 159

4.4 Conclusions ... 161

References ... 164

5 Optical Properties ... 169

5.1 Results and Discussion ... 170

5.1.1 Effect of Element Concentration ... 170

5.1.1.1 Singly Doped Thin Films: SiZO ... 170

5.1.1.2 Singly Doped Thin Films: IZO ... 172

5.1.1.3 Co-Doped Thin Films: InSiZO ... 174

5.1.2 Effect of Film Thickness ... 177

5.1.2.1 Singly Doped Thin Films: SiZO ... 177

5.1.2.2 Singly Doped Thin Films: IZO ... 183

5.1.2.3 Co-Doped Thin Films: InSiZO ... 184

5.2 Conclusions ... 185

References ... 187

6 Structural Studies ... 189

6.1 XRD Studies ... 190

6.1.1 Effect of Element Concentration ... 190

6.1.1.1 Singly Doped Thin Films: SiZO ... 190

6.1.1.2 Singly Doped Thin Films: IZO ... 195

6.1.1.3 Co-Doped Thin Films: InSiZO ... 198

6.1.2 Effect of Film Thickness ... 201

6.2 AFM and SEM Studies 204
6.2.1 Effect of Element Concentration 204
6.2.1.1 Singly Doped Thin Films: SiZO 204
6.2.1.2 Singly Doped Thin Films: IZO 207
6.2.1.3 Co-Doped Thin Films: InSiZO 208
6.2.2 Effect of Film Thickness 211
6.3 TEM Studies 215
6.3.1 The Microstructure of ZnO, SiZO, and IZO 216
6.3.2 The Microstructure of InSiZO 219
6.3.5 Chemistry of Films Measured with EDX Spectra 221
6.3.6 Crystallography 223
6.4 XPS Studies 224
6.5 Conclusions 231
References 235
7 Summary Discussion and Conclusions 239
7.1 Summary Discussion 240
7.1.1 The Metal-Insulator Transition 240
7.1.2 Grain Boundary Effects 247
7.1.3 The Co-Doping Mechanism 253
7.1.4 The Figure of Merit 258
7.2 Conclusions 261
7.3 Further Work 263
References 266
Appendices 270
Chapter 2 271
A2.1 Swanepoel Calculator 271
A2.2 Film Thickness Measurement 278
Chapter 3 279
A3.1 Thermal Distribution on the Heating Platform 279

Chapter 5 280

A5.1 Effect of Film Thickness: SiZO 280

A5.2 Effect of Film Thickness: IZO 281

A5.3 Effect of Film Thickness: InSiZO 283

Chapter 6 285

A6.1 AFM and SEM Studies: IZO 285

A6.2 Effect of Film Thickness: IZO 287

A6.3 Effect of Film Thickness: InSiZO 289

A6.4 TEM 1 291

A6.5 TEM 2 293

A6.6 TEM 3 294

A6.7 EDX 297

A6.8 Crystallography 300

Chapter 7 301

A7.1 Grain Boundary Effects 301

References 304

Publications 305

List of Figures

Figure 1.1: Primary indium refinery production by country from 2009 to 2013. Reproduced from Lokanc et al. [1] with permission from OSTI. 2

Figure 1.2: Photo of an InSiZO thin film (inset) illustrating its high transparency. The red line is the outline of the film. 3

Figure 1.3: Band diagrams for undoped, n-type, and p-type semiconductors. A new filled level is formed between the valence and conduction bands for n-type semiconductors. An empty level is formed between the valence and conduction band for p-type semiconductors. 4

Figure 1.4: Band diagrams for ITOs with small x appearing as insulators and larger x appearing as metals. E_F is the Fermi level energy, E_C is the bottom of the conduction band, E_V is the top of the valence band, and V_O are the oxygen vacancies. Reproduced from Edwards et al. [6] with permission from the Royal Society of Chemistry. 4

Figure 1.5: The reflection coefficients of an ITO layer as a function of electron carrier concentrations with various wavelengths. Reproduced from Edwards et al. [6] with permission from the Royal Society of Chemistry. 8

Figure 1.6: The skin depths as a function of the mobilities and the carrier concentrations (electron densities) at a fixed wavelength value of 800 nm. The electrical resistivities are also labeled. Reproduced from Edwards et al. [6] with permission from the Royal Society of Chemistry. 10

Figure 1.7: Schematic of a typical surface LED structure. Reprinted from Porch et al. [34], with the permission of AIP Publishing. 11

Figure 1.8: Schematic of a typical module structure of a thin-film photovoltaic cell. Republished with permission from Slocombe et al. [35-37]; permission conveyed through Copyright Clearance Center, Inc. 12

Figure 1.9: Schematic of a thermal evaporation process. Reproduced from Hardy [41] with permission from Semicore. 14

Figure 1.10: Schematic of an e-beam evaporation process. Reproduced from Hardy [41]

with permission from Semicore. 15

Figure 1.11: Schematic of a pulsed laser deposition process. Reproduced from Schwarz [42] with permission from Schwarz. 16

Figure 1.12: Schematic of a sputtering process. Reproduced from Hughes [44] with permission from Hughes. 17

Figure 1.13: Schematic of a chemical vapour deposition process. Reproduced from [48] with permission from Strem Chemicals. 18

Figure 1.14: Schematic of a sol-gel process. Reproduced from Mahmood et al. [53] with permission from InTech. 19

Figure 1.15: Schematic of a spin coating process. Reproduced from Norrman [56] with permission from the Royal Society of Chemistry. 20

Figure 1.16: Schematic of the spray pyrolysis process used in this investigation. 21

Figure 1.17: Photo of a spray pyrolysis apparatus in a laboratory. 21

Figure 1.18: Schematic of the zinc acetylacetonate structure. 24

Figure 1.19: Schematic of zinc acetylacetonate decomposition mechanism in an acidic solution. Adapted from Ambrozic et al. [91] with permission from the Royal Society of Chemistry. 25

Figure 1.20: Graph of reported minimum resistivity values for doped ZnO (black circles), In_2O_3 (blank triangles), and SnO_2 (blank squares). Reproduced from Otiti [77] with permission from Otiti. 26

Figure 1.21: Schematic of ZnO crystal structures including cubic rocksalt (a), cubic zinc blende (b), and hexagonal wurtzite (c). Zn atoms are grey circles and O atoms are black circles. Reprinted from Ozgur [93], with the permission of AIP Publishing. 30

Figure 1.22: Transmittance, reflectance, and absorption spectra of a TCO material. Reproduced from Pasquarelli et al. [151] with permission from the Royal Society of Chemistry. 33

Figure 1.23: Schematic of the optical band shift due to the Burstein-Moss effect. 33

Figure 1.24: Unit cell of hexagonal wurtzite ZnO (a). (b) ZnO crystal model viewed from the $[\bar{1}\bar{1}20]$ (left) and the [0001] (right). Zn atoms (grey circles), O atoms (red

circles), octahedral (dashed), and tetrahedral (solid) interstitial sites. Reproduced from Fumiyasu et al. [179] with permission from National Institute for Materials Science. 39

Figure 1.25: Schematic of a 2 × 2 × 2 ZnO supercell model indicating substitutional and interstitial Si atoms. Reproduced from Wu et al. [191] with permission from MDPI. 40

Figure 1.26: Calculated band structures of ZnO (a), substitutional SiZO (b), octahedral interstitial SiZO (c), and tetrahedral interstitial SiZO (d). Adapted from Wu et al. [191] with permission from MDPI. 42

Figure 1.27: Schematic of a 3 × 3 × 2 supercell containing substitutional and interstitial In atoms. Reproduced from Wu et al. [195] with permission from MDPI. 43

Figure 2.1: Bragg's Law. 60

Figure 2.2: Intensity ratio of XRD patterns as a function of weight percentage of phases. Data are taken from Spurr et al. [30] 62

Figure 2.3: A schematic illustration of an AFM instrument. © IOP Publishing. Reproduced from Daniel et al. [46] with permission. All rights reserved. 67

Figure 2.4: Force between the tip and the surface as a function of the corresponding distance between them. Reproduced from Goldsbury et al. [48] with permission from Wiley. 68

Figure 2.5: Schematic diagram of different signals arisen from the interactions between the electron beam and the sample. 71

Figure 2.6: Schematic diagram of a SEM system. Reprinted from Zhou et al. [58] by permission from Springer. 72

Figure 2.7: Schematic setup of a TEM instrument. Reproduced from [73] with permission from Physics World. 75

Figure 2.8: Photographs of the wafer pieces before (a) and after (b) carbon and Pt-Pd coating. The darker, opaque parts of the wafer pieces indicate the film proximity to the edge of the Al stub. 77

Figure 2.9: SEM images taken during the FIB lift-out of thin films. Deposition of the

protective Pt strip (a). Bulk milling to isolate three sides of the section (b). The positioning of the section to an OmniProbe grid (c). The roughly milled section in place prior to final milling (d). Monitoring lamella thickness during thinning stages (e). The final lamella ready for the TEM (f). 78

Figure 2.10: The TEM-ready cross sections of all four samples. The order of preparation was D → A.. 79

Figure 2.11: Schematic diagram of the electron excitation in XPS. Reproduced from Jang [82] with permission from Jang. 80

Figure 2.12: Schematic diagram of Auger effect. Reproduced from Yun [89] with permission from UTEP... 81

Figure 2.13: Wide survey scan spectra of ZnO. Reproduced from Dai et al. [91] with permission from OSA Publishing. 82

Figure 2.14: Schematic diagram of an XPS spectrometer. Reprint from Tougaard et al. [84], with permission from Elsevier.. 83

Figure 2.15: Schematic diagram of an ICP source. Reproduced from [117] with permission from PerkinElmer. 89

Figure 2.16: Schematic diagram of a quadrupole mass filter. Reproduced from [117] with permission from PerkinElmer. 89

Figure 2.17: The ICP-MS detection limit for the elements in the periodic tables. Reproduced from [117] with permission from PerkinElmer.................................... 90

Figure 2.18: An example of a calibration curve for Pb. Reproduced from [113] with permission from PerkinElmer. 91

Figure 2.19: A schematic diagram of a typical UV-Vis-NIR spectrometer. Reproduced from [128] with permission from MSU. 93

Figure 2.20: Schematic diagram of a transmission process. 95

Figure 2.21: Transmission and reflection of a film on a substrate. The glass substrate is much thicker than the film. Reproduced from Dorranian et al. [144] with permission from Springer. 98

Figure 2.22: Transmittance spectra of a film on a substrate. T is the transmittance of the

sample. T_s is the transmittance of the substrate. T_M and T_m are the maxima and minima curves of the transmittance T, respectively. Reproduced from Dorranian et al. [144] with permission from Springer. 100

Figure 2.23: Schematic diagram of internal reflection. 102

Figure 2.24: Schematic diagram of specular reflection. 103

Figure 2.25: Schematic diagram of diffuse reflection. Reproduced from Khoshhesab [147] with permission from InTech. 103

Figure 2.26: Schematic of the Hall effect in a rectangular parallelepiped conductor. Reproduced from [167] with permission from NIST. 108

Figure 2.27: Schematic of the geometries used for Hall effect and van der Pauw measurements. Reproduced from [167] with permission from NIST. 109

Figure 2.28: Schematic of a van der Pauw technique in the measurement of R_A and R_B. Reproduced from [167] with permission from NIST. 110

Figure 2.29: Schematic of a van der Pauw technique in the measurement of V_H. Reproduced from [167] with permission from NIST. 111

Figure 2.30: Photo of a Hall measurement system. 112

Figure 3.1: Schematic of the spray pyrolysis process used in this investigation. 125

Figure 3.2: Photo of a spray pyrolysis apparatus in a laboratory. 125

Figure 3.3: Photo of mounting a substrate. 126

Figure 3.4: Calibration of the heater surface temperature. 127

Figure 3.5: Schematic of steps to generate current-carrying electrons in our thin films from the preparation of starting materials and solutions to the final thin films. 128

Figure 3.6: Film thicknesses of ZnO (a), SiZO (c_p = 3%) (b), IZO (c_p = 6%) (c), and InSiZO (c_p = 6% In-3% Si) (d) thin films prepared from varying amounts of precursor solutions. 129

Figure 3.7: Si/In concentrations in the films for SiZO (a)/IZO (b) thin films containing varying amounts of Si/In. 130

Figure 3.8: Zn quantities in SiZO (a) and IZO (c) thin films and transfer efficiencies for SiZO (b) and IZO (d) thin films containing varying amounts of Si/In. The error bars

demonstrate the maximum possible errors of 5%. [1, 2] 132

Figure 3.9: Si/In quantities in SiZO (a)/IZO (c) thin films and their transfer efficiencies for SiZO (b)/IZO (d) thin films containing varying amounts of Si/In. 133

Figure 3.10: In and Si concentrations in the films for InSiZO (In-c_p = 3% Si) (a) and InSiZO (c_p = 6% In-Si) (b) thin films. 134

Figure 3.11: Si/In concentrations in the films for SiZO (c_p = 3%) (a), IZO (c_p = 6%) (b), and InSiZO (c_p = 6% In-3% Si) (c) thin films prepared from varying amounts of precursor solutions. 136

Figure 4.1: Electrical properties of $Zn_{1-x}Al_xO_y$ and $Zn_{1-x}In_xO_y$ thin films for various ZnO compositions. Conductivities, carrier concentrations, and mobilities are shown in diagram (a), (b), and (c), respectively. [10, 48] Reprinted from Kirby and Dover [48], with permission from Elsevier. 147

Figure 4.2: A thin film model for dielectric modelling. 151

Figure 4.3: Electrical properties of ZnO and SiZO thin films containing varying amounts of Si. 152

Figure 4.4: Doping efficiencies and carrier concentrations of SiZO thin films containing varying amounts of Si. 154

Figure 4.5: Electrical properties of ZnO and IZO thin films containing varying amounts of In. 155

Figure 4.6: Doping efficiencies and carrier concentrations of IZO thin films containing varying amounts of In. 156

Figure 4.7: Electrical properties of InSiZO (red) thin films containing varying amounts of In and 0.6% Si. Electrical properties of IZO (black) thin films are plotted for comparisons. The blue area shows the superior performance of co-doped ZnO thin films. 158

Figure 4.8: Electrical properties of InSiZO (red) thin films containing varying amounts of Si and 2% In. Electrical properties of SiZO (black) thin films are plotted for comparisons. 159

Figure 4.9: Electrical properties of ZnO (a), SiZO (0.6%) (b), IZO (2%) (c), and InSiZO

(2% In-0.6% Si) (d) thin films of various thicknesses. 161

Figure 5.1: UV-Vis-NIR optical transmittance (a) and reflectance (b) spectra of ZnO and SiZO thin films containing varying amounts of Si. The data is not corrected for the glass substrate to show the comparisons with the glass substrate. The plasma wavelengths λ_p calculated from the dielectric modelling of optical spectra are shown as the straight line and the area. 171

Figure 5.2: Graph of $(\alpha h\nu)^2$ as a function of photon energies (a) and band gaps (b) for ZnO and SiZO thin films containing varying amounts of Si. It shows a maximum value of the band gap corresponding to the highest carrier concentration.......................... 172

Figure 5.3: UV-Vis-NIR optical transmittance (a) and reflectance (b) spectra of ZnO and IZO thin films containing varying amounts of In. 173

Figure 5.4: Graph of $(\alpha h\nu)^2$ as a function of photon energies (a) and band gaps (b) for ZnO and IZO thin films containing varying amounts of In. 174

Figure 5.5: UV-Vis-NIR optical transmittance (a) and reflectance (b) spectra of InSiZO thin films containing varying amounts of In and 0.6% Si. 175

Figure 5.6: Graph of $(\alpha h\nu)^2$ as a function of photon energies (a) and band gaps (b) for InSiZO thin films containing varying amounts of In and 0.6% Si. 176

Figure 5.7: UV-Vis-NIR optical transmittance (a) and reflectance (b) spectra of InSiZO thin films containing varying amounts of Si and 2% In. 177

Figure 5.8: Graph of $(\alpha h\nu)^2$ as a function of photon energies (a) and band gaps (b) for InSiZO thin films containing varying amounts of Si and 2% In. 177

Figure 5.9: UV-Vis-NIR optical transmittance (a) and reflectance (b) spectra of ZnO thin films of various thicknesses. 178

Figure 5.10: Graph of $(\alpha h\nu)^2$ as a function of photon energies (a) and band gaps (b) for ZnO thin films of various thicknesses. 179

Figure 5.11: UV-Vis-NIR optical transmittance spectra of four identical SiZO (0.6%) thin films with the thickness of 197 nm showing the reproducibility. The average visible optical transmittance corrected for the glass substrate is also labeled. 180

Figure 5.12: Graph of band gaps and crystallite sizes calculated from EMA of SiZO (0.6%)

thin films of various thicknesses. 182

Figure 5.13: Average visible optical transmittance (400 - 750 nm) corrected for the glass substrate of ZnO (a) and SiZO (0.6%) (b) thin films of various thicknesses......... 183

Figure 5.14: UV-Vis-NIR optical transmittance spectra of selected SiZO, IZO, and InSiZO thin films with the best electrical performance. Their average visible transmittances are labelled. 184

Figure 6.1: XRD patterns of ZnO and SiZO thin films containing varying amounts of Si. 191

Figure 6.2: $TC_{(100)}$, $TC_{(002)}$, and $TC_{(101)}$ values for ZnO and SiZO thin films containing varying amounts of Si. 193

Figure 6.3: Lattice parameters of ZnO and SiZO thin films containing varying amounts of Si. 194

Figure 6.4: XRD patterns of ZnO and IZO thin films containing varying amounts of In. 195

Figure 6.5: $TC_{(100)}$, $TC_{(002)}$ and $TC_{(101)}$ values for ZnO and IZO thin films containing varying amounts of In. 197

Figure 6.6: Lattice parameters of ZnO and IZO thin films containing varying amounts of In. 198

Figure 6.7: XRD patterns of InSiZO thin films containing varying amounts of In and 0.6% Si. 199

Figure 6.8: $TC_{(100)}$, $TC_{(002)}$ and $TC_{(101)}$ values for InSiZO thin films containing varying amounts of In and 0.6% Si. 200

Figure 6.9: Lattice parameters of InSiZO thin films containing varying amounts of In and 0.6% Si. 201

Figure 6.10: XRD patterns of ZnO (a) and SiZO (0.6%) (b) thin films of various thicknesses. 202

Figure 6.11: XRD patterns IZO (2%) (a) and InSiZO (2% In-0.6% Si) (b) thin films of various thicknesses. 203

Figure 6.12: AFM images of ZnO and SiZO thin films containing varying amounts of Si.

.... 205

Figure 6.13: RMS surface roughnesses of ZnO and SiZO thin films containing varying amounts of Si calculated from the AFM data. 205

Figure 6.14: SEM images of ZnO and SiZO thin films containing varying amounts of Si. 206

Figure 6.15: Grain sizes of ZnO and SiZO thin films containing varying amounts of Si calculated from SEM images. 207

Figure 6.16: Schematic diagram for crystal growth orientations of ZnO (undoped or doped) thin films grown on a glass substrate. (a) A polygonal structure; (b) A ridge-like structure; (c) a pyramidal-like structure (hexagonal cylindrical with a pyramidal tip or not); (d) A pyramidal tip structure. Reproduced from Tsai et al. [27] with permission from Beilstein-Institut. 207

Figure 6.17: AFM images of InSiZO thin films containing varying amounts of In and 0.6% Si. 209

Figure 6.18: RMS surface roughnesses of InSiZO thin films containing varying amounts of In and 0.6% Si calculated from the AFM data. 209

Figure 6.19: SEM images of InSiZO thin films containing varying amounts of In and 0.6% Si. 210

Figure 6.20: Grain sizes of InSiZO thin films containing varying amounts of In and 0.6% Si calculated from SEM images...211

Figure 6.21: AFM images of ZnO thin films of various thicknesses. 212

Figure 6.22: RMS surface roughnesses of ZnO thin films of various thicknesses calculated from the AFM data. 212

Figure 6.23: SEM images of ZnO thin films of various thicknesses. 212

Figure 6.24: Grain sizes of ZnO thin films of various thicknesses calculated from SEM images. 213

Figure 6.25: AFM images of SiZO (0.6%) thin films of various thicknesses.............. 213

Figure 6.26: RMS surface roughness of SiZO (0.6%) thin films of various thicknesses calculated from the AFM data. The deviation of the middle point is due to

experimental errors in AFM measurements. 214

Figure 6.27: SEM images of SiZO (0.6%) thin films of various thicknesses. 214

Figure 6.28: Grain sizes of SiZO (0.6%) thin films of various thicknesses calculated from SEM images. 215

Figure 6.29: ZnO: The overall microstructure (a) and example of an irregular grain, strongly diffracting (b) which displays the boundary of the grain. A grain containing planar faults is seen in (c). The black spots are the voids. The red lines draw the outlines of the key structures. 216

Figure 6.30: ZnO: An under-focused BF image shows white lines delineating the grain boundaries (a). HRTEM images show the dense network of crystalline material with no evidence of glassy films between grains (b). FIB artefacts are seen as 3 - 5 nm 'blobs' just below the interface (these have been seen on other films with glass substrates). 217

Figure 6.31: IZO: Under-focused BF image showing the boundaries between grains (a). HRTEM image of the nucleating interface shows good clear lattice contrast (b). 218

Figure 6.32: Selected area diffraction pattern (a) taken from a 1070 nm diameter patch in the thicker part of the FIB lamella of ZnO (b). 218

Figure 6.33: BF images of the thicker part (a) and thin part (b) of the lamella of InSiZO. Over-milling between these two regions results in a film-free window between them. 219

Figure 6.34: Under-focused BF images showing the grain boundaries in the nucleating layer for a thicker area (a) corresponding to the upper left of **Figure 6.33**(b) and thin area (beyond the lower right corner of previous **Figure 6.33**(b)). 220

Figure 6.35: HRTEM images of the grains at the nucleating layers at different sites of the interface seen in **Figure 6.33**(b). Note the divergent triangular profile of the grains in (b). 220

Figure 6.36: Structure of a percolating grain at large scale (a) and finer scales within 200 nm of the interface (b) and within 50 nm of the interface (c). 221

Figure 6.37: EDX spectra taken from ZnO, SiZO, IZO, and InSiZO thin films at the points

indicated in images at roughly bottom, middle, and top from the initial interfaces. 222

Figure 6.38: Montage of the 40 cm camera length diffraction patterns of the four films (a), working clockwise from top left: InSiZO, IZO, SiZO and ZnO. The calibration pattern from gold under identical conditions (b). 223

Figure 6.39: XPS wide survey spectra of ZnO (a), SiZO (0.6%) (b), IZO (2%) (c), and InSiZO (2% In-0.6% Si) (d) thin films. 225

Figure 6.40: XPS high resolution Si 2p spectra of SiZO (0.6% Si) (a) and InSiZO (2% In-0.6% Si) (b) thin films. 226

Figure 6.41: XPS high resolution In 3d spectra of IZO (2% In) (a) and InSiZO (2% In-0.6% Si) (b) thin films. 226

Figure 6.42: XPS high resolution Zn 2p spectra of SiZO (a), IZO (b), and InSiZO (In-0.6% Si) (c) thin films. Zn $2p_{3/2}$ and Zn $2p_{1/2}$ peaks are shown as blue and red lines for ZnO and doped ZnO thin films, respectively. Their binding energies are also labelled. 227

Figure 6.43: XPS high resolution O 1s spectra of SiZO (a) and IZO (b) thin films. O_I and O_{II} peaks are shown as red and green straight lines for all the films, respectively. 229

Figure 6.44: XPS high resolution Cl 2p spectra of IZO (2%) thin films. 230

Figure 7.1: The room temperature electrical resistivities of materials including metals and non-metals. Republished with permission from Edwards [1] et al. and Ehrenreich [2]; permission conveyed through Copyright Clearance Center, Inc. 240

Figure 7.2: Schematic of impurity band conduction for various carrier concentrations. n_c is the critical carrier concentration where a MIT occurs, and n_{cb} is the carrier concentration where impurity band merges with the conduction band. Republished with permission from Vai et al. [3]; permission conveyed through Copyright Clearance Center, Inc. 241

Figure 7.3: Mott-Edwards-Sienko plot showing the relationship between the effective Bohr radius a_H^* and the critical carrier concentration n_c for MIT. The shaded region includes the surveyed TCOs. The data are from [3, 7-16]. The plot is republished with permission from Vai et al. [3]; permission conveyed through Copyright Clearance

Center, Inc. which originates from Edwards and Sienko. [16] 242

Figure 7.4: Hall effect carrier concentrations (a), mobilities (b), and resistivities (c) as a function of temperature for undoped and doped ZnO thin films with the indicated carrier concentrations n_{RT} at room temperature. 244

Figure 7.5: The Ioffe-Regel parameters $k_F l_e$ as a function of carrier concentrations of ZnO, SiZO, IZO, and InSiZO thin films at room temperature. The red dash line shows $k_F l_e = 1$ where a MIT occurs. The blue area shows the critical carrier concentration for a MIT. 246

Figure 7.6: Conductivity as a function of carrier concentration for various TCOs at high temperature (300 K) and low temperature (77 K). The plot is adapted with permission from Vai et al. [3]; permission conveyed through Copyright Clearance Center, Inc. The literature data are from [23-28].. 247

Figure 7.7: Schematic band diagram near a grain boundary of a TCO thin film. Φ_b is the potential barrier height, E_F is the Fermi level energy, E_C is the bottom of the conduction band, and E_V is the top of the valence band. Reproduced from Nguyen et al. [29] with permission from the Royal Society of Chemistry............................ 248

Figure 7.8: A typical UV-Vis-NIR optical reflectance spectra of SiZO (0.6%) thin films. The simulation spectrum is shown as the red curve... 249

Figure 7.9: Optical (red) and Hall (black) electrical properties of SiZO, IZO, and InSiZO (In-0.6% Si) thin films. 251

Figure 7.10: Plots of $\text{In}(\mu_{gb}T^{1/2})$ against 1 / T for ZnO, SiZO (0.6%), IZO (2%), and InSiZO (2% In-0.6% Si) thin films. The linear fitted curves are shown as black solid lines and the magenta lines show the range of data for fitting............................. 252

Figure 7.11: Electrical properties of SiZO (a), IZO (b), and InSiZO (c) thin films. The red lines and red area show the substitutional limits of the dopants. The inserted labels (b) - (g) are the corresponding models in **Figure 7.12**. 255

Figure 7.12: Substitutional doping models for singly doped and co-doped ZnO thin films. Each empty small pane represents a substitutional Zn site and each filled small pane represents a substitutional Si or In defect. These models are just schematic and do not

represent any geometry information (e.g., they are two-dimensional rather than three-dimensional.). Initial Zn sites (a), part of sites occupied by Si (b), part of sites occupied by Si and In (c), part of sites occupied by In (d), solubility limit of Si (e), solubility limit of Si and In (f), and solubility limit of In (g). The solubility limits of Si and In are 0.6% and 2%, respectively. 256

Figure 7.13: Electrical resistivities and average visible transmittances as a function of In and Si concentrations for singly doped and co-doped ZnO thin films. The examples of SiZO (green), IZO (blue), and InSiZO (In-0.6% Si) (magenta) thin films are also shown. 257

Figure 7.14: Co-doping design model for InSiZO thin films for electrical (a) and optical (b) properties. The visible transmittance values are corrected for the glass substrate. 258

Figure 7.15: Figure of Merits as a function of dopant concentrations for SiZO (a), IZO (b), and InSiZO (c) thin films. 259

Figure 7.16: Figure of Merits as a function of In concentrations for the comparisons of IZO and InSiZO thin films. The blue area shows the superior performance of co-doped ZnO thin films. 260

Figure 7.17: Cost-based Figure of Merits as a function of In concentrations for the comparisons of IZO and InSiZO thin films. The blue area shows the superior performance of co-doped ZnO thin films. The commercial ITO (90%) value is shown as reference. 261

Figure A.1: Thermal distribution on the Heating Platform with a set temperature of ~ 40 °C observed by a thermal camera. The iron heating platform is also shown. ... 279

Figure A.2: UV-Vis-NIR optical transmittance (a) and reflectance (b) spectra of SiZO (0.6%) thin films of various thicknesses. 280

Figure A.3: Graph of $(\alpha h\nu)^2$ as a function of photon energies (a) and band gaps (b) for SiZO (0.6%) thin films of various thicknesses. 280

Figure A.4: UV-Vis-NIR optical transmittance (a) and reflectance (b) spectra of IZO (2%) thin films of various thicknesses. 281

Figure A.5: Graph of $(\alpha h\nu)^2$ as a function of photon energies (a) and band gaps (b) for IZO

(2%) thin films of various thicknesses. 281

Figure A.6: Graph of band gaps and crystallite sizes calculated from EMA of IZO (2%) thin films of various thicknesses. 282

Figure A.7: Average visible optical transmittance (400 - 750 nm) corrected for the glass substrate of IZO (2%) thin films of various thicknesses. 282

Figure A.8: UV-Vis-NIR optical transmittance (a) and reflectance (b) spectra of InSiZO (2% In-0.6% Si) thin films of various thicknesses. 283

Figure A.9: Graph of $(\alpha h\nu)^2$ as a function of photon energies (a) and band gaps (b) for InSiZO (2% In-0.6% Si) thin films of various thicknesses. 283

Figure A.10: Graph of band gaps and crystallite sizes calculated from EMA of InSiZO (2% In-0.6% Si) thin films of various thicknesses. 284

Figure A.11: Average visible optical transmittance (400 - 750 nm) corrected for the glass substrate of InSiZO (2% In-0.6% Si) thin films of various thicknesses. 284

Figure A.12: AFM images of ZnO and IZO thin films containing varying amounts of In. 285

Figure A.13: RMS surface roughnesses of ZnO and IZO thin films containing varying amounts of In calculated from the AFM data. 285

Figure A.14: SEM images of ZnO and IZO thin films containing varying amounts of In. 286

Figure A.15: Grain sizes of ZnO and IZO thin films containing varying amounts of In calculated from SEM images. 286

Figure A.16: AFM images of IZO (2%) thin films of various thicknesses. 287

Figure A.17: RMS surface roughness of IZO (2%) thin films of various thicknesses calculated from the AFM data. 287

Figure A.18: SEM images of IZO (2%) thin films of various thicknesses. 287

Figure A.19: Grain sizes of IZO (2%) thin films of various thicknesses calculated from SEM images. 288

Figure A.20: AFM images of InSiZO (2% In-0.6% Si) thin films of various thicknesses. 289

Figure A.21: RMS surface roughness of InSiZO (2% In-0.6% Si) thin films of various thicknesses calculated from the AFM data. 289

Figure A.22: SEM images of InSiZO (2% In-0.6% Si) thin films of various thicknesses. 290

Figure A.23: Grain sizes of InSiZO (2% In-0.6% Si) thin films of various thicknesses calculated from SEM images. 290

Figure A.24: SiZO: BF images of the thicker part of the lamella (a) and the thinner (b). 291

Figure A.25: Thick (a) and thin (b) parts of the lamella for IZO. Substantial thinning of the protective Pt strip is seen at the bottom right of both images. 292

Figure A.26: Under-focused BF image of SiZO, showing grain boundaries as white lines (a). HRTEM images of the boundary show clear crystalline lattice fringes right down to the glass boundary (b). 293

Figure A.27: DF image of SiZO (a) and (c) showing the large irregular morphology of the bigger grains that thread through the film. The BF image in (b) is the counterpart to (c). 294

Figure A.28: The selected area diffraction pattern from ~ 1 μm diameter patch of the thicker area of SiZO (a). The BF image of the area with the area recorded indicated (b). 295

Figure A.29: BF image of IZO (a) with the corresponding diffraction pattern (b). Two DF images were taken with the objective aperture positions shown by coloured circles (diameters are roughly correct). The DF image from the fourth ring (c) shows their corresponding diffracting grains. In (d) the aperture spans the first three rings. ... 296

Figure A.30: EDX spectra taken from ZnO at the points indicated in the image at roughly 100 nm (blue), 350 nm (red), and 500 nm (green) from the initial interface. 297

Figure A.31: EDX spectra taken from SiZO (0.6%) at the points indicated in the image at roughly 100 nm (blue), 300 nm (red), and 500 nm (green) from the initial interface. 298

Figure A.32: EDX spectra taken from IZO (2%) at the points indicated in the image at

roughly 100 nm (red), 300 nm (green), and 500 nm (blue) from the initial interface. 298

Figure A.33: EDX spectra taken from InSiZO (2% In-0.6% Si) at the points indicated along the 'super grain' in the image at roughly 100 nm (red), 350 nm (green), and 500 nm (blue) from the initial interface. 299

Figure A.34: The diffraction pattern of InSiZO with the predicted rings for hexagonal ZnO ($P6_3mc$) assuming lattice parameters a = 0.329 nm, c = 0.5241 nm. Note: the reflections {0001} and {0003} are forbidden, but may be excited by double diffraction, i.e., they are weak.. 300

Figure A.35: UV-Vis-NIR optical reflectance spectra of IZO (2%) thin films. The simulation spectrum is shown as the red curve... 301

Figure A.36: UV-Vis-NIR optical reflectance spectra of InSiZO (2% In-0.6% Si) thin films. The simulation spectrum is shown as the red curve. 301

Figure A.37: Optical (red) and Hall (black) electrical properties of SiZO (0.6%) thin films of various thicknesses. 302

Figure A.38: Optical (red) and Hall (black) electrical properties of IZO (2%) thin films of various thicknesses. 302

Figure A.39: Optical (red) and Hall (black) electrical properties of InSiZO (2% In-0.6% Si) thin films of various thicknesses. 303

List of Tables

Table 1.1: Properties of doped ZnO thin films with various dopants deposited by PLD. Data are from Liu et al. [27] 27

Table 1.2: Ionic radii of various elements. Data are taken from Shannon. [105]..... 28

Table 4.1: A summary of optical and electrical properties of reported IZO thin films. 144

Table 6.1: Element contents in ZnO, SiZO, IZO, and InSiZO thin films determined by EDX and ICP-MS. The compositions of elements in the films at the three locations: top, middle, and bottom are determined by EDX. Please refer to the detailed EDX analysis in **Appendix A6.7**. 223

Table 6.2: The ratio of O_{II} area to the total area ($O_I + O_{II} + O_{III} + O_{IV}$) for ZnO, SiZO, and IZO thin films calculated from XPS high resolution spectra. 230

Table 7.1: The values of Φ_b and L derived from the fitted curves for the samples. The electron effective mass $m^* = 0.3m_0$ is used in the calculation. [38, 39] 253

Table 7.2: A summary of thin films with best resistivities from the thesis and the literatures. 262

Table A.1: Comparisons of film thicknesses measured by Swanepoel method and TEM. 278

Chapter 1
Introduction

1.1 Aim of the Project

Indium-based transparent conducting oxides (TCOs) are widely used in optoelectronic devices. The global production of primary refined indium was 770 tonnes with the price of ca. $700 / kg in 2013, and China supplied 40% of it (**Figure 1.1**). [1, 2] However, due to the high price of In and its scarcity globally, TCOs with no or reduced In content have been studied by more and more people. [3] The first goal of this project is to use inexpensive zinc-based TCOs (ZnO) to replace expensive indium-based TCOs (typically ITO) in applications. The replacement of In by Zn can significantly reduce the TCO cost and avoid depleting the limited amounts of In available. [4, 5] The second goal of this project is to understand how doping affects compositions and crystal structures of various combinations of Si and In in ZnO and to study comprehensively how doping, film thickness, and other parameters influence the electrical and optical properties of doped TCOs. The third goal of this project is to develop an applicable non-vacuum deposition method with suitable TCO materials to satisfy the requirements on both the performance and cost which is reflected in revised Figure of Merit.

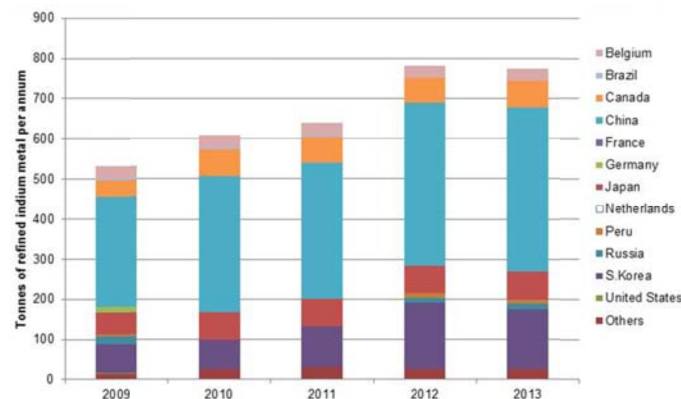

Figure 1.1: Primary indium refinery production by country from 2009 to 2013. Reproduced from Lokanc et al. [1] with permission from OSTI.

To achieve the first and third goal, a series of doped ZnO thin films have been made using spray pyrolysis (a solution-based thin film deposition technique) and characterised by a number of different techniques. (**Figure 1.2**) Singly doped (Si or In) ZnO thin films have

been explored together with co-doped (Si and In together) ZnO thin films. The detailed properties of such films have not previously been investigated. To achieve the second goal, structure analyses, elemental analyses, and data modelling studies have been carried out. Three series of films have been made and compared with each other and the optical and electrical properties have also been explored. Therefore, I can understand TCOs more deeply to shed more light on the essential differences in the zinc-based and indium-based TCOs.

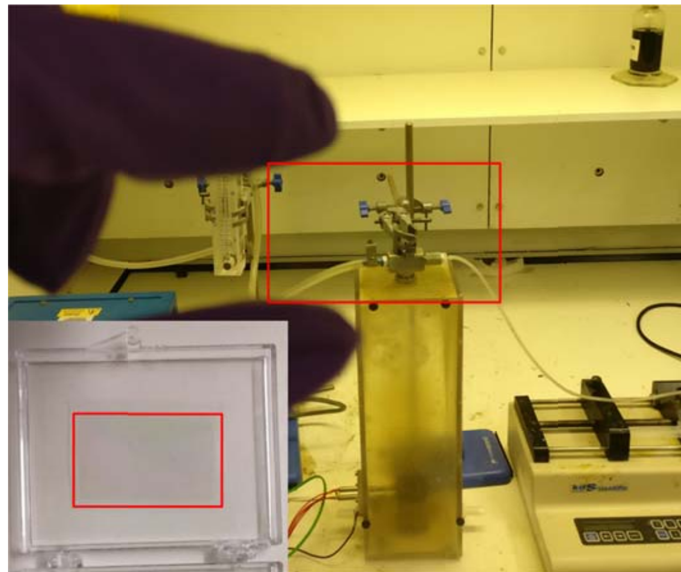

Figure 1.2: Photo of an InSiZO thin film (inset) illustrating its high transparency. The red line is the outline of the film.

The general band diagrams formed from n-type and p-type semiconductors are shown in **Figure 1.3**. Edwards et al. [6] published the band diagrams for ITOs and representative TCO materials, showing Sn atoms substituting In atoms in the lattice as n-type dopants. (**Figure 1.4**) A small amount of impurity dopant leads to the Fermi level energy laying below the bottom of the conduction band, while the Fermi level energy is above the bottom of the conduction band for a large amount of impurity dopant. [6, 7]

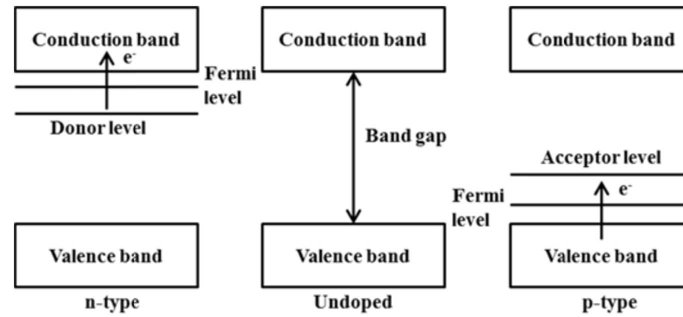

Figure 1.3: Band diagrams for undoped, n-type, and p-type semiconductors. A new filled level is formed between the valence and conduction bands for n-type semiconductors. An empty level is formed between the valence and conduction band for p-type semiconductors.

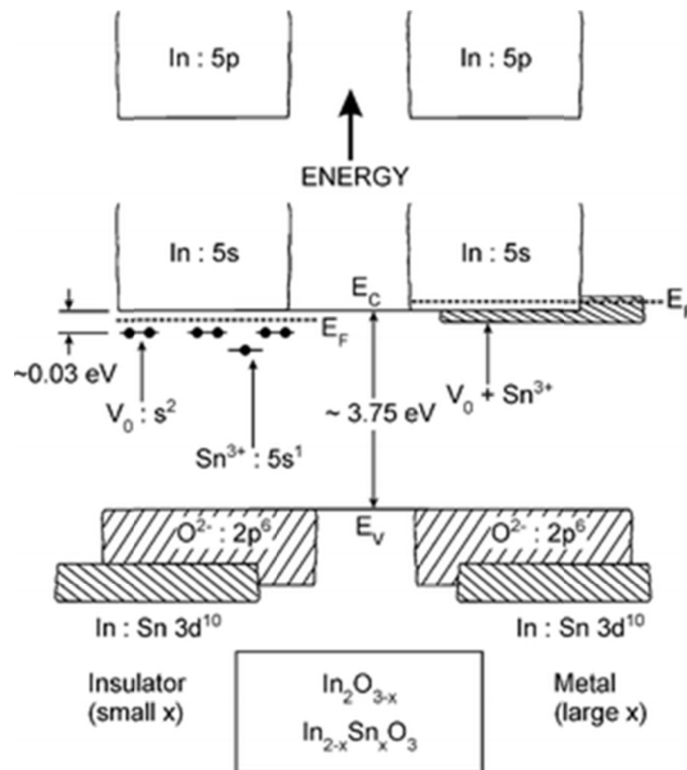

Figure 1.4: Band diagrams for ITOs with small x appearing as insulators and larger x appearing as metals. E_F is the Fermi level energy, E_C is the bottom of the conduction band, E_V is the top of the valence band, and V_O are the oxygen vacancies. Reproduced from Edwards et al. [6] with permission from the Royal Society of Chemistry.

For the first time the total chemical composition of elements in the bulk of a TCO material has been studied here using the technique of ICP-MS. Unlike surface analysis techniques such

as XPS [8] and EDX [9] adopted in previous research, ICP-MS can give the quantities and contents of the elements in the whole bulk rather than those on the surface. [10] It is very important to know the total chemical composition of a TCO thin film; thus I can investigate the origin of any observed differences. Moreover, I can also observe what the percentage of starting materials is finally deposited into a TCO thin film by our spray pyrolysis method. I have also investigated the variation of the crystal structure growth along the film thickness direction by a full TEM exploration, which is indispensable for the control of the film deposition and growth, the choice of the substrate, etc. It is also the first time that Si and In co-doped ZnO thin films have been successfully synthesised, which also have a good optoelectronic performance. The material design, the investigation of properties, and the fundamental explanations are discussed in this thesis.

1.2 Brief Experiment Design

Zinc acetylacetonate was used as a starting material to make the Zn precursor which decomposed to form ZnO thin films. Silicon tetraacetate and indium chloride were added into the Zn precursor to make SiZO, IZO, and InSiZO thin films. The doped ZnO thin films exhibit improved optical transparencies and electrical conductivities compared to undoped ZnO thin films. Dopant species, dopant concentration, and relative ratio of dopants were set as parameters to investigate the changes in optical property, electrical property, structure, morphology, and element concentration in the films. All the related properties of zinc-based thin films were compared with each other to find which had optimal optical and electrical properties.

1.3 Transparent Conducting Oxides

TCOs have been widely used in flat-panel displays, touchscreens, photovoltaics, smart windows, etc. for their high transparency at visible wavelengths and high electrical

conductivity. [11] TCO-related industries have grown fast with the expansion of information technology, mobile networks, and telecommunications. The fields of transparent thin-film transistors and flexible transparent displays are led by companies such as Samsung and LG. [12] The combination of both transparency (at the visible wavelengths of 400 - 750 nm) and electrical conductivity is possessed by groups of metal oxide materials which have wide band gaps of over 3.2 eV. [13] TCOs generally have a good reflectivity in the near-infrared region. Their band gaps are over 3.2 eV which is in the ultraviolet region far away from the visible region thus enabling the transparency at visible wavelengths. Typical TCO materials should have a low electrical resistivity (10^{-4} - 10^{-3} Ωcm) and a high optical transparency (> 80% in the visible region). [14]

TCO materials were first discovered by the German scientist Bädeker [15, 16] in 1907 by using a vapour deposition method to thermally oxidise sputtered Cd metal into transparent CdO thin films, which have good electrical conductivities. After CdO was discovered, a series of binary oxides were also found to be both highly transparent and conductive including ZnO, In_2O_3, SnO_2, Ga_2O_3, Sb_2O_5, etc. [17] Besides those, ternary oxides have been found such as $MgIn_2O_4$, $ZnIn_2O_3$, $GaInO_3$, etc. [18] What is more, representative quaternary oxides were obtained by doping ternary oxides such as Y doped $CdSb_2O_6$ [19]. The most suitable materials both in terms of excellent transparency and conductivity are based on doped indium oxide (In_2O_3) such as tin doped indium oxide (ITO) and fluorine doped tin oxide (FTO). [20] The good conductivity (~ 10^4 Scm^{-1}) and excellent optical transparency (~ 85 % or higher) make ITO outstanding amongst TCOs. [21] Moreover, high quality ITO can be prepared on a large scale in industry and is suitable for commercial applications. However, the lack of In reserves and high costs are the negative aspects of In use. [22] Though FTO is much cheaper, the harsh deposition conditions which require a very high reaction temperature (650 °C) [23] make it difficult to be applied in the manufacture of flexible or plastic electronic devices. [24]

Low cost, high durability and non-toxicity make ZnO an attractive alternative to the commonly used ITO. [25] ZnO has a direct and wide band gap in the near-ultraviolet spectral

region and a large free-exciton binding energy so that excitonic emission processes can persist at or even above room temperature. [26] One of the key challenges in developing ZnO based TCOs is finding the best metal dopants and their concentrations, in order to achieve the highest electrical conductivity. Unlike SnO_2 and In_2O_3 based TCOs, efficient doping of group III elements into the ZnO structure could decrease the resistivity significantly, potentially realising a future low cost TCO for electronic and optoelectronic applications. [27]

Edwards et al. [6] reported that the basic materials physics of TCOs are very important thus giving a clue to the applications in optoelectronic devices. The frequency-dependent dielectric function $\varepsilon(\omega)$ can be expressed as the Drude form.

$$\varepsilon(\omega) = \varepsilon_1(\omega) - i\varepsilon_2(\omega) = \varepsilon_\infty - \frac{\omega_N^2 \tau^2}{1+\omega^2\tau^2} - i\frac{1}{\omega}\left(\frac{\omega_N^2 \tau}{1+\omega^2\tau^2}\right)$$

Equation 1.1

Where ε_1 is the real part, ε_2 is the imaginary part, ε_∞ is the high frequency dielectric constant of the material, ω is the frequency, τ is the relaxation time, $\omega_N = ne^2 / \varepsilon_0 m^*$, n is the carrier concentration, e is the electron carrier charge, ε_0 is the permittivity of free space, and m* is the electron effective mass. The plasma frequency ω_p is defined when $\varepsilon_1(\omega_p) = 0$. [6] The material can have high reflectance as the frequency is less than the plasma frequency leading to a negative value of ε_1. The plasma frequency ω_p can be described as below.

$$\omega_p = \left(\frac{\omega_N^2}{\varepsilon_\infty} - \frac{1}{\tau^2}\right)^{1/2}$$

Equation 1.2

For the material with high carrier concentration and high mobility, the plasma frequency ω_p can be simplified as follows.

$$\omega_p = \frac{\omega_N}{\sqrt{\varepsilon_\infty}} = (\frac{ne^2}{\varepsilon_\infty \varepsilon_0 m*})^{1/2}$$

Equation 1.3

It can be seen that the plasma frequency depends on the carrier concentration since ω_p is proportional to $n^{1/2}$ which is the limit of TCOs. Based on the dielectric function, the reflection coefficient R(ω) is expressed as below.

$$R(\omega) = (\frac{\sqrt{\varepsilon(\omega)} - 1}{\sqrt{\varepsilon(\omega)} + 1})^2$$

Equation 1.4

Figure 1.5 shows the reflection coefficient of an ITO layer calculated from the Drude form. The reflection coefficient is close to 100%, and the absorption is weak if the frequency is lower than the plasma frequency.

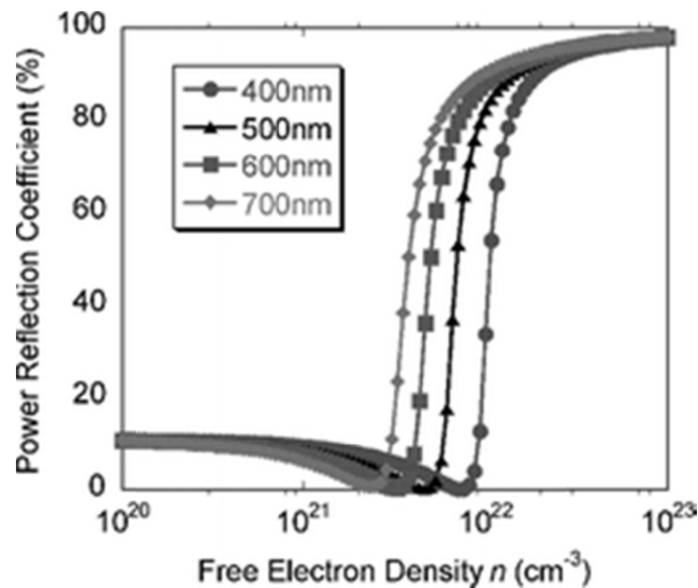

Figure 1.5: The reflection coefficients of an ITO layer as a function of electron carrier concentrations with various wavelengths. Reproduced from Edwards et al. [6] with permission from the Royal Society of Chemistry.

The transmission coefficient T is determined by $T(t) / T(0) \approx \exp(-2t / \delta)$ where t is the film thickness and δ is called the skin depth which determines the transparency of a TCO material. The absorption $A(t) \approx 1 - R$ or $1 - T$ depending on the definition. Porch et al. [28] calculated the skin depth δ which can be written as below.

$$\delta = \frac{c}{\omega}\left(\frac{2}{\sqrt{\varepsilon_1^2 + \varepsilon_2^2} - \varepsilon_1}\right)^{1/2}$$

Equation 1.5

Where c is the speed of light.

The visible transparency of a TCO material is considered acceptable if the frequency is less than the plasma frequency; therefore the skin depth is approximately proportional to $\omega^2\mu / n$ where μ is the mobility. (**Figure 1.6**) It is clear that increasing carrier concentration lowers the skin depth thus reducing the transparency. However, increasing the mobility increases the skin depth therefore higher transparency is achieved. It gives a clue for the design of TCOs that improving the mobility can achieve higher conductivity and maintain good transparency. However, increasing the carrier concentration can improve the conductivity but lose the transparency.

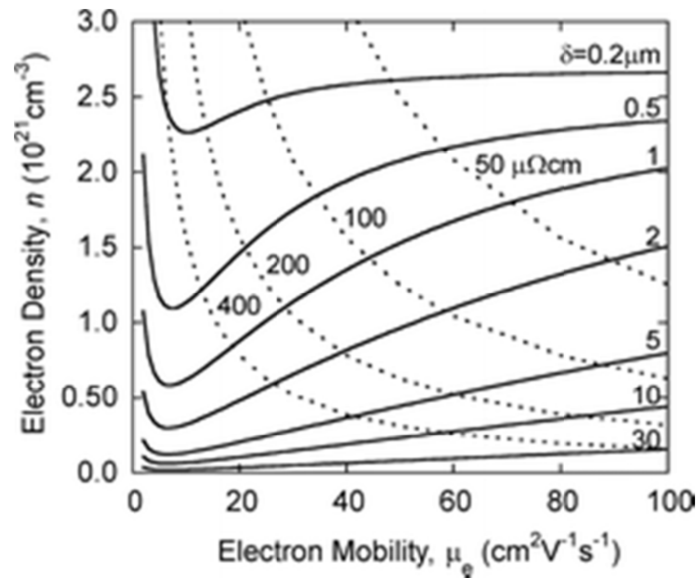

Figure 1.6: The skin depths as a function of the mobilities and the carrier concentrations (electron densities) at a fixed wavelength value of 800 nm. The electrical resistivities are also labeled. Reproduced from Edwards et al. [6] with permission from the Royal Society of Chemistry.

1.4 Applications of Transparent Conducting Oxides

TCOs can be applied widely in optoelectronic devices, solar cells, smart windows, flat-panel displays (FPDs), etc. [11] FPDs are used in touch screens, televisions, mobile phones, etc. and demand is increasing quickly. [29] TCOs should be deposited on larger substrates which can be 1 m^2. [29] Besides good conductivities and transparencies, uniform film surfaces are also required [30]. Most of TCOs are made by using DC magnetron sputtering to get high conductivities. [31] If TCOs are deposited on polymer substrates, the deposition techniques which can maintain the low temperature of the substrates, must be used. [31] TCOs can also be used as window coatings in thermal insulating windows. [32] The TCO coating can absorb or reflect infrared from the sunlight and remain transparent in the visible region, which can keep the temperature constant. Electrochromic windows are another applications for TCOs, which can change their colours and light transmittances by application of electric current. [33]

TCOs can be used as transparent current spreading layers in light emitting diodes (LEDs) thus evenly spreading the injected current to the 'near surface' area. **Figure 1.7** shows the schematic of a typical surface LED structure. r_0 is the metal contact of radius, I_d ($= I_c + I_s$) is the diode current, I_c is the direct injected current, and I_s is the spreading current which can reach the p-n junction to produce the light passing through the TCO layer. Porch et al. [34] investigated the current spreading process and used a Figure of Merit to consider the requirement of the TCO layers in LEDs including the fraction and the effectiveness of the spreading current, and the transparency of the layer. The fraction f can be expressed as $f = I_s / I_c \propto (n\mu t)^{1/2}$ where n is the carrier concentration, μ is the mobility, and t is the film/layer thickness. As discussed in the previous section, the transparency of the layer is determined by the transmission coefficient T expressed as $T(t) / T(0) \approx \exp(-2t / \delta)$. To achieve the goal of making high performance TCO layers for LEDs, the current spreading/fraction f and the transmission coefficient T should simultaneously be as high as possible. However, the feasible optimisation is to maximise the mobility μ and keep a reasonable carrier concentration n which is not too high since the skin depth δ is approximately proportional to $\omega^2\mu / n$.

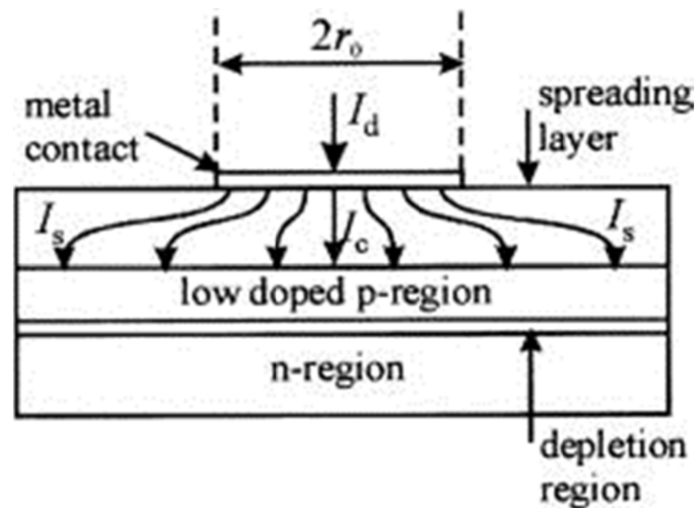

Figure 1.7: Schematic of a typical surface LED structure. Reprinted from Porch et al. [34], with the permission of AIP Publishing.

Another important application of TCOs is for thin-film photovoltaic cells. **Figure 1.8** shows a

schematic of a typical module structure of a thin-film photovoltaic cell. The TCO layer can spread the current by connecting the active cells. The important role of the TCO layer is the power transmission T_T including optical T_{opt} and electrical T_{elec} through the thin-film photovoltaic cell. Slocombe et al. [35] and Porch et al. [28, 34] found that The total power transmission is proportional to the value of $T_{elec} \times T_{opt} = n\mu t \times \exp(-2t / \delta)$. [28, 34, 35] The optimisation of the TCO layer depends on the maximisation of the power transmission T_T. However, the conflicts between the carrier concentration and mobility still exist which are similar to the case of LEDs. Therefore, the optimisation values of higher mobility and lower carrier concentration are required to achieve the best power transmission for photovoltaic cells.

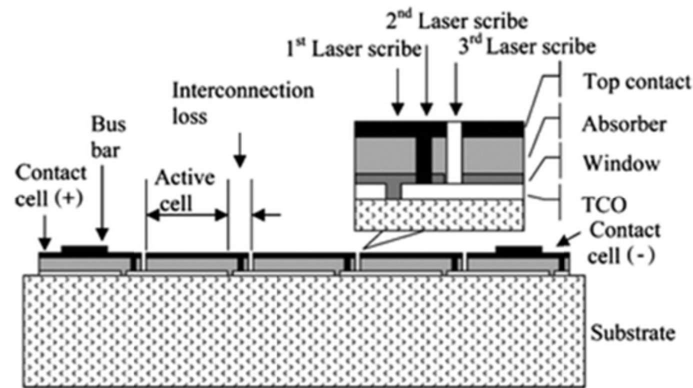

Figure 1.8: Schematic of a typical module structure of a thin-film photovoltaic cell. Republished with permission from Slocombe et al. [35-37]; permission conveyed through Copyright Clearance Center, Inc.

1.5 Thin Film Deposition Techniques

The performances and properties of thin films highly depend on the deposition techniques and their related parameters. Generally, the deposition method of thin films can be divided into two categories, the physical deposition method and the chemical deposition method. The physical deposition method uses high energy, normally electrical energy, to transfer the compounds from starting materials to the targeted substrate. The compounds are directed by

the electric field, the magnetic field, or other forces to deposit on the substrate. Many parameters can vary the performance and the quality of the films including the temperature, the gas pressure, the mixing of gases, the input energy, the reacting time, the position of the substrate, etc. The available physical deposition methods can be thermal evaporation, e-beam evaporation, ion plating, pulsed laser deposition, magnetron sputtering, DC sputtering, RF sputtering, reactive sputtering, plasma spray, thermal spray, etc. [38] The chemical deposition method usually uses flowing liquids or gases to transfer the compounds to the substrate, where the films are formed by chemical reactions. The big family of chemical deposition methods includes chemical vapour deposition (CVD), electroplating, electroless plating, sol-gel process, atomic layer deposition (ALD), spray pyrolysis, etc. [39]

1.5.1 Physical Deposition Methods

Vacuum Evaporation

Vacuum evaporation is an easy to operate and is a fast deposition method involving heating and evaporating the starting materials in vacuum, followed by the transfer and deposition on a substrate. This method can be applied in the electronics industry, such as electronic circuits, optical sensors, and conducting polymers. [40]

Thermal evaporation evaporates the starting materials in vacuum, followed by the vaporised particles hitting a substrate (**Figure 1.9**). The vaporised particles then condense on the substrate forming a thin film. The film can be either a single material or a mixture of several materials of various thicknesses from angstroms to micrometres. The choice of starting materials is flexible, and can be simple substances and molecular compounds. The substrates are usually glasses; however, wafers, metals, and semi-finished materials can also be the choice. [41]

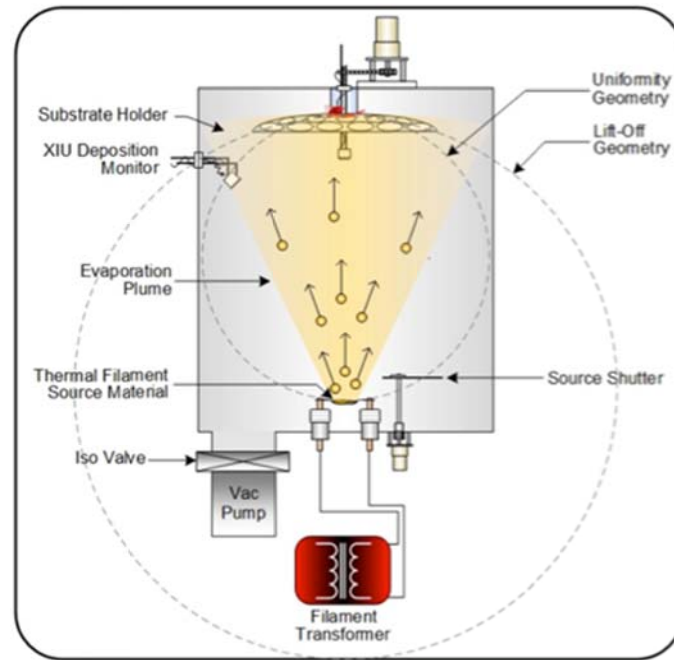

Figure 1.9: Schematic of a thermal evaporation process. Reproduced from Hardy [41] with permission from Semicore.

E-beam evaporation operates in a similar way to thermal evaporation, but it is an upgraded technique (**Figure 1.10**). The heating source is changed into a high energy focused electron beam, which heats the starting materials uniformly and obtains a faster deposition speed. The e-beam source generates electrons, which are accelerated and directed to the starting materials. A cooling system is assembled to prevent any unnecessary reactions and protect any key components of the equipment. It can also deposit films with multiple materials by assembling more than one e-beam source, thus evaporating different materials in the synthesis process. [41]

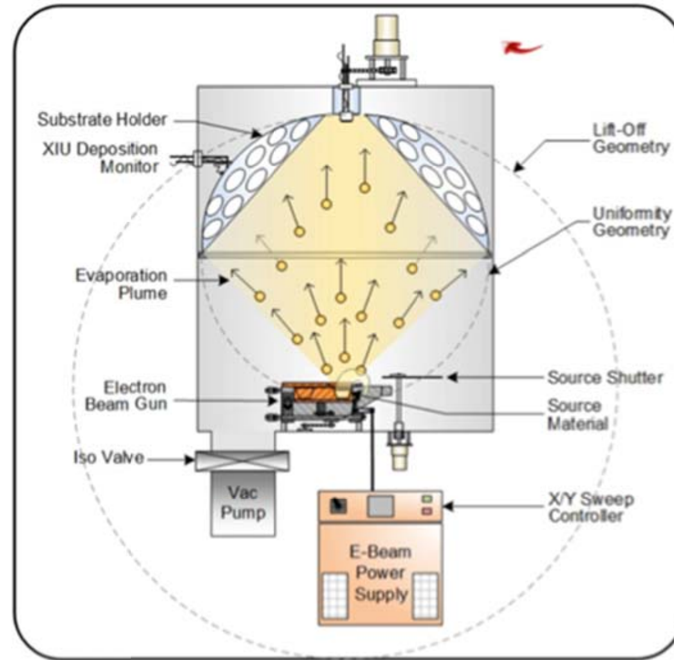

Figure 1.10: Schematic of an e-beam evaporation process. Reproduced from Hardy [41] with permission from Semicore.

Pulsed laser deposition (PLD) uses high energy pulsed laser to ablate the target materials in vacuum, thus producing vaporised particles to be deposited as films on the substrate (**Figure 1.11**). The interaction between the laser beam and the target material ablates small fragments, followed by a transfer process to the substrate. The advantage of PLD is that the ablated small particles have similar stoichiometry to the original target material due to the mechanism of the material ablation, which is different from the vacuum evaporation process. Therefore, PLD can be a well-controlled technique to deposit films with a specific stoichiometry. [42]

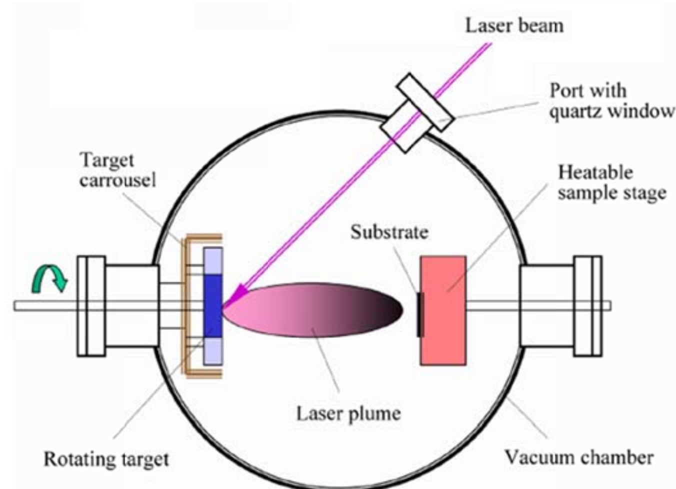

Figure 1.11: Schematic of a pulsed laser deposition process. Reproduced from Schwarz [42] with permission from Schwarz.

Sputtering

Sputtering uses high energy particles to strike the target material; thus the atoms, which come out of the target material, are deposited on a various substrate including glasses, wafers, and semi-finished materials (**Figure 1.12**). It was first discovered by Peter J. Clarke in 1970 [43] when he made the first sputter gun in the history to deposit high quality films on the atomic level in vacuum. The vacuum reactor is usually filled with inert gas (such as argon). The target material is negatively charged to start the generation of the plasma. The argon atoms are positively charged due to the loss of the outer shell electrons in the collision process with the electrons from the target materials with negative charges. The attraction between the positively charged argon ions and negatively charged target material leads to a strong bombardment to ablate particles off the target material. The particles with very high kinetic energies travel a distance and are finally deposited on the substrate. Sputtering is an atomic-level deposition technique, which is more accurate and has better film quality compared with the thermal evaporation method. The composition and the property of the particles highly depend on the input energy, the momentum of the ions, the target properties, the nature of the target surface, etc. The sputtering types are magnetron, DC, RF, and reactive sputtering. [44]

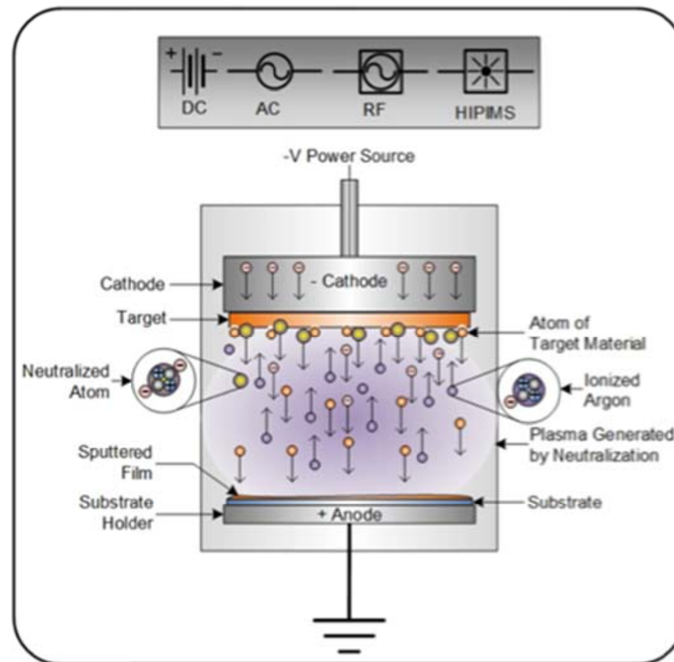

Figure 1.12: Schematic of a sputtering process. Reproduced from Hughes [44] with permission from Hughes.

1.5.2 Chemical Deposition Methods

Chemical Vapour Deposition

Chemical vapour deposition (CVD) breaks the starting materials down to smaller molecules into the gas phase, and then the films are formed on the substrate (**Figure 1.13**). [45] There are two parts in the deposition process. One is the homogeneous gas phase reaction; the other is the heterogeneous film formation process on the substrate. CVD is generally carried out in vacuum to prevent any side products formed from the atmosphere or the incorporation of unreacted starting materials and to enhance the vapourisation of the precursor. There are different types of CVD techniques including atmospheric pressure chemical vapour deposition (APCVD), metalorganic chemical vapour deposition (MOCVD), low pressure chemical vapour deposition (LPCVD), ultrahigh vacuum chemical vapour deposition (UHVCVD), and laser chemical vapour deposition (LCVD). [46] Atomic layer deposition

(ALD) is a special CVD technique. ALD can precisely adjust the thickness growth of a film on the scale of angstroms, as well as the composition of the film. Consequently, ALD is better than other CVD or even physical vapor deposition (PVD) methods based on its advantages of the mapping of a surface, the thickness adjustment, and the film composition control. [47]

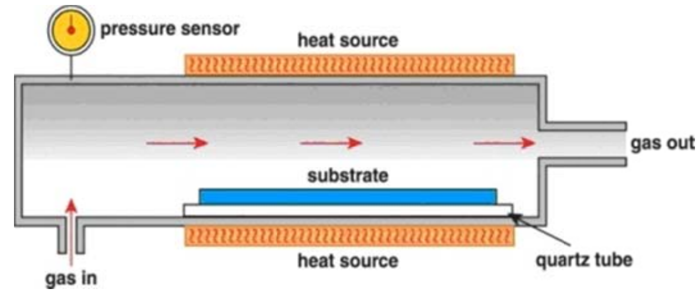

Figure 1.13: Schematic of a chemical vapour deposition process. Reproduced from [48] with permission from Strem Chemicals.

Sol-Gel Process

The sol-gel process [49] makes films from a colloidal solution called a sol and an integrated network called a gel (**Figure 1.14**). The gel is formed by the sol as an assembly of small particles and polymers. The sol is the homogeneous distribution of small particles in the liquid while the gel is the assembled network incorporated with the liquid. The forces or the interactions, such as van der Waals forces and hydrogen bonds, inside the sol are usually weak while those inside the gel are covalent bonds, which are incapable of being reversed. In the whole film deposition process, a drying process is always required to dispose of any solvents or residuals from the starting materials. However, the shrinkage and densification of the wet film usually occur due to the capillary forces. The final step to obtain a solid film is a thermal treatment or sintering for the condensation reaction or any other reactions, which leads to a desirable product of a film with acceptable quality. Two types of gels can be formed in different drying processes. A xerogel is formed in a normal evaporation process where the porous network structure is damaged, whereas an aerogel is formed in a supercritical condition where the porous network is still maintained and present. [50-52]

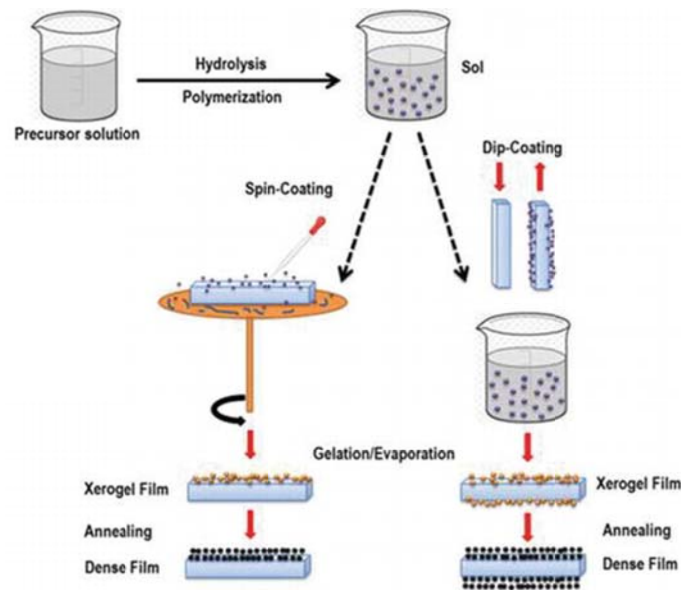

Figure 1.14: Schematic of a sol-gel process. Reproduced from Mahmood et al. [53] with permission from InTech.

Spin Coating

Spin coating is used to deposit films from a precursor solution or a mixture with a high spinning speed (**Figure 1.15**). It is widely used to make extremely smooth and ultrathin films with the thicknesses of less than 100 nm. Spin coating is an advanced technique to deposit good quality thin films with an easy and rapid operation process. The quality, structure, and uniformity of the films can be retained consistently due to the rapid drying process, which is attributed to the high airflow and the high spin speed. There are varieties of parameters leading to the variations of the film performance including the precursor solution, the solvent, the spin speed, the temperature for drying, the atmosphere, the airflow speed, and the viscosity of the precursor. [54, 55]

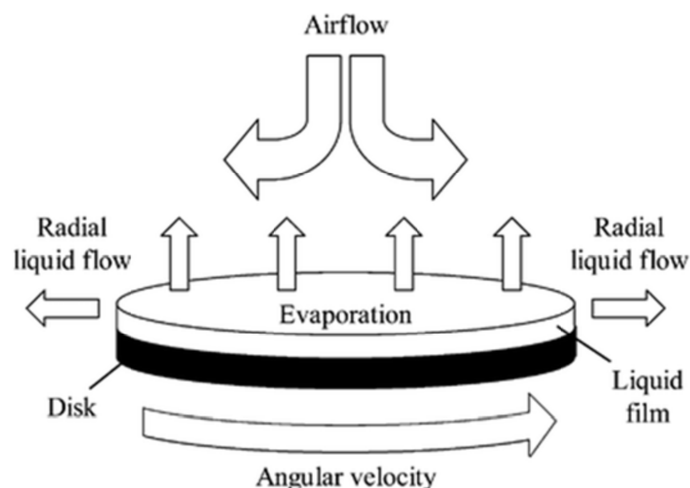

Figure 1.15: Schematic of a spin coating process. Reproduced from Norrman [56] with permission from the Royal Society of Chemistry.

Spray Pyrolysis

Spray pyrolysis is the technique I use in this thesis, which deposits thin films on a heated substrate by spraying on a precursor solution (**Figure 1.16** and **Figure 1.17**). The decomposition, reaction, and formation of a thin film occur at the surface of the hot substrate. It is a widely used deposition technique to make metal oxide thin films such as SnO_x, an example of a TCO. [57] Chamberlin and Skarman [58] reported their work on the deposition of CdS films for solar cells [59, 60] in the early development of the technique in 1966. Maudes et al. [61] and Pamplin et al. [62] reviewed and summarised the spray pyrolysis technique in the deposition of transparent conductors. I can zoom in on the technique and discuss the control process, the parameter setting, the film quality and property analysis, and its applications. [63]

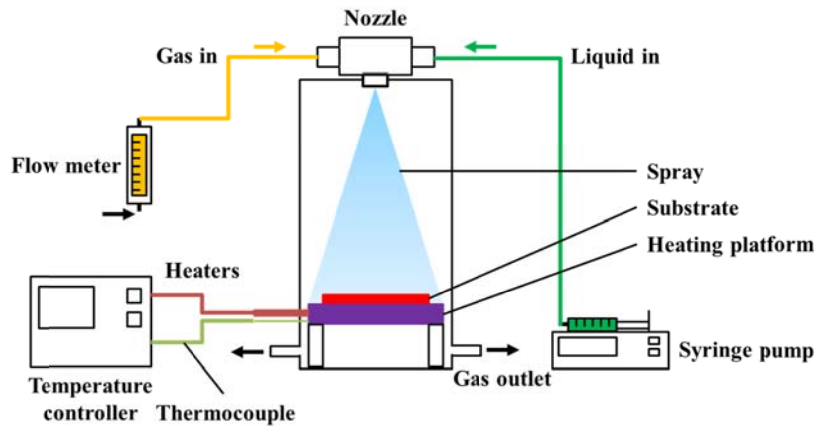

Figure 1.16: Schematic of the spray pyrolysis process used in this investigation.

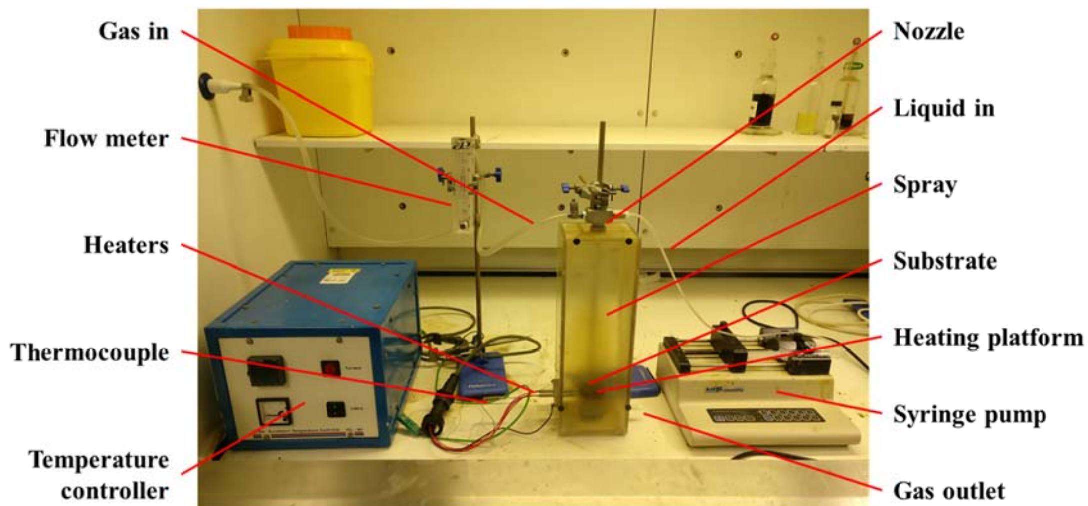

Figure 1.17: Photo of a spray pyrolysis apparatus in a laboratory.

Viguie et al. [64] classified the spray pyrolysis as two different processes depending on the reactions. One process is that the evaporation of the solvent is on the substrate surface, followed by a solid reaction. The other process is that the solvent evaporation occurs before the precursor droplets reach the substrate surface and the solid strikes to the substrate surface. Either of these processes is affected by the flow rate of the carrier gas, the precursor solution concentration, the deposition temperature, the distance between the spray nozzle and the substrate, the precursor solution pumping speed, the size of the droplet, the solvent, etc. The low cost of spray pyrolysis and the high film uniformity make it a promising technique to be used in industry. There is no requirement for high vacuum or expensive equipment compared

to CVD methods and physical deposition methods. It is more friendly and flexible to make doped thin films by changing the composition of the precursor solution. The film thickness can be easily controlled by adjusting the precursor solution volume, which is a straightforward process. The deposition temperature for spray pyrolysis is usually 600 °C or less, which makes it friendly and less restricted to the substrate material compared to some high energy deposition methods such as sputtering. Spray pyrolysis can also make thin films with complicated layer compositions such as the distribution of various chemical compositions along the thickness direction of a film. A huge variety of thin films can be deposited by spray pyrolysis including oxides, adamantine copper compounds, and binary/ternary chalcogenides. [65]

The film deposited by spray pyrolysis sometimes has small grain sizes, which can be a disadvantage. However, a post annealing process can improve the quality and the crystallinity of the film, thus enhancing the performance of the film. [63]

1.6 ZnO

ZnO is a low cost TCO material and is used widely in applications such as photovoltaic solar cells due to its high electrical conductivity and optical transparency. Although there has been a huge development in TCO materials in the past decades, a better TCO material is still required for photovoltaic solar cells. The ideal electrical resistivity and visible transparency are 10^{-5} Ωcm and 80%, respectively. [66] Thin film photovoltaic solar cells [67], could reduce their cost by using less and cheap raw materials, as well as optimising the manufacturing process. The TCO material is one of the key components in solar cells and can determine their efficiency. It is generally easier to obtain ZnO thin films with a good transparency, whereas it is more difficult to get a good electrical resistivity. The lowest reported electrical resistivity is ~ 10^{-4} Ωcm. [68] In most cases, a higher electrical conductivity is associated with a lower transparency; therefore, the optimisation of both properties can be challenging. [69] There are

many parameters that determine the electrical and optical properties of ZnO thin films including the intrinsic defects, the surface morphology, the nature of the dopant, the doping effect, the grain structure and arrangement, the grain boundaries, the in-grain effect, the crystal structure, etc.

The most common way to improve the electrical and optical properties of ZnO thin films is by doping, which can be n-type or p-type. Group III and VII elements [70] are usually used as n-type dopants while group I and V elements [71] behave as p-type dopants for ZnO thin films. The improved electrical conductivity by n-type doping is attributed to both intrinsic and extrinsic donor defects. However, the enhancement of p-type doping is similar to that of n-type doping, but it is rarely used due to technical difficulties and non-reproducibility. [72]

The reported n-type dopants in group III are B, Al, Ga, and In, and TCOs containing them show relatively low resistivities and high transparencies. [73] However, their low resistivities are still not low enough to be used in photovoltaic solar cells. Co-doping becomes a potential option in improving electrical conductivity and has been explored by a few researchers. Dutta et al. [74] reported Al-N co-doped ZnO thin films to have better visible transparencies than those of N singly doped ZnO thin films. Hyun-il [75] reported B and Al co-doped ZnO thin films with a lowest observed electrical resistivity of 5.16×10^{-4} Ωcm and highest visible transparency of 85%. What is more, it was reported that the electrical and optical properties could also be even improved by using Al and Ga as the dopants due to the superior doping performance of Ga compared with B.

P-type doping to enhance electrical and optical properties is rarely used due to the reduced choice in the dopants and difficulties in the control of the reactions. The commonly used p-type dopants are group V elements including N, P, and As. [71] Nevertheless the doping mechanism for N is still not fully understood and the stability of these materials is a restriction for N doped ZnO thin films. The co-doping of ZnO thin films between N and other elements such as Al, Ga, In, and Si has been attempted. [76] The results show that Al and Ga

are acceptable for use while In and Si are not when co-doped with N in ZnO thin films. The p-type doped thin films clearly highlight the restrictions in the conductivity, the stability, and the control in the synthesis and doping process. The co-doping for In and N may be a possible combination, but that requires further exploration. [77]

1.7 Precursors for ZnO

The precursors are normally a mixture of compounds containing the cationic or anionic dopant in a range of solvents. The precursors, which are typically used to deposit ZnO thin films, include zinc acetate [78-80], zinc acetylacetonate [81-83], zinc nitrate [84-86], and zinc chloride [87, 88]. Additionally, acetate, acetylacetone, nitrate, or chloride are also introduced into the solution, since the corresponding compounds are available in the commercial market at a low cost. Metal-organic compounds can also be precursors, but the appropriate solvents must be carefully selected.

Zinc acetylacetonate hydrate ($Zn(C_5H_7O_2)_2 \cdot xH_2O$) is a white crystalline powder with a solubility of 6.9 g / L in water at room temperature. [89] In the solid state structure of zinc acetylacetonate, a six-membered ring is formed by the O atoms of the acetylacetonate ligands bonding to a Zn atom (**Figure 1.18**) with a tetrahedral geometry.

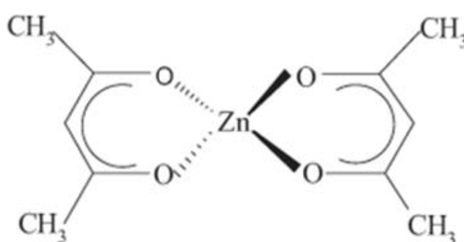

Figure 1.18: Schematic of the zinc acetylacetonate structure.

There are two steps in the formation process of ZnO thin films from starting materials. (**Figure 1.19**) Acetylacetone undergoes an alcoholysis reaction in an acidic solution and then

produces acetone, isopropyl acetate, and Zn-OH species. [90] Zn-OH species finally experience a condensation reaction forming products with Zn-O-Zn bonds, which are then converted into ZnO thin films (**Figure 1.19**). [90]

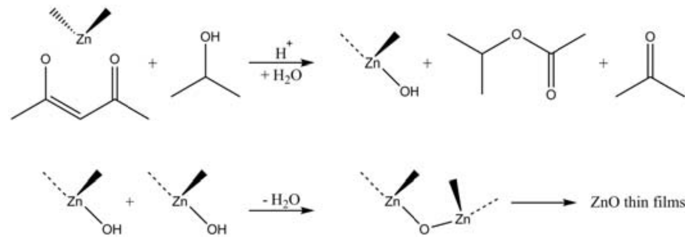

Figure 1.19: Schematic of zinc acetylacetonate decomposition mechanism in an acidic solution. Adapted from Ambrozic et al. [91] with permission from the Royal Society of Chemistry.

A thermal decomposition process for zinc acetylacetonate in a humid atmosphere was reported by Arii et al. [92] as shown below. Here the acetylacetonate ligand is protonated and lost as acetylacetone.

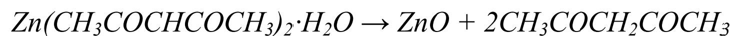

$$Zn(CH_3COCHCOCH_3)_2 \cdot H_2O \rightarrow ZnO + 2CH_3COCH_2COCH_3$$

Equation 1.6

By controlling the partial pressure of water vapour, crystalline ZnO was synthesised at a temperature below 100 °C. [92]

1.8 Doping of ZnO

Usually pure, polycrystalline ZnO thin films have limited intrinsic electrical properties. [93] Therefore polycrystalline ZnO thin films need to be doped with suitable impurity elements including group III, VII, and IV elements to enhance their stability and electrical properties. Extrinsic dopants play an important role in populating the conduction band so that both the carrier concentration and the conductivity and of ZnO are increased. The lowest reported

resistivity value is 1.2 - 2 × 10^{-4} Ωcm. [77, 94] **Figure 1.20** shows the reported minimum resistivity values for doped ZnO, In_2O_3, and SnO_2 in the period 1970 - 2000. The minimum resistivity values for In_2O_3 and SnO_2 are 1 - 2 × 10^{-4} and 3 - 4 × 10^{-4}Ωcm, respectively in 1980 - 2000. However, doped ZnO has made great progress in decreasing the minimum resistivity value, thus approaching that of ITO with a value of ~ 0.7 x 10^{-4} Ωcm deposited by PLD. [77]

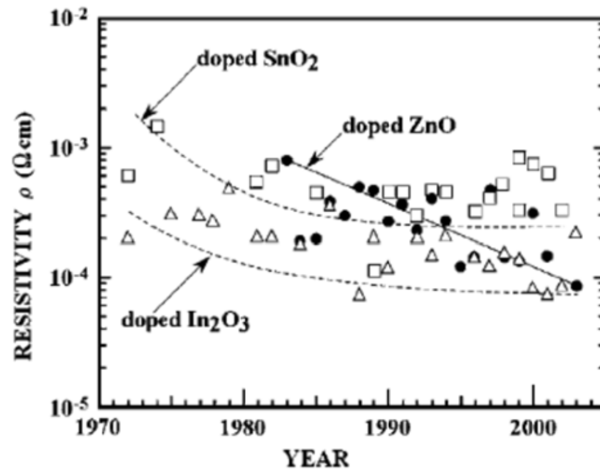

Figure 1.20: Graph of reported minimum resistivity values for doped ZnO (black circles), In_2O_3 (blank triangles), and SnO_2 (blank squares). Reproduced from Otiti [77] with permission from Otiti.

The doping performance is determined by the solubility of the dopant in the lattice, the compensation of the dopant from native defects, the dopant activation energy, etc. In practice, p-type doping is more difficult than n-type doping due to the low solubility of the p-type dopants and the compensation from the existing n-type character. [95]

1.8.1 n-Type Doping

Doping of n-type for ZnO can be intrinsic or extrinsic by intrinsic defects and impurity doping, respectively. Either Zn interstitials or oxygen vacancies can be intrinsic defects contributing to intrinsic n-type doping. Meanwhile, both substitutional and interstitial hydrogen leads to extra donor density in the ZnO lattice in this case. The precise argument for the mechanism of the extra or excess electron generation is still unresolved. [77]

The impurity dopants for ZnO can be group III (B [96, 97], Al, Ga, and In [98]), IV, and VII (F [99]) elements. [70] Al and Ga are widely used and investigated by numerous researchers, who found that the film deposition technique can determine the solubility limit of dopants and the position which dopants take up. **Table 1.1** shows the properties of doped ZnO thin films with various dopants deposited by PLD. All the doping contents were optimised to obtain a good performance both in electrical and optical properties. [27]

Dopants	Target content (%)	Thickness (nm)	Resistivity (Ωcm)	Transmittance (%)
Al	2	500	4.5×10^{-4}	88%
Ga	5	200	8.12×10^{-4}	> 90%
In	40	> 1000	4.02×10^{-4}	> 85%
F	2	200	4.83×10^{-4}	> 90%
Si	2	~ 150	6.2×10^{-4}	~ 80%

Table 1.1: Properties of doped ZnO thin films with various dopants deposited by PLD. Data are from Liu et al. [27]

The group III elements including B, Al, Ga, and In are normally good donors in doped ZnO. A high temperature can excite the extra electrons in the donor level into the conduction band. Hu et al. [100] deposited AZO thin films with a high carrier concentration of 8×10^{20} cm^{-3} by CVD. **Table 1.2** shows the ionic radii of various elements. The smaller ionic radius of Al^{3+} (0.39 Å) makes it easier to replace Zn^{2+} (0.6 Å) in the ZnO lattice, leading to a contraction of the unit cell. However, the ionic radius of Ga^{3+} is closer to that of Zn^{2+} leading to a smaller lattice distortion even on a higher doping level than that of Al^{3+}. [98, 101] Consequently, Ga doping can achieve excellent performance in the electrical properties for doped ZnO thin films. [102] Geng et al. [103] deposited AZO thin films on a Si (100) substrate by ALD. The electrical resistivity reduces as the Al doping level increases with the minimum value of 9.36 $\times 10^{-4}$ Ωcm when the Al concentration is 2.7 at%. However, the film crystallinity is weakened with the increasing Al doping level. Ko et al. [104] found that the degradation of GZO thin

films at a high doping level with a carrier concentration of 10^{20} cm^{-3} does not occur, which differs from AZO thin films.

Ions	Charge	Coordination	Ionic radius (Å)
Zn	2	4	0.6
Zn	2	6	0.74
Al	3	4	0.39
Al	3	6	0.535
In	3	4	0.62
In	3	6	0.8
Si	4	4	0.26
Si	4	6	0.4

Table 1.2: Ionic radii of various elements. Data are taken from Shannon. [105]

The group IIIB elements (e.g., Sc and Y) can also be proper dopants to deposit films with good electrical and optical properties by sputtering. The reported resistivities of Sc and Y doped ZnO thin films are 3.1×10^{-4} Ω cm and 7.9×10^{-4} Ω cm, respectively. Both of these films have high visible transparencies of ~ 85%. [106] The lower resistivity in Sc doping is due to the closer ionic radii between Sc^{3+} and Zn^{2+} compared with those of Y^{3+} and Zn^{2+}. [106] Most of the rare earth metals have a high risk in supply due to politics or their distributions, whereas for Sc this is not the case. [107] Meanwhile, AZO thin films, which are cheaper and have no supply risk, can beat Sc doped ZnO thin films. Therefore, Sc is less attractive than other dopants such as Al. [14]

Group VII elements, especially F, also behave as n-type dopants to improve the electrical properties of ZnO thin films. [99] F can occupy the substitutional sites of oxygen in the lattice successfully due to the close ionic radii of F^- (1.31 Å) and O^{2-} (1.38 Å). Cao et al. reported that F doped ZnO thin films deposited by PLD have good performance in both electrical and optical properties with a carrier concentration of 5.43×10^{20} cm^{-3}, a mobility of 23.8 cm^2 / Vs,

a resistivity of 4.8×10^{-4} Ωcm, and a very high visible transparency of over 90%. [27, 108]

1.8.2 p-Type Doping

Doping of p-type for ZnO thin films are more difficult to make compared to n-type ones. [93, 109-112] ZnO is an intrinsic n-type conductor with native oxygen vacancies, which is not helpful to p-type doping. [71, 93, 109-112] What is more, the native defects of ZnO compensate the p-type dopants. [113-116] These three reasons make p-type doping very hard in ZnO. The excitation of extra electrons in the valence band into the acceptor level is difficult for the dopants of group I (Li, Na, and K) and group IB elements (Cu, Ag, and Au). [117-119] N is the only proper acceptor in ZnO because O has a much larger electronegativity [120] than P, As, and Sb in ZnO. [117] Therefore, the reported p-type doped ZnO thin films are few. [121-130] It has been proposed that p-type dopants P, As, and Sb occupy substitutional Zn sites, followed by formation of lattices with Zn vacancies. [131] However, the high formation energy suggests that such reactions are impossible. [124-129] Different from N doped ZnO [123, 130], no stable p-n junctions in ZnO have been reported. It is why I cannot say successful p-type doping such as P, As, and Sb has been obtained due to a lack of a reliable report on the observed performance and the existence of a stable structure. [26]

1.8.3 Co-Doping

Co-doping is an effective method to obtain doped ZnO thin films with high optoelectronic performance. The most important co-doping, which can enhance the electrical conductivity of ZnO thin films, is achieved by using two n-type electron donation dopants. If both of these dopants are cations to occupy the substitutional Zn sites in the lattice, it is called cation-cation co-doping. Some of the reported cation-cation co-doped ZnO thin films are Al-Ga [132, 133], and Al-Si [134] deposited by vacuum techniques. There is another co-doping called cation-anion co-doping if one of the dopants occupies the substitutional Zn sites and the other

anions substitute O sites in the lattice. The reported cation-anion co-doped ZnO thin films include Al-F [135, 136], In-F [137-140], and Al-Cl [141]. The extra electrons, which are provided by the second donor dopant, can enhance the electrical conductivity of co-doped ZnO thin films.

1.9 Structure of ZnO

Most of the binary compounds formed from Group II and VI have the cubic zinc blende structure or hexagonal wurtzite structure (**Figure 1.21**). Each cation is tetrahedrally surrounded by four anions while each anion is also tetrahedrally surrounded by four cations. The cation is sp^3 tetrahedrally coordinated with an ionic character in the bond. The most thermodynamically stable structure of ZnO is hexagonal wurtzite. However, the zinc blende structure can form if growth occurs on a cubic substrate while the rocksalt structure can be formed at high pressure. [93]

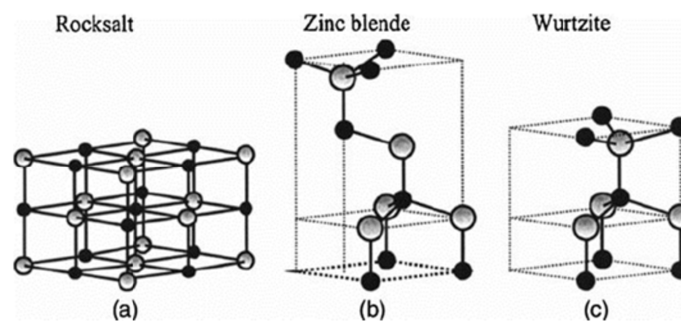

Figure 1.21: Schematic of ZnO crystal structures including cubic rocksalt (a), cubic zinc blende (b), and hexagonal wurtzite (c). Zn atoms are grey circles and O atoms are black circles. Reprinted from Ozgur [93], with the permission of AIP Publishing.

The unit cell parameters of hexagonal wurtzite structure are a = b and c. The relation between a and c is $c / a = \sqrt{(8 / 3)} = 1.633$. Its space group belongs to C_{6v}^4 or $P6_3mc$. [142] The structure is hexagonal-close-packed with $u = 3 / 8 = 0.375$, where u is the bond length parallel to the c axis. Each unit cell contains two Zn atoms and two O atoms. Each Zn atom is

tetrahedrally coordinated with four O atoms, and vice versa. The actual ZnO crystal structure may distort from ideal with a modified value of u or c / a. The normal parameters a and b are in a range of 3.2475 - 3.2501 Å while 5.2042 - 5.2075 Å is for parameter c. The value of c / a and u can be more flexible in a range of 1.593 - 1.6035 and 0.383 - 0.3856, respectively. The lattice distortion may depend on its stability and ionicity. The possible distortion of the unit cell can also be attributed to Zn anti-site defects, Zn interstitial defects, oxygen vacancies, etc. [93]

Hexagonal wurtzite ZnO can be transformed into the rocksalt structure at high pressure. Hence the decreased lattice parameters lead to an increased interionic Coulomb interaction. The rocksalt structure is sixfold coordinated and belongs to Fm3m. However, the stabilisation of the rocksalt structure for the crystalline overlayer on a crystalline substrate is impossible. Bates et al. [143] reported that the transformation of ZnO from hexagonal wurtzite structure to the rocksalt structure occurs at a pressure of 10 GPa and its volume decreases by 17%. This structure can be stable for a long time at ambient pressure and a temperature of over 100 °C. Gerward et al. [144] and Recio et al. [145] studied the ZnO structure transformation by using energy-dispersive X-ray diffraction (EDXRD) with synchrotron radiation. They found the transformation starts at a pressure of 10 GPa and finishes at a pressure of 15 GPa. It also indicates that a large portion of the rocksalt structure persists even at a pressure of zero.

The zinc blende structure of ZnO can be stabilised by growth on cubic substrates including ZnS [146], ZnS/GaAs [147], and Si/SiO_2/Pt/Ti [148]. The substrate acts as a template to prevent the tendency to form the thermodynamically stable hexagonal wurtzite structure. The space group of the zinc blende structure is $F\bar{4}3m$ with face-centred-cubic structures. Each unit cell contains two Zn atoms and two O atoms. Each Zn atom is tetrahedrally coordinated with four O atoms, and vice versa.

1.10 Optical Properties of ZnO

The optical properties of TCO materials are related to the electronic properties. The Drude free electron model can be used to explain the interaction between light (i.e., electromagnetic radiation) and conduction electrons. [149] **Figure 1.22** shows the transmittance, reflectance, and absorption spectra of a TCO material. The whole spectra consist of three regions according to the wavelength. One region covers the visible wavelength, which is 400 - 750 nm or 3.1 - 1.7 eV. A TCO material must be transparent in this region. The light can be absorbed due to band-to-band transitions in the short wavelength region, normally < 350 nm or 3.5 eV. A steep drop in transmittance and an increase in absorption can be observed at the same time. The typical band gaps for most TCO materials are larger than 3 eV. In the long wavelength region (> 1500 nm), I can observe a decrease in transmittance and an increase in reflectance. Meanwhile, a maximum absorption is present indicating the equal frequency of the light and that of oscillation of electrons in the TCO material. The corresponding wavelength at this maximum absorption is called the plasma wavelength λ_p. If the light wavelength is less than the plasma wavelength, the material is transparent because the wavefunction of the conduction electrons can oscillate and the radiation can propagate. However, if the light wavelength is larger than the plasma wavelength, the wavefunction attenuates and the radiation can not propagate; hence a reflection occurs. The square of the plasma wavelength is inversely proportional to the carrier concentration; therefore, there is a balance between the transmittance and the carrier concentration. One of the possible ways to enhance electrical conductivity without lowering the visible transparency is to improve the electrical mobility rather than the carrier concentration. It can be achieved by reducing so-called in-grain scatterings and grain boundary effects. [150]

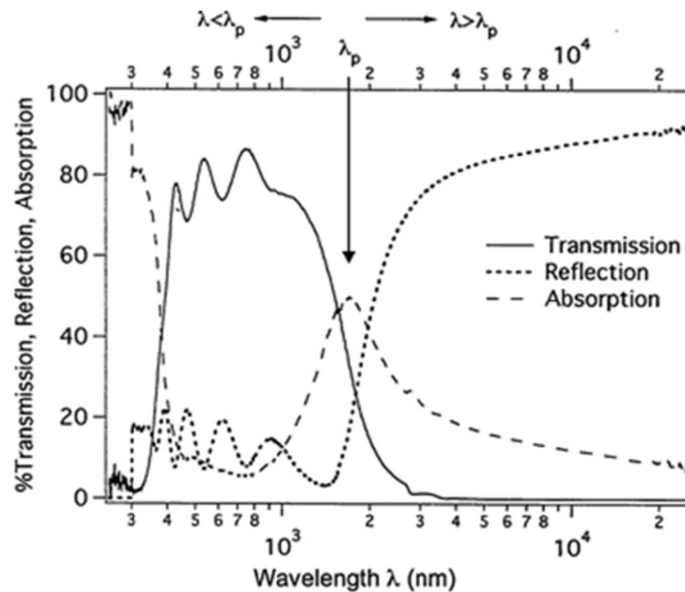

Figure 1.22: Transmittance, reflectance, and absorption spectra of a TCO material. Reproduced from Pasquarelli et al. [151] with permission from the Royal Society of Chemistry.

The optical band shift is attributed to the Burstein-Moss (BM) band-filling effect (**Figure 1.23**). The optical band gap blue shift for heavily doped TCO materials is due to the block of lower states in the conduction band. [152, 153] Lai et al. [154] observed a blue shift of the optical band gap in AZO thin films.

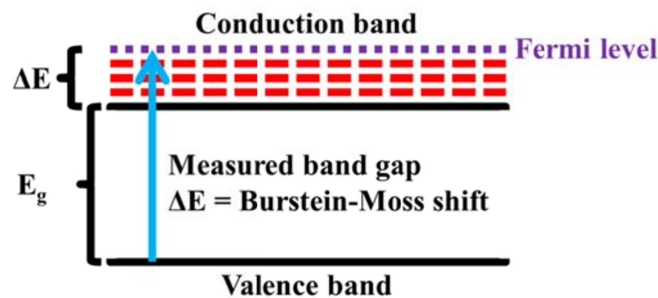

Figure 1.23: Schematic of the optical band shift due to the Burstein-Moss effect.

It has been shown that the BM shift Δ_{BM} is proportional to $n^{2/3}$, where n is the carrier concentration. [155, 156] The magnitude of the shift can be calculated as below.

$$\Delta E_{BM} = \frac{h^2}{8m^*}(\frac{3n}{\pi})^{2/3}$$

Equation 1.7

Where h is the Planck constant, m* is the electron effective mass, and n is the carrier concentration.

1.11 Electrical Properties of ZnO

Electrical conductivity is one of the key properties for TCO materials; therefore a full understanding is essential to design appropriate TCO thin films. The electrical conductivity σ is defined in the following equation. [157]

$$\sigma = ne\mu$$

Equation 1.8

Where n is the carrier concentration, e is the electron carrier charge (1.602×10^{-19} C), and μ is the mobility.

The electrical resistivity ρ can be expressed as below. [14]

$$\rho = \frac{1}{\sigma}$$

Equation 1.9

Crystalline ITO thin films have electrical conductivities of ~ 5000 Scm^{-1} while amorphous IZO thin films have the electrical conductivities of 1000 - 3000 Scm^{-1}. The metallic conductor copper and a typical insulator have conductivities of ~ 10^5 Scm^{-1} and ~ 10^{-18} Scm^{-1}, respectively. [158] The

electrical conductivity is therefore determined by both the carrier concentration and the carrier mobility. Metals have carrier concentrations of 10^{22} - 10^{23} cm^{-3} while the values for amorphous IZO thin films are 10^{19} - 10^{21} cm^{-3}. Copper has a mobility of 59 cm^2 / Vs [159] while the values for amorphous IZO thin films are 10 - 50 cm^2 / Vs [160-163]. Yan et al. reported that an extremely high mobility with a value of 600 cm^2 / Vs is obtained in CdO. [164]

Mobility μ indicates the ability of carriers to travel inside a material, which can be expressed as follows. [165]

$$\mu = \frac{e\tau}{m^*}$$

Equation 1.10

Where τ is the average time between scattering events and m* is the carrier effective mass.

A higher mobility depends on a longer average scattering time and smaller carrier effective mass. Matthiesen's rule [159] describes that the mobility is attributed by additive independent scattering processes as expressed in the following equation.

$$\frac{1}{\mu_{total}} = \sum \frac{1}{\mu_i}$$

Equation 1.11

Where μ_{total} is the observed total mobility and μ_i is the mobility of the *i*th scattering process.

The main scattering processes for a doped TCO material are recognised as ionised impurity scattering, acoustic phonon scattering, and grain boundary scattering. However, which of these scattering processes is dominant depends on the conditions. The ionised impurity scattering is significant for a heavily doped TCO material. [166] A relatively high temperature

results in a significant acoustic phonon scattering. [167] The mobility of polycrystalline TCO materials is usually limited by the grain boundary scattering. [168-170] However, spray pyrolysis, as well as other solution deposition processes, generate pores in the thin films due to the decomposition of solutions. The porosity and the possible phase separation can lead to additional scattering thus further reducing the carrier mobility. [171]

It is necessary to control the crystal growth for a crystalline TCO thin film, a larger grain growth is usually preferred to reduce the scattering. However, the high temperatures needed for this condition are not suitable for some plastic or polymer substrates. Importantly, some amorphous TCO thin films have very high electrical conductivities. Hosono [172-174] proposed that heavy post-transition metal cations, which have electron configurations of $(n - 1)d^{10}ns^0$ $(n \geq 5)$, can have a good conductivity by the large s-orbital overlap in these oxide materials. The spherical s-orbitals are not directional; therefore, no long-range directional bonding is required for electronic conduction. This is the fundamental reason why amorphous structures can also have a high conductivity. Typical mobility values of amorphous TCO thin films such as IZO, InGaZnO, CdGeO, ZnSnO, and AgSbO are in the range of 10 - 50 cm^2 / Vs. [172-174]

The carriers for electronic conductivity can arise from either intrinsic defects or extrinsic impurity doping. When the temperature is higher than 0 K, interstitials and vacancies can be generated as defects in an ideal crystal driven by the entropy. Kröger-Vink notation [175] expresses the electron generation from a crystal as shown below.

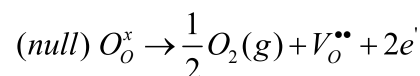

$$(null)\ O_O^x \rightarrow \frac{1}{2} O_2(g) + V_O^{\bullet\bullet} + 2e^{'}$$

Equation 1.12

Where $V_O^{\bullet\bullet}$ is the oxygen vacancy and $e^{'}$ is the ionised free electron. The non-stoichiometric material is formed due to the oxygen vacancies. Therefore, the equilibrium constant K is expressed

as follows.

$$K = [V_O^{\bullet\bullet}][e']^2 p_{O_2}^{1/2}$$

Equation 1.13

Where $[V_O^{\bullet\bullet}]$ is the concentration of oxygen vacancies, $[e']$ is the concentration of free electrons, and p_{O_2} is the partial pressure of oxygen. Since $[V_O^{\bullet\bullet}] = 1/2\,[e']$, the carrier electron concentration n is expressed as follows.

$$n = [e'] = (2K)^{1/3} p_{O_2}^{-1/6} \propto \sigma$$

Equation 1.14

Where σ is the electrical conductivity. It indicates that a lower oxygen partial pressure improves the electrical conductivity. Carrying out the synthesis or the annealing process in a low oxygen partial pressure condition (e.g., nitrogen atmosphere) can increase the carrier concentration thus obtaining a higher conductivity. The extrinsic impurity doping can also introduce extra carriers for conduction. In MZO (M is an element with an oxidation state of +3) thin films, M^{3+} occupies the substitutional Zn^{2+} sites to generate extra free electrons by charge neutrality. The equation is written as below. [171]

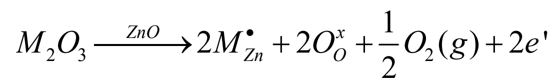

$$M_2O_3 \xrightarrow{ZnO} 2M_{Zn}^{\bullet} + 2O_O^x + \frac{1}{2}O_2(g) + 2e'$$

Equation 1.15

1.12 Correlation of Optical and Electrical Properties

The relation between electronic band structures and optical properties, such as transmittance and reflectance, is usually expressed in terms of dielectric functions. These dielectric functions can relate optical parameters to electrical parameters. The relationship between the optical carrier concentration n_{opt} and Drude plasma frequency ω_p is written as follows. [176, 177]

$$n_{opt} = \frac{m^* \varepsilon_0 \omega_p^2}{q^2}$$

Equation 1.16

Where q is the electron carrier charge, ε_0 is the permittivity of free space, and m* is the electron effective mass. The details of the correlations are discussed in **Chapter 2** and **Chapter 4**.

1.13 Defect Models of ZnO

1.13.1 Zinc and Oxygen Defect Models

The native defects of hexagonal wurtzite ZnO include vacancies and interstitials. The donor-type defects are the oxygen deficiency or the Zn excess due to the oxygen vacancy or the Zn interstitial. The acceptor-type defects are oxygen excess or Zn deficiency, which is attributed to oxygen interstitials or Zn vacancies. There are two choices for interstitials, octahedral and tetrahedral sites (**Figure 1.24**). Fumiyasu et al. [178] reported that the occupation of the Zn interstitial in tetrahedral sites is dynamically unstable. However, the oxygen interstitial has a possibility to form an O_2-molecule-like configuration, which can

reduce the energy and thus can be stabilised.

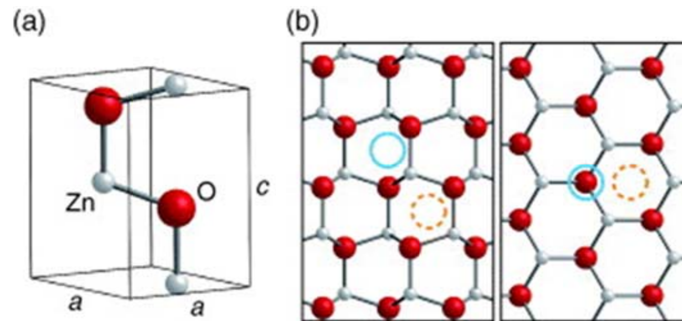

Figure 1.24: Unit cell of hexagonal wurtzite ZnO (a). (b) ZnO crystal model viewed from the $[\bar{1}\bar{1}20]$ (left) and the [0001] (right). Zn atoms (grey circles), O atoms (red circles), octahedral (dashed), and tetrahedral (solid) interstitial sites. Reproduced from Fumiyasu et al. [179] with permission from National Institute for Materials Science.

There are two possible sites for the Zn interstitial, the octahedral site and the tetrahedral site. However, the literature reports suggest that the tetrahedral site was either energetically unfavourable [180-184] or dynamically unstable [116, 178, 185]. Therefore, the Zn interstitial is considered to be the octahedral site. Look et al. [186] reported that the donor energy for the Zn interstitial was 30 meV, which indicates the excitation of electrons from donor states into the conduction band is easy. The formation energy of the Zn interstitial is very high even at the oxygen-poor limit, suggesting a low concentration in n-type ZnO under thermal equilibrium.

The Zn vacancy is a dominant acceptor-type defect for ZnO in theory. [187, 188] The experiment result from Tuomisto et al. [189] also suggested that the Zn vacancy cannot be the main contribution to the p-type ZnO since electrons in the valence band are difficult to be excited into the acceptor states. The formation of the Zn vacancy is difficult in the oxygen-poor condition, suggesting the acceptor-type Zn vacancy is impossible.

The possible types for the oxygen interstitial include occupying octahedral interstitial sites and the O_2-molecule-like configurations, which is also called a split interstitial [116]. The

formation energy of the octahedral interstitial is higher than the Zn vacancy [116, 190]. However, the O_2-molecule-like configuration has lower formation energy than that of the octahedral interstitial, and it is electrically inactive, i.e., no extra electrons for conduction can be generated. [116]. In a word, the oxygen interstitial has very high formation energies or is electrically inactive; therefore, these defects are rarely present in thermal equilibrium.

1.13.2 Silicon Defect Models

There are three types of Si defects in ZnO including substitutional, octahedral interstitial, and tetrahedral interstitial Si defects. [191] The substitutional defect occurs if Si^{4+} ions occupy Zn^{2+} sites in the ZnO lattice. The octahedral interstitial or tetrahedral interstitial defect is formed if Si^{4+} ions take up the original empty octahedral or tetrahedral space in the ZnO lattice, respectively. The substitutional, octahedral interstitial, and tetrahedral interstitial Si defects are labelled as 1, 2, and 3, respectively in **Figure 1.25**.

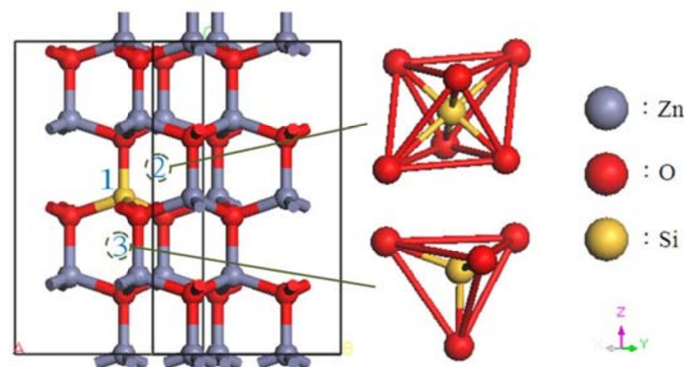

Figure 1.25: Schematic of a 2 × 2 × 2 ZnO supercell model indicating substitutional and interstitial Si atoms. Reproduced from Wu et al. [191] with permission from MDPI.

The DFT calculation from Wu et al. [191] indicates that the formation of the substitutional defect is easier than that of octahedral interstitial and tetrahedral interstitial defects. The free electrons entering the conduction band, therefore, increases as the Si concentration increases. The lower formation energy for a substitutional defect suggests it is the preferred doping site

for Si in the ZnO lattice.

Wu et al. [191] also calculated the band structures of ZnO, substitutional SiZO, octahedral interstitial SiZO, and tetrahedral interstitial SiZO (**Figure 1.26**). Each band structure of SiZO has a shifted Fermi level to the conduction band indicating an n-type characteristic. Therefore, the substitutional SiZO has a larger band gap compared with that of ZnO. [192] What is more, the interstitial Si defect can also reduce the transmittance of SiZO thin films. [191] It is known that the effective mass is inversely proportional to the curvature of the energy band, which can be expressed as below. [193]

$$m^* = \hbar^2 (\frac{d^2 E}{dk^2})^{-1}$$

Equation 1.17

Where ħ is the reduced Planck constant, E is the band energy, and k is the wavevector.

The substitutional-based impurity doping SiZO has a slightly smaller curvature of the conduction band compared with ZnO. However, the curvatures of the conduction bands for these two interstitial SiZOs are much flatter, suggesting larger electron effective masses. The substitutional SiZO has more free electrons available for electronic conduction. However, a fraction of the electrons are trapped for interstitial SiZOs thus they have less free electrons for an electronic conduction. [191] It is similar for IZO as well as reported by Zhou et al. [194] The electrical conductivity is inversely proportional to the electron effective mass. Consequently, interstitial defects increase the electron effective mass thus reducing the electrical mobility and conductivity. Typically, substitutional defects can generate more free electrons thus improving the conductivity.

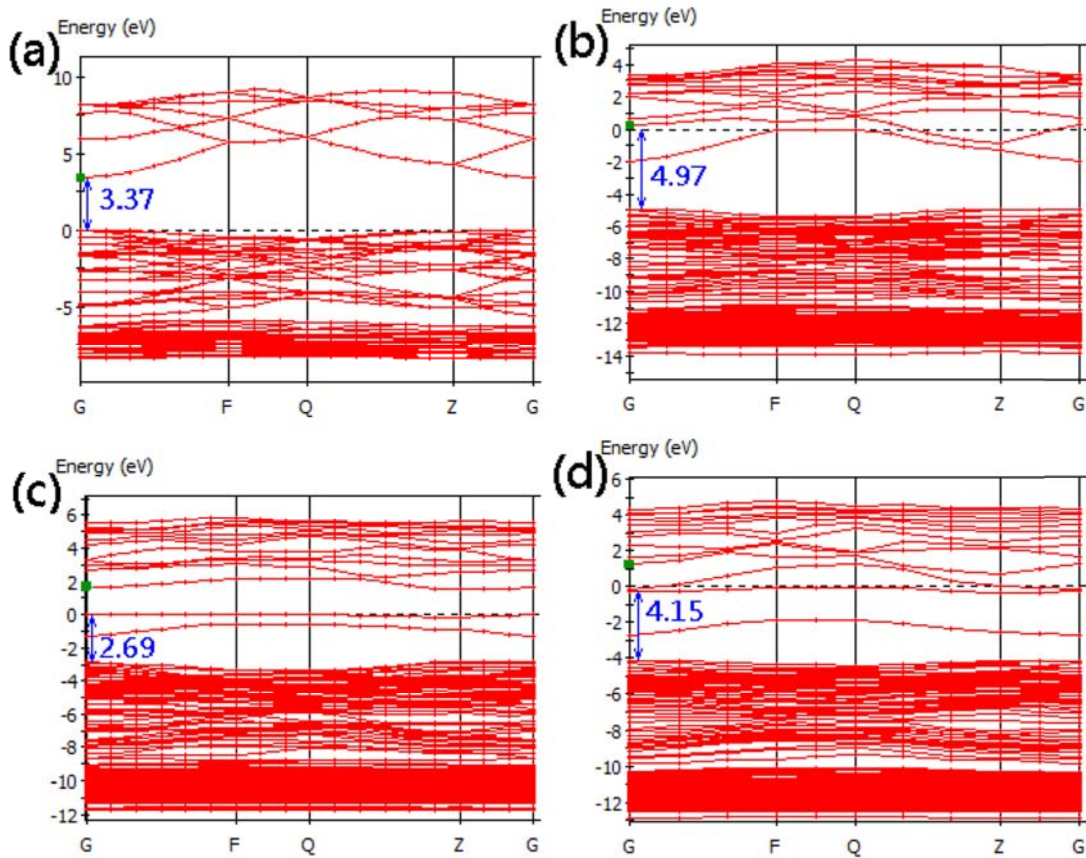

Figure 1.26: Calculated band structures of ZnO (a), substitutional SiZO (b), octahedral interstitial SiZO (c), and tetrahedral interstitial SiZO (d). Adapted from Wu et al. [191] with permission from MDPI.

1.13.3 Indium Defect Models

There are four types of In defects in ZnO including substitution in Zn^{2+} sites, substitution in oxygen sites, tetrahedral interstitial, and octahedral interstitial, which are labelled as 1, 2, 3, and 4, respectively In **Figure 1.27**. [194] The formation of substitution in Zn sites, tetrahedral interstitial, and octahedral interstitial is similar to those of Si defects as discussed. The substitutional defect in oxygen sites occurs if In^{3+} ions occupy O^{2-} sites in the ZnO lattice.

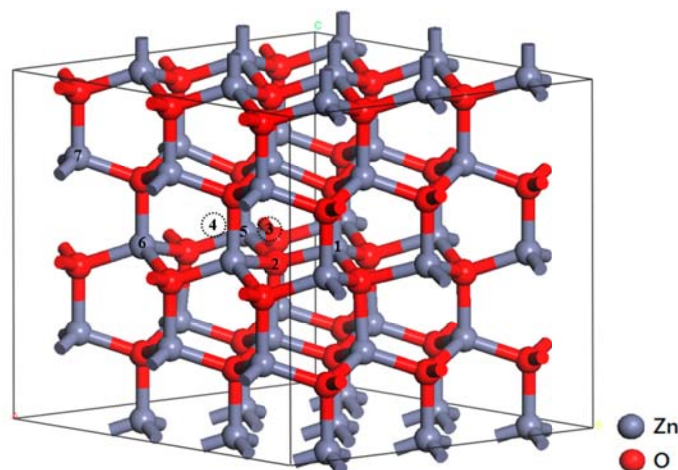

Figure 1.27: Schematic of a 3 × 3 × 2 supercell containing substitutional and interstitial In atoms. Reproduced from Wu et al. [195] with permission from MDPI.

DFT calculations suggest that the formation energy for the substitution in Zn^{2+} sites is easier than that of octahedral interstitial and tetrahedral interstitial defects. However, the substitution in oxygen sites is most difficult compared to those of other defects, indicating the formation of the substitutional in oxygen sites is highly unfavourable. The lower formation energy for the interstitial In defects is due to the In being in the hexagonal channel viewing along the c axis of the wurtzite structure. [194] The preferred doping site for In in the ZnO lattice is the substitutional in Zn^{2+} sites due to their low formation energy. An expansion of the lattice can be observed, which is due to the larger ionic radius of In compared to Zn. [194]

1.14 Conclusions

The singly and co-doping of ZnO thin films by spray pyrolysis have been comprehensively studied with the main original contributions including

1. It is the first time In and Si co-doped ZnO thin films have been successfully synthesised with high optoelectronic performances.

2. I have studied the total chemical composition of elements in the bulk of a TCO material

which is also the first time.

3. The percentage of starting materials which are transformed into a TCO thin film from precursor solutions by the spray pyrolysis method has been investigated, which has not been discussed before.

4. The limitations, restrictions, and effects in doping, including crystal structure growth along the film thickness direction, have been carefully discussed, thus enlightening us for further development in co-doping and material design.

This chapter is followed by various background information of experimental techniques and data acquisition methods in Chapter 2, which have been used in this thesis. Chapter 3 talks about the transfer issues of starting materials from precursor solutions to thin films in the process of spray pyrolysis. Two key optoelectronic properties, electrical and optical, are discussed in Chapter 4 and Chapter 5, respectively. Chapter 6 studies the structure of undoped and doped ZnO thin films thus understanding how doing affects the performance of the films. In the last part of the thesis, some fundamental theories are discussed including the metal-insulator transition, grain boundary effects, and the co-doping mechanism. What is more, the Figure of Merit and the optimised Figure of Merit are demonstrated to show the advantages of co-doping. Finally, the further work gives a hint to the next researcher on the topic of TCOs.

References

[1] Lokanc, M., Eggert, R. & Redlinger, M. 2015. The Availability of Indium: The Present, Medium Term, and Long Term. USA: National Renewable Energy Lab. (NREL), Golden, CO (United States).

[2] Tolcin, A. C. 2014. *2014 Minerals Yearbook,* USA, U.S. Department of the Interior, U.S. Geological Survey.

[3] Shtereva, K., Tvarozek, V., Sutta, P., Kovac, J. & Novotny, I. 2009. Experimental Studies on Doped and Co-Doped ZnO Thin Films Prepared by RF Diode Sputtering. *Micro Electronic and Mechanical Systems.* London: InTech.

[4] Humphries, M. 2010. *Rare Earth Elements: The Global Supply Chain,* Washington, D.C., Diane Publishing.

[5] Jha, A. R. 2014. *Rare Earth Materials: Properties and Applications,* Boca Raton, CRC Press.

[6] Edwards, P. P., Porch, A., Jones, M. O., Morgan, D. V. & Perks, R. M. 2004. Basic Materials Physics of Transparent Conducting Oxides. *Dalton Transactions*, 2995-3002.

[7] Fan, J. C. C. & Goodenough, J. B. 1977. X‐Ray Photoemission Spectroscopy Studies of Sn‐Doped Indium‐Oxide Films. *Journal of Applied Physics,* 48, 3524-3531.

[8] Islam, M. N., Ghosh, T., Chopra, K. & Acharya, H. 1996. XPS and X-ray Diffraction Studies of Aluminum-Doped Zinc Oxide Transparent Conducting Films. *Thin Solid Films,* 280, 20-25.

[9] Caglar, M., Ilican, S., Caglar, Y. & Yakuphanoglu, F. 2009. Electrical Conductivity and Optical Properties of ZnO Nanostructured Thin Film. *Applied Surface Science,* 255, 4491-4496.

[10] Montaser, A. 1998. *Inductively Coupled Plasma Mass Spectrometry,* New York, John Wiley & Sons.

[11] Lewis, B. G. & Paine, D. C. 2000. Applications and Processing of Transparent Conducting Oxides. *MRS Bulletin,* 25, 22-27.

[12] Cheng, I. & Wagner, S. 2009. Overview of Flexible Electronics Technology. *In:* Wong, W. S. & Salleo, A. (eds.) *Flexible Electronics: Materials and Applications.* Boston, MA: Springer US.

[13] Orita, M., Ohta, H., Hirano, M. & Hosono, H. 2000. Deep-Ultraviolet Transparent Conductive β-Ga2O3 Thin Films. *Applied Physics Letters,* 77, 4166-4168.

[14] Dixon, S. C., Scanlon, D. O., Carmalt, C. J. & Parkin, I. P. 2016. n-Type Doped Transparent Conducting Binary Oxides: An Overview. *Journal of Materials Chemistry C,* 4, 6946-6961.

[15] Baedeker, K. 1907. Über die Elektrische Leitfähigkeit und die Thermoelektrische Kraft Einiger Schwermetallverbindungen. *Annalen der Physik,* 327, 749-766.

[16] Gurumurugan, K., Mangalaraj, D., Narayandass, S. K., Sekar, K. & Vallabhan, C. G. 1994. Characterization of Transparent Conducting CdO Films Deposited by Spray Pyrolysis. *Semiconductor Science and Technology,* 9, 1827.

[17] Minami, T., Miyata, T. & Yamamoto, T. 1999. Stability of Transparent Conducting Oxide Films for Use at High Temperatures. *Journal of Vacuum Science & Technology A: Vacuum, Surfaces, and Films,* 17**,** 1822-1826.

[18] Boscarino, S. 2015. *Ultra-Thin Transparent Electrodes for Energy Applications.* University of Catania.

[19] Dali, S. E., Jayachandran, M. & Chockalingam, M. J. 1999. New Transparent Electronic Conductor, MgIn2O4 Spinel. *Journal of Materials Science Letters,* 18**,** 915-917.

[20] Major, S., Kumar, S., Bhatnagar, M. & Chopra, K. 1986. Effect of Hydrogen Plasma Treatment on Transparent Conducting Oxides. *Applied Physics Letters,* 49**,** 394-396.

[21] Kim, H., Pique, A., Horwitz, J., Mattoussi, H., Murata, H., Kafafi, Z. & Chrisey, D. 1999. Indium Tin Oxide Thin Films for Organic Light-Emitting Devices. *Applied Physics Letters,* 74**,** 3444-3446.

[22] Alfantazi, A. & Moskalyk, R. 2003. Processing of Indium: A Review. *Minerals Engineering,* 16**,** 687-694.

[23] Yang, J. K., Liang, B., Zhao, M. J., Gao, Y., Zhang, F. C. & Zhao, H. L. 2015. Reference of Temperature and Time During Tempering Process for Non-Stoichiometric FTO Films. *Scientific Reports,* 5**,** 15001.

[24] Ginley, D. S. & Bright, C. 2011. Transparent Conducting Oxides. *MRS Bulletin,* 25**,** 15-18.

[25] Minami, T. 2008. Substitution of Transparent Conducting Oxide Thin Films for Indium Tin Oxide Transparent Electrode Applications. *Thin Solid Films,* 516**,** 1314-1321.

[26] Anderson, J. & Van de Walle, C. G. 2009. Fundamentals of Zinc Oxide as a Semiconductor. *Reports on Progress in Physics,* 72**,** 126501.

[27] Liu, Y., Li, Y. & Zeng, H. 2013. ZnO-Based Transparent Conductive Thin Films: Doping, Performance, and Processing. *Journal of Nanomaterials,* 2013**,** 9.

[28] Porch, A., Morgan, D. V., Perks, R. M., Jones, M. O. & Edwards, P. P. 2004. Electromagnetic Absorption in Transparent Conducting Films. *Journal of Applied Physics,* 95**,** 4734-4737.

[29] Crawford, G. 2005. *Flexible Flat Panel Displays,* England, John Wiley & Sons.

[30] Minami, T. 2008. Present Status of Transparent Conducting Oxide Thin-Film Development for Indium-Tin-Oxide (ITO) Substitutes. *Thin Solid Films,* 516**,** 5822-5828.

[31] Lewis, B. G. & Paine, D. C. 2011. Applications and Processing of Transparent Conducting Oxides. *MRS Bulletin,* 25**,** 22-27.

[32] Lampert, C. M. 2003. Large-Area Smart Glass and Integrated Photovoltaics. *Solar Energy Materials and Solar Cells,* 76**,** 489-499.

[33] Deepa, M., Srivastava, A., Sood, K. & Agnihotry, S. 2006. Nanostructured Mesoporous Tungsten Oxide Films with Fast Kinetics for Electrochromic Smart Windows. *Nanotechnology,* 17**,** 2625.

[34] Porch, A., Morgan, D. V., Perks, R. M., Jones, M. O. & Edwards, P. P. 2004. Transparent Current Spreading Layers for Optoelectronic Devices. *Journal of Applied Physics,* 96**,** 4211-4218.

[35] Slocombe, D., Porch, A., Pepper, M. & Edwards, P. P. 2012. The Mott Transition and Optimal Performance of Transparent Conducting Oxides in Thin-Film Solar Cells. *Energy & Environmental Science,* 5**,** 5387-5391.

[36] Chopra, K. L., Paulson, P. D. & Dutta, V. 2004. Thin-Film Solar Cells: An Overview. *Progress in Photovoltaics: Research and Applications,* 12**,** 69-92.

[37] Birkmire, R. W. & Eser, E. 1997. Polycrystalline Thin Film Solar Cells:Present Status and Future Potential. *Annual Review of Materials Science,* 27**,** 625-653.

[38] Kern, W. 2012. *Thin Film Processes II,* London, Elsevier.

[39] Jilani, A., Abdel-wahab, M. S. & Hammad, A. H. 2017. Advance Deposition Techniques for Thin Film and Coating. *In:* Nikitenkov, N. N. (ed.) *Modern Technologies for Creating the Thin-film Systems and Coatings.* London: InTech.

[40] Seo, O. & Jo, J. 2007. *Method of Fabricating ZnO Film and Thin Film Transistor Adopting the ZnO Film*. US20070172591A1.

[41] Hardy, N. 2013. *What is Thin Film Deposition By Thermal Evaporation?* : Semicore Equipment, Inc. Available: http://www.semicore.com/news/71-thin-film-deposition-thermal-evaporation [Accessed 10 March 2019].

[42] Schwarz, R. 2018. *Pulsed Laser Deposition (PLD) - Abstract*. Available: http://groups.ist.utl.pt/rschwarz/rschwarzgroup_files/PLD_files/PLD.htm [Accessed 10 March 2019].

[43] Greene, J. E. 2017. Review Article: Tracing the Recorded History of Thin-Film Sputter Deposition: From the 1800s to 2017. *Journal of Vacuum Science & Technology A,* 35**,** 05C204.

[44] Hughes, M. 2014. *What is Sputtering? Magnetron Sputtering?* : Semicore Equipment, Inc. Available: http://www.semicore.com/what-is-sputtering [Accessed 10 March 2019].

[45] Archer, N. 1979. Chemical Vapour Deposition. *Physics in Technology,* 10**,** 152.

[46] Choy, K. L. 2003. Chemical Vapour Deposition of Coatings. *Progress in Materials Science,* 48**,** 57-170.

[47] Johnson, R. W., Hultqvist, A. & Bent, S. F. 2014. A Brief Review of Atomic Layer Deposition: From Fundamentals to Applications. *Materials Today,* 17**,** 236-246.

[48] 2013. *Applications of Metal Halide Precursors in CVD/ALD Processes*. Strem Chemicals. Available: https://www.azonano.com/article.aspx?ArticleID=3432 [Accessed 10 March 2019].

[49] Brinker, C. J. & Scherer, G. W. 1990. *Sol-Gel Science,* San Diego, Academic Press.

[50] 2018. *Sol-Gel Coatings*. Available: http://www.orioncoat.com/resources/sol-gel/ [Accessed 10 March 2019].

[51] 2006. *Sol-Gel Methods*. Available: http://www.uio.no/studier/emner/matnat/kjemi/KJM5100/h06/undervisningsmateriale/10KJM5100_2006_sol_gel_d.pdf [Accessed 10 March 2019].

[52] 2018. *Sol-Gel Process*. Available: https://en.wikipedia.org/wiki/Sol%E2%80%93gel_process [Accessed 10 March 2019].

[53] Mahmood, A. & Naeem, A. 2017. Sol-Gel-Derived Doped ZnO Thin Films: Processing, Properties, and Applications. *In:* Chandra, U. (ed.) *Recent Applications in Sol-Gel Synthesis.* Rijeka: InTech.

[54] Kontturi, E. 2016. *Spin Coating*. Available: https://mycourses.aalto.fi/pluginfile.php/215575/mod_folder/content/0/Spin%20coating%202016.pdf?forcedownload=1 [Accessed 10 March 2019].

[55] 2018. *Spin Coating: A Guide to Theory and Techniques*. Available: https://www.ossila.com/pages/spin-coating [Accessed 10 March 2019].

[56] Norrman, K., Ghanbari-Siahkali, A. & Larsen, N. B. 2005. 6 Studies of Spin-Coated Polymer Films. *Annual Reports Section "C" (Physical Chemistry),* 101**,** 174-201.

[57] Mochel, J. M. 1951. *Electrically Conducting Coatings on Glass and Other Ceramic Bodies*. US2564707A.

[58] Chamberlin, R. & Skarman, J. 1966. Chemical Spray Deposition Process for Inorganic Films. *Journal of the Electrochemical Society,* 113**,** 86-89.

[59] Chamberlin, R., Skarman, J., Koopman, D. & Blakely, L. 1963. Feasibility Investigation Of Chemically Sprayed Thin Film Photovoltaic Converters. USA: National Cash Register Company, Dayton, Ohio.

[60] Chamberlin, R. R. & Skarman, J. S. 1966. Chemically Sprayed Thin Film Photovoltaic Converters. *Solid-State Electronics,* 9**,** 819-823.

[61] Sanz Maudes, J. & Rodríguez, T. 1980. Sprayed SnO2 Films: Growth Mechanism and Film Structure Characterization. *Thin Solid Films,* 69**,** 183-189.

[62] Pamplin, B. 1979. Spray Pyrolysis of Ternary and Quaternary Solar Cell Materials. *Progress in Crystal Growth and Characterization,* 1**,** 395-403.

[63] Mooney, J. B. & Radding, S. B. 1982. Spray Pyrolysis Processing. *Annual Review of Materials Science,* 12**,** 81-101.

[64] Viguie, J. & Spitz, J. 1975. Chemical Vapor Deposition at Low Temperatures. *Journal of the Electrochemical Society,* 122**,** 585-588.

[65] Sabnis, S., Bhadane, P. A. & Kulkarni, P. 2013. Process Flow of Spray Pyrolysis Technique. *Journal of Applied Physics,* 4**,** 7-11.

[66] Minami, T. 2000. New n-Type Transparent Conducting Oxides. *MRS Bulletin,* 25**,** 38-44.

[67] Shah, A., Torres, P., Tscharner, R., Wyrsch, N. & Keppner, H. 1999. Photovoltaic Technology: The Case for Thin-Film Solar Cells. *Science,* 285**,** 692-698.

[68] Jeong, W., Kim, S. & Park, G. 2006. Preparation and Characteristic of ZnO Thin Film with High and Low Resistivity for an Application of Solar Cell. *Thin Solid Films,* 506**,** 180-183.

[69] Scaife, B. K. P. 1998. *Principles of Dielectrics,* New York, Oxford University Press.

[70] Klingshirn, C. 2010. Introduction. *Zinc Oxide.* Heidelberg: Springer.

[71] Look, D. C. & Claflin, B. 2004. P‐Type Doping and Devices Based on ZnO. *Physica Status Solidi (B),* 241**,** 624-630.

[72] Park, C., Zhang, S. & Wei, S. 2002. Origin of p-Type Doping Difficulty in ZnO: The Impurity Perspective. *Physical Review B,* 66**,** 073202.

[73] Minami, T., Sato, H., Nanto, H. & Takata, S. 1985. Group III Impurity Doped Zinc Oxide Thin Films Prepared by RF Magnetron Sputtering. *Japanese Journal of Applied Physics,* 24**,** L781.

[74] Dutta, M., Ghosh, T. & Basak, D. 2009. N Doping and Al-N Co-Doping in Sol-Gel ZnO Films: Studies of Their Structural, Electrical, Optical, and Photoconductive

Properties. *Journal of Electronic Materials,* 38, 2335-2342.
[75] Kang, H. & Lee, K. 2010. Optical and Electrical Properties of Aluminum and Boron Co-Doped Zinc Thin Films as Functions of the Substrate Temperature. *Journal of the Korean Physical Society,* 57, 260-263.
[76] Zhang, X., Fan, H., Zhao, Y., Sun, J., Wei, C. & Zhang, C. 2007. Fabrication of High Hole-Carrier Density p-Type ZnO Thin Films by N-Al Co-Doping. *Applied Surface Science,* 253, 3825-3827.
[77] Otiti, T. 2014. Review of Zinc Oxide Thin Films. Arlington, Virginia: Air Force Research Laboratory.
[78] Kim, G. H., Shin, H. S., Du Ahn, B., Kim, K. H., Park, W. J. & Kim, H. J. 2009. Formation Mechanism of Solution-Processed Nanocrystalline InGaZnO Thin Film as Active Channel Layer in Thin-Film Transistor. *Journal of the Electrochemical Society,* 156, H7-H9.
[79] Ohyama, M., Kozuka, H., Yoko, T. & Sakka, S. 1996. Preparation of ZnO Films with Preferential Orientation by Sol-Gel Method. *Journal of the Ceramic Society of Japan,* 104, 296-300.
[80] Ohyama, M., Kozuka, H. & Yoko, T. 1998. Sol‐Gel Preparation of Transparent and Conductive Aluminum‐Doped Zinc Oxide Films with Highly Preferential Crystal Orientation. *Journal of the American Ceramic Society,* 81, 1622-1632.
[81] Maldonado, A., Olvera, M. de la L., Guerra, S. T. & Asomoza, R. 2004. Indium-Doped Zinc Oxide Thin Films Deposited by Chemical Spray Starting from Zinc Acetylacetonate: Effect of the Alcohol and Substrate Temperature. *Solar Energy Materials and Solar Cells,* 82, 75-84.
[82] Lucio-López, M., Luna-Arias, M., Maldonado, A., Olvera, M. de la L. & Acosta, D. 2006. Preparation of Conducting and Transparent Indium-Doped ZnO Thin Films by Chemical Spray. *Solar Energy Materials and Solar Cells,* 90, 733-741.
[83] Lucio-López, M., Maldonado, A., Castanedo-Pérez, R., Torres-Delgado, G. & Olvera, M. de la L. 2006. Thickness Dependence of ZnO: In Thin Films Doped with Different Indium Compounds and Deposited by Chemical Spray. *Solar Energy Materials and Solar Cells,* 90, 2362-2376.
[84] Yin, S. & Sato, T. 2005. Mild Solution Synthesis of Zinc Oxide Films with Superhydrophobicity and Superhydrophilicity. *Journal of Materials Chemistry,* 15, 4584-4587.
[85] Vernardou, D., Kenanakis, G., Couris, S., Koudoumas, E., Kymakis, E. & Katsarakis, N. 2007. pH Effect on the Morphology of ZnO Nanostructures Grown with Aqueous Chemical Growth. *Thin Solid Films,* 515, 8764-8767.
[86] Wang, Z., Qian, X., Yin, J. & Zhu, Z. 2004. Aqueous Solution Fabrication of Large-Scale Arrayed Obelisk-Like Zinc Oxide Nanorods with High Efficiency. *Journal of Solid State Chemistry,* 177, 2144-2149.
[87] El Manouni, A., Manjón, F., Mollar, M., Marí, B., Gómez, R., López, M. & Ramos-Barrado, J. 2006. Effect of Aluminium Doping on Zinc Oxide Thin Films Grown by Spray Pyrolysis. *Superlattices and Microstructures,* 39, 185-192.
[88] El Hichou, A., Addou, M., Ebothe, J. & Troyon, M. 2005. Influence of Deposition Temperature (Ts), Air Flow Rate (f) and Precursors on Cathodoluminescence

Properties of ZnO Thin Films Prepared by Spray Pyrolysis. *Journal of Luminescence,* 113, 183-190.

[89] 2018. *Zinc(II) Acetylacetonate, ACROS Organics™*. Available: https://www.fishersci.com/shop/products/zinc-ii-acetylacetonate-acros-organics-3/p-3527094 [Accessed 10 March 2019].

[90] Adkins, H., Kutz, W. & Coffman, D. D. 1930. The Alcoholysis of Certain 1,3-Diketones in the Presence of Hydrogen Chloride. *Journal of the American Chemical Society,* 52, 3212-3221.

[91] Ambrozic, G., Djerdj, I., Skapin, S. D., Zigon, M. & Orel, Z. C. 2010. The Double Role of P-Toluenesulfonic Acid in the Formation of ZnO Particles with Different Morphologies. *CrystEngComm,* 12, 1862-1868.

[92] Arii, T. & Kishi, A. 2006. Humidity Controlled Thermal Analysis. *Journal of Thermal Analysis and Calorimetry,* 83, 253-260.

[93] Özgür, Ü., Alivov, Y. I., Liu, C., Teke, A., Reshchikov, M. A., Doğan, S., Avrutin, V., Cho, S. & Morkoç, H. 2005. A Comprehensive Review of ZnO Materials and Devices. *Journal of Applied Physics,* 98, 041301.

[94] Kortan, A. R. 2014. Experimental and Theoretical Pursuit of the Ultimate Conductivity in ZnO. Washington, D.C.: Wright State University: Semiconductor Research Center.

[95] Zhang, S., Wei, S. & Zunger, A. 2001. Intrinsic n-Type Versus p-Type Doping Asymmetry and the Defect Physics of ZnO. *Physical Review B,* 63, 075205.

[96] Favier, A., Muñoz, D., Martín de Nicolás, S. & Ribeyron, P. J. 2011. Boron-Doped Zinc Oxide Layers Grown by Metal-Organic CVD for Silicon Heterojunction Solar Cells Applications. *Solar Energy Materials and Solar Cells,* 95, 1057-1061.

[97] Huang, Q., Wang, Y., Wang, S., Zhang, D., Zhao, Y. & Zhang, X. 2012. Transparent Conductive ZnO: B Films Deposited by Magnetron Sputtering. *Thin Solid Films,* 520, 5960-5964.

[98] Sans, J. A., Sánchez-Royo, J. F., Segura, A., Tobias, G. & Canadell, E. 2009. Chemical Effects on the Optical Band-Gap of Heavily Doped ZnO: MIII (M=Al,Ga,In): An Investigation by Means of Photoelectron Spectroscopy, Optical Measurements Under Pressure, and Band Structure Calculations. *Physical Review B,* 79.

[99] Bhachu, D. S., Sankar, G. & Parkin, I. P. 2012. Aerosol Assisted Chemical Vapor Deposition of Transparent Conductive Zinc Oxide Films. *Chemistry of Materials,* 24, 4704-4710.

[100] Hu, J. & Gordon, R. G. 1992. Textured Aluminum‐Doped Zinc Oxide Thin Films from Atmospheric Pressure Chemical‐Vapor Deposition. *Journal of Applied Physics,* 71, 880-890.

[101] Zhao, J. L., Sun, X. W., Ryu, H. & Moon, Y. B. 2011. Thermally Stable Transparent Conducting and Highly Infrared Reflective Ga-Doped ZnO Thin Films by Metal Organic Chemical Vapor Deposition. *Optical Materials,* 33, 768-772.

[102] Park, S., Ikegami, T. & Ebihara, K. 2006. Effects of Substrate Temperature on the Properties of Ga-Doped ZnO by Pulsed Laser Deposition. *Thin Solid Films,* 513, 90-94.

[103] Geng, Y., Guo, L., Xu, S., Sun, Q., Ding, S., Lu, H. & Zhang, D. 2011. Influence of Al Doping on the Properties of ZnO Thin Films Grown by Atomic Layer Deposition. *The Journal of Physical Chemistry C,* 115**,** 12317-12321.

[104] Ko, H. J., Chen, Y. F., Hong, S. K., Wenisch, H., Yao, T. & Look, D. C. 2000. Ga-Doped ZnO Films Grown on GaN Templates by Plasma-Assisted Molecular-Beam Epitaxy. *Applied Physics Letters,* 77**,** 3761-3763.

[105] Shannon, R. D. 1976. Revised Effective Ionic Radii and Systematic Studies of Interatomic Distances in Halides and Chalcogenides. *Acta Crystallographica Section A,* 32**,** 751-767.

[106] Minami, T., Yamamoto, T. & Miyata, T. 2000. Highly Transparent and Conductive Rare Earth-Doped ZnO Thin Films Prepared by Magnetron Sputtering. *Thin Solid Films,* 366**,** 63-68.

[107] Pellegrini, M. 2014. Critical Raw Materials for the EU: Report of the Ad-Hoc Working Group on Defining Critical Raw Materials. Europe: European Commission, Enterprise and Industry.

[108] Cao, L., Zhu, L., Jiang, J., Zhao, R., Ye, Z. & Zhao, B. 2011. Highly Transparent and Conducting Fluorine-Doped ZnO Thin Films Prepared by Pulsed Laser Deposition. *Solar Energy Materials and Solar Cells,* 95**,** 894-898.

[109] Look, D. C. 2001. Recent Advances in ZnO Materials and Devices. *Materials Science and Engineering: B,* 80**,** 383-387.

[110] Ogale, S. B. 2006. *Thin Films and Heterostructures for Oxide Electronics,* Boston, Springer.

[111] Nickel, N. H. & Terukov, E. 2006. *Zinc Oxide - A Material for Micro- and Optoelectronic Applications: Proceedings of the NATO Advanced Research Workshop on Zinc Oxide as a Material for Micro- and Optoelectronic Applications, held in St. Petersburg, Russia, from 23 to 25 June 2004,* Netherlands, Springer.

[112] Jagadish, C. & Pearton, S. J. 2011. *Zinc Oxide Bulk, Thin Films and Nanostructures: Processing, Properties, and Applications,* Amsterdam, Elsevier.

[113] Janotti, A. & Van de Walle, C. G. 2005. Oxygen Vacancies in ZnO. *Applied Physics Letters,* 87**,** 122102.

[114] Janotti, A. & Van de Walle, C. G. 2006. New Insights into the Role of Native Point Defects in ZnO. *Journal of Crystal Growth,* 287**,** 58-65.

[115] Janotti, A. & Van de Walle, C. G. 2006. Hydrogen Multicentre Bonds. *Nature Materials,* 6**,** 44.

[116] Janotti, A. & Van de Walle, C. G. 2007. Native Point Defects in ZnO. *Physical Review B,* 76**,** 165202.

[117] Park, C. H., Zhang, S. B. & Wei, S. 2002. Origin of p-Type Doping Difficulty in ZnO: The Impurity Perspective. *Physical Review B,* 66**,** 073202.

[118] Lee, E. & Chang, K. J. 2004. Possible p-Type Doping with Group-I Elements in ZnO. *Physical Review B,* 70**,** 115210.

[119] Wardle, M. G., Goss, J. P. & Briddon, P. R. 2005. Theory of Li in ZnO: A Limitation for Li-Based p-Type Doping. *Physical Review B,* 71**,** 155205.

[120] Harrison, W. A. 2004. *Elementary Electronic Structure: Revised,* Singapore, World Scientific Publishing Company.

[121] Minegishi, K., Koiwai, Y., Kikuchi, Y., Yano, K., Kasuga, M. & Shimizu, A. 1997. Growth of p-Type Zinc Oxide Films by Chemical Vapor Deposition. *Japanese Journal of Applied Physics,* 36**,** L1453.

[122] Mathew, J., Hitoshi, T. & Tomoji, K. 1999. p-Type Electrical Conduction in ZnO Thin Films by Ga and N Codoping. *Japanese Journal of Applied Physics,* 38**,** L1205.

[123] Look, D. C., Reynolds, D. C., Litton, C. W., Jones, R. L., Eason, D. B. & Cantwell, G. 2002. Characterization of Homoepitaxial p-Type ZnO Grown by Molecular Beam Epitaxy. *Applied Physics Letters,* 81**,** 1830-1832.

[124] Aoki, T., Hatanaka, Y. & Look, D. C. 2000. ZnO Diode Fabricated by Excimer-Laser Doping. *Applied Physics Letters,* 76**,** 3257-3258.

[125] Kim, K., Kim, H., Hwang, D., Lim, J. & Park, S. 2003. Realization of p-Type ZnO Thin Films via Phosphorus Doping and Thermal Activation of the Dopant. *Applied Physics Letters,* 83**,** 63-65.

[126] Ryu, Y. R., Zhu, S., Look, D. C., Wrobel, J. M., Jeong, H. M. & White, H. W. 2000. Synthesis of p-Type ZnO Films. *Journal of Crystal Growth,* 216**,** 330-334.

[127] Ryu, Y. R., Lee, T. S. & White, H. W. 2003. Properties of Arsenic-Doped p-Type ZnO Grown by Hybrid Beam Deposition. *Applied Physics Letters,* 83**,** 87-89.

[128] Xiu, F. X., Yang, Z., Mandalapu, L. J., Zhao, D. T., Liu, J. L. & Beyermann, W. P. 2005. High-Mobility Sb-Doped p-Type ZnO by Molecular-Beam Epitaxy. *Applied Physics Letters,* 87**,** 152101.

[129] Chu, S., Lim, J. H., Mandalapu, L. J., Yang, Z., Li, L. & Liu, J. L. 2008. Sb-Doped P-ZnO / Ga-Doped N-ZnO Homojunction Ultraviolet Light Emitting Diodes. *Applied Physics Letters,* 92**,** 152103.

[130] Tsukazaki, A., Ohtomo, A., Onuma, T., Ohtani, M., Makino, T., Sumiya, M., Ohtani, K., Chichibu, S. F., Fuke, S., Segawa, Y., Ohno, H., Koinuma, H. & Kawasaki, M. 2004. Repeated Temperature Modulation Epitaxy for p-Type Doping and Light-Emitting Diode Based on ZnO. *Nature Materials,* 4**,** 42.

[131] Limpijumnong, S., Zhang, S. B., Wei, S. & Park, C. H. 2004. Doping by Large-Size-Mismatched Impurities: The Microscopic Origin of Arsenic- or Antimony-Doped p-Type Zinc Oxide. *Physical Review Letters,* 92**,** 155504.

[132] Kim, J., Bae, J., Hong, T., Won, M., Yoon, J., Lee, B. & Lee, H. 2010. Optical and Electrical Properties of ZnO Films, Codoped with Al and Ga Deposited at Room Temperature by an RF Sputtering Method. *Thin Solid Films,* 518**,** 6179-6183.

[133] Lee, W., Shin, S., Jung, D., Kim, J., Nahm, C., Moon, T. & Park, B. 2012. Investigation of Electronic and Optical Properties in Al-Ga Codoped ZnO Thin Films. *Current Applied Physics,* 12**,** 628-631.

[134] Nomoto, J., Miyata, T. & Minami, T. 2009. Transparent Conducting Si-Codoped Al-Doped ZnO Thin Films Prepared by Magnetron Sputtering Using Al-Doped ZnO Powder Targets Containing SiC. *Journal of Vacuum Science & Technology A: Vacuum, Surfaces, and Films,* 27**,** 1001-1005.

[135] Altamirano-Juárez, D. C., Torres-Delgado, G., Jiménez-Sandoval, S., Jiménez-Sandoval, O. & Castanedo-Pérez, R. 2004. Low-Resistivity ZnO: F: Al Transparent Thin Films. *Solar Energy Materials and Solar Cells,* 82**,** 35-43.

[136] Choi, B., Kim, I., Kim, D., Lee, K., Lee, T., Cheong, B., Baik, Y. & Kim, W. 2005.

Electrical, Optical and Structural Properties of Transparent and Conducting ZnO Thin Films Doped with Al and F by RF Magnetron Sputter. *Journal of the European Ceramic Society,* 25**,** 2161-2165.

[137] Maldonado, A., Rodríguez-Baez, J. & Olvera, M. de la L. 2011. Physical Properties of Indium and Fluorine Codoped Zinc Oxide Thin Films Deposited by Chemical Spray. *Materials Chemistry and Physics,* 129**,** 109-115.

[138] Vimalkumar, T., Poornima, N., Jinesh, K., Kartha, C. S. & Vijayakumar, K. 2011. On Single Doping and Co-Doping of Spray Pyrolysed ZnO Films: Structural, Electrical and Optical Characterisation. *Applied Surface Science,* 257**,** 8334-8340.

[139] Morales-Saavedra, O., Castaneda, L., Banuelos, J. & Ortega-Martínez, R. 2008. Morphological, Optical, and Nonlinear Optical Properties of Fluorine-Indium-Doped Zinc Oxide Thin Films. *Laser Physics,* 18**,** 283.

[140] Keskenler, E., Turgut, G. & Doğan, S. 2012. Investigation of Structural and Optical Properties of ZnO Films Co-Doped with Fluorine and Indium. *Superlattices and Microstructures,* 52**,** 107-115.

[141] Gledhill, S., Grimm, A., Greiner, D., Bohne, W., Lux-Steiner, M. & Fischer, C. 2011. Doping Induced Structural and Compositional Changes in ZnO Spray Pyrolysed Films and the Effects on Optical and Electrical Properties. *Thin Solid Films,* 519**,** 4293-4298.

[142] Kim, S., Jeong, S. & Cho, C. 2003. Structural Reconstruction of Hexagonal to Cubic ZnO Films on Pt/Ti/SiO2/Si Substrate by Annealing. *Applied Physics Letters,* 82**,** 562-564.

[143] Bates, C. H., White, W. B. & Roy, R. 1962. New High-Pressure Polymorph of Zinc Oxide. *Science,* 137**,** 993-993.

[144] Gerward, L. & Olsen, J. S. 1995. The High-Pressure Phase of Zincite. *Journal of Synchrotron Radiation,* 2**,** 233-235.

[145] Recio, J. M., Blanco, M. A., Luaña, V., Pandey, R., Gerward, L. & Staun Olsen, J. 1998. Compressibility of the High-Pressure Rocksalt Phase of ZnO. *Physical Review B,* 58**,** 8949-8954.

[146] Kogure, T. & Bando, Y. 1993. Formation of ZnO Nanocrystals in the Cubic Phase Was Reported by Electron-Beam Induced Oxidation of ZnS Surfaces During TEM Observations. *Journal of Electron Microscopy,* 47**,** 7903.

[147] Ashrafi, A. B. M. A., Ueta, A., Avramescu, A., Kumano, H., Suemune, I., Ok, Y. & Seong, T. 2000. Growth and Characterization of Hypothetical Zinc-Blende ZnO Films on GaAs(001) Substrates with ZnS Buffer Layers. *Applied Physics Letters,* 76**,** 550-552.

[148] Kim, S.-K., Jeong, S.-Y. & Cho, C.-R. 2003. Structural Reconstruction of Hexagonal to Cubic ZnO Films on Pt/Ti/SiO2/Si Substrate by Annealing. *Applied Physics Letters,* 82**,** 562-564.

[149] Kittel, C. 1996. *Introduction to Solid State Physics,* New York, Wiley.

[150] Calnan, S. & Tiwari, A. 2010. High Mobility Transparent Conducting Oxides for Thin Film Solar Cells. *Thin Solid Films,* 518**,** 1839-1849.

[151] Pasquarelli, R. M., Ginley, D. S. & O'Hayre, R. 2011. Solution Processing of Transparent Conductors: From Flask to Film. *Chemical Society Reviews,* 40**,**

5406-5441.
[152] Zeng, H., Cai, W., Hu, J., Duan, G., Liu, P. & Li, Y. 2006. Violet Photoluminescence from Shell Layer of Zn / ZnO Core-Shell Nanoparticles Induced by Laser Ablation. *Applied Physics Letters,* 88**,** 171910.
[153] Zeng, H., Duan, G., Li, Y., Yang, S., Xu, X. & Cai, W. 2010. Blue Luminescence of ZnO Nanoparticles Based on Non‐Equilibrium Processes: Defect Origins and Emission Controls. *Advanced Functional Materials,* 20**,** 561-572.
[154] Lai, K., Zhu, Y., Dai, Y. & Huang, B. 2012. Intrinsic Defect in BiNbO4: A Density Functional Theory Study. *Journal of Applied Physics,* 112**,** 043706.
[155] Banyai, L. & Koch, S. W. 1986. Absorption Blue Shift in Laser-Excited Semiconductor Microspheres. *Physical Review Letters,* 57**,** 2722-2724.
[156] Yang, Y. H., Chen, X. Y., Feng, Y. & Yang, G. W. 2007. Physical Mechanism of Blue-Shift of UV Luminescence of a Single Pencil-Like ZnO Nanowire. *Nano Letters,* 7**,** 3879-3883.
[157] Neamen, D. A. 1997. *Semiconductor Physics and Devices,* New York, McGraw-Hill.
[158] Kasap, S. O. 2006. *Principles of Electronic Materials and Devices,* New York, McGraw-Hill.
[159] Hummel, R. E. 2001. *Electronic Properties of Materials,* New York, Springer.
[160] Leenheer, A. J., Perkins, J. D., Van Hest, M. F., Berry, J. J., O'Hayre, R. P. & Ginley, D. S. 2008. General Mobility and Carrier Concentration Relationship in Transparent Amorphous Indium Zinc Oxide Films. *Physical Review B,* 77**,** 115215.
[161] Perkins, J., Van Hest, M., Taylor, M. & Ginley, D. 2009. Conductivity and Transparency in Amorphous In-Zn-O Transparent Conductors. *International Journal of Nanotechnology,* 6**,** 850-859.
[162] Taylor, M. P., Readey, D. W., Van Hest, M. F., Teplin, C. W., Alleman, J. L., Dabney, M. S., Gedvilas, L. M., Keyes, B. M., To, B. & Perkins, J. D. 2008. The Remarkable Thermal Stability of Amorphous In‐Zn‐O Transparent Conductors. *Advanced Functional Materials,* 18**,** 3169-3178.
[163] Taylor, M. P., Readey, D. W., Teplin, C. W., Van Hest, M. F., Alleman, J. L., Dabney, M. S., Gedvilas, L. M., Keyes, B. M., To, B. & Perkins, J. D. 2004. The Electrical, Optical and Structural Properties of InxZn1-xOy ($0 \leqslant x \leqslant 1$) Thin Films by Combinatorial Techniques. *Measurement Science and Technology,* 16**,** 90.
[164] Yan, M., Lane, M., Kannewurf, C. R. & Chang, R. P. H. 2001. Highly Conductive Epitaxial CdO Thin Films Prepared by Pulsed Laser Deposition. *Applied Physics Letters,* 78**,** 2342-2344.
[165] Chun, S. K. & Wang, K. L. 1992. Effective Mass and Mobility of Holes in Strained Si/Sub 1-x/Ge/Sub x/ Layers on. *IEEE transactions on electron devices,* 39**,** 2153-2164.
[166] Bellingham, J., Phillips, W. & Adkins, C. 1992. Intrinsic Performance Limits in Transparent Conducting Oxides. *Journal of Materials Science Letters,* 11**,** 263-265.
[167] Kikuchi, N., Kusano, E., Nanto, H., Kinbara, A. & Hosono, H. 2000. Phonon Scattering in Electron Transport Phenomena of ITO Films. *Vacuum,* 59**,** 492-499.
[168] Seto, J. Y. 1975. The Electrical Properties of Polycrystalline Silicon Films. *Journal of Applied Physics,* 46**,** 5247-5254.

[169] Orton, J. & Powell, M. 1980. The Hall Effect in Polycrystalline and Powdered Semiconductors. *Reports on Progress in Physics,* 43**,** 1263.

[170] Prins, M., Grosse-Holz, K., Cillessen, J. & Feiner, L. 1998. Grain-Boundary-Limited Transport in Semiconducting SnO2 Thin Films: Model and Experiments. *Journal of Applied Physics,* 83**,** 888-893.

[171] Hosono, H. & Paine, D. C. 2010. *Handbook of Transparent Conductors,* New York, Springer.

[172] Hosono, H. 2006. Ionic Amorphous Oxide Semiconductors: Material Design, Carrier Transport, and Device Application. *Journal of Non-Crystalline Solids,* 352**,** 851-858.

[173] Nomura, K., Kamiya, T., Ohta, H., Uruga, T., Hirano, M. & Hosono, H. 2007. Local Coordination Structure and Electronic Structure of the Large Electron Mobility Amorphous Oxide Semiconductor In-Ga-Zn-O: Experiment and Ab Initio Calculations. *Physical Review B,* 75**,** 035212.

[174] Hosono, H., Kikuchi, N., Ueda, N. & Kawazoe, H. 1996. Working Hypothesis to Explore Novel Wide Band Gap Electrically Conducting Amorphous Oxides and Examples. *Journal of Non-Crystalline Solids,* 198**,** 165-169.

[175] Kröger, F. A. & Vink, H. J. 1956. Relations Between the Concentrations of Imperfections in Crystalline Solids. *In:* Seitz, F. & Turnbull, D. (eds.) *Solid State Physics.* Amsterdam: Academic Press.

[176] Drude, P. 1900. Zur Elektronentheorie der Metalle. *Annalen der Physik,* 306**,** 566-613.

[177] Drude, P. 1900. Zur Elektronentheorie der Metalle; II. Teil. Galvanomagnetische und Thermomagnetische Effecte. *Annalen der Physik,* 308**,** 369-402.

[178] Fumiyasu, O., Minseok, C., Atsushi, T., Atsuto, S. & Isao, T. 2010. Native Defects in Oxide Semiconductors: A Density Functional Approach. *Journal of Physics: Condensed Matter,* 22**,** 384211.

[179] Fumiyasu, O., Minseok, C., Atsushi, T. & Isao, T. 2011. Point Defects in ZnO: An Approach from First Principles. *Science and Technology of Advanced Materials,* 12**,** 034302.

[180] Oba, F., Togo, A., Tanaka, I., Paier, J. & Kresse, G. 2008. Defect Energetics in ZnO: A Hybrid Hartree-Fock Density Functional Study. *Physical Review B,* 77**,** 245202.

[181] Kohan, A. F., Ceder, G., Morgan, D. & Van de Walle, C. G. 2000. First-Principles Study of Native Point Defects in ZnO. *Physical Review B,* 61**,** 15019-15027.

[182] Oba, F., Nishitani, S. R., Isotani, S., Adachi, H. & Tanaka, I. 2001. Energetics of Native Defects in ZnO. *Journal of Applied Physics,* 90**,** 824-828.

[183] Oba, F., Nishitani, S. R., Isotani, S., Adachi, H. & Tanaka, I. 2001. Erratum: “Energetics of Native Defects in ZnO” [J. Appl. Phys. 90, 824 (2001)]. *Journal of Applied Physics,* 90**,** 3665-3665.

[184] Zhao, J., Zhang, W., Li, X., Feng, J. & Shi, X. 2006. Convergence of the Formation Energies of Intrinsic Point Defects in Wurtzite ZnO: First-Principles Study by Projector Augmented Wave Method. *Journal of Physics: Condensed Matter,* 18**,** 1495.

[185] Sokol, A. A., French, S. A., Bromley, S. T., Catlow, C. R. A., van Dam, H. J. J. & Sherwood, P. 2007. Point Defects in ZnO. *Faraday Discussions,* 134**,** 267-282.

[186] Look, D. C., Hemsky, J. W. & Sizelove, J. R. 1999. Residual Native Shallow Donor

in ZnO. *Physical Review Letters,* 82**,** 2552-2555.

[187] Lany, S. & Zunger, A. 2007. Dopability, Intrinsic Conductivity, and Nonstoichiometry of Transparent Conducting Oxides. *Physical Review Letters,* 98**,** 045501.

[188] Lany, S. & Zunger, A. 2005. Anion Vacancies as a Source of Persistent Photoconductivity in II-VI and Chalcopyrite Semiconductors. *Physical Review B,* 72**,** 035215.

[189] Tuomisto, F., Ranki, V., Saarinen, K. & Look, D. C. 2003. Evidence of the Zn Vacancy Acting as the Dominant Acceptor in n-Type ZnO. *Physical Review Letters,* 91**,** 205502.

[190] Erhart, P., Klein, A. & Albe, K. 2005. First-Principles Study of the Structure and Stability of Oxygen Defects in Zinc Oxide. *Physical Review B,* 72**,** 085213.

[191] Wu, H., Peng, Y. & Shen, T. 2012. Electronic and Optical Properties of Substitutional and Interstitial Si-Doped ZnO. *Materials,* 5**,** 2088.

[192] Luo, J. T., Zhu, X. Y., Chen, G., Zeng, F. & Pan, F. 2012. The electrical, Optical and Magnetic Properties of Si-Doped ZnO Films. *Applied Surface Science,* 258**,** 2177-2181.

[193] Seeger, K. 1999. Energy Band Structure. *Semiconductor Physics.* Berlin: Springer.

[194] Zhou, X. H., Hu, Q. H. & Fu, Y. 2008. First-Principles LDA+U Studies of the In-Doped ZnO Transparent Conductive Oxide. *Journal of Applied Physics,* 104**,** 063703.

[195] Wu, H., Chen, H. & Zhu, Y. 2016. Effects of Al-Impurity Type on Formation Energy, Crystal Structure, Electronic Structure, and Optical Properties of ZnO by Using Density Functional Theory and the Hubbard-U Method. *Materials,* 9**,** 647.

Chapter 2

Experimental Techniques and Data Acquisition

2.1 X-Ray Diffraction

2.1.1 Introduction

X-ray diffraction (XRD) is a powerful, important and non-destructive characterisation technique to analyse a wide range of types of materials including powders, crystals or even liquids. [1] XRD is a basic method for the analysis of materials both in scientific research and industrial manufacture. [2] XRD can identify the crystalline phases of a lot of types of materials and the quantitative phase analysis follows the qualitative analysis. XRD specialises in detecting, exhibiting, and calculating the three-dimensional crystalline structure of compounds. It is widely used in structure design, structure calculation, and material synthesis. [3] The various applications of XRD can be summarised as follows. [4, 5]

1. To determine crystal structures of materials and natural minerals, through determination of their unit cell parameters. [6]

2. To determine purities and compositions of samples followed by a Rietveld refinement to calculate crystal structures. [7]

3. To characterise thin film samples, which is the case for experiments reported in this thesis. I can calculate the stress and the strain of the lattice, determine the degree of crystallinity and the quality of the film, extract the crystallite size, and measure the preferred orientation of grains on the film surface in the polycrystalline sample via texture information. [8] If X-ray reflectivity (XRR) is used, the film density, thickness, and roughness can be determined by fitting the theoretical model with experimental data. [9]

The advantage of the technique is that it produces a rapid method to obtain the primary information on a sample. The measurement process is always straightforward and no complicated sample preparation is needed before detecting. The XRD equipment is not

expensive and can be easily accessed in many research departments. [10] However, there are also some limitations for this technique. [11] XRD operates best with single phase materials and analysis is complex when multiple phases are present. The JCPDS cards or Powder Diffraction Files are indispensable in either phase identification or quantitative analysis. [12] The sample must be prepared as a ground powder (< 10 μm), [13] which requires 0.1 g of sample. The detection limit is around 2% for a specific composition in a mixture which is so high compared to some other techniques such as ICP-MS, XPS, and EDX. [14] The calculation of unit cell parameters and structures are complicated for non-isometric crystal structures when indexing the patterns. It can suffer peak overlay, especially at high angles. [5]

2.1.2 Principles of the Technique

The incident X-rays can diffract and interact with crystalline layers of the materials due to the comparable wavelength of X-rays with the crystalline layer distance. [15] The diffraction patterns are collected, which have the structure information of a sample. The diffraction patterns are used as the fingerprint of the crystal structure since the unique diffraction patterns can only be attributed to the specific crystal structure and the array of layers. [16] The overall diffraction patterns are composed of the diffraction patterns contributed by each phase in the mixed sample. The powder XRD intensities are distributed in one-dimensional space, and the data collected is the array of the diffraction peak intensity and the corresponding 2θ (θ is the angle between the incident X-ray and the surface). [17] However, X-ray crystallography produces three-dimensional data to show the electron density in the lattice, which is different from powder XRD. [18]

The unit cell is a simplest repeating unit of crystals, which is built up of particles with repeating patterns. [13] The terminologies Miller indices and reciprocal lattices are introduced to describe the geometry of lattice arrangements, directions, and structures determined by XRD. [19] To define the Miller indices of a plane, three vectors are chosen along the unit cell

edges in the cubic system as a, b, and c. The intersection points of a specific plane and three vectors can be found. These three ratios of these three points are converted into their reciprocals and expressed as a set of integer values (hkl). [20] Sir William H. Bragg and his son Sir William L. Bragg [21] first introduced a fundamental theory to describe the relations between angle of incidence, layer distance, and incident beam wavelength, which is called Bragg's Law. As the incident beam approaches the plane surface with the angle of incidence θ, the reflected beam has the same angle θ, which is called the angle of reflection (**Figure 2.1**). If the path difference of these two incident beams is equal to an integral multiple of the incident beam wavelength, a constructive interference occurs. [22]

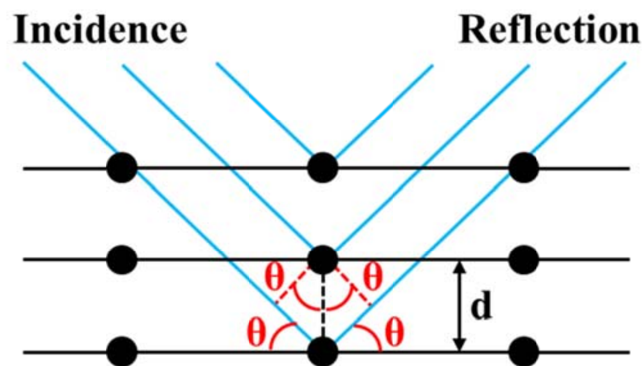

Figure 2.1: Bragg's Law.

Bragg's Law links the crystal layer distance with the angle of reflection generated from the X-ray incident beam. Only constructive interference from specific angles of incidence can be regarded as proper signals to display. It expressed as the equation below. [23]

$$n\lambda = 2d\sin\theta$$

Equation 2.1

Where λ is the incident X-ray wavelength, d is the crystal layer distance or the path difference, θ is the angle of incidence (the angle between the incident beam and the plane), and n is an integer.

D-spacing d_{hkl} is defined as the distance between adjacent planes, as shown in Bragg's equation, which is determined by the Miller indices (hkl), and the lattice parameters a, b, and c. The relations can be expressed as the following equation. [24]

$$\frac{1}{d_{hkl}^2}=\frac{h^2}{a^2}+\frac{k^2}{b^2}+\frac{l^2}{c^2}$$

Equation 2.2

We can determine the lattice parameters and crystal structure, which are deduced from d-spacing values calculated from Bragg's Law. Since each phase contributes independent unique diffraction patterns, it also possible to qualitatively detect the phases mixed in a sample and to calculate their individual contents. [3, 25]

2.1.3 Applications of XRD

2.1.3.1 Phase Identification

XRD phase identification can, in theory and usually in practice, tell one compound apart from another in a mixture. [26] The measured XRD patterns are compared with standard XRD data to identify the materials present. The ICDD International database provides XRD data, which contains name, chemical formula, crystal structure/category, standard reference diffraction patterns, etc. [27] It was reported in 2006 that the PDF4 release has a collection of 254,873 Digital XRD patterns from a wide range of inorganic and organic crystalline substances, which are both theoretically calculated and taken from experimental data. [28]

2.1.3.2 Quantitative Phase Analysis

The quantitative phase analysis is based on the diffraction intensity ratios in XRD patterns.

[29] Alexander and Klug [12] optimise the analysis process by introducing integrated line intensity ratios in one set of XRD patterns of a sample, and gives highly accurate results. Total absorption coefficients do not need to be calculated and microabsorption effect errors can be wiped out, which makes the whole process simpler. **Figure 2.2** shows an example of the intensity ratio of XRD patterns as a function of weight percentage of phases reported by Spurr et al. [30] It indicates a linear relationship between the intensities of patterns and weight percentages for phases in a mixture. The relations between the intensities of patterns and weight percentages of various components can be described as follows. [31]

$$\frac{I_\alpha}{I_\beta} = K\frac{w_\alpha}{w_\beta}$$

Equation 2.3

Where I_α and I_β are the intensities of phase α and phase β in XRD patterns, respectively. w_α and w_β are the weight percentages of phase α and phase β, respectively. K is called the calibration constant. The calibration constants can be deduced from the standard experimental measurements, Rietveld refinements, and reported reference intensity ratios (RIR). [32]

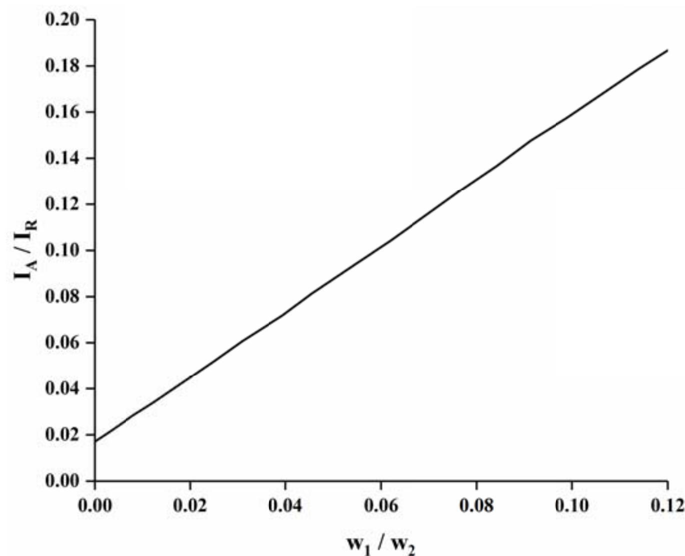

Figure 2.2: Intensity ratio of XRD patterns as a function of weight percentage of phases. Data are taken from Spurr et al. [30]

2.1.3.3 Lattice Parameters

The lattice parameters a, b, and c are used to represent the side length of the unit cell, and meanwhile α, β, and γ three angles between each pair of these three sides are also included. [33] 2θ angles are the diffraction peak positions defined by the size and shape of the unit cell. The corresponding peak intensities are related to the electron densities, the arrangements of atoms, and the atomic numbers. Another parameter called peak width is affected by the XRD equipment itself, the crystallite size, the stress and the strain, etc. The equations below give the calculations of lattice parameters in a cubic crystal system. [25]

$$d_{hkl}^2 = a^2 / (h^2 + k^2 + l^2)$$

Equation 2.4

$$\sin^2\theta = \frac{\lambda^2}{4a^2}(h^2 + k^2 + l^2)$$

Equation 2.5

Where a is the side length of the cubic unit cell, (hkl) are Miller indices, d_{hkl} is the spacing of adjacent scattering layers, θ is the angle of incidence, and λ is the wavelength of incident X-rays.

Consequently, the unit cell volume is calculated from the lattice parameters. The number of a specific kind of an atom can also be calculated from the density and the volume of the unit cell, followed by the results of formula weight or the formula unit number. The equation for the unit cell volume V is given by. [34]

$$V = abc\sqrt{1 + 2\cos\alpha\cos\beta\cos\gamma - \cos^2\alpha - \cos^2\beta - \cos^2\gamma}$$

Equation 2.6

Where a, b, and c are the side lengths of the unit cell, and α, β, and γ are the corresponding angles.

For cubic lattices where a = b = c, α = β = γ = 90°, the unit cell volume is simplified as below.

$$V = a^3$$

Equation 2.7

2.1.3.4 Crystallite Size

A sharp and narrow diffraction peak is attributed to a perfect crystallinity, whereas imperfect crystallinity leads to a broadening peak. [35] Another cause of broadening peaks is reduced crystallite sizes, which can be ignored for large crystallite sizes (> 200 nm). Paul Scherrer [36] first reported in 1918 that small crystallite size leads to broadening of diffraction peaks. An equation linking the crystallite size and the diffraction peak width was proposed by him, and called the Scherrer equation. [37]

$$\tau = \frac{K\lambda}{\beta\cos\theta}$$

Equation 2.8

Where τ is the average crystallite size, K is the Scherrer constant (it depends on the crystallite shape and the commonly used value is 0.87 - 1.0), λ is the wavelength of incident X-ray, β is the line broadening at half the maximum intensity (FWHM), and θ is the Bragg angle (the angle of incidence).

2.1.4 Instrumentation

The XRD measurement was carried out on a PANalytical Empyrean diffractometer, operating with the Bragg-Brentano geometry, a fixed X-ray source, anti-scatter slits, reflection transmission spinner stage, and PIXcel1D detector. The emission current was 40 mA and the anode voltage was 45 kV with the monochromated radiation wavelength Cu K-α1 = 1.5405980 Å. The spectra were recorded at 2θ from 10° to 80°. Samples were placed on the reflection transmission spinner stage with a fixed rotation speed to keep the crystallite orientation.

2.2 Atomic Force Microscopy

2.2.1 Introduction

Atomic force microscopy (AFM) is a surface sensitive characterisation technique to obtain high resolution surface topographic images of samples. The resolution can be on the scale of molecular or even atomic ranges. The spatial resolution depends on the type of the tip, which is generally in the range of 1 - 20 nm. [38] AFM presents topographic images, which contain abundant information including the chemical arrangement of molecules or atoms, the stiffness, the friction, and the electrical and magnetic properties. A sharp microfabricated tip is the core component in an AFM instrument. It scans across the surface of a sample when the tip connects to a cantilever of AFM. The forces between the tip and the sample surface can deflect the cantilever, thus changing the movement and status of a laser beam, which is used to monitor the motion of the cantilever. Finally, the surface images are obtained from the photodiode processed by software. [39] There are numbers of modes or ways for AFM to collect surface images such as contact mode and tapping mode. [40] If the tip of AFM is in a static state, i.e., it does not move horizontally but just vertically, a force spectroscopy can be

obtained. It applied 5 pN - 50 μN forces to a stationary surface spot and records the height values to get the information on the mechanical, physical, or chemical properties of the sample. It can measure nanomechanical properties if the tip inserts into a depth of the surface, or it can measure bond rupture and molecular pulling if kept a small distance from the surface. [41]

AFM generally has here different modes called contact mode, non-contact mode, and tapping mode. [42] In contact mode, the repulsive force between the tip and the surface keeps constant; therefore, the deflection of the cantilever is also constant. The software then records the movement of the laser beam which monitors the cantilever movement to illustrate the topographic images. In non-contact mode, as its name, the tip does not contact the surface of a sample but oscillates close the surface. The amplitude of cantilever changes due to the attractive Van der Waals forces between the tip and the sample surface, which is recorded as the surface topographic images. In tapping mode, the tip just taps on the resonant frequency on the sample surface with a constant oscillation amplitude to keep a constant interaction between the tip and the surface. The cantilever movement is then recorded as the surface images. [43, 44]

2.2.2 Principles of the Technique

The key component in AFM is the cantilever with a small tip to measure the force or potential energy when interacting with a sample surface. The height of the surface is measured by positioning the tip close to the surface, while the bond rupture and molecular pulling can be detected if a small distance between the tip and the surface is maintained. [45] **Figure 2.3** shows a schematic illustration of an AFM instrument. When the tip moves along the surface of a sample, the deflection of the cantilever corresponds to the morphology of the surface. The change of the cantilever alters the position of the reflected laser beam on the photodiode. Finally, the signals from the photodiode transfer into the topographic image of the surface.

[46]

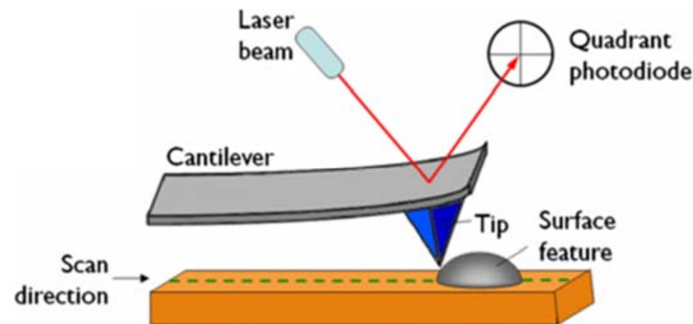

Figure 2.3: A schematic illustration of an AFM instrument. © IOP Publishing. Reproduced from Daniel et al. [46] with permission. All rights reserved.

The cantilever has a small tip at one end to detect the forces, which depends on the nature of the instrument, i.e., the elastic strength of the cantilever, and the distance between the surface and the tip. It can be expressed as the equation below, which is famous as Hooke's Law. [47]

$$F = - kx$$

Equation 2.9

Where F is the force, k is the elastic constant, and x is the deflection of the cantilever. Generally, it should be assumed that if the elastic constant of the cantilever (0.1 - 1 N / m) is smaller than that of the surface, I can observe the deflection of the cantilever. Many empirical results indicate that the force is in the range of nN to μN in the air. [43]

2.2.3 Applications of AFM

The deflection of the cantilever is attributed to the force between the surface and the tip, which varies as a function of the distance between them. The long-range attractive or repulsive forces can be measured if the tip is pushed to and pulled away from the sample surface. These forces can determine the chemical and mechanical properties of the surface.

[48]

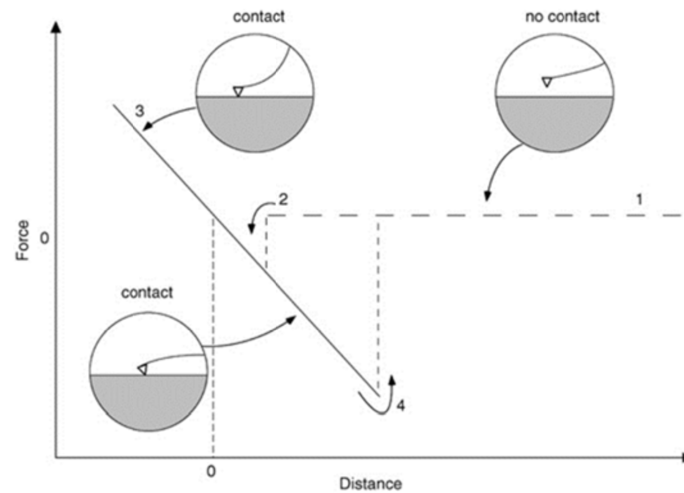

Figure 2.4: Force between the tip and the surface as a function of the corresponding distance between them. Reproduced from Goldsbury et al. [48] with permission from Wiley.

Figure 2.4 shows the force between the tip and the surface as a function of the corresponding distance between them. The diagram illustrates the whole process for a tip to approach the surface, touch the surface, and finally move away from the surface. The four steps in **Figure 2.4** comprise: [48]

1. The tip approaches the surface from far away without any forces.

2. The attractive forces make the tip start to contact with the surface in a specific distance.

3. The forces increase to a maximum value with the reduced distance between the tip and the surface. It is similar to the process when the tip is pushed into the depth of the surface. [49]

4. As the tip is pulled away from the surface, the adhesion forces or the attractive effects from the surface molecules or ligands resist the complete separation of the tip and the surface; therefore the tip undergoes a stronger force compared to that in Step 2. [50]

2.2.4 Instrumentation

AFM images were measured on a Bruker Dimension Icon Atomic Force Microscope using a Bruker silicon probe with a resonant frequency of 75 kHz and a spring constant of 3 N / m. The measurement was carried out in air with an examined area size of 5 μm × 5 μm. Gwyddion software [51] was used for AFM data visualisation and analysis. It can be used for general height field and image processing, for instance for the analysis of profilometry data or thickness maps from imaging spectrometer.

2.3 Scanning Electron Microscopy

2.3.1 Introduction

The scanning electron microscope (SEM) is a multifunction characterisation instrument to measure the morphology and the chemical composition of a sample. The SEM images and the related detections arise from the interactions between the sample and the high energy electrons introduced by a focused beam with a high voltage. The surface morphology, the chemical composition, the grain orientation and structure, and the grain size can be extracted from the SEM results. [52] In general analysis process, two-dimensional images can be taken out to indicate the distribution of microstructures in the space, especially the in-plane structure information. Normally, the SEM instrument can collect the images in the range of 5 μm - 1 cm with the magnification of 20× - 30,000× and the resolution of 50 - 100 nm, suggested by Swapp. Moreover, SEM can also determine the chemical composition combined with EDX, as well as the crystal size, structure and orientation combined with EBSD in a qualitative way. [53]

2.3.2 Principles of the Technique

The generation of SEM images is due to the detection of signals arisen from the interactions between the electron beam and the sample (**Figure 2.5**). The interactions are composed of two types, i.e., inelastic and elastic. The generation of secondary electrons (SE), which is widely used to image a sample is attributed to inelastic interactions. [54] The energy is transferred from the incident electron beam to the atoms in the sample, owing to the interactions between the incident electrons and atoms and electrons in the sample. Finally, the excitation of electrons with sufficient energies occurs as the ionisation process of the sample, which leads to the generation of secondary electrons. The operation energy is usually less than 50 eV to obtain SEM images. [55]

Another type of signals used to image the sample are backscattered electrons (BSE), which arise from elastic interactions. [56] The incident electrons elastically scattered with a larger angle, which are due to the elastic collision between the incident electrons and the nucleus or the outer shell electrons in the sample. The word 'elastic' means that there is no energy loss during the collision process. [57]

The figure also shows some other signals besides secondary electrons and backscattered electrons. The collection of signals includes Auger electrons, X-ray continuum, and characteristic X-rays. [58]

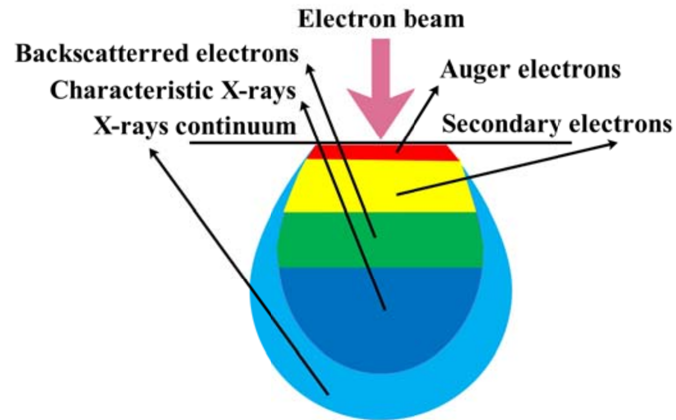

Figure 2.5: Schematic diagram of different signals arisen from the interactions between the electron beam and the sample.

SEM is a complex system with various components and a schematic diagram of its setup is shown in **Figure 2.6**. The electron gun is the electron source to generate a high energy incident beam. [59] The secondary electron detector is the key component to generate images in SEM. [60] The backscattered electron detector can also be assembled if required in some cases. [61] The other parts can include anode, alignment coil, lens, scan coil, specimen holder, specimen stage, and specimen chamber. Computers, power supply, and a vacuum system can also be an essential support for the equipment to work properly. [53]

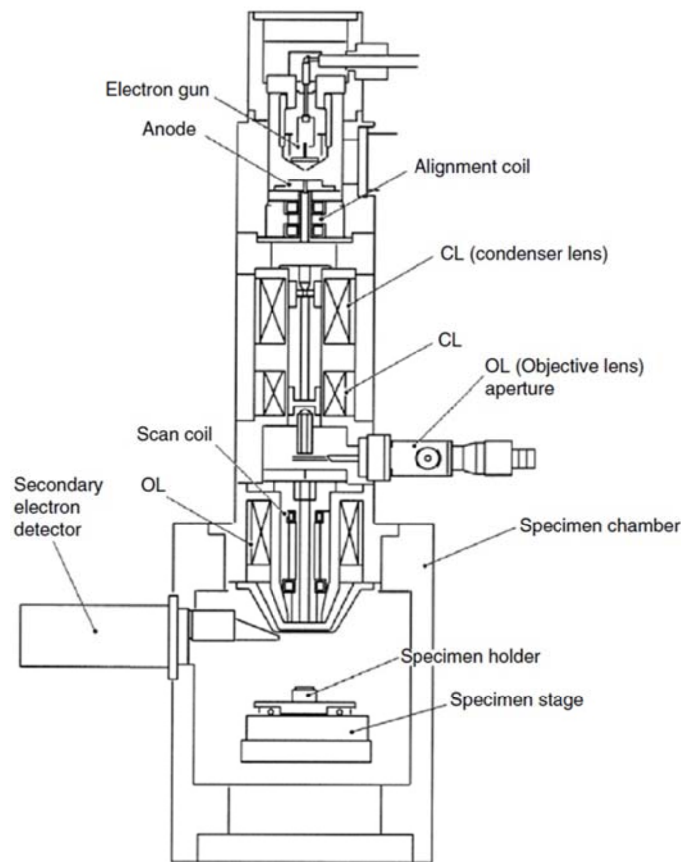

Figure 2.6: Schematic diagram of a SEM system. Reprinted from Zhou et al. [58] by permission from Springer.

2.3.3 Applications of SEM

SEM is a widely used imaging technique to analyse the morphology and the structure distribution in the space of a sample, based on the high resolution images including secondary electron imaging (SEI) and backscattered electron imaging (BSEI). [62] It can measure and indicate a very small size and a tiny crystal structure on the scale of 50 nm. It can take quantitative or semi-quantitative analysis incorporated with EDX, BSE, and EBSD. [63] EDX can draw the element distribution map and calculate the chemical composition of a sample. BSE is powerful to detect the composition of phases quickly. [64] EBSD is a commonly used method to illustrate the crystallographic orientation in the materials. [65]

2.3.4 Instrumentation

SEM images were carried out on a JEOL JSM-840F Scanning Electron Microscope located in David Cockayne Centre for Electron Microscopy, University of Oxford. Samples were mounted onto SEM stubs by using conducting carbon cement and sputtered with platinum before collecting the SEM images. The accelerating voltage was 5 kV with magnification from 10,000 × to 50,000 ×. The emission current was around 13 μA and probe current was 2×10^{-11} A. DISS 5 software was used to acquire and process SEM digital images.

2.4 Transmission Electron Microscopy

2.4.1 Introduction

The transmission electron microscope (TEM) is a powerful tool to visualise the internal structure directly on the scale of nanometres in the characterisation of the materials. [66] The reason for the low scale or the high magnification TEM can reach is due to the short wavelength electron beam generated by a high energy source, which is impossible with the relative long wavelength of visible light used in the optical microscope. [67] Just as its name ‘transmission’, the sample needs to be prepared as a very thin specimen to allow the high energy electron beam to penetrate through. The structure information such as grain boundaries, voids, grain sizes, and grain growths can be obtained due to the interactions between the incident electrons and the sample. [68] In this thesis, TEM has been valuable in the analysis of element distribution along the vertical direction, visualising the defects and void in bulk, indicating the grain growth and its size, and comparing the film quality. By the incorporation of EDX, EELS, etc., TEM can also analyse the chemical composition or the oxidation state. [69]

2.4.2 Principles of the Technique

The fundamental theory for TEM and the optical microscope are similar. TEM can detect at a very small scale, even down to atomic resolution in exceptional cases. [69] The high energy electron beam passes through a thin specimen and interacts with the sample. The image is determined by the amount of the electrons that penetrate through the specimen. If most of the incident electrons are deflected inside the materials, this part of the image is dark. However, if these electrons almost pass through the sample with little deflection, this part of the image is bright. The grey part of the image is due to the medium interactions between the incident electrons and sample. [70] TEM images have a high magnification of 1,000,000 × and a resolution of 1 nm or less, suggested by AMMRF. [67] Combined with other quantitative detectors, a larger range of properties can be observed such as crystal structures, grain sizes and growths, and defects. [70]

TEM is a precision instrument and a ray diagram indicates the heart of TEM. **Figure 2.7** shows a schematic setup of a TEM instrument. The illumination system transfers the incident electrons to the sample. [71] These lenses are used to focus the electron beam in a specific direction to pass through the sample and reach the screen. There are two working modes for TEM, i.e., image mode and diffraction mode. If the objective plane is the image plane, the image mode is observed on the screen. However, the diffraction mode arises with the diffraction patterns showing on the screen when the back focus plane is adjusted as the objective plane. [72]

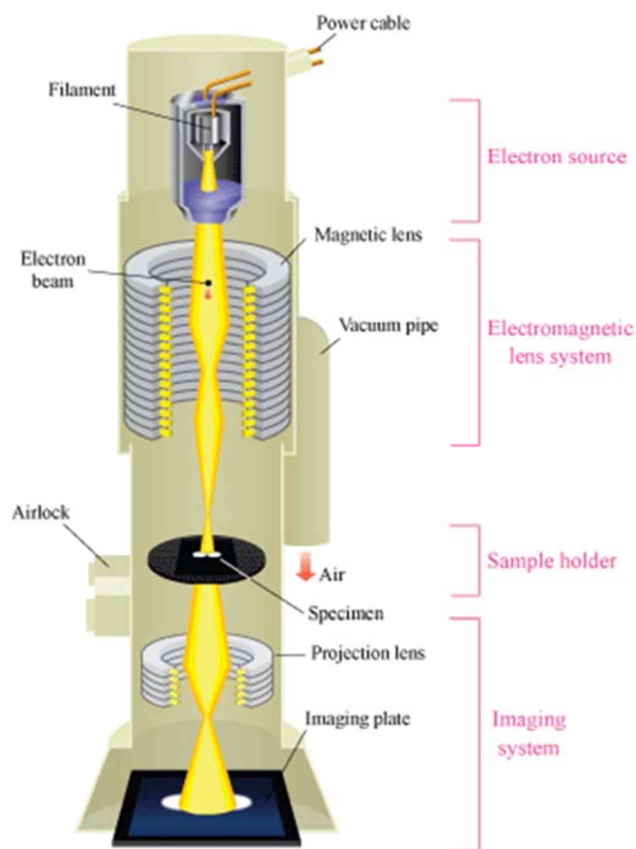

Figure 2.7: Schematic setup of a TEM instrument. Reproduced from [73] with permission from Physics World.

2.4.3 Applications of TEM

The common information for a material obtained by TEM includes the cross-sectional morphology, the crystal structure, the environment of grains, the grain boundary, and the grain orientation. [74] It can also combine with other characterisation techniques such as EDX to give quantitative analysis. TEM can be applied in a wide range of research fields. [75] I can draw the cross-sectional images of materials, and three-dimensional images can also be obtained with a series of groups of images. [76] The composition and bonding information are detectable incorporated with other techniques. A series of diffraction patterns can be collected for the crystal structure analysis. The advantage of TEM compared with surface powder XRD is that the TEM patterns indicate the structure inside the bulk, whereas, powder XRD only

represents the surface structure. [77]

2.4.4 Instrumentation

TEM was carried out on a JEOL JEM-2010 Transmission Electron Microscope. It used a LaB_6 cathode at a beam energy of 200 keV. All images were taken on a Gatan 794 MultiScan camera. EDX spectra were taken on a Si(Li) Thermo Fisher EDX system. The samples were mounted onto an aluminium stub using silver glue, followed by coating with carbon and Pt/Pd before insertion into FIB-SEM. FIB-SEM was an FEI Nova NanoLab 200 (Hillsboro, Oregon). The electron energy for all SEM work was 5 keV, the ion energy for all lift-out work and sample thinning was 30 keV. 5 keV ion energy was used for removing thick amorphous surface layers. TEM sample preparation used the 'lift-out' method with the focused ion beam by the extraction of the cross-section and the thinning to electron transparency. Samples were then inserted into TEM for the measurement. EDX spectra were acquired with an electron probe with a diameter of between 50 and 100 nm. The sample was tilted 15° towards the EDX detector to reduce X-ray shadowing. Three points were measured for each film, with collection times varying between 300 and 600 seconds per spectrum.

The four wafers were cleaved into two pieces, using a diamond-tipped pencil to initiate the crack and shear stress to break them in two. An optical microscope was used to identify the correct film-bearing side of the glass using Newton's fringes at the film edge and tracking the height relative to dust on the surfaces. The four pieces destined for the microscope were glued to a 1inch (25.4 mm) diameter Al stub using Ag glue (**Figure 2.8**(a)). Care was taken to establish Ag-glue bridges between the topmost films and the Al stub on every side of the piece so that electrical discharge can prevail during ion-beam preparation. Each sample was marked with red permanent ink marks, e.g., ● for ZnO, ●● for SiZO, etc., to ensure unambiguous identification in the FIB-SEM. Before insertion into the FIB-SEM, the sample was coated; first with evaporated carbon (graphite tapered rods heated to white hot) several

times to ensure a reasonably good, continuous amorphous carbon coverage. This resulted in a layer thickness of approximately 100 nm. Second, a magnetron sputtered Pt/Pd alloy film to a nominal thickness of 20 nm. The two-coating approach has worked previously with films on glass substrates - the carbon ensures good continuous coverage for electrical contact and the Pt-Pd serves three purposes: (1) its high atomic number (relative to carbon) helps identify the top surface in the TEM; (2) the high density prevents stray ions penetrating into the carbon film and damaging it; (3) the metal film acts as a heat diffuser to prevent the film melting. The dark-metallic appearance of the four samples and their identifying marks are easy to see in **Figure 2.8**(b).

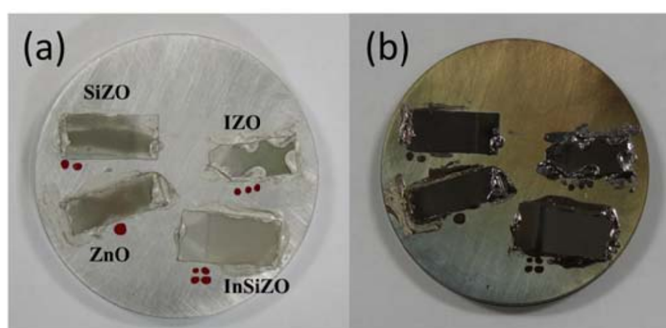

Figure 2.8: Photographs of the wafer pieces before (a) and after (b) carbon and Pt-Pd coating. The darker, opaque parts of the wafer pieces indicate the film proximity to the edge of the Al stub.

TEM sample preparation used the 'lift-out' method with the focused ion beam. This comprises two stages: Stage 1 is the extraction of the cross-section. 15 μm × 2 μm protective Pt strips were deposited, first with a 5 keV electron beam (to a height of 300 nm) and then a 30 keV Ga^+ beam to an additional height of 2500 nm (**Figure 2.9**(a)). The Pt is deposited by the beam-induced dissociation of trimethyl(methylcyclopentadienyl)platinum (IV) injected close to the extraction point by the insertion of a long, thin hollow needle. The location of the protective Pt strip was chosen to avoid large pieces of dust and any conspicuous anomalies in the electron beam image (**Figure 2.9**(a)). High-current (3 to 7 nA) ion beam was used to mill around the Pt strip on three sides to a nominal depth of 5 μm to roughly cut a cross-sectioned slab (**Figure 2.9**(b)). A stand-off distance of 1 to 2 μm from the Pt strip was used to prevent excessive milling of the Pt. A medium-current ion beam (0.5 to 1 nA) was used to sculpt this

down to a tidier 2.5 μm × 20 μm piece. After milling 45° slots underneath the slab and establishing a single mechanical bridge to the remaining wafer, a tungsten needle was applied to the free end of the slab and Pt 'welded' to it. A 1 nA ion probe severed to the lamella and wafer removed to leave the free-standing extracted slab (**Figure 2.9**(c)). This resulted in a 2 to 2.5 μm thick lamella attached to a copper 4-post OmniProbe using a Pt 'weld'.

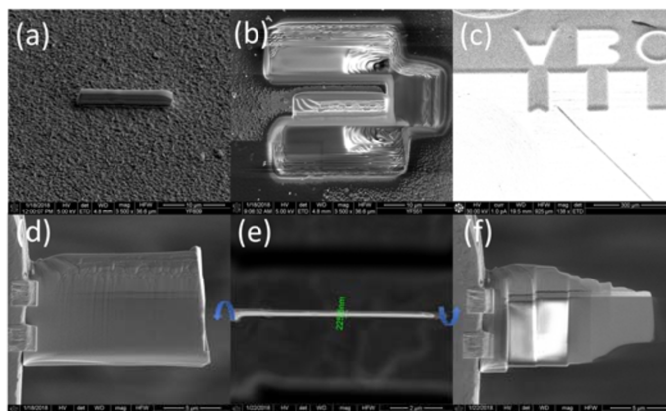

Figure 2.9: SEM images taken during the FIB lift-out of thin films. Deposition of the protective Pt strip (a). Bulk milling to isolate three sides of the section (b). The positioning of the section to an OmniProbe grid (c). The roughly milled section in place prior to final milling (d). Monitoring lamella thickness during thinning stages (e). The final lamella ready for the TEM (f).

Stage 2 is the thinning to electron transparency (**Figure 2.9**(c) to (f)). The slab is thinned using cleaning cross sections, which progressively removes material from the outside in using finer, lower ion current probes to improve milling precision. Typically, the lamella thickness is halved for each run. Electron beam images of the lamella are used to monitor thickness between each stage (**Figure 2.9**(e)). Thinning terminates when the SEM image shows enhanced brightening at the thinnest edges (**Figure 2.9**(f)). The array of TEM cross sections ready for the TEM is shown in **Figure 2.10**. TEM examination began with the first prepared film (ZnO, pillar D) and worked towards InSiZO (pillar A).

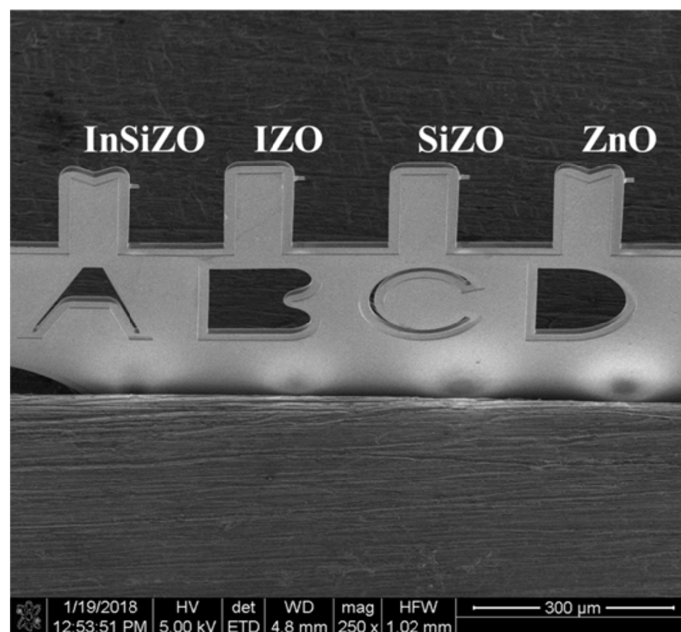

Figure 2.10: The TEM-ready cross sections of all four samples. The order of preparation was D → A.

2.5 X-Ray Photoelectron Spectroscopy

2.5.1 Introduction

X-ray photoelectron spectroscopy (XPS) is the most commonly used technique to determine elemental composition, oxidation states, and the chemical environment of atoms on the sample surface (< 10 nm). [78] XPS can also qualitatively and quantitatively analyse all the elements with a detection limit of 0.05 at% from Li to U except H and He. [79] Besides its high accuracy, the quantity of the sample required for the XPS detection is small.

2.5.2 Principles of the Technique

XPS process starts from the generation of X-rays (the energy is 1486.6 eV for Al K_α or 1253.6 eV for Mg K_α). [80] When an incident X-ray beam interacts with the sample, electrons in the atomic or molecular orbitals of the samples are excited and ejected out of the orbitals due to the absorption of the energy from X-rays (**Figure 2.11**). The equation to describe this process

is as follows. [81]

$$E_B = h\nu - E_K - w$$

Equation 2.10

Where E_B is the binding energy of the core electrons relative to the Fermi level, $h\nu$ is the photon energy of incident X-rays, E_K is the kinetic energy of the excited and ejected electrons, and w is the work function of the sample.

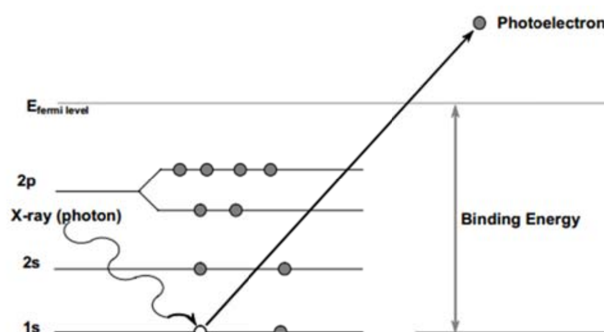

Figure 2.11: Schematic diagram of the electron excitation in XPS. Reproduced from Jang [82] with permission from Jang.

The equation can be described in terms of the electrons absorbing the incident X-ray photon energy, and being excited and ejected out of the orbitals by overcoming the work function of the sample. The binding energy is a characteristic parameter for the orbital electrons. Generally, the binding energy is calibrated with a standard to improve the accuracy. [83] For example, C 1s binding energy is the most commonly used one for calibration. The XPS spectra are shown as the intensity as a function of the binding energy or the kinetic energy. The conversion between these two energies is shown in **Equation 2.10**. [84] XPS can discriminate different element species due to the different binding energies of core electron for different atoms or elements. The chemical environment of the elements can be precisely observed by comparing the shifts of the binding energies of specific atoms. By referring to the XPS database, XPS can also indicate the oxidation state of the elements. [85]

Another emission generated from the Auger effect is usually incorporated into XPS to give additional information (**Figure 2.12**). After the core electron is excited and ejected as discussed in the XPS process, a vacancy is left behind which can be occupied by electron in the outer orbitals to occupy. The energy which is released in this process, is transferred to a third electron to eject it out of the orbital. Thus electron is called an Auger electron. [86] The Auger electron energy depends on the characteristic energy level of the orbital, which can be affected by the environment and the bonding condition. Compared to normal XPS signals, Auger signals exist at higher binding energy region in the spectra due to a lower kinetic energy in the Auger emission process. [87] As Auger electrons are typically from valence electrons in chemical bonds, it can be a sensitive method to understand the bond properties, the chemical environment, and the oxidation state. This technique is always called Auger electron spectroscopy (AES). [88]

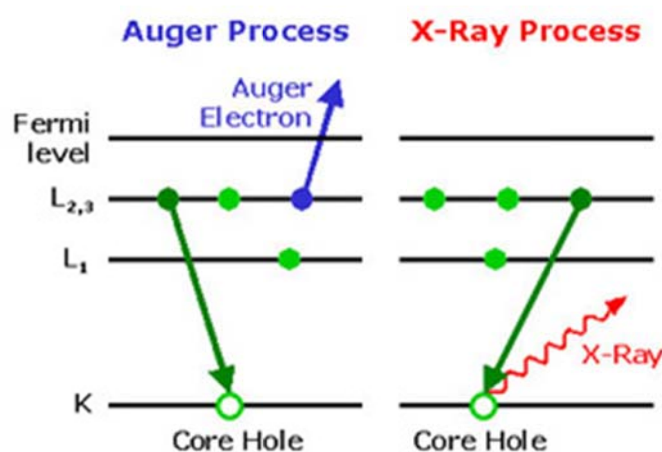

Figure 2.12: Schematic diagram of Auger effect. Reproduced from Yun [89] with permission from UTEP.

In XPS, the electrons after excitation and ejection can be regarded as free electrons with energy higher than the Fermi level. Therefore, the measured energy can quantitatively link to the bonding information and the oxidation state. It can be used as a fingerprint to distinguish one chemical bond from another or one oxidation state from another. [90] XPS can also study

complicated electronic structures in a large number of compounds, which are semiconductors in our case of this thesis. [84]

One example of the wide survey scan spectra of ZnO prepared at 180°C reported by Dai et al. [91] is shown in **Figure 2.13**. The peaks indicate the presence of Zn 2p, Zn LMM, Zn 3s, Zn 3p, Zn 3d, O KLL, O 1s, and C 1s as labelled in the spectra. No peaks belonging to other compounds or elements are detected, showing that the sample is simply ZnO. [91]

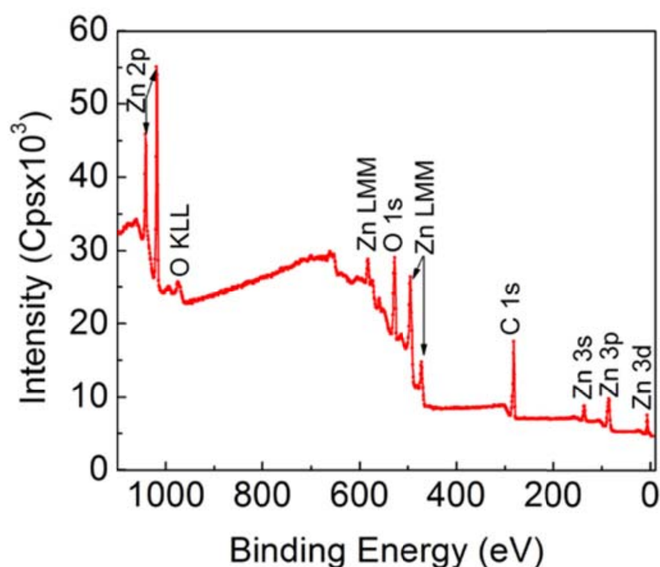

Figure 2.13: Wide survey scan spectra of ZnO. Reproduced from Dai et al. [91] with permission from OSA Publishing.

A schematic diagram of an XPS spectrometer is shown in **Figure 2.14**. The XPS spectrometer is a precise and complicated instrument with numbers of components. Among them, the indispensable parts include the X-ray source, the lens to direct electrons, the sample stage, electron energy analyser, and the detector. [92] All the process is carried in an ultrahigh vacuum (UHV) chamber. The lens can be adjusted to various magnifications and detect a range of elements, and it can also change the detecting area if required.

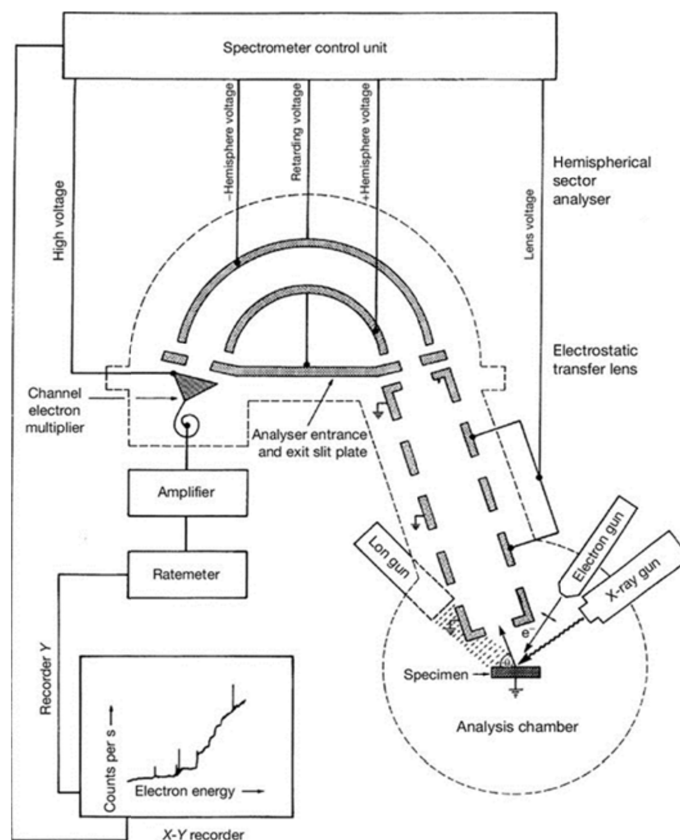

Figure 2.14: Schematic diagram of an XPS spectrometer. Reprint from Tougaard et al. [84], with permission from Elsevier.

There are many options for the choice of the X-ray source. The normally used source is Al K_α (1486.6 eV) or Mg K_α (1253.6 eV). There are also some higher energy sources available including Si K_α (1740 eV), Zr L_α (2042 eV), and Ag L_α (2984 eV). [84, 93] The linewidth of the X-ray source is one of the main factors affecting the resolution in XPS. During the XPS operation, a crystal monochromator is usually fitted to improve the resolution by decreasing the linewidth of the X-ray source from 0.85 eV to 0.35 eV. [94] However, the side effect is that it decreases the intensity at the same time. One requirement for the sample to be analysed in XPS is that it must be stable with no damage occurring under UHV. Therefore, this powerful technique may not be very friendly to volatile species, liquids, or biological samples. The sample size is normally 1 cm × 1 cm and inserted into the vacuum chamber. Any residual materials or contaminations can be removed by the inert ion gun. This inert ion gun can also etch vertically into the sample from its surface to allow an analysis along the depth, which can be ~ 1 μm. [95]

The hemispherical analyser records the XPS spectra based on the selected electrons, which can pass through a grid system and arrive at the electron multiplier. [96] The electrical potential used to select the electrons is recorded as part of the XPS spectra. The electron multiplier is used to detect the electrons consisting of several arrays to increase the resolution and intensity. [97] The main part of the equipment is a mu-metal shield against static or low-frequency magnetic fields. [98] The operation is in a UHV chamber with a low pressure of 10^{-9} mbar to isolate from the outer environment and improve the sensitivity in identification of the surface. Tougaard et al. [84] reported that the absorption and the chemical reaction between the sample surface and gas occur within several seconds in the pressure of 10^{-6} mbar. However, the time is a few hours if the pressure is 10^{-9} mbar.

The other XPS components consist of the instrument control system, data output system, data processing system, etc. I can interoperate both qualitative and quantitative results obtained from XPS. [84]

2.5.3 Applications of XPS

2.5.3.1 Qualitative Analysis

As each element has its own characteristic binding energy; therefore, the observed peaks in the XPS spectra can indicate the presence of the element. [99] However, the XPS peaks are mixed with the peaks from Auger emissions. I need to separate them from the XPS peaks by using the standard database. [100] XPS can detect the whole range of the periodic table from Li to U except H and He; thus some light element identification is possible such as halogens and organic compounds. In order to obtain the X-ray with single energy, a monochromator is widely used to filter out $K_{\alpha 3,4}$ and K_{β} in the X-ray radiation. [101]

2.5.3.2 Chemical Analysis

XPS can also provide the information on the chemical environment of the sample, which is related to the binding energy as shown in the XPS spectra. As the binding energy depends on and is affected by the chemical environment for both core electrons and valence electrons, XPS can indicate the effect on the electrons from the chemical environment. [90] Chemical shift is used to describe the electrostatic potential variations in the orbitals of the sample, which is determined by the oxidation state, the deficiency, impurity doping, the defect, and the environment. These chemical shifts can be used to examine the chemical information by referring to the standard database. [102]

2.5.3.3 Energy Loss Features

The interactions between the ejected electrons from the photoionisation and the sample reduce the measured kinetic energy, thus causing an energy loss in the process. [103] This energy loss makes the binding energy shift to a higher value. The process usually consists of intrinsic excitation effects and extrinsic excitation effects. The intrinsic excitation effects occur before the electrons finally leave the atom. The vacancy left behind due to the excitation of the electrons interacts with the electrons in the valence band. It excites these valence electrons to the empty states. Consequently, the kinetic energy of the ejected electrons is reduced, thus increasing the binding energy. If unpaired electrons exist in the valence band, the coupling between the unpaired valence electrons and unpaired core electrons leads to a multiplet splitting, which can be observed in the XPS spectra. [104] The extrinsic excitation effects happen during the process when the ejected electrons leave the atom and approach the sample surface. They can excite the electrons in the valence band of the sample, leading to an energy loss to shift the binding energy to a higher value. [105]

2.5.3.4 Depth of Analysis

As XPS is a surface sensitive measurement technique, the photoelectrons cannot penetrate too deep into the sample. The depth of the XPS characterisation can be expressed in the following equation. [106]

$$I_d = I_0 \cdot e^{-\frac{z}{\lambda \cos\theta}}$$

Equation 2.11

Where I_d is the number of the electrons travel out of the sample surface without energy loss, I_0 is the number of the electrons originated at a depth z, z is the depth, θ is the electron emission angle, and λ is the electron attenuation length. λ mainly depends on the kinetic energy of the electrons. The value of λ is 0.5 - 3 nm for XPS analysis, suggested by Touggard et al [84]. The depth is generally to 3λ in the XPS analysis because 95% of the electrons can travel out of the sample surface without energy loss, which are originated at this depth. It is calculated from **Equation 2.11**. It indicates that the depth is 1.5 - 10 nm [84]. Angle-resolved XPS (ARXPS) can be introduced to have better sensitivity than normal XPS since it reduces the depth by changing emission angle θ. Alternatively, You can also tilt the sample surface to reduce the depth for XPS analysis. [107]

2.5.3.5 Quantitative Analysis

The quantitative analysis of elemental compositions is possible since the peak intensity in XPS is proportional to the quantity or the content of each element. However, peak area is always used instead of its intensity after normalisation with atomic sensitivity factors (ASF) [84]. The equation to express the content of an element/atom is as follows. [108, 109]

$$f_i = \frac{\frac{A_i}{ASF_i}}{\sum_j \frac{A_j}{ASF_j}}$$

Equation 2.12

where f_i is the content of element/atom i, A_i is the area of the peak for i, A_j is the area of the peak for j, ASF_i is its ASF for i, and ASF_j is its ASF for j. ASF depends on not only the element species but also the atomic orbitals or the energy levels. A larger ASF also means a larger ionisation cross section. [85]

The analysis of elemental compositions on the sample surface is not accurate if the element distribution along the depth is not homogenous since the number of the electrons travel out of the sample surface is less for a larger depth. [84]

2.5.4 Instrumentation

XPS was carried out on a Kratos Axis Supra X-ray photoelectron spectrometer with a monochromated aluminium source. Charge neutralisation was used throughout. Survey scans were collected between 1200 to 0 eV binding energy, at 160 eV pass energy, 1 eV intervals, and 300 seconds / sweep with two sweeps being collected. High-resolution Zn 2p, O 1s, In 3d, C 1s, Cl 2p, and Si 2p XPS spectra were also collected at 20 eV pass energy and 0.1 eV intervals for each analysis point over an appropriate energy range, with one 300 seconds / sweep for all elements. The data collected was calibrated in intensity using a transmission function characteristic of the instrument (determined using software from NPL) to make the values instrument independent. The data can then be quantified using theoretical Schofield relative sensitivity factors. All data has been calibrated relative to a C 1s position of 285.0 eV for C-C/C-H type carbon environments.

CasaXPS software was used to process XPS spectra. Its features include full quantification, configurable quantification reports, different background types, asymmetric and symmetric line-shapes, easy-to-use propagation of processing, and annotation and peak models. [110]

2.6 Inductively Coupled Plasma Mass Spectrometry

2.6.1 Introduction

Inductively coupled plasma mass spectrometry (ICP-MS) is a powerful analytical method to determine the elemental contents accurately, which has been widely used since first introduced in 1983. [111] ICP-MS was used in geology to analyse the elemental compositions in the minerals in the early period, especially for rare-earth elements. [112] There are many advantages for ICP-MS to be used as a superior analysis technique. Its detection limit is parts per trillion (ppt) for a variety of elements, which is better than almost all the other elemental analysis techniques. It also has the best productivity since a series of samples can be detected one by one automatically without any manual operations. Detection is possible over nine orders of magnitude and isotopic measurement are possible as well. [113]

2.6.2 Principles of the Technique

An ICP-MS instrument is the combination of an inductively coupled plasma (ICP) source and a mass spectrometer. The elements in the sample need to be converted into ions by the ICP source (**Figure 2.15**), followed by analysis in the mass spectrometer. The mass spectrometer separates the ions based on their various mass-to-charge ratios (m / e). [114] **Figure 2.16** shows a commonly used quadrupole mass filter. Only the ions with a specific mass-to-charge ratio can pass through the filter and reach the detector. The mass-to-charge ratio of interest can be set by the instrument. [115] The atoms of the elements in the sample are converted to

ions by the high-temperature ICP source; therefore ICP-MS can achieve much greater resolution than other MS methods. [116]

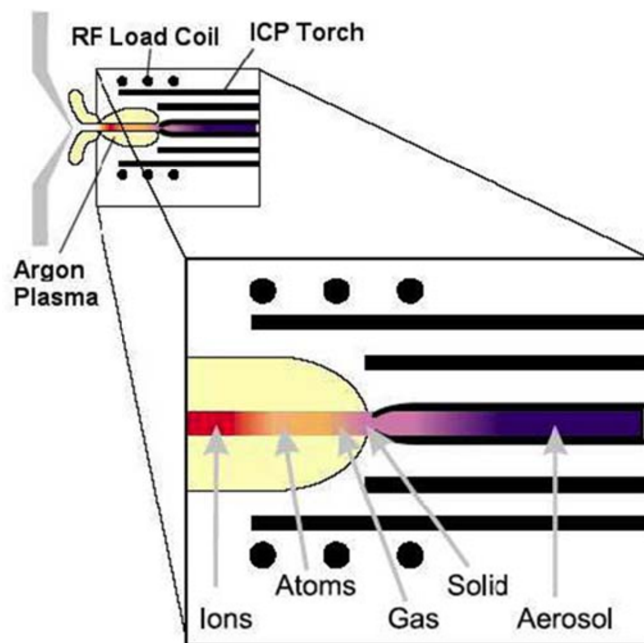

Figure 2.15: Schematic diagram of an ICP source. Reproduced from [117] with permission from PerkinElmer.

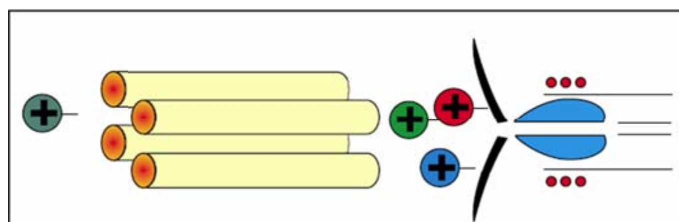

Figure 2.16: Schematic diagram of a quadrupole mass filter. Reproduced from [117] with permission from PerkinElmer.

Figure 2.17 shows the ICP-MS detection limit for the elements in the periodic tables. The detection limit is attributed to the instrument itself, the sample preparation, the nature of the sample, the operation process, etc. In this thesis, Zn, Si, and In are detected by ICP-MS and all of them have reasonably high detection limits as shown in the figure. [112]

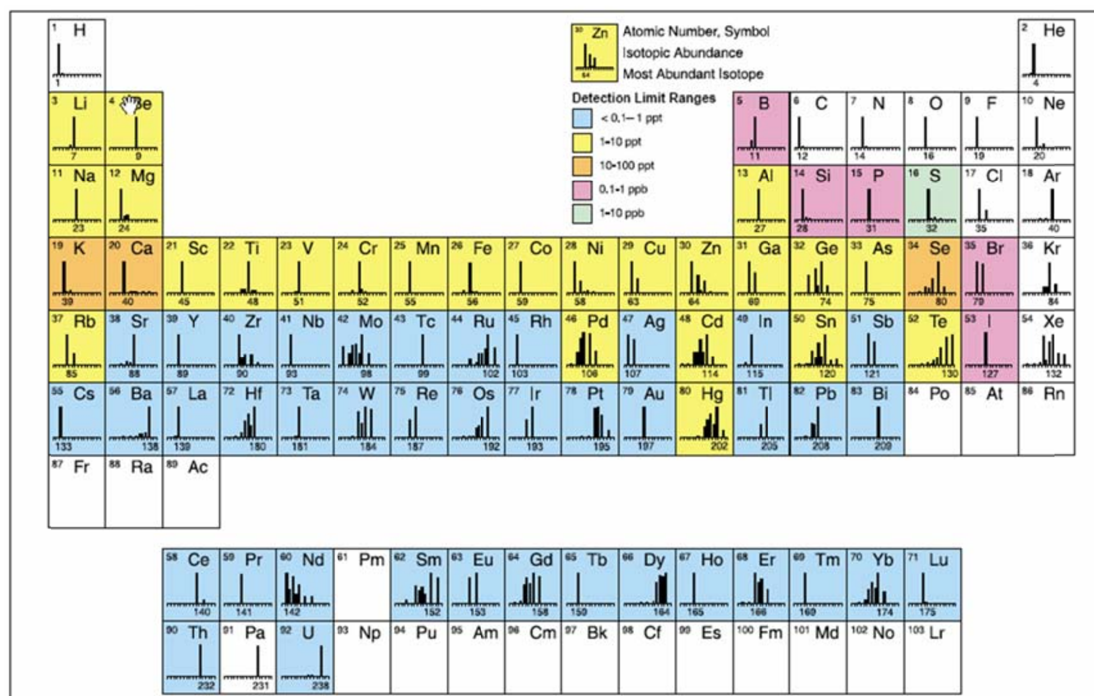

Figure 2.17: The ICP-MS detection limit for the elements in the periodic tables. Reproduced from [117] with permission from PerkinElmer.

2.6.3 Applications of ICP-MS

2.6.3.1 Semi-Quantitative Analysis

Semi-quantitative analysis can be regarded as a preliminary quantitative analysis. It can present a high-quality semi-quantitative analysis in minutes after a simple calibration with a standard solution. [118] It can qualitatively identify the presence of elements and their rough concentrations. Therefore, a series of optimised parameters can be used in the further quantitative analysis to give more accurate results. What is more, the semi-quantitative analysis can suggest a clue to find the causes of possible interferences and minimise them in the following steps. [119]

2.6.3.2 Quantitative Analysis

The idea for the quantitative analysis of ICP-MS is the comparison of experimental data with the standard calibration curve (**Figure 2.18**). The standard calibration curve is generated by the liquid calibration standards. [120] Finally, the concentration of a specific element can be obtained by referring to the measured data with its standard calibration curve. [113]

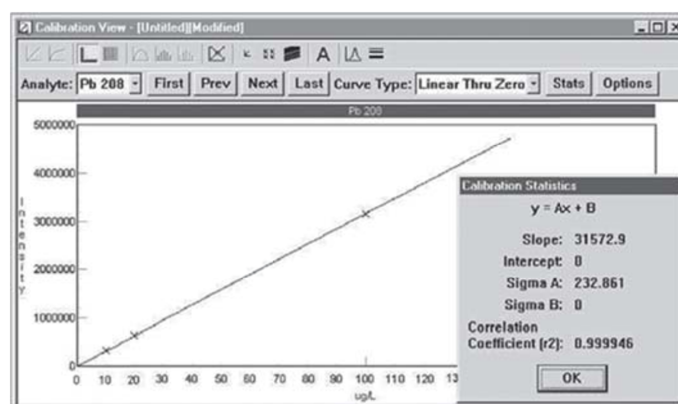

Figure 2.18: An example of a calibration curve for Pb. Reproduced from [113] with permission from PerkinElmer.

2.6.3.3 Isotope Ratio

ICP-MS can detect the isotopes based on their different mass-to-charge ratios; therefore ICP-MS is competent for the determination of the mixture of isotopes. It is widely used in characterisation of minerals, in the nuclear industry, for contamination determination, etc. [113]

2.6.4 Instrumentation

ICP-MS was carried out on an Agilent 4500 Inductively Coupled Plasma Mass Spectrometer. Solid thin film samples were digested in 10 mL 2% (v / v) diluted nitric acid to make solutions prior to analysis. Solutions should normally be aqueous, filtered (removing

particles > 0.45 μm) and with a total dissolved solids content of less than 1000 ppm. Calibrations were obtained using external calibration analysis (a series of standards of known transition element concentrations were prepared to form a linear relationship for calibration). A quality check was done by using an external standard to dilute and measure from a custom bought multi-element solution.

2.7 Ultraviolet-Visible-Near-Infrared Absorption Spectroscopy

2.7.1 Introduction

Ultraviolet-visible-near-infrared (UV-Vis-NIR) absorption spectroscopy measures the change of an incident beam after passing through a sample or being reflected on a sample surface. [121] UV-Vis-NIR spectroscopy consists of large groups of measurements in the ultraviolet, visible, and near-infrared regions including transmission, absorption, and reflection. [122] The normal operating wavelength range for a commercially available UV-Vis-NIR spectrometer is 200 - 2500 nm. Near-infrared properties are one of the key properties for various categories of materials including optical devices, components for laser instruments, near-infrared filters and sensors, etc. All of these can be successfully characterised by the UV-Vis-NIR spectroscopy. [123]

UV-Vis-NIR spectroscopy is extensively applied in many fields of science and technology. It can quantitatively measure the concentration of a sample since the concentration is linear related to the absorption of the spectra. [124] It can also characterise the electronic structure of a sample because the excitation energy for the electrons in a sample is in the range of ultraviolet and visible wavelengths. [125] Of course, the characterisation of the optical properties is the primary job for UV-Vis-NIR spectroscopy. It can detect the visible wavelength range of human sight (400 - 750 nm), [126] which is indispensable for the

development in any optical systems such as touch screens and window coatings. There are mainly two branches in the application of UV-Vis-NIR spectroscopy. One is the determination of optical properties; the other is the detection of the material concentration in various phases. [127]

2.7.2 Principles of the Technique

A schematic diagram of a typical UV-Vis-NIR spectrometer is shown in **Figure 2.19**. The beam of light generated from the light sources is separated by the diffraction gating. The monochromatic beam is obtained after passing through a filter. A half mirror splits the monochromatic beam into two beams with equal intensities. One beam passes through the sample, and the other beam passes through the reference. Both of these two beams are measured by the detectors.

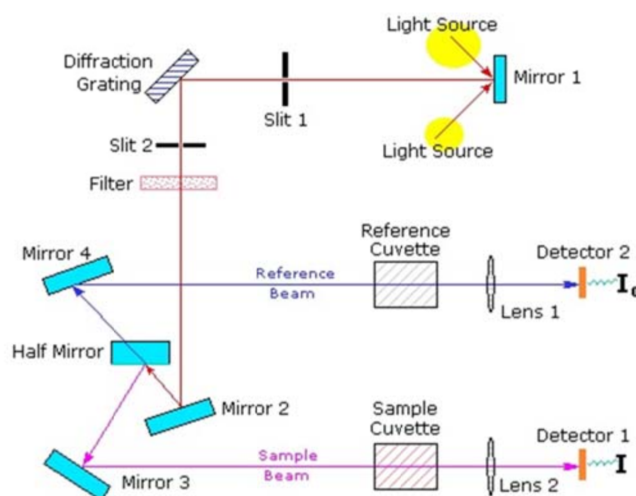

Figure 2.19: A schematic diagram of a typical UV-Vis-NIR spectrometer. Reproduced from [128] with permission from MSU.

The intensity of the beam passing through the reference is recorded as I_0, and the intensity of the beam passing through the sample is recorded as I. Transmittance T can be defined as the equation below (**Figure 2.20**). [129]

$$T = \frac{I}{I_0}$$

Equation 2.13

We can obtain the transmittance spectra by plotting the transmittance against the wavelength. The relationship between the transmittance and absorption can be shown in the following equation. [130]

$$A = -\log T = -\log \frac{I}{I_0}$$

Equation 2.14

Where A is the absorbance of the beam after passing through the sample. T, I, and I_0 have been defined in **Equation 2.13**. If A = 0 or T = 1, it indicates that all the light has passed through the sample and no absorption occurs. I can draw the absorbance spectra by plotting the absorption against the wavelength. The wavelength for maximum absorbance is defined as λ_{max}. [128, 131, 132]

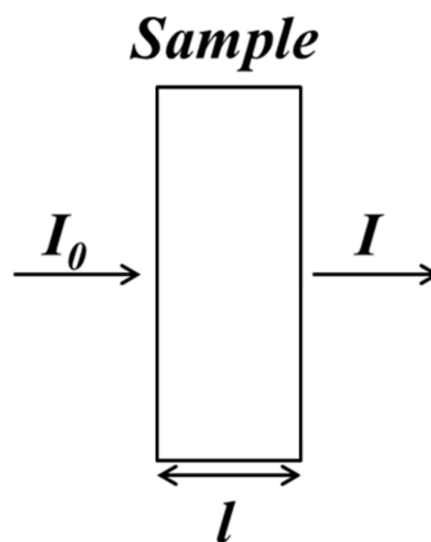

Figure 2.20: Schematic diagram of a transmission process.

2.7.3 Applications of UV-Vis-NIR Spectroscopy

2.7.3.1 Identification of Compounds

The wavelength for maximum absorbance is determined by energy levels in a molecule. I can qualitatively identify a structure or a compound by comparing the UV-Vis-NIR absorption spectra with the standard reference spectra in the database. [133] The excitation of the electrons occurs from occupied to unoccupied molecular orbitals. The electrons can absorb the energy from the beam of light, and then are excited to a higher energy level. [134]

2.7.3.2 Beer-Lambert Law

Each compound has its own characteristic absorbance at a specific wavelength. The sample is generally dissolved in a transparent solvent to avoid any absorbance from the solvent. Water, ethanol, hexane, and cyclohexane are commonly used solvents for absorption spectra. [135] The concentration of the sample in the solution should be reasonably low to allow the beam of light to pass it through as much as possible. It can make more light reach the detector and improve the sensitivity.

The Beer-Lambert Law shows that the absorbance of a sample is linearly related to its concentration, which can be expressed as follows. [136]

$$A = \varepsilon l c$$

Equation 2.15

Where A is the absorbance of a sample, ε is the molar extinction coefficient, l is the path length, and c is the concentration of the sample. The molar extinction coefficient is a characteristic constant for a sample, which is related to the wavelength. I can calculate the

concentration based on the measured and known values A, ε, and l. [137]

2.7.3.3 Calculation of Optical Constant

Various optical constants such as absorption coefficient and optical band gap can be calculated. [138, 139] The value of the absorption coefficient α is obtained from the transmittance spectra in the UV-Vis-NIR spectroscopy and is calculated by using the following equation. [140]

$$\alpha = \frac{2.303 \times \log \frac{1}{T}}{t}$$

Equation 2.16

Where T is the transmittance and t is the thickness of the sample.

The optical band gap can be calculated from the absorption coefficient α and the transmittance spectra. The optical band gap is calculated from the Tauc relation. [141]

$$\alpha h\nu = A(h\nu - E_g)^{\frac{1}{2}}$$

Equation 2.17

Where A is a constant, E_g is the optical band gap, and ν is the incident frequency. By plotting a graph of $(\alpha h\nu)^2$ against hν, the intercept of the extrapolated straight line of the plots and the straight line αhν = 0 is the value of the optical band gap.

2.7.3.4 Calculation of Film Thickness

Swanepoel developed an envelope method to calculate film thickness and other optical

properties based on the interference fringes in the transmittance spectra. [142, 143] The calculated value is accurate and acceptable compared with the observed film thickness from the TEM cross-sectional image. Please refer to **Appendix A2.2** for details. **Figure 2.21** shows the transmittance and reflectance spectra of a film on a substrate. Film thickness d, absorption coefficient α, and refractive index n are labelled in the figure. I assume the absorption coefficient α_s of the transparent glass substrate is 0. n_0 is the refractive index of the air, which is 1. The interference fringes shown in **Figure 2.22** are attributed to the following equation. [143]

$$2nd = m\lambda$$

Equation 2.18

Where n is the refractive index, d is the film thickness, λ is wavelength, and m is an integer for maxima and half-integer for minima.

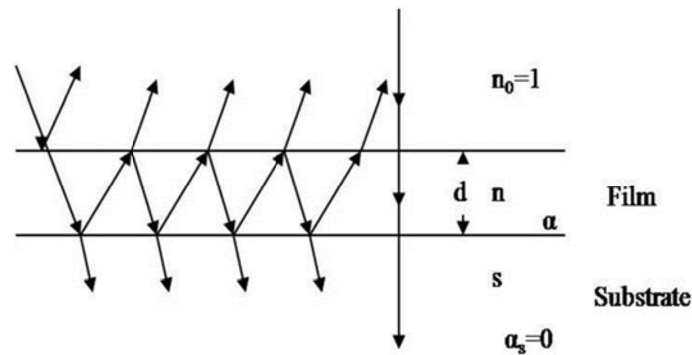

Figure 2.21: Transmission and reflection of a film on a substrate. The glass substrate is much thicker than the film. Reproduced from Dorranian et al. [144] with permission from Springer.

The refractive index s of the substrate can be calculated from the transmittance of the substrate T_s by the following equation. [143]

$$s = \frac{1}{T_s} + (\frac{1}{T_s^2} - 1)^{1/2}$$

Equation 2.19

The maxima fitting curve T_M and the minima fitting curve T_m can be observed in **Figure 2.22**. The equation showing the relationship between the reflective index n, T_M, and T_m is expressed as below. [143]

$$n = [N + (N^2 - s^2)^{1/2}]^{1/2}$$

Equation 2.20

$$N = 2s(T_M - T_m) / T_M T_m + (s^2 + 1) / 2$$

Equation 2.21

The refractive index of the glass substrate is regarded as 1.51, i.e., s = 1.51. The film thickness can be calculated as follows. [143]

$$d = \frac{\lambda_1 \lambda_2}{2(\lambda_1 n_2 - \lambda_2 n_1)}$$

Equation 2.22

Where n_1 is the refractive index for the maxima curve at λ_1 and n_2 is the refractive index for the minima curve at λ_2. λ_1 should be adjacent to λ_2.

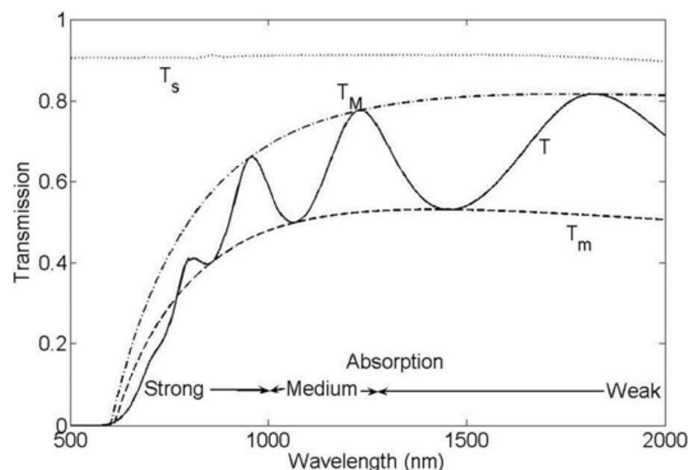

Figure 2.22: Transmittance spectra of a film on a substrate. T is the transmittance of the sample. T_s is the transmittance of the substrate. T_M and T_m are the maxima and minima curves of the transmittance T, respectively. Reproduced from Dorranian et al. [144] with permission from Springer.

2.7.4 Instrumentation

UV-Vis-NIR spectroscopy was carried out on a PerkinElmer Lambda 19 UV/Vis/NIR spectrophotometer. It is a dual-beam spectrometer which can measure from about 175 nm to 3300 nm encompassing 95% of the solar spectrum. Its optical setup is double-beam, all-reflecting and double monochromator. The light source is a deuterium lamp for UV and halogen lamp for Vis/NIR, and the detector is PMT for UV/Vis and PbS for NIR. [145] The spectra were collected at room temperature from 250 nm to 2500 nm with a data collection interval of 3 nm.

2.8 Reflectance Spectroscopy

2.8.1 Introduction

When an incident beam hits a sample, the photons can pass it through, be absorbed, or be reflected from the surface. [146] The reflection generally consists of internal reflection,

specular reflection, and diffuse reflection. All of these happen at the same time. The specular reflection occurs when the angle of reflection is equal to the angle of incidence. However, the diffuse reflection occurs at a rough surface with no specific reflecting direction. [147]

2.8.2 Principles of the Technique

Reflection occurs when an incident beam strikes the sample surface. The complex refractive index m can be expressed as follows. [148]

$$m = n + i\kappa$$

Equation 2.23

Where n is the real part of the index, and κ is the imaginary part of the index or called the extinction coefficient.

The reflectance R can be expressed by the Fresnel equation. [149]

$$R = [(n - 1)^2 + \kappa^2] / [(n + 1)^2 + \kappa^2]$$

Equation 2.24

2.8.3 Applications of Reflectance Spectroscopy

2.8.3.1 Internal Reflectance Spectroscopy

Internal reflectance spectroscopy (IRS) is usually called attenuated total reflectance (ATR) spectroscopy. [150] The internal reflection is observed when the incident beam passes from a high density medium to a low density medium. The larger angle of incidence leads to a larger portion of the reflection beam. The total internal reflection occurs when the angle of incidence is larger than the critical angle (**Figure 2.23**). Meanwhile, only the reflection beam can be

observed and no beam can pass through the second medium. This technique does not damage the sample and can be used to examine a huge range of materials from solids to liquids, or even gases. [147, 151]

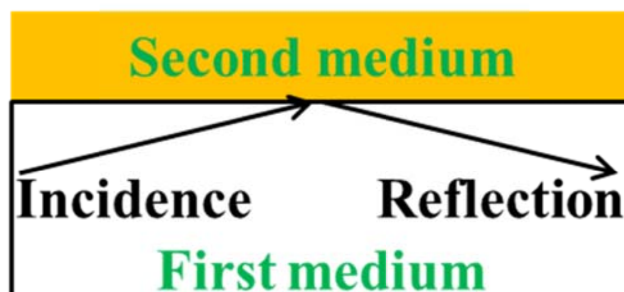

Figure 2.23: Schematic diagram of internal reflection.

2.8.3.2 Specular Reflectance Spectroscopy

Specular reflectance spectroscopy occurs when the incident beam strikes the sample surface and is reflected to a specific direction where the angle of reflection is equal to the angle of incidence. [152] Similarly to internal reflectance spectroscopy, it is also a non-destructive characterisation technique. It is commonly used in calculations of film thickness and refractive index, and dielectric modelling. [151]

If a film is deposited on a reflective sample surface, a reflection-absorption model is carried out (**Figure 2.24**). The conversion of the reflectance spectra and absorption spectra is based on the Kramers-Kronig relations. [153] In this model, the reflectance consists of two components. One is the specular reflectance at the surface of the thin layer. The other beam passes through the thin layer surface and is specularly reflected at the reflective surface. Finally, it passes through the thin layer surface again leading to a reflection. In this thesis, specular reflectance spectroscopy is used to investigate the optical properties of the thin films in details. [147]

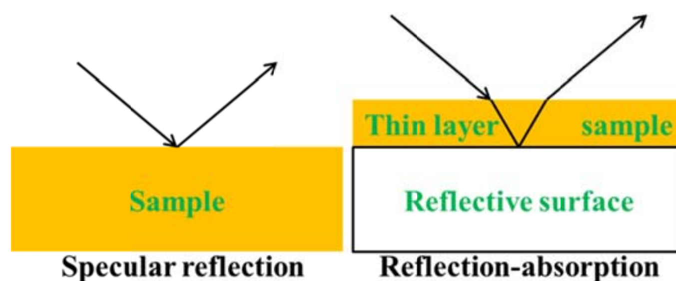

Figure 2.24: Schematic diagram of specular reflection.

2.8.3.3 Diffuse Reflectance Spectroscopy

Diffuse Reflectance Spectroscopy (DRS) is generated by the interactions between the incident beam and the rough sample surface, followed by the reflection in every possible direction (**Figure 2.25**). [154] The overall spectra always consist of transmittance, specular reflectance, internal reflectance, and the diffuse reflectance itself. [151] Since specular reflectance is incorporated into the measured diffuse reflectance spectroscopy, it is necessary to separate them and obtain a 'pure' diffuse reflectance spectrum. [147]

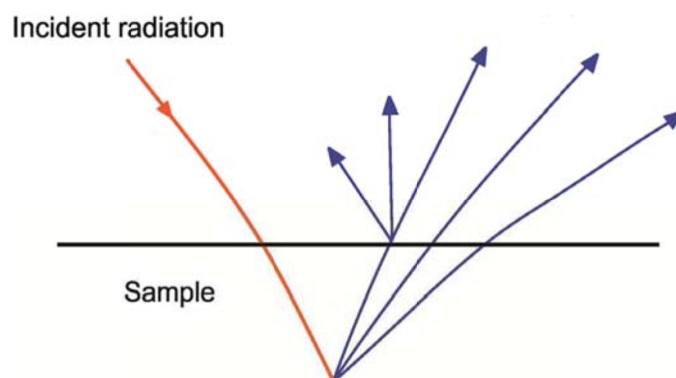

Figure 2.25: Schematic diagram of diffuse reflection. Reproduced from Khoshhesab [147] with permission from InTech.

2.8.4 Instrumentation

UV-Vis-NIR reflectance spectroscopy was carried out on an Agilent Cary 5000 UV-Vis-NIR

spectrometer. This is a dual-beam spectrometer which can measure from about 175 nm to 3300 nm. It uses a PbSmart NIR detector for an extended photometric range. It uses a floating Al casting and double Littrow monochromator to get minimal noise and stray light. It uses Schwarzchild coupling optics for higher accuracy at low transmission levels to get maximum light throughput. Agilent Cary WinUV software, modular Windows-based software, is used to control the spectrometer and a number of optional accessories, perform powerful analysis, collect and analyse data, and store and display graphs. A spectral reflection accessory is used to measure reflectance spectra. The spectra were collected at room temperature from 250 nm to 2500 nm with a data collection interval of 1 nm.

2.9 Dielectric Modelling

2.9.1 Introduction

The optical spectra contain plentiful factors such as on band structure, in-grain carrier concentration, mobility, defects, morphology, etc. I measure transmittance and reflectance spectra to do dielectric modelling, thus making a deduction of optical carrier concentration and mobility, and grain boundaries is also based on it. [155]

The relations between optical constants and electrical properties can be described by using the Drude model [156, 157], which is a classical model to analyse the dielectric function on the assumption that it arises from free carrier electrons. Optical properties, electrical properties, and grain boundaries are the fundamental aspects in the research of TCOs; therefore, dielectric modelling is an appropriate method to explain these. [155]

2.9.2 Principles of the Technique

The dielectric function is based on Maxwell's equations. Therefore, the Lorentz oscillator

model is introduced to describe the electron performance, which is assumed to be the classical harmonic oscillators. A detailed discussion appears in **Chapter 4**.

2.9.3 Applications of Dielectric Function

Refractive index is related to the speed of an electromagnetic wave travel through a material. A higher refractive index leads to a slower speed for the waves inside materials. The refractive index is a complex function to describe the velocity and the loss during the propagation of the waves. The real part is related to the reduction of the wave propagation velocity while the imaginary part is related to the exponential reduction of the wave amplitude during the propagation as shown in **Equation 2.23**. [158]

The extinction coefficient κ can be calculated from the absorption coefficient α as shown in the following equation. [159]

$$\kappa = \lambda\alpha / 4\pi$$

Equation 2.25

Where λ is the wavelength. The reflectance R is expressed as **Equation 2.24**.

2.9.4 Instrumentation

UV-Vis-NIR reflectance spectroscopy was carried out on an Agilent Cary 5000 UV-Vis-NIR spectrophotometer as stated before. The dielectric function was carried out, calculated and modelled on the software J.A. Woollam WVASE. It is designed to fit optical spectra, such as reflectance, transmittance, ellipsometry, Drude-Lorentz, and many other dielectric-function models. J.A. Woollam WVASE has a powerful and fast fitting engine based on a root mean square (RMS) algorithm and a broad collection of proven physical models. It allows you to fit

manually or automatically several datasets of different types and use different models simultaneously. [160]

2.10 Hall Effect Measurement

2.10.1 Introduction

When an electric current travels through a conductor in a magnetic field, a voltage, which is perpendicular and transverse to the current direction, is generated due to the deflection of charger carriers of the current. This phenomenon, which is called Hall effect, is observed by Edwin Hall in 1879. [161] The induced voltage, which is called Hall voltage [162], confirms the presence of the charge carriers in the conductor and gives a possible way to indicate the charge carrier concentration. In practice, the Hall effect is an easy, rapid, and straightforward method to measure charge carrier concentration, carrier mobility, and electric resistivity of materials. These advantages make it a widely used technique both in research and in industry. [163]

2.10.2 Principles of the Technique

2.10.2.1 Hall Effect

Figure 2.26 shows the schematic of the Hall effect in a rectangular parallelepiped conductor. When an electric current travels through a rectangular parallelepiped conductor along the x axis, the carrier electron experiences a magnetic force $F_m = qvB$ perpendicular to both the magnetic field and the current direction, where q is the electron charge 1.602×10^{-19} C, v is the velocity of the electron, and B is the magnetic field. The electric field becomes stronger as more electrons are pushed to one side of the rectangular parallelepiped conductor by the magnetic force. The electron starts to suffer an electric force $F_e = qE$ in the opposite direction

of the magnetic force, where E is the generated electric field. Finally, these two Lorentz forces [164] become equal to make a balance, i.e. $F_m = qvB = F_e = qE$. The voltage generated by the electric field is called the Hall voltage $V_H = IB / qnd$, where I is the electric current, n is the bulk carrier concentration, and d is the thickness. If sheet carrier concentration n_s ($n_s = nd$) is used to replace the bulk carrier concentration, the equation is expressed as follows. [165]

$$n_s = \frac{IB}{qV_H}$$

Equation 2.26

Consequently, bulk n or sheet n_s carrier concentration can be calculated from measured values of I, B, q, and V_H. What is more, the direction of the Hall voltage depends on the type of carriers, i.e. negatively charged electrons or positively charged holes. The van der Pauw technique can then be used to determine the sheet resistance R_S. The carrier mobility can be calculated from the equation below. [166]

$$\mu = \frac{V_H}{R_S IB} = \frac{1}{qn_S R_S}$$

Equation 2.27

The electrical resistivity ρ can also be calculated by using the equation $\rho = R_S d$. [167]

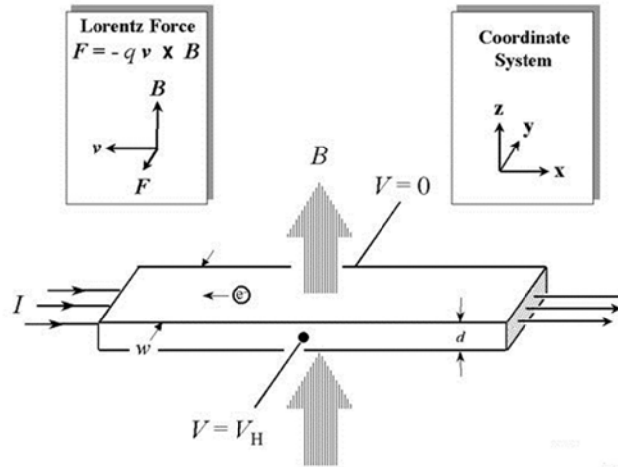

Figure 2.26: Schematic of the Hall effect in a rectangular parallelepiped conductor. Reproduced from [167] with permission from NIST.

2.10.2.2 The van der Pauw Technique

Both of the shape of the sample and the way it assembled within the instrument highly affect the accuracy in the measurement. **Figure 2.27** shows the schematic of the geometries used for Hall effect and van der Pauw measurements. [168] The ohmic contacts are needed to connect the sample with the wires from the instrument. The sizes of the contacts and the thicknesses of the samples can lead to errors in the measurement. It is always preferred to make these two parameters as small as possible compared with the contact-contact distances. [169] (a) and (b) illustrate good examples of mounting the samples. Cloverleaf design can reduce the effect of the contact size thus leading to smaller errors. Due to the difficulties in preparing the samples like the shapes of (a), squares or rectangles in (b) are commonly used in this thesis.

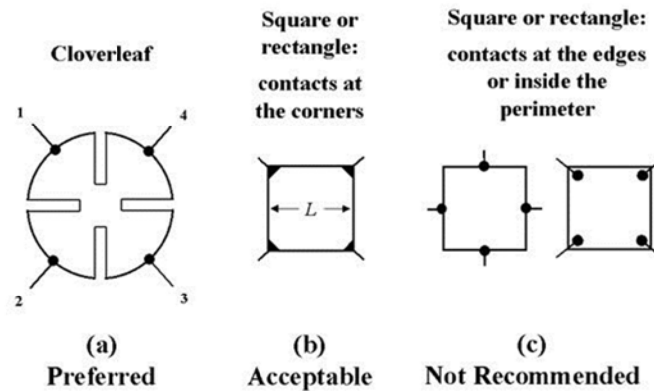

Figure 2.27: Schematic of the geometries used for Hall effect and van der Pauw measurements. Reproduced from [167] with permission from NIST.

The sheet resistance R_S and carrier mobility can be determined by the van der Pauw technique. The sample is always prepared as a shape of square or rectangle, which is connected with four wires at four ohmic contacts distributed at four corners of the sample. **Figure 2.28** shows the schematic of a van der Pauw technique in the measurement of R_A and R_B. R_A and R_B are the resistances as measured in the figure. The voltage V_{43} between Point 4 and Point 3 is measured as current I_{12} travels between Point1 and Point 2. Similarly, the voltage V_{14} between Point 1 and Point 4 is measured as current I_{23} travels between Point 2 and Point 3. The resistances R_A and R_B can be calculated as the equation below. [168]

$$R_A = \frac{V_{43}}{I_{12}}$$
$$R_B = \frac{V_{14}}{I_{23}}$$

Equation 2.28

The sheet resistance R_S is related to R_A and R_B by the van der Pauw equation as follows. [170]

$$\exp(-\pi \frac{R_A}{R_S}) + \exp(-\pi \frac{R_B}{R_S}) = 1$$

Equation 2.29

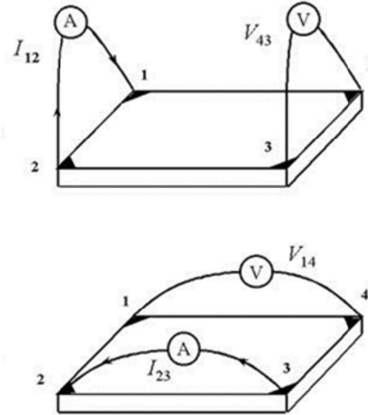

Figure 2.28: Schematic of a van der Pauw technique in the measurement of R_A and R_B. Reproduced from [167] with permission from NIST.

The Hall voltage V_H can also be determined by the van der Pauw technique. **Figure 2.29** shows a schematic of a van der Pauw technique in the measurement of V_H. When current I passes between Point 1 and Point 3, the voltage between Point 2 and Point 4 is measured as the Hall voltage V_H. Consequently, the sheet carrier concentration n_s, as well as the bulk carrier concentration $n = n_s / d$, can be calculated from **Equation 2.26**.

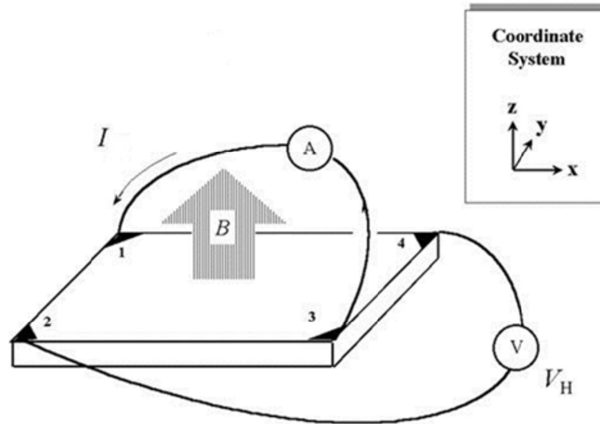

Figure 2.29: Schematic of a van der Pauw technique in the measurement of V_H. Reproduced from [167] with permission from NIST.

The limitations and the errors for the Hall and van der Pauw measurements depend on the thickness and the uniformity of a sample, the size of the ohmic contacts and their separated distance, the stability of electrical properties with a light, environment temperature, etc. [167, 170]

2.10.3 Instrumentation

Electrical properties (resistivity, carrier concentration, and mobility) were carried out by using van der Pauw and Hall Bar measurements on an Ecopia HMS-3000 Hall measurement system (**Figure 2.30**). The HMS-3000 includes software with I-V curve capability for checking the ohmic integrity of the user made sample contacts. The systems can be used to characterise various materials from 300 K to 77 K (room temperature to liquid nitrogen temperature). The magnetic flux density is 0.55 T provided by permanent magnets. Thin film samples were mounted onto a PCB Sample Holder by annealing with a conductive material indium to ensure good probe contact to make four ohmic contacts on the four corners of the thin films (5 mm × 5 mm). The input current is 1 nA - 20 mA and 0.5 mA is normally used. The parameters are input (usually thin film thickness) and the output results can be carrier concentration,

mobility, resistivity, and conductivity. [171]

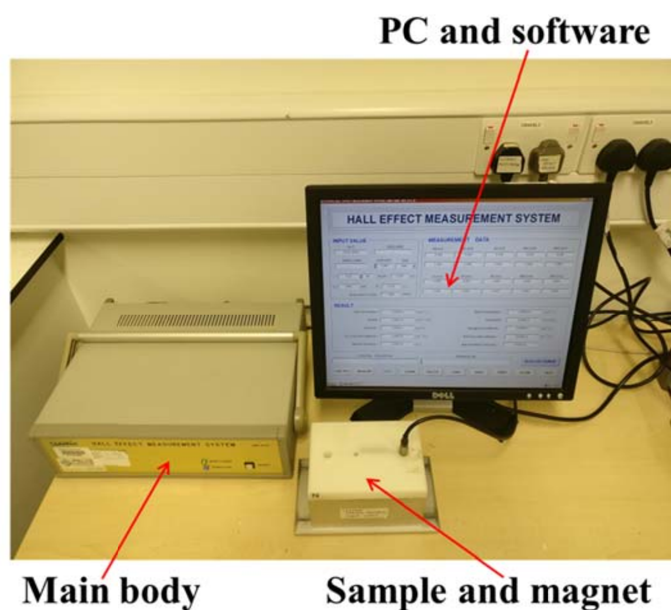

Figure 2.30: Photo of a Hall measurement system.

All the data in this thesis is based on over 700 samples made in the past few years. The relevant results are accurate and reproducible.

References

[1] Ermich, M. & Opper, D. 2011. *XRD for the Analyst Getting Acquainted with the Principles,* Almelo, PANalytical.

[2] Deng, Z., Chen, X., Wang, Y., Fang, E., Zhang, Z. & Chen, X. 2014. Headspace Thin-Film Microextraction Coupled with Surface-Enhanced Raman Scattering as a Facile Method for Reproducible and Specific Detection of Sulfur Dioxide in Wine. *Analytical Chemistry,* 87**,** 633-640.

[3] 2018. *X-Ray Diffraction*. Rigaku. Available: https://www.rigaku.com/en/techniques/xrd [Accessed 10 March 2019].

[4] Dutrow, B. L. & Clark, C. M. 2018. *X-Ray Powder Diffraction (XRD)*. Available: https://serc.carleton.edu/research_education/geochemsheets/techniques/XRD.html [Accessed 10 March 2019].

[5] Kaufmann, E. N. 2003. *Characterization of Materials,* Hoboken, Wiley.

[6] Belsky, A., Hellenbrandt, M., Karen, V. L. & Luksch, P. 2002. New Developments in the Inorganic Crystal Structure Database (ICSD): Accessibility in Support of Materials Research and Design. *Acta Crystallographica Section B,* 58**,** 364-369.

[7] Kannan, S., Goetz‐Neunhoeffer, F., Neubauer, J. & Ferreira, J. 2008. Ionic Substitutions in Biphasic Hydroxyapatite and β-Tricalcium Phosphate Mixtures: Structural Analysis by Rietveld Refinement. *Journal of the American Ceramic Society,* 91**,** 1-12.

[8] Segmüller, A., Noyan, I. & Speriosu, V. 1989. X-Ray Diffraction Studies of Thin Films and Multilayer Structures. *Progress in Crystal Growth and Characterization,* 18**,** 21-66.

[9] Schmitt, J., Gruenewald, T., Decher, G., Pershan, P. S., Kjaer, K. & Loesche, M. 1993. Internal Structure of Layer-By-Layer Adsorbed Polyelectrolyte Films: A Neutron and X-Ray Reflectivity Study. *Macromolecules,* 26**,** 7058-7063.

[10] Cherner, Y. E. 2014. Customizable Virtual X-Ray Laboratory: An Innovative Tool for Interactive Online Teaching and Learning. *121st ASEE Annual Conference & Exposition.* Indianapolis, IN: American Society for Engineering Education.

[11] Badenhorst, H. 2014. Microstructure of Natural Graphite Flakes Revealed by Oxidation: Limitations of XRD and Raman Techniques for Crystallinity Estimates. *Carbon,* 66**,** 674-690.

[12] Klug, H. P. & Alexander, L. E. 1974. *X-Ray Diffraction Procedures: For Polycrystalline and Amorphous Materials,* New York, Wiley-VCH.

[13] West, A. R. 1999. *Basic Solid State Chemistry,* New York, John Wiley & Sons Inc.

[14] Zhao, Z., Buscaglia, V., Viviani, M., Buscaglia, M. T., Mitoseriu, L., Testino, A., Nygren, M., Johnsson, M. & Nanni, P. 2004. Grain-Size Effects on the Ferroelectric Behavior of Dense Nanocrystalline BaTiO3 Ceramics. *Physical Review B,* 70**,** 024107.

[15] In-Hang, S. 2012. *Multiple Diffraction of X-Rays in Crystals,* Berlin, Springer.

[16] Zuo, X., Cui, G., Merz, K. M., Zhang, L., Lewis, F. D. & Tiede, D. M. 2006. X-Ray Diffraction "Fingerprinting" of DNA Structure in Solution for Quantitative

Evaluation of Molecular Dynamics Simulation. *Proceedings of the National Academy of Sciences,* 103**,** 3534-3539.

[17] O'neill, H. & St, C. 1992. Temperature Dependence of the Cation Distribution in Zinc Ferrite (ZnFe2O4) from Powder XRD Structural Refinements. *European Journal of Mineralogy***,** 571-580.

[18] Pan, Q., Guo, P., Duan, J., Cheng, Q. & Li, H. 2012. Comparative Crystal Structure Determination of Griseofulvin: Powder X-Ray Diffraction Versus Single-Crystal X-Ray Diffraction. *Chinese Science Bulletin,* 57**,** 3867-3871.

[19] Kalsin, A. M., Fialkowski, M., Paszewski, M., Smoukov, S. K., Bishop, K. J. & Grzybowski, B. A. 2006. Electrostatic Self-Assembly of Binary Nanoparticle Crystals with a Diamond-Like Lattice. *Science,* 312**,** 420-424.

[20] David, W. I. F., Shankland, K., McCusker, L. B. & Bärlocher, C. 2002. *Structure Determination from Powder Diffraction Data,* Oxford, Oxford University Press.

[21] Bragg, W. H. & Bragg, W. L. 1913. The Reflection of X-Rays by Crystals. *Proceedings of the Royal Society of London A,* 88**,** 428-438.

[22] Rakitzis, T. P., Kandel, S. A., Alexander, A. J., Kim, Z. H. & Zare, R. N. 1998. Photofragment Helicity Caused by Matter-Wave Interference from Multiple Dissociative States. *Science,* 281**,** 1346-1349.

[23] Jurczuk, K., Galeski, A., Mackey, M., Hiltner, A. & Baer, E. 2015. Orientation of PVDF α and γ Crystals in Nanolayered Films. *Colloid and Polymer Science,* 293**,** 1289-1297.

[24] Chatterjee, S. K. 2008. Crystals and X-Ray. *Crystallography and the World of Symmetry***,** 43-56.

[25] Smart, L. E. & Moore, E. A. 2012. *Solid State Chemistry: An Introduction,* Boca Raton, CRC Press.

[26] Lee, Y. & Tseng, T. 1992. Phase Identification and Electrical Properties in ZnO-Glass Varistors. *Journal of the American Ceramic Society,* 75**,** 1636-1640.

[27] 1997. *International Centre for Diffraction Data (ICDD)*. JCPDS-ICDD. Available: http://www.icdd.com/ [Accessed 10 March 2019].

[28] Maguire, T. 2006. ICDD Spring Meetings. *Powder Diffraction,* 21**,** 250-255.

[29] Bish, D. L. & Howard, S. A. 1988. Quantitative Phase Analysis Using the Rietveld Method. *Journal of Applied Crystallography,* 21**,** 86-91.

[30] Spurr, R. A. & Myers, H. 1957. Quantitative Analysis of Anatase-Rutile Mixtures with an X-Ray Diffractometer. *Analytical Chemistry,* 29**,** 760-762.

[31] Karlak, R. F. & Burnett, D. S. 1966. Quantitative Phase Analysis by X-Ray Diffraction. *Analytical Chemistry,* 38**,** 1741-1745.

[32] Speakman, S. A. 2013. *Introduction to X-Ray Powder Diffraction Data Analysis*. Center for Materials Science and Engineering at MIT. Available: http://prism.mit.edu/xray/introduction%20to%20xrpd%20data%20analysis.pdf [Accessed 10 March 2019].

[33] Warren, B. E. 1990. *X-Ray Diffraction,* New York, Dover Publications.

[34] Cullity, B. D. & Stock, S. R. 2014. *Elements of X-Ray Diffraction,* London, Pearson Education.

[35] Ruland, W. 1964. Crystallinity and Disorder Parameters in Nylon 6 and Nylon 7.

Polymer, 5**,** 89-102.
[36] Scherrer, P. 1912. Bestimmung der Inneren Struktur und der Größe von Kolloidteilchen Mittels Röntgenstrahlen. *In:* Zsigmondy, R. (ed.) *Kolloidchemie Ein Lehrbuch.* Berlin: Springer.
[37] Ingham, B. & Toney, M. F. 2014. 1 - X-Ray Diffraction for Characterizing Metallic Films. *Metallic Films for Electronic, Optical and Magnetic Applications.* Cambridge: Woodhead Publishing.
[38] Rugar, D. & Hansma, P. 1990. Atomic Force Microscopy. *Physics Today,* 43**,** 23-30.
[39] Binnig, G., Quate, C. F. & Gerber, C. 1986. Atomic Force Microscope. *Physical Review Letters,* 56**,** 930-933.
[40] Giessibl, F. J. 2003. Advances in Atomic Force Microscopy. *Reviews of Modern Physics,* 75**,** 949-983.
[41] 2012. *Introduction to AFM - Atomic Force Microscopy*. NPL. Available: http://www.npl.co.uk/science-technology/surface-and-nanoanalysis/surface-and-nanoanalysis-basics/introduction-to-afm-atomic-force-microscopy [Accessed 10 March 2019].
[42] Ishida, N., Inoue, T., Miyahara, M. & Higashitani, K. 2000. Nano Bubbles on a Hydrophobic Surface in Water Observed by Tapping-Mode Atomic Force Microscopy. *Langmuir,* 16**,** 6377-6380.
[43] Wilson, R. A. & Bullen, H. A. 2018. Basic Theory Atomic Force Microscopy (AFM). Kentucky: Northern Kentucky University.
[44] Skoog, D. A., Crouch, S. R. & Holler, F. J. 2007. *Principles of Instrumental Analysis,* Belmont, CA, Thomson Brooks/Cole.
[45] Eaton, P. & West, P. 2010. *Atomic Force Microscopy,* Oxford, Oxford University Press.
[46] Daniel, J. B., William, A. B., Neal, C., Jennifer, K. & Neil, H. T. 2012. Single-Molecule Studies of DNA Transcription Using Atomic Force Microscopy. *Physical Biology,* 9**,** 021001.
[47] Cappella, B. & Dietler, G. 1999. Force-Distance Curves by Atomic Force Microscopy. *Surface Science Reports,* 34**,** 1-104.
[48] Goldsbury, C. S., Scheuring, S. & Kreplak, L. 2009. Introduction to Atomic Force Microscopy (AFM) in Biology. *Current Protocols in Protein Science,* 58**,** 17.7.1-17.7.19.
[49] Meyer, E. 1992. Atomic Force Microscopy. *Progress in Surface Science,* 41**,** 3-49.
[50] Blanchard, C. R. 1996. Atomic Force Microscopy. *The Chemical Educator,* 1**,** 1-8.
[51] Nečas, D. & Klapetek, P. 2012. Gwyddion: An Open-Source Software for SPM Data Analysis. *Central European Journal of Physics,* 10**,** 181-188.
[52] Goldstein, J. I., Newbury, D. E., Michael, J. R., Ritchie, N. W., Scott, J. H. J. & Joy, D. C. 2017. *Scanning Electron Microscopy and X-Ray Microanalysis,* New York, Springer.
[53] Swapp, S. 2017. *Scanning Electron Microscopy (SEM)*. Available: https://serc.carleton.edu/research_education/geochemsheets/techniques/SEM.html [Accessed 10 March 2019].
[54] Seiler, H. 1983. Secondary Electron Emission in the Scanning Electron Microscope.

Journal of Applied Physics, 54**,** R1-R18.

[55] Sealy, C. P., Castell, M. R. & Wilshaw, P. R. 2000. Mechanism for Secondary Electron Dopant Contrast in the SEM. *Microscopy,* 49**,** 311-321.

[56] Lloyd, G. E. 1987. Atomic Number and Crystallographic Contrast Images with the SEM: A Review of Backscattered Electron Techniques. *Mineralogical Magazine,* 51**,** 3-19.

[57] Reimer, L. 2013. *Scanning Electron Microscopy: Physics of Image Formation and Microanalysis,* Berlin, Springer.

[58] Zhou, W., Apkarian, R., Wang, Z. L. & Joy, D. 2007. Fundamentals of Scanning Electron Microscopy (SEM). *In:* Zhou, W. & Wang, Z. L. (eds.) *Scanning Microscopy for Nanotechnology: Techniques and Applications.* New York, NY: Springer New York.

[59] Robinson, B. W. & Nickel, E. H. 1979. A Useful New Technique for Mineralogy: The Backscattered-Electron/Low Vacuum mode of SEM Operation. *American Mineralogist,* 64**,** 1322-8.

[60] Suganuma, T. 1985. Measurement of Surface Topography Using SEM with Two Secondary Electron Detectors. *Microscopy,* 34**,** 328-337.

[61] Robinson, V. 1974. The Construction and Uses of an Efficient Backscattered Electron Detector for Scanning Electron Microscopy. *Journal of Physics E: Scientific Instruments,* 7**,** 650.

[62] Inagaki, S., Guan, S., Fukushima, Y., Ohsuna, T. & Terasaki, O. 1999. Novel Mesoporous Materials with a Uniform Distribution of Organic Groups and Inorganic Oxide in Their Frameworks. *Journal of the American Chemical Society,* 121**,** 9611-9614.

[63] Salem, A., Glavicic, M. & Semiatin, S. 2008. A Coupled EBSD/EDS Method to Determine the Primary-And Secondary-Alpha Textures in Titanium Alloys with Duplex Microstructures. *Materials Science and Engineering: A,* 494**,** 350-359.

[64] Shindo, D. & Oikawa, T. 2002. Energy Dispersive X-Ray Spectroscopy. *Analytical Electron Microscopy for Materials Science.* Tokyo: Springer.

[65] Schwartz, A. J., Kumar, M., Adams, B. L. & Field, D. P. 2000. *Electron Backscatter Diffraction in Materials Science,* New York, Springer.

[66] Williams, D. B. & Carter, C. B. 1996. The transmission electron microscope. *Transmission Electron Microscopy.* New York: Springer.

[67] 2018. Transmission Electron Microscope Training Module. Sydney: Australian Microscopy & Microanalysis Research Facility.

[68] Huang, P. Y., Ruiz-Vargas, C. S., Van der Zande, A. M., Whitney, W. S., Levendorf, M. P., Kevek, J. W., Garg, S., Alden, J. S., Hustedt, C. J. & Zhu, Y. 2011. Grains and Grain Boundaries in Single-Layer Graphene Atomic Patchwork Quilts. *Nature,* 469**,** 389.

[69] 2010. *Transmission Electron Microscopy (TEM).* Available: https://warwick.ac.uk /fac/sci/physics/current/postgraduate/regs/mpagswarwick/ex5/techniques/structural/tem/ [Accessed 10 March 2019].

[70] Burghardt, R. C. & Droleskey, R. 2006. Transmission Electron Microscopy. *Current Protocols in Microbiology,* 3**,** 2B. 1.1-2B. 1.39.

[71] Egerton, R. F. 2005. *Physical Principles of Electron Microscopy,* Boston, MA, Springer.

[72] Ding, Y. 2018. *Fundamental Theory of Transmission Electronic Microscopy*. Available: http://www.nanoscience.gatech.edu/zlwang/research/tem.html [Accessed 10 March 2019].

[73] *Basic Principle of Transmission Electron Microscope*. Available: http://www.hk-phy.org/atomic_world/tem/tem02_e.html [Accessed 10 March 2019].

[74] Browning, N., Chisholm, M. & Pennycook, S. 2006. Atomic-Resolution Chemical Analysis Using a Scanning Transmission Electron Microscope. *Nature,* 444**,** 235.

[75] 2018. *Applications and Practical Uses - What the TEM Can Do*. Australian Microscopy & Microanalysis Research Facility. Available: http://www.ammrf.org.au/myscope/tem/background/practical/ [Accessed 10 March 2019].

[76] Douglas, S. M., Dietz, H., Liedl, T., Högberg, B., Graf, F. & Shih, W. M. 2009. Self-Assembly of DNA into Nanoscale Three-Dimensional Shapes. *Nature,* 459**,** 414.

[77] Era, H., Ide, Y., Nino, A. & Kishitake, K. 2005. TEM Study on Chromium Nitride Coatings Deposited by Reactive Sputter Method. *Surface and Coatings Technology,* 194**,** 265-270.

[78] Van der Heide, P. 2011. *X-ray Photoelectron Spectroscopy: An Introduction to Principles and Practices,* Hoboken, Wiley.

[79] Hollander, J. M. & Jolly, W. L. 1970. X-Ray Photoelectron Spectroscopy. *Accounts of Chemical Research,* 3**,** 193-200.

[80] Anderson, J., Kuhn, M. & Diebold, U. 1996. Epitaxially Grown Fe3O4 Thin Films: An XPS Study. *Surface Science Spectra,* 4**,** 266-272.

[81] Bubert, H., Rivière, J. C. & Werner, W. S. 2011. X-Ray Photoelectron Spectroscopy (XPS). *Surface and Thin Film Analysis***,** 9-41.

[82] Jang, K. 2013. *X-Ray Photoelectron Spectroscopy (XPS)*. Available: https://wiki.utep.edu/display/~kjang/XPS# [Accessed 10 March 2019].

[83] Seah, M., Gilmore, I. & Beamson, G. 1998. XPS: Binding Energy Calibration of Electron Spectrometers 5 - Re ‐ Evaluation of the Reference Energies. *Surface and Interface Analysis,* 26**,** 642-649.

[84] Tougaard, S. 2013. X-Ray Photoelectron Spectroscopy. *Chemistry, Molecular Sciences and Chemical Engineering.* Amsterdam: Elsevier.

[85] Wang, H. & Linford, M. 2015. X-ray Photoelectron Spectroscopy and Auger Electron Spectroscopy: Comparison and Basic Principles. *Vacuum Technology & Coating*.

[86] Chang, C. C. 1971. Auger Electron Spectroscopy. *Surface Science,* 25**,** 53-79.

[87] Chen, M., Wang, X., Yu, Y., Pei, Z., Bai, X., Sun, C., Huang, R. & Wen, L. 2000. X-Ray Photoelectron Spectroscopy and Auger Electron Spectroscopy Studies of Al-Doped ZnO Films. *Applied Surface Science,* 158**,** 134-140.

[88] Riviere, J. 1973. Auger Electron Spectroscopy. *Contemporary Physics,* 14**,** 513-539.

[89] Yun, Y. 2010. *Auger Electron Spectroscopy*. Available: https://wiki.utep.edu/display/~yyun/Auger+Electron+Spectroscopy [Accessed 10 March 2019].

[90] Descostes, M., Mercier, F., Thromat, N., Beaucaire, C. & Gautier-Soyer, M. 2000. Use of Xps in the Determination of Chemical Environment and Oxidation State of Iron and Sulfur Samples: Constitution of a Data Basis in Binding Energies for Fe and

S Reference Compounds and Applications to the Evidence of Surface Species of an Oxidized Pyrite in a Carbonate Medium. *Applied Surface Science,* 165**,** 288-302.

[91] Dai, J., Yuan, M., Zeng, J., Dai, Q., Lan, S., Xiao, C. & Tie, S. 2015. Three-Photon-Induced Blue Emission with Narrow Bandwidth from Hot Flower-Like ZnO Nanorods. *Optics Express,* 23**,** 29231-29244.

[92] Watts, J. F. 1994. X-Ray Photoelectron Spectroscopy. *Surface Science Techniques***,** 5-23.

[93] West, R. H. 1983. *High Energy X-Ray Sources for Photoelectron Spectroscopy.* University of Surrey.

[94] Pfluger, P. & Street, G. 1984. Chemical, Electronic, and Structural Properties of Conducting Heterocyclic Polymers: A View by XPS. *The Journal of Chemical Physics,* 80**,** 544-553.

[95] Lumsden, J. 1986. X-Ray Photoelectron Spectroscopy. *ASM Handbook,* 10**,** 568-580.

[96] Ebel, H., Ebel, M. F., Mantler, M., Barnegg-Golwig, G., Svagera, R. & Gurker, N. 1990. Imaging Xps with a Hemispherical Analyzer and Multichannelplate Detection. *Surface Science,* 231**,** 233-239.

[97] Seah, M. & Smith, G. 1990. Quantitative AES and XPS: Determination of the Electron Spectrometer Transmission Function and the Detector Sensitivity Energy Dependencies for the Production of True Electron Emission Spectra in AES and XPS. *Surface and Interface Analysis,* 15**,** 751-766.

[98] Knapp, G., Keenylside, M. & Griffin, C. 1990. A High Energy Resolution, High Spatial Resolution Photoemission Microscope. *Surface and Interface Analysis,* 15**,** 786-790.

[99] Lee, A. Y., Blakeslee, D. M., Powell, C. J. & Rumble Jr, J. R. 2002. Development of the Web-Based NIST X-Ray Photoelectron Spectroscopy (XPS) Database. *Data Science Journal,* 1**,** 1-12.

[100] Harrison, K. & Hazell, L. 1992. The Determination of Uncertainties in Quantitative XPS/AES and Its Impact on Data Acquisition Strategy. *Surface and Interface Analysis,* 18**,** 368-376.

[101] Ernst, M. & Sloof, W. 2008. Unraveling the Oxidation of Ru Using XPS. *Surface and Interface Analysis,* 40**,** 334-337.

[102] McIntyre, N., Sunder, S., Shoesmith, D. & Stanchell, F. 1981. Chemical Information from XPS-Applications to the Analysis of Electrode Surfaces. *Journal of Vacuum Science and Technology,* 18**,** 714-721.

[103] Simonsen, A. C., Yubero, F. & Tougaard, S. 1997. Quantitative Model of Electron Energy Loss in XPS. *Physical Review B,* 56**,** 1612.

[104] Oku, M., Suzuki, S., Ohtsu, N., Shishido, T. & Wagatsuma, K. 2008. Comparison of Intrinsic Zero-Energy Loss and Shirley-Type Background Corrected Profiles of XPS Spectra for Quantitative Surface Analysis: Study of Cr, Mn and Fe Oxides. *Applied Surface Science,* 254**,** 5141-5148.

[105] Tougaard, S. 1986. Background Removal in X-Ray Photoelectron Spectroscopy: Relative Importance of Intrinsic and Extrinsic Processes. *Physical Review B,* 34**,** 6779.

[106] Smart, R., McIntyre, S., Bancroft, M. & Bello, I. 2018. *X-Ray Photoelectron*

Spectroscopy. Available: http://mmrc.caltech.edu/SS_XPS/XPS_PPT/XPS_Slides.pdf [Accessed 10 March 2019].

[107] Fulghum, J. E. 1993. Determination of Overlayer Thickness by Angle-Resolved XPS: A Comparison of Algorithms. *Surface and Interface Analysis,* 20**,** 161-173.

[108] Wagner, C., Davis, L., Zeller, M., Taylor, J., Raymond, R. & Gale, L. 1981. Empirical Atomic Sensitivity Factors for Quantitative Analysis by Electron Spectroscopy for Chemical Analysis. *Surface and Interface Analysis,* 3**,** 211-225.

[109] Wagner, C. 1983. Sensitivity factors for XPS Analysis of Surface Atoms. *Journal of Electron Spectroscopy and Related Phenomena,* 32**,** 99-102.

[110] 2018. *CasaXPS: Processing Software for XPS, AES, SIMS and More*. CasaXPS. Available: http://www.casaxps.com/ [Accessed 10 March 2019].

[111] Hunt, J. 2008. Celebrating 25 years of Inductively Coupled Plasma-Mass Spectrometry. *American Laboratory***,** 1-4.

[112] Wolf, R. E. 2005. *What is ICP-MS?* Available: https://crustal.usgs.gov/laboratories/icpms/intro.html [Accessed 10 March 2019].

[113] 2011. The 30-Minute Guide to ICP-MS. USA: PerkinElmer.

[114] Montaser, A. 1998. *Inductively Coupled Plasma Mass Spectrometry,* New York, John Wiley & Sons.

[115] Beauchemin, D. 2010. Inductively Coupled Plasma Mass Spectrometry. *Analytical Chemistry,* 82**,** 4786-4810.

[116] Zhang, X. & Cresswell, M. 2016. Chapter 3 - Materials Characterization of Inorganic Controlled Release. *In:* Zhang, X. & Cresswell, M. (eds.) *Inorganic Controlled Release Technology.* Boston: Butterworth-Heinemann.

[117] 2001. The 30-Minute Guide to ICP-MS. USA: PerkinElmer.

[118] Craig, C., Jarvis, K. E. & Clarke, L. J. 2000. An Assessment of Calibration Strategies for the Quantitative and Semi-Quantitative Analysis of Calcium Carbonate Matrices by Laser Ablation-Inductively Coupled Plasma-Mass Spectrometry (LA-ICP-MS). *Journal of Analytical Atomic Spectrometry,* 15**,** 1001-1008.

[119] Amarasiriwardena, C. J., Gercken, B., Argentine, M. D. & Barnes, R. M. 1990. Semi-Quantitative Analysis by Inductively Coupled Plasma Mass Spectrometry. *Journal of Analytical Atomic Spectrometry,* 5**,** 457-462.

[120] Halicz, L. & Günther, D. 2004. Quantitative Analysis of Silicates Using LA-ICP-MS with Liquid Calibration. *Journal of Analytical Atomic Spectrometry,* 19**,** 1539-1545.

[121] Brabson, G. D. 1986. Ultraviolet/Visible Absorption Spectroscopy. *ASM Handbook,* 10**,** 60-71.

[122] Woolley, J. T. 1971. Reflectance and Transmittance of Light by Leaves. *Plant Physiology,* 47**,** 656-662.

[123] Siesler, H. W., Ozaki, Y., Kawata, S. & Heise, H. M. 2008. *Near-Infrared Spectroscopy: Principles, Instruments, Applications,* Weinheim, John Wiley & Sons.

[124] Weckhuysen, B. M. 2004. Ultraviolet-Visible Spectroscopy.

[125] Liu, G., Niu, P., Sun, C., Smith, S. C., Chen, Z., Lu, G. Q. & Cheng, H. 2010. Unique Electronic Structure Induced High Photoreactivity of Sulfur-Doped Graphitic C3N4. *Journal of the American Chemical Society,* 132**,** 11642-11648.

[126] Sun, Y. & Xia, Y. 2003. Gold and Silver Nanoparticles: A Class of Chromophores

with Colors Tunable in the Range from 400 to 750 nm. *Analyst,* 128**,** 686-691.

[127] Tissue, B. M. 2002. Ultraviolet and Visible Absorption Spectroscopy. *Characterization of Materials*.

[128] 2018. *UV-Visible Spectroscopy*. Available: https://www2.chemistry.msu.edu/faculty/reusch/virttxtjml/spectrpy/uv-vis/uvspec.htm [Accessed 10 March 2019].

[129] 2018. *Beer's Law*. Sheffield Hallam University. Available: https://teaching.shu.ac.uk/hwb/chemistry/tutorials/molspec/beers1.htm [Accessed 10 March 2019].

[130] Hughes, H. K. 1963. Beer's Law and the Optimum Transmittance in Absorption Measurements. *Applied Optics,* 2**,** 937-945.

[131] Vo, K. 2015. *Spectrophotometry*. Available: https://chem.libretexts.org/Core/Physical_and_Theoretical_Chemistry/Kinetics/Reaction_Rates/Experimental_Determination_of_Kinetcs/Spectrophotometry [Accessed 10 March 2019].

[132] Ödeen, A., Hart, N. S. & Håstad, O. 2009. Assessing the Use of Genomic DNA as a Predictor of the Maximum Absorbance Wavelength of Avian SWS1 Opsin Visual Pigments. *Journal of Comparative Physiology A,* 195**,** 167-173.

[133] Clark, J. 2017. *Using UV-Visible Absorption Spectra*. Available: https://www.chemguide.co.uk/analysis/uvvisible/analysis.html#top [Accessed 10 March 2019].

[134] Herzberg, G. 1950. *Molecular Spectra and Molecular Structure,* New York, D. Van Nostrand Company, Inc.

[135] Pirrung, M. C. 2016. *Handbook of Synthetic Organic Chemistry,* Amsterdam, Elsevier Science.

[136] Calloway, D. 1997. Beer-Lambert Law. *Journal of Chemical Education,* 74**,** 744.

[137] de Dios, A. C. 2018. *Introduction to the U-2001 UV/Visible Spectrophotometer*. Available: https://bouman.chem.georgetown.edu/S00/handout/spectrometer.htm [Accessed 10 March 2019].

[138] Krishna, A., Vijayan, N., Riscob, B., Gour, B. S., Haranath, D., Philip, J., Verma, S., Jayalakshmy, M. S., Bhagavannarayana, G. & Halder, S. K. 2014. Phase Matching, X-Ray Topography, Optical and Thermal Analysis of L-Alanine Cadmium Chloride Monohydrate: A Nonlinear Optical Material. *Applied Physics A,* 114**,** 1257-1265.

[139] Suresh, S., Mani, P. & Anand, K. 2012. Growth, Optical and Electrical Properties of L-Prolinium Tartrate NLO Single Crystals. *Growth,* 43.

[140] Thukral, K., Vijayan, N., Rathi, B., Bhagavannaryana, G., Verma, S., Philip, J., Krishna, A., Jeyalakshmy, M. S. & Halder, S. K. 2014. Synthesis and Single Crystal Growth of L-Proline Cadmium Chloride Monohydrate and Its Characterization for Higher Order Harmonic Generation Applications. *CrystEngComm,* 16**,** 2802-2809.

[141] Tauc, J., Grigorovici, R. & Vancu, A. 1966. Optical Properties and Electronic Structure of Amorphous Germanium. *Physica Status Solidi (B),* 15**,** 627-637.

[142] Manifacier, J. C., Gasiot, J. & Fillard, J. P. 1976. A Simple Method for the Determination of the Optical Constants n, k and the Thickness of a Weakly Absorbing Thin Film. *Journal of Physics E: Scientific Instruments,* 9**,** 1002.

[143] Swanepoel, R. 1983. Determination of the Thickness and Optical Constants of Amorphous Silicon. *Journal of Physics E: Scientific Instruments,* 16**,** 1214.

[144] Dorranian, D., Dejam, L. & Mosayebian, G. 2012. Optical Characterization of Cu3N Thin Film with Swanepoel Method. *Journal of Theoretical and Applied Physics,* 6**,**

13.
[145] 2016. *Perkin-Elmer UV/Vis/NIR Spectrophotometer Lambda 19*. Soft Materials Laboratory. Available: http://softmaterials.engr.wisc.edu/instr_uv_vis_lambda19.html [Accessed 10 March 2019].
[146] Wendlandt, W. W. & Hecht, H. G. 1966. *Reflectance Spectroscopy,* New York, John Wiley & Sons Inc.
[147] Khoshhesab, Z. M. 2012. Reflectance IR Spectroscopy. *In:* Theophanides, T. (ed.) *Infrared Spectroscopy.* London: InTech.
[148] Willis, C. 1970. The Complex Refractive Index of Particles in a Flame. *Journal of Physics D: Applied Physics,* 3**,** 1944.
[149] Kortüm, G. 2012. *Reflectance Spectroscopy: Principles, Methods, Applications,* Berlin, Springer.
[150] Mirabella Jr, F. 1985. Internal Reflection Spectroscopy. *Applied Spectroscopy Reviews,* 21**,** 45-178.
[151] Andor. 2018. *Absorption / Transmission / Reflection Spectroscopy*. Available: http://www.andor.com/learning-academy/absorption-transmission-reflection-spectroscopy-an-introduction-to-absorption-transmission-reflection-spectroscopy [Accessed 10 March 2019].
[152] Lipert, R. J., Lamp, B. D. & Porter, M. D. 1998. 3 Specular Reflection Spectroscopy. *Modern Techniques in Applied Molecular Spectroscopy,* 14**,** 83.
[153] Lucarini, V., Saarinen, J. J., Peiponen, K. & Vartiainen, E. M. 2005. *Kramers-Kronig Relations in Optical Materials Research,* Berlin, Springer.
[154] Kubelka, P. 1931. Ein Beitrag zur Optik der Farbanstriche (Contribution to the Optic of Paint). *Zeitschrift fur technische Physik,* 12**,** 593-601.
[155] Dresselhaus, M. 2001. Solid State Physics Part II Optical Properties of Solids. Cambridge, MA: Massachusetts Institute of Technology.
[156] Drude, P. 1900. Zur Elektronentheorie der Metalle. *Annalen der Physik,* 306**,** 566-613.
[157] Drude, P. 1900. Zur Elektronentheorie der Metalle; II. Teil. Galvanomagnetische und Thermomagnetische Effecte. *Annalen der Physik,* 308**,** 369-402.
[158] Rumpf, R. C. 2016. Electromagnetic Properties of Materials - Lorentz and Drude Models. El Paso: The University of Texas at El Paso.
[159] Morris, D. P. 2009. Optical Properties of Water. *In:* Likens, G. E. (ed.) *Encyclopedia of Inland Waters.* Oxford: Academic Press.
[160] 2008. *Guide to Using WVASE 32: Spectroscopic Ellipsometry Data Acquisition and Analysis Software,* Lincoln, NE, J. A. Woollam Company, Incorporated.
[161] Hall, E. H. 1879. On a New Action of the Magnet on Electric Currents. *American Journal of Mathematics,* 2**,** 287-292.
[162] MacDonald, A., Rice, T. & Brinkman, W. 1983. Hall Voltage and Current Distributions in an Ideal Two-Dimensional System. *Physical Review B,* 28**,** 3648.
[163] Popovic, R. S. 2003. *Hall Effect Devices: Magnetic Sensors and Characterization of Semiconductors,* Hoboken, CRC Press.
[164] Jackson, J. D. 2012. *Classical Electrodynamics,* New Delhi, John Wiley & Sons.
[165] Chien, C. 2013. *The Hall Effect and Its Applications,* New York, Springer.

[166] Tedesco, J. L., VanMil, B. L., Myers-Ward, R. L., McCrate, J. M., Kitt, S. A., Campbell, P. M., Jernigan, G. G., Culbertson, J. C., Eddy Jr, C. R. & Gaskill, D. K. 2009. Hall Effect Mobility of Epitaxial Graphene Grown on Silicon Carbide. *Applied Physics Letters,* 95**,** 122102.

[167] 2018. *Hall Effect Measurements*. NIST. Available: https://www.nist.gov/pml/engineering-physics-division/popular-links/hall-effect [Accessed 10 March 2019].

[168] Van der Pauw, L. J. 1958. A Method of Measuring Specific Resistivity and Hall Effect of Discs of Arbitrary Shape. *Philips Research Reports,* 13**,** 1-9.

[169] Bierwagen, O., Ive, T., Van de Walle, C. G. & Speck, J. S. 2008. Causes of Incorrect Carrier-Type Identification in van der Pauw-Hall Measurements. *Applied Physics Letters,* 93**,** 242108.

[170] Chwang, R., Smith, B. & Crowell, C. 1974. Contact Size Effects on the van der Pauw Method for Resistivity and Hall Coefficient Measurement. *Solid-State Electronics,* 17**,** 1217-1227.

[171] 2018. *Ecopia HMS-3000 Hall Measurement System*. Available: http://four-point-probes.com/ecopia-hms-3000-hall-measurement-system/ [Accessed 10 March 2019].

Chapter 3

From Precursor Solutions to Thin Films

3.1 Experimental

Undoped and doped ZnO thin films were deposited by the spray pyrolysis technique at a specific substrate temperature. Undoped ZnO precursor solutions were prepared by dissolving zinc acetylacetonate hydrate ($Zn(C_5H_7O_2)_2 \cdot xH_2O$, 99.995% trace metals basis, Sigma-Aldrich) in a 2 : 1 volume ratio solvent of isopropanol ($(CH_3)_2CHOH$, ≥ 99.7%, Sigma-Aldrich) and distilled water (Ondeo Purite Select Analyst). The concentration of zinc acetylacetonate in the precursor was 0.15 mol / L. 10 droplets of glacial acetic acid (CH_3CO_2H, ≥ 99.7%, Alfa Aesar) were added to a 10 mL precursor solution by using a 1 mL plastic Pasteur pipette to prevent any hydrolysis of zinc acetylacetonate. The precursor solution was stirred for 30 minutes to yield a clear solution before filtering through a qualitative filter paper (Whatman). The precursor solution should finally be clear and homogeneous. 10 mL of filtered precursor solution was used for each film deposition unless stated otherwise. To make films of different thicknesses, various volumes (0 - 10 mL) of precursor solutions were used for each film deposition.

To make SiZO precursor solutions, silicon tetraacetate ($Si(OCOCH_3)_4$, 98%, Sigma-Aldrich) was added to undoped ZnO precursor solutions prepared as above. The quantity of silicon tetraacetate added depended on molar ratios of Si and Zn (Si concentration = [Si] / [Zn] × 100%). The Si containing precursor was stirred for 24 hours to yield a clear solution or a homogeneous mixture before filtering through a qualitative filter paper (Whatman). The precursor solution should finally be clear and homogeneous.

IZO precursor solutions were made by adding indium chloride hydrate ($InCl_3 \cdot xH_2O$, 99.99% metals basis, Alfa Aesar) into undoped ZnO precursor solutions. Similarly, InSiZO precursor solutions were made by adding indium chloride hydrate ($InCl_3 \cdot xH_2O$, 99.99% metals basis, Alfa Aesar) and silicon tetraacetate ($Si(OCOCH_3)_4$, 98%, Sigma-Aldrich) into undoped ZnO precursor solutions. The quantity of starting materials added and the other procedures were determined the same as stated above.

Figure 3.1 and **Figure 3.2** show the spray pyrolysis apparatus. The substrate was a 32 mm × 24 mm borosilicate glass rectangular coverslip (0.13 - 0.17 mm thick, Fisherbrand), which was cleaned in a mixture of distilled water and acetone by using an ultrasonic cleaner. The substrate was then dried in the room temperature and further cleaned with a jet of pure dry nitrogen.

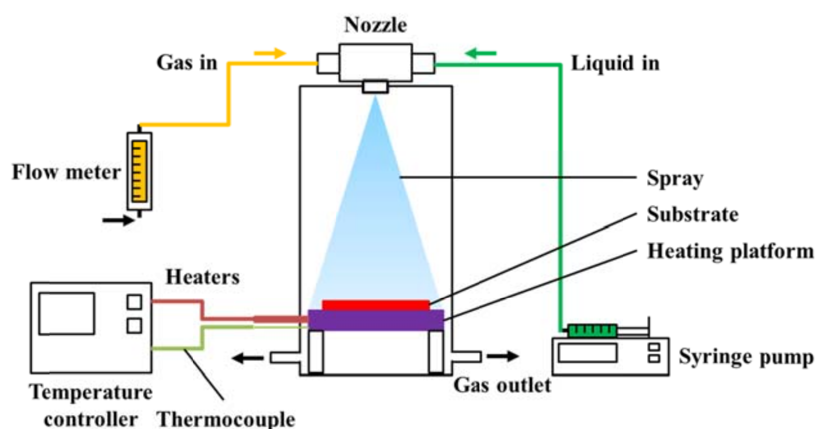

Figure 3.1: Schematic of the spray pyrolysis process used in this investigation.

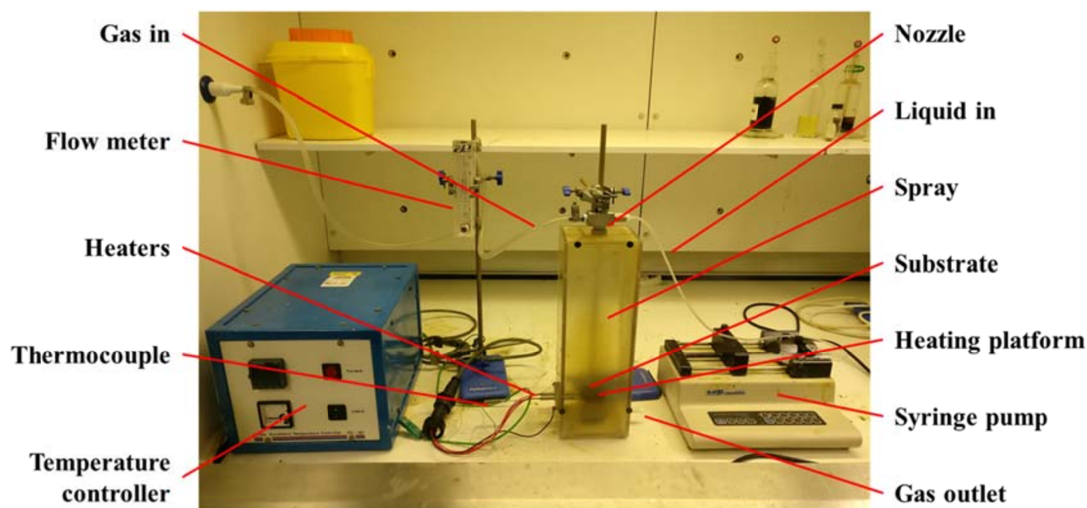

Figure 3.2: Photo of a spray pyrolysis apparatus in a laboratory.

The substrate cap was placed upside down on a flat surface or bench before putting the glass substrate in the substrate cap. The heating block was then placed upside down into the

substrate cap and on the top of the glass substrate, followed by tightening the screws of the substrate cap. The substrate was finally mounted on a stainless steel heating platform with two cartridge heaters inserted into two holes of the heating block. (**Figure 3.3**)

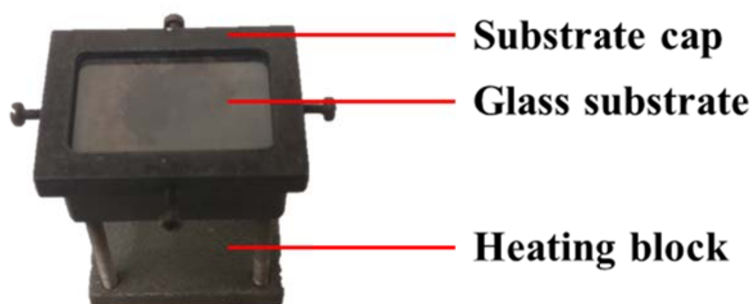

Figure 3.3: Photo of mounting a substrate.

The temperature of the heating platform as controlled by a Eurotherm PID temperature controller, and a thermocouple stainless steel probe was inserted into a small hole of the heating block. The heater surface temperature was kept at ~ 310 °C during the spray pyrolysis. The precursor solution was pumped into an atomiser nozzle (BETE XA PR-050) by a syringe infusion pump (KDS 200 Legacy Dual Syringe Infusion Pump, KD Scientific) with a flow rate of 0.55 mL / min. 'House' dry nitrogen was used as the carrier gas to blow the precursor solution onto the glass substrate with a flow rate of 14.5 L / min. The distance between the nozzle and the glass substrate was 30 cm. The chamber was flushed with dry nitrogen to eliminate any air, and the heating platform was heated at a rate of 30 °C / min and held at a specific deposition temperature for 20 minutes before pumping the precursor solution. The temperature was held for 5 minutes after finishing pumping the precursor solution. The heating platform was then cooled down to the room temperature at a rate of 25 °C / min before the product was taken out of the chamber.

Based on temperature calibration experiments by measuring the heater surface temperature and the heating block temperature at the same time, the heater surface temperature is considerably lower than the heater setting temperature, and the linear fitting equation is shown in **Figure 3.4**. The equation shows that the heater surface temperature is ~ 70% of the

heater setting temperature. In this thesis, any film deposition temperature is expressed as the heater surface temperature unless otherwise stated to avoid any confusion. However, the thermal distribution on the heating platform is not uniform. Therefore, further optimisation of the synthesis kit can be done to avoid this problem. Please refer to **Appendix A3.1** for details.

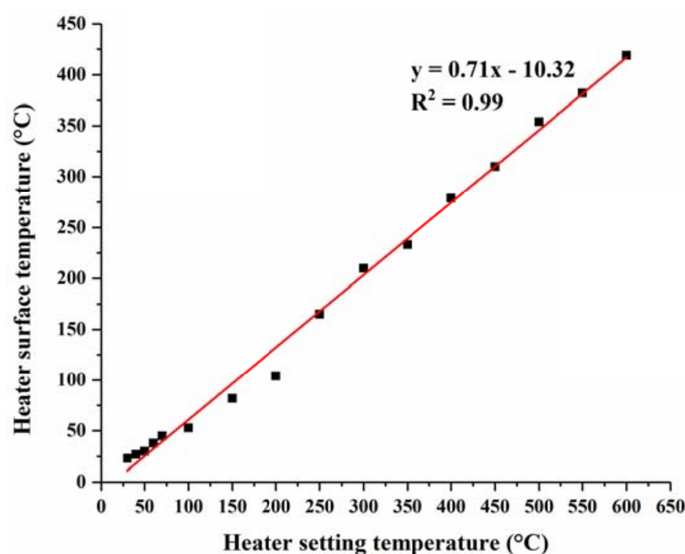

Figure 3.4: Calibration of the heater surface temperature.

3.2 Results and Discussion

3.2.1 Thickness Control of Thin Films

There are four experimental steps to generate conduction in thin films from our synthetic approach, as shown in **Figure 3.5**. In this chapter, I focus on the process from starting precursor materials and solutions to thin films to explore firstly the variations of film thickness and chemical compositions.

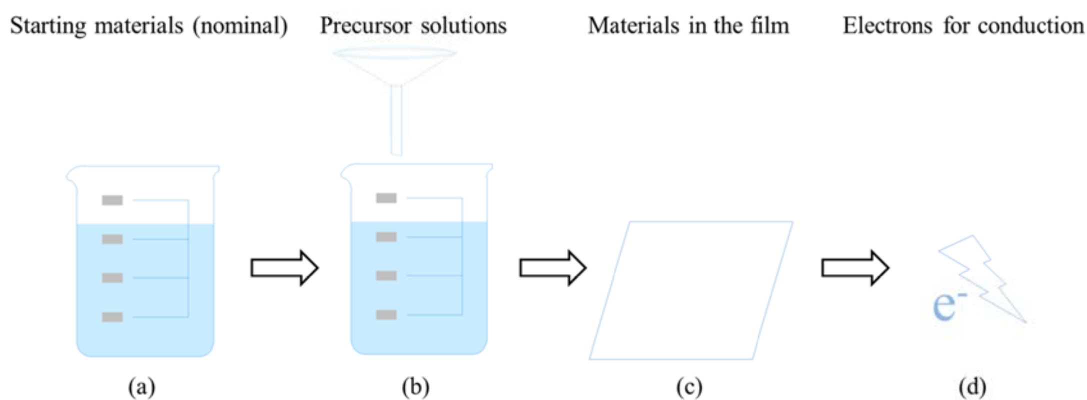

Figure 3.5: Schematic of steps to generate current-carrying electrons in our thin films from the preparation of starting materials and solutions to the final thin films.

Remarkably, the control of the film thickness is relatively straightforward for spray pyrolysis by simply, but carefully controlling the precursor solution volume and the deposition conditions. The thicknesses of ZnO, SiZO, IZO, and InSiZO thin films increase as precursor solution volumes increase showing a linear relationship (**Figure 3.6**). The linear regressions show that 1 mL of precursor solutions can make films with a thickness of ~ 58 - 68 nm.

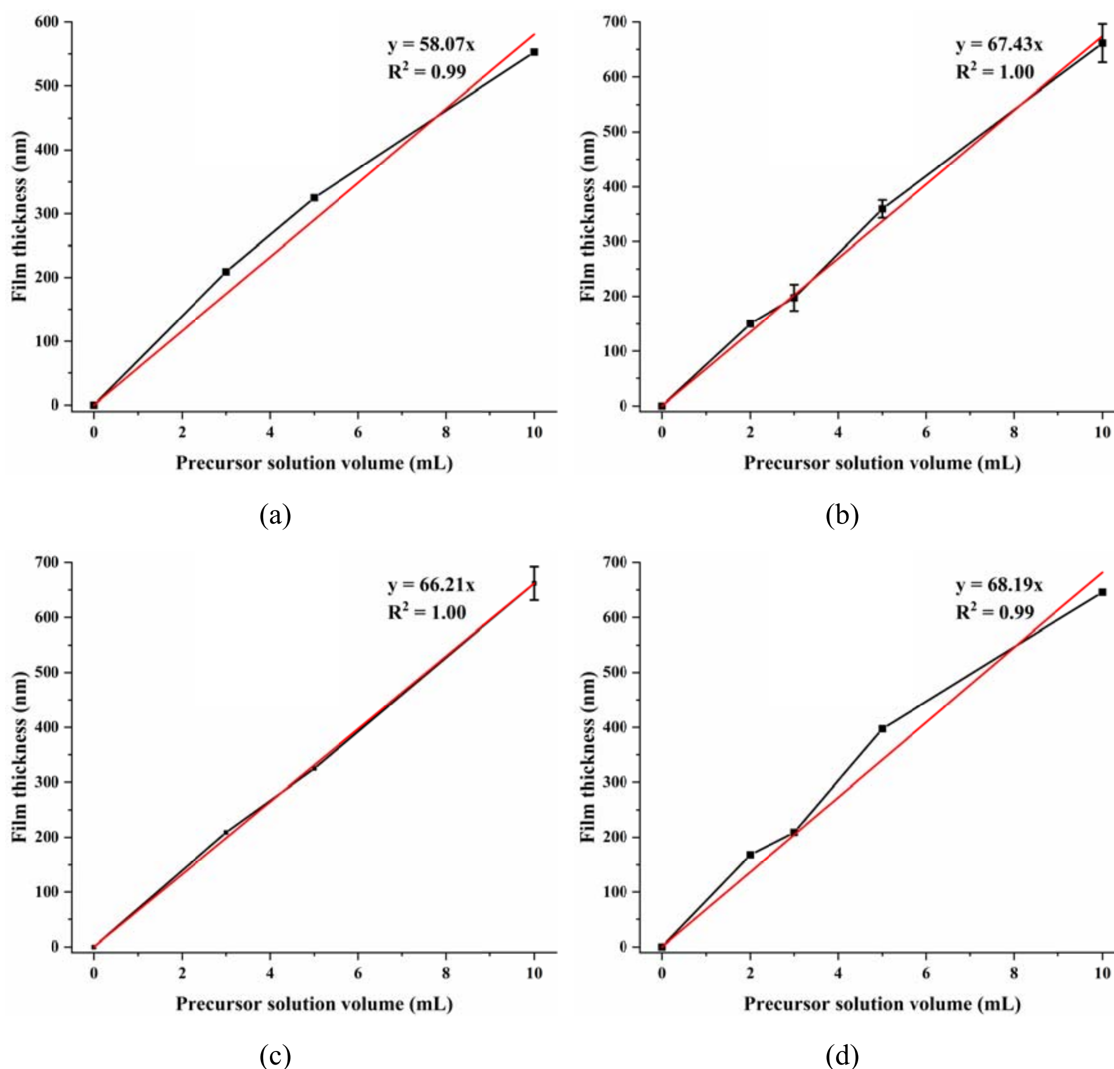

Figure 3.6: Film thicknesses of ZnO (a), SiZO (c_p = 3%) (b), IZO (c_p = 6%) (c), and InSiZO (c_p = 6% In-3% Si) (d) thin films prepared from varying amounts of precursor solutions.

3.2.2 Elemental Analysis of ZnO Thin Films

3.2.2.1 Effect of Element Concentration: From Precursor Solutions to Thin Films

3.2.2.1.1 Singly Doped Thin Films

Element concentrations in the thin films are different from the concentrations in the precursor solutions because of a variety of processes in which the elemental concentrations in the film are reduced below those of the precursor solution. As optical and electrical properties are

associated with the element concentrations in the films themselves, it is necessary to study the relationships between element concentrations in the films c_f and the concentrations in the precursor solutions c_p. I find that the element concentrations in the films are much lower, and show a linear relationship between these two concentrations. The element concentrations in the films as a function of the concentrations in the precursor solutions are shown in **Figure 3.7**. The error bars in the graphs are estimated by the standard deviations of a set of data values of the reproducible samples. Some error bars are invisible since they are pretty small.

The linear regressions show that Si/In concentrations in the films are approximately one-third of their concentrations in the precursor solutions, as might be expected given the nature of the spray pyrolysis technique. Si and In show no differences in the ratio of (concentrations in the films) to (concentrations in the precursor solutions). In this thesis, element concentrations are expressed as element concentrations in the films c_f, unless otherwise stated.

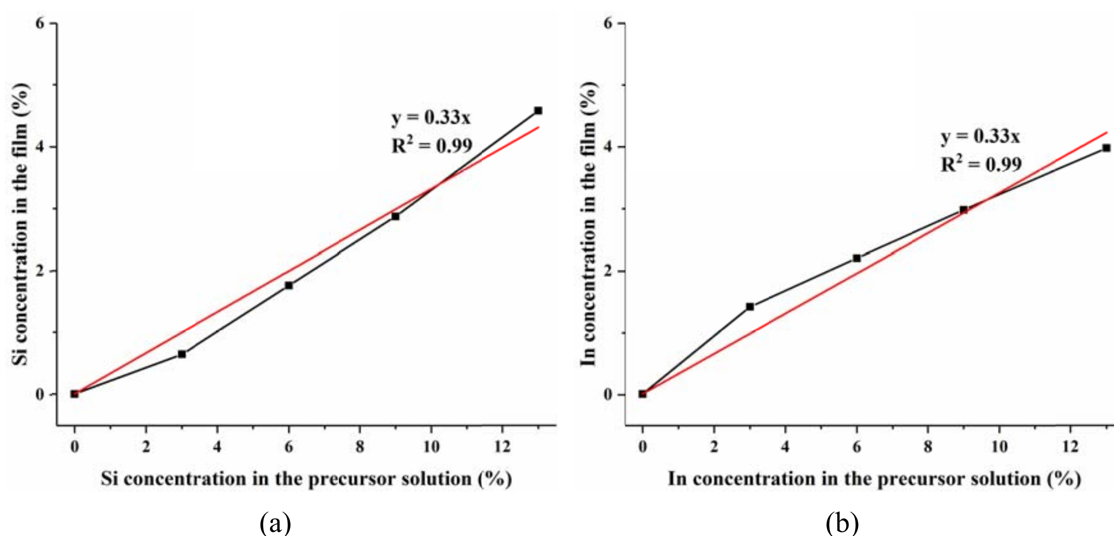

Figure 3.7: Si/In concentrations in the films for SiZO (a)/IZO (b) thin films containing varying amounts of Si/In.

We define the transfer efficiency of a particular element as the ratio of the experimentally determined (from the ICP-MS data) element's quantity in the film as compared to the element's quantity in the precursor solution. The transfer efficiency of an element is therefore

determined according to the following equation.

$$Transfer\,efficiency = \frac{n_{film}}{n_{precursor\ solution}} \times 100\%$$

Equation 3.1

Where n_{film} is the element quantity in the film and $n_{precursor\ solution}$ is the element quantity in the precursor solution.

Figure 3.8 shows the Zn quantities in the thin films and the experimentally determined transfer efficiencies for Zn containing varying amounts of Si/In. The maximum possible errors for ICP-MS measurements are normally 5% [1, 2], which have been shown in the figures. The Zn quantities in the films decrease as the Si or In concentrations increase. This suggests Si/In replaces Zn. Therefore the transfer efficiencies for Zn also decrease as the Si/In concentrations increase (**Figure 3.8**). The maximum value of the transfer efficiencies for Zn is ~ 1.6% suggesting only ~ 1.6% of the Zn is transferred from starting precursor solutions to the thin films, i.e., ~ 98.4% of the Zn is lost to the container walls, etc. during the whole spray pyrolysis process.

The low transfer efficiencies for Zn show that the synthesis of thin films by using spray pyrolysis as used is relatively wasteful of starting materials, but in these experiments no attempt has been made to reduce these losses. However, I note that somewhat similar losses also occur even in conventional vacuum deposition processes. For example, some reported PLDs have less than 1% of the ionised fraction in the plume at the substrate position. [3-6]

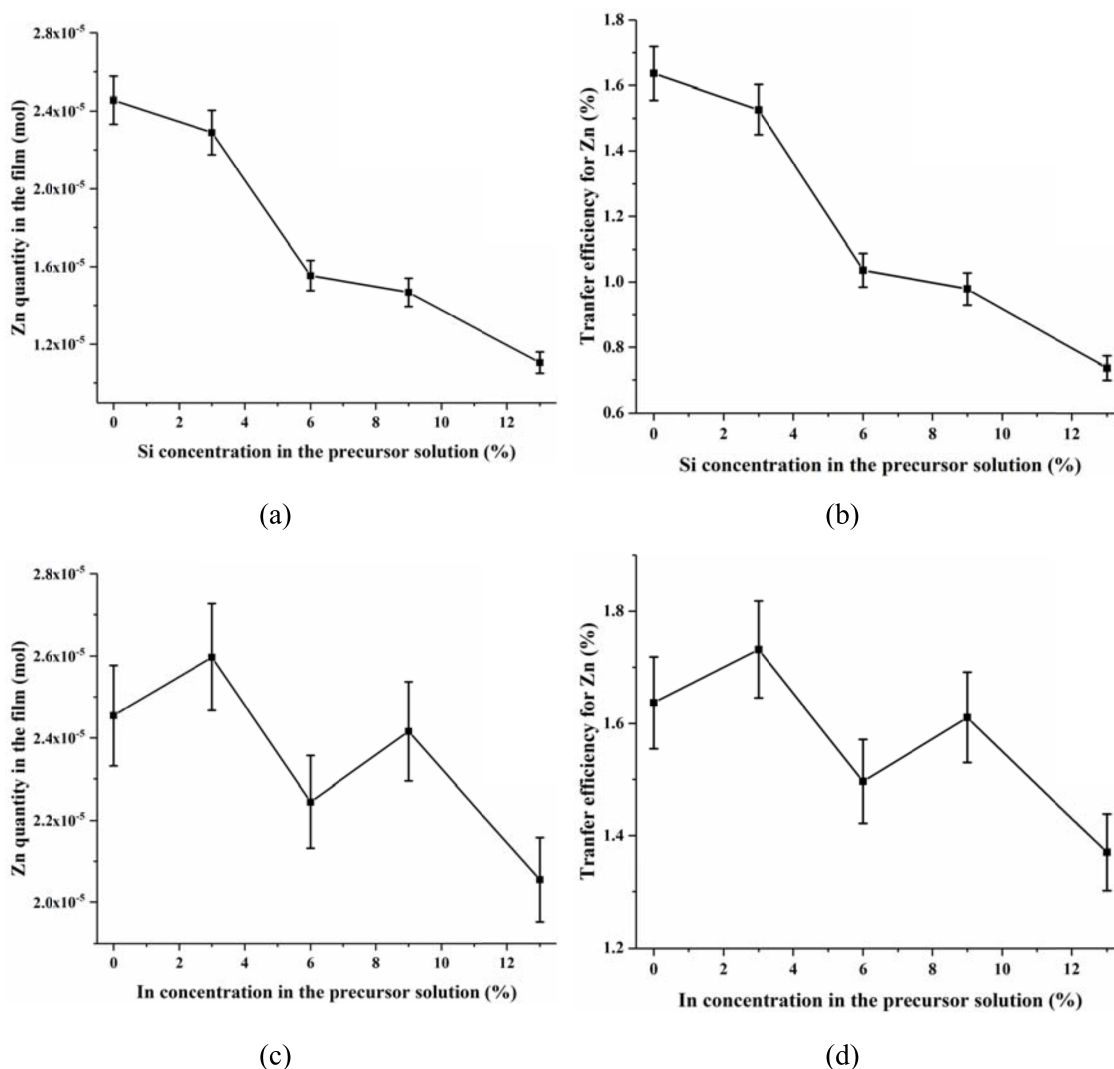

Figure 3.8: Zn quantities in SiZO (a) and IZO (c) thin films and transfer efficiencies for SiZO (b) and IZO (d) thin films containing varying amounts of Si/In. The error bars demonstrate the maximum possible errors of 5%. [1, 2]

Figure 3.9 shows the Si/In quantities in the films and their transfer efficiencies for thin films containing varying amounts of Si/In. The Si/In quantities in the films increase as the Si/In concentrations in the precursor solutions increase showing a linear relationship. However, the transfer efficiencies of Si/In decrease as the Si/In concentrations in the precursor solutions increase. The fluctuations in (b) are negligible. SiZO thin films have a maximum transfer efficiency value of ~ 0.3% for Si, which means only ~ 0.3% of the Si is transferred to films. Similarly, the value for IZO thin films is ~ 0.8%. The transfer efficiencies of Si/In are much lower than those of Zn (~ 1.6%). It shows that different elements have different transfer

efficiencies from starting materials to films in the synthesis process using spray pyrolysis.

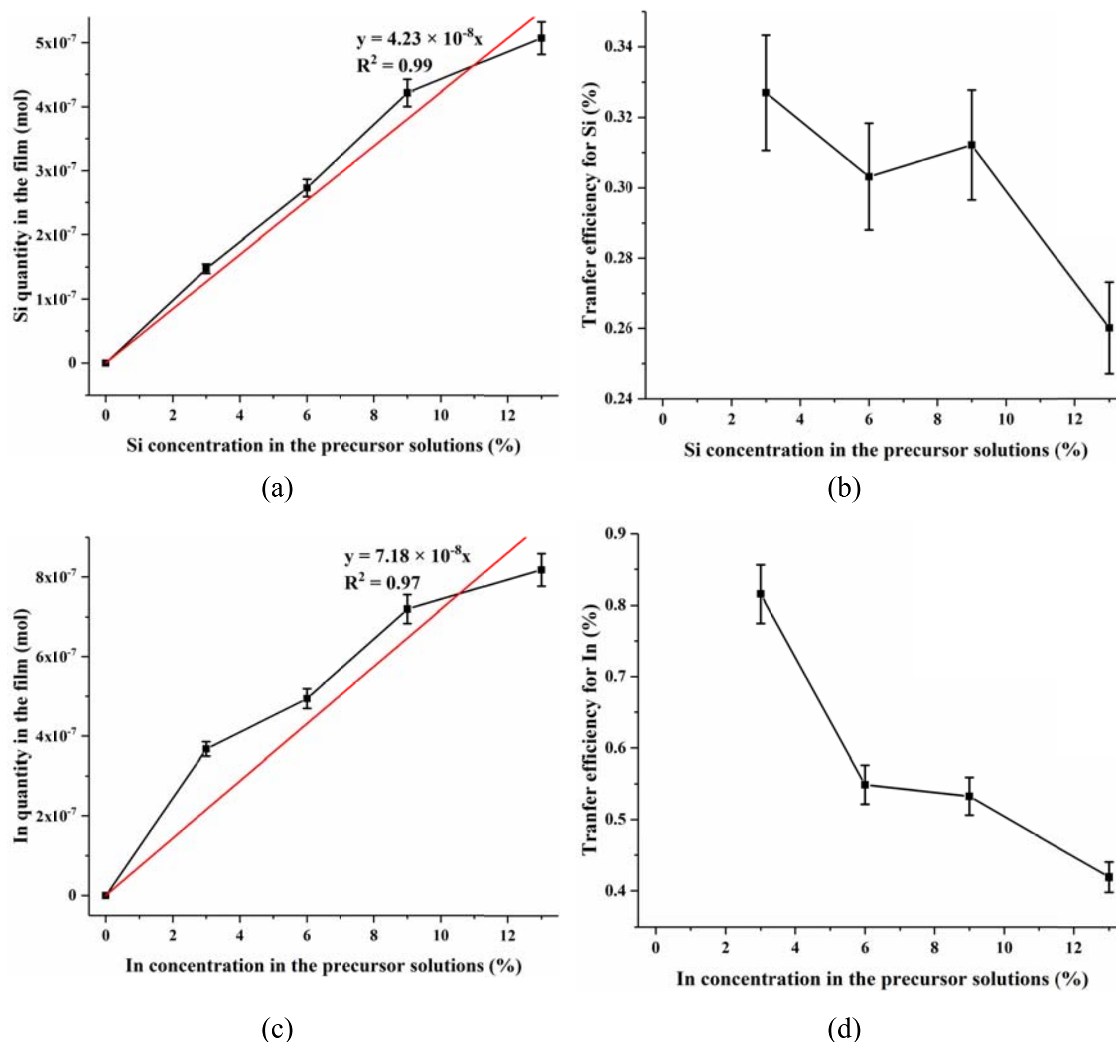

Figure 3.9: Si/In quantities in SiZO (a)/IZO (c) thin films and their transfer efficiencies for SiZO (b)/IZO (d) thin films containing varying amounts of Si/In.

3.2.2.1.2 Co-Doped Thin Films

InSiZO thin films are studied as co-doped thin films to compare with the singly doped SiZO and IZO thin films. The conductivity of singly doped thin films is limited by the solubility of the dopant. Co-doping is the process of potentially adding a second dopant to the primary dopant in an attempt to increase the solid solubility of both dopants, thus increasing the carrier concentration and the conductivity of thin films. [7] The second dopant behaves in two

possible ways. The first is that the second dopant does not affect the primary dopant concentrations in the films. The second way is that the second dopant competes with the primary dopant; therefore, the primary dopant concentrations become lower in the co-doped films.

The In and Si concentrations determined in our thin films as a function of concentrations in the precursor solutions are shown in **Figure 3.10**. The In and Si concentrations in the films are much lower than those in the precursor solutions and show a linear relationship. It is similar to singly doped thin films. The Si/In concentrations in the films are approximately one-third of their concentrations in the precursor solutions for InSiZO (In-c_p = 3% Si)/InSiZO (c_p = 6% In-Si) thin films, which are the same as those for SiZO and IZO thin films (**Figure 3.7**). It indicates that adding a second dopant does not affect the element concentrations of the primary dopant in the films, that is to say, the important conclusion is that the second dopant does not compete with the primary dopant in InSiZO thin films. This finding is corroborated by the constant values of primary dopant concentrations in the films as the concentrations in the precursor solutions are fixed as constants in InSiZO thin films. 0.6 ± 0.1% of Si is in the films for InSiZO (In-c_p = 3% Si) thin films and 1.8 ± 0.4% of In is in the films for InSiZO (c_p = 6% In-Si) thin films (**Figure 3.10**).

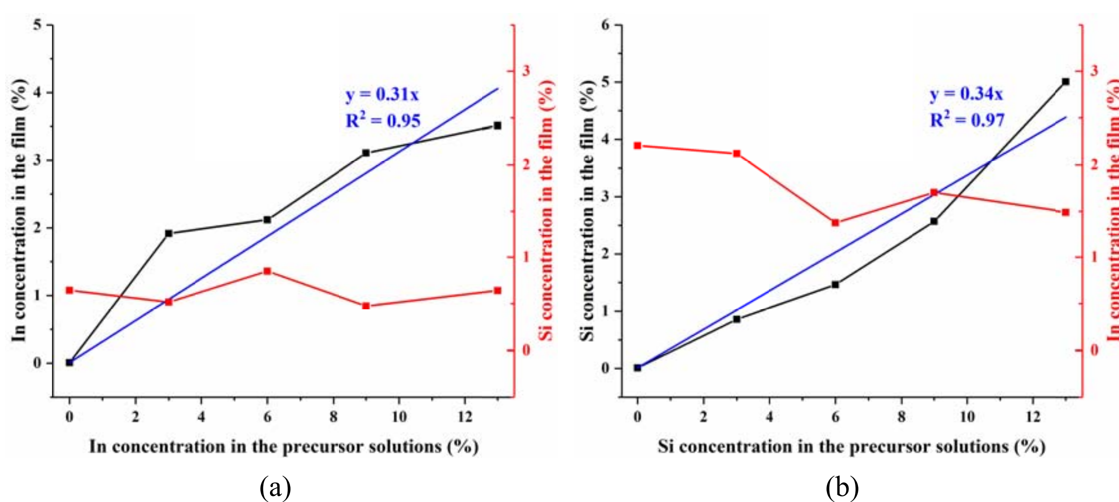

Figure 3.10: In and Si concentrations in the films for InSiZO (In-c_p = 3% Si) (a) and InSiZO (c_p = 6% In-Si) (b) thin films.

3.2.2.2 Effect of Film Thickness

When the film thicknesses are controlled by the spray pyrolysis using reduced volumes of precursor solutions, any resulting variations in element concentrations in the films are crucial. The element concentrations in the films for SiZO, IZO, and InSiZO thin films remain constant for varying film thicknesses, that is to say, they are independent of the variation of the film thicknesses (**Figure 3.11**). The Si/In concentrations in the films for SiZO (c_p = 3%)/IZO (c_p = 6%) thin films of varying thicknesses are 0.9 ± 0.3%/2.3 ± 0.1%, meanwhile, the In and Si concentrations in the films for InSiZO (c_p = 6% In-3% Si) thin films of varying thicknesses are 1.8 ± 0.3% and 1.0 ± 0.3%, respectively. The constant chemical compositions in the films for the films having different thicknesses represent an advantage of the spray pyrolysis technique.

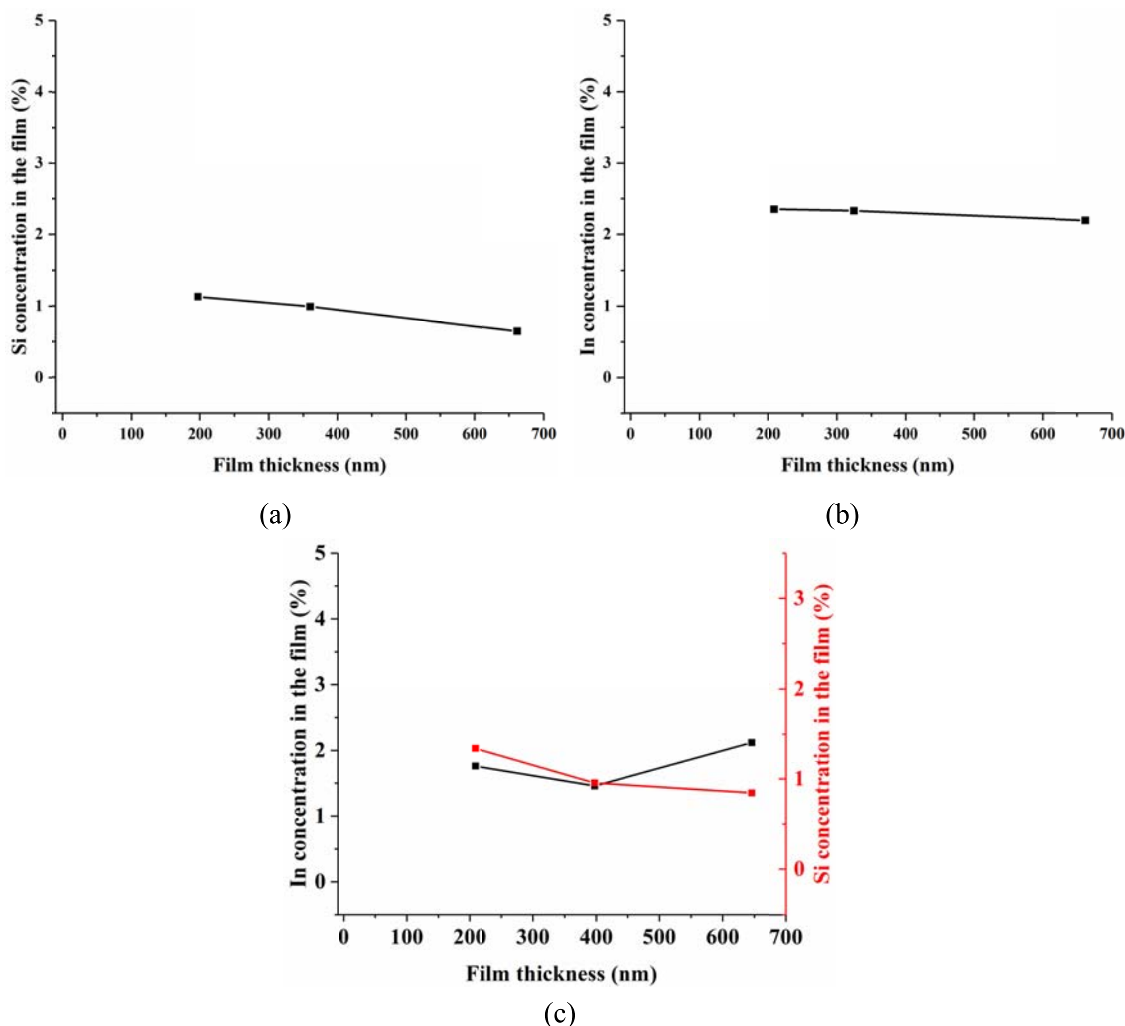

Figure 3.11: Si/In concentrations in the films for SiZO (c_p = 3%) (a), IZO (c_p = 6%) (b), and InSiZO (c_p = 6% In-3% Si) (c) thin films prepared from varying amounts of precursor solutions.

3.3 Conclusions

This work represents the first study in which the total chemical compositions of elements in bulk of thin films have been fully determined. This is different from the surface elemental analysis (e.g., XPS, EDX, etc.) used in studying TCO thin films in previous publications; the ICP-MS technique gives the total chemical compositions of elements in bulk of thin films, not just the surface chemical compositions. Optical and electrical properties are completely linked to the nature of both bulk and surface chemical and physical properties; therefore, these properties are mainly attributed to the chemical compositions in the films instead of those in

starting materials or precursor solutions.

One of the advantages of the spray pyrolysis technique is the easy control of the film thickness by changing the precursor solution volume. Thus, I find linear relationships between the thicknesses of ZnO, SiZO, IZO, and InSiZO thin films and the precursor solution volumes. Remarkably, 1 mL of precursor solutions can make films with a thickness of ~ 58 - 68 nm. The other advantage of the spray pyrolysis technique is that the element concentrations in the films are independent of the variation of both precursor solution volumes and film thicknesses. Thus films with different thicknesses can be produced by simply changing the precursor solution volumes using the spray pyrolysis technique; and importantly, thus the resulting chemical compositions of films are the same, irrespective of film thickness.

In all cases, the impurity element concentrations in the films are much lower than those in the precursor solutions. Typically, The Si/In concentrations in the films are approximately one-third of their concentrations in the precursor solutions for SiZO/IZO thin films. There are no differences between Si and In for the ratio of concentrations in the films and in the precursor solutions, that is to say, the dopant used is irrelevant to the ratio.

The limitation of the conductivity of singly doped thin films is the solubility of the dopant. Adding a second dopant to the primary dopant is called co-doping in an attempt to increase the carrier concentration and the conductivity of thin films. [7] The In/Si concentrations in the films are approximately one-third of their concentrations in the precursor solutions for InSiZO (In-c_p = 3% Si)/InSiZO (c_p = 6% In-Si) thin films, which are the same as those for IZO and SiZO thin films. The values of primary dopant concentrations in the films are fixed as constants in InSiZO thin films. This work demonstrates that the element concentrations of the primary dopant in the films are not affected by adding a second dopant, i.e., importantly, the second dopant does not compete with the primary dopant in InSiZO thin films.

The Zn quantities in the films decrease as the Si or In concentrations increase, which suggests

Si/In replaces Zn. Therefore the transfer efficiencies of Zn also decrease as the Si/In concentrations increase. No more than ~ 1.6% of the Zn is transferred from starting precursor solutions to the resulting thin films, that is to say, ~ 98.4% of the Zn is lost during the whole synthesis process. The low transfer efficiencies indicate that the synthesis of thin films by using spray pyrolysis is relatively wasteful of starting materials. However, a similar loss of material is evident in vacuum processed films. [3-6]

The Si/In quantities in the films as a function of Si/In concentrations in the precursor solutions exhibit a linear relationship. However, their transfer efficiencies decrease as the Si/In concentrations increase. Similar to that of Zn, no more than ~ 0.3% of the Si is transferred from starting materials to films, and the value for IZO thin films is ~ 0.8%. The different transfer efficiencies between Si, In, and Zn show that different elements have different transfer efficiencies in the synthesis process by using spray pyrolysis.

This work shows that spray pyrolysis is a powerful method to deposit high-quality transparent conducting thin films. The easy control of film thicknesses and chemical compositions in the films indicate that the spray pyrolysis technique is a practical method which needs further optimisation, particularly in the loss of material to the spray pyrolysis chamber.

References

[1] Hickman, D. P., Maclean, S., Shepley, D. & Shaw, R. K. 2001. Inductively Coupled Plasma Mass Spectrometry Uranium Error Propagation. Washington, D.C: U.S. Department of Energy.

[2] Cheatham, M. M., Sangrey, W. F. & White, W. M. 1993. Sources of Error in External Calibration ICP-MS Analysis of Geological Samples and an Improved Non-Linear Drift Correction Procedure. *Spectrochimica Acta Part B: Atomic Spectroscopy,* 48**,** 487-506.

[3] Tuttle, J. R., Albin, D. S. & Noufi, R. 1991. Thoughts on the Microstructure of Polycrystalline Thin Film CuInSe2 and Its Impact on Material and Device Performance. *Solar Cells,* 30**,** 21-38.

[4] Bulgakov, A. V. & Bulgakova, N. M. 1995. Dynamics of Laser-Induced Plume Expansion into an Ambient Gas During Film Deposition. *Journal of Physics D: Applied Physics,* 28**,** 1710.

[5] Geohegan, D. B. 1992. Fast Intensified-CCD Photography of YBa2Cu3O7-x Laser Ablation in Vacuum and Ambient Oxygen. *Applied Physics Letters,* 60**,** 2732-2734.

[6] Izumi, H., Ohata, K., Sawada, T., Morishita, T. & Tanaka, S. 1991. Cumulative Laser Irradiation Effects on Ions in the Plume of YBa2Cu3O7-δ and Particulates at the Film Surface. *Applied Physics Letters,* 59**,** 2950-2952.

[7] Mallick, A. & Basak, D. 2018. Revisiting the Electrical and Optical Transmission Properties of Co-Doped ZnO Thin Films as n-Type TCOs. *Progress in Materials Science,* 96**,** 86-110.

Chapter 4

Electrical Properties

4.1 Introduction

Usually pure, polycrystalline ZnO thin films have limited intrinsic electrical properties. [1] Therefore polycrystalline ZnO thin films need to be doped with suitable impurity elements including group III, VII, and IV elements, among others to enhance their electrical properties. Extrinsic dopants play an important role in populating the conduction band of the host ZnO so that both the carrier concentration and the conductivity of ZnO are increased. Optimising both the electrical and optical properties in the ZnO material thin films is achieved by the careful control of the doping process. These doping elements are categorised into n-type and p-type. The most commonly researched dopants include group III, VII, and IV elements for n-type and group I or V for p-type conductivity. Effective doping is achieved when oxygen vacancies are created by achieving a charge balance after an addition of a cation with a charge other than 2+ for Zn^{2+} ions or an anion with a charge other than 2- for O^{2-} ions. The extrinsic dopants in group III are B, Al, Ga, and In, while the extrinsic dopants of group VII elements are halogens such as F, Cl, and Br. The extrinsic dopants in group IV are Si, Ge, and Sn.

4.1.1 Singly Doped Thin Films: SiZO

Recently ZnO has attracted interest as a transparent and conductive coating material because of its low cost for large-scale coating applications. [2-7] Group IV elements Si, Ge, and Sn can be used as indirect multi-electron donors as oxygen vacancies are created by achieving charge neutrality balance after the addition of a cation with a charge (4+ or higher) other than 2+ for Zn^{2+} ions in ZnO thin films. Clatot et al. [8] studied the optoelectronic properties of ZnO-based n-type TCOs as a function of cationic doping (Al, Ga, Si, Ge, and Sn). In the visible region, SiZO (3%) thin films exhibit a transmittance higher than 80% for a resistivity as low as 8×10^{-4} Ωcm when grown at 100 °C under 1.0 Pa oxygen pressure by using PLD. Minami et al. [9] first reported SiZO thin films by RF magnetron sputtering showing a group IV element can act as an effective dopant in ZnO thin films. A minimum resistivity of 3.8×10^{-4} Ωcm and a visible transmittance over 85% were obtained in SiZO thin films prepared

from a target of 2 wt% SiO_2 mixed with ZnO by using RF magnetron sputtering.

In this chapter, SiZO as one type of singly doped ZnO thin films fabricated using spray pyrolysis has been studied.

4.1.2 Singly Doped Thin Films: IZO

AZO, GZO and IZO have been widely studied for group III element doped ZnO. The limitations of impurity doping such as the doping position of impurity ions and the solid solubility limit in the host lattice are important in thin film deposition techniques. [10]

Highly transparent films with a low resistivity of the order of 10^{-4} Ωcm have been achieved for impurity doped ZnO thin films. The resistivity is generally lowered by doping with group III elements such as B, Al, Ga and In into ZnO thin films, and also that a more stable resistivity for use at a high temperature can be attained for these films in comparison with undoped ZnO thin films. [11-16] The group III impurity dopants such as B, Al, Ga, and In are proper donors when substituting Zn^{2+} ions in the ZnO lattice. [10] For these group III elements in ZnO, the electrons from the impurity states can be easily excited into the conduction band of ZnO. [17-19] Effective doping is achieved when oxygen vacancies are created by achieving charge balance after addition of a cation with a charge other than 2+ for Zn^{2+} ions. These doping effects are obtained from each group III element, and the dopant acts primarily as an effective indirect donor as the 'excess' electrons come from oxide ions being converted to molecular oxygen in ZnO. [9] Recently, IZO has been proposed for applications as TCOs due to its high electrical conductivity, high optical transparency in the visible region of 400 nm to 750 nm, smooth surface morphology, and easy low-cost deposition operation. [20-25]

A summary of the optical and electrical properties of reported IZO thin films is shown in **Table 4.1**. Lee at al. have studied the electrical properties of IZO thin films as a function of

annealing temperature deposited on polyethylene terephthalate (PET) substrates by RF magnetron sputtering. [26] The lowest resistivity value of 6.2×10^{-4} Ωcm for IZO films was obtained by annealing in an atmosphere of hydrogen and nitrogen mixture at 200 °C. Chen et al. have studied the electrical properties of In-N co-doped ZnO thin films as a function of In concentrations. [27] The best electrical properties with the resistivity of 16.1 Ωcm and Hall mobility of 1.13 cm^2 / Vs are obtained at an In concentration of 0.14 at%. Kim et al. got the lowest resistivity of 4×10^{-4} Ωcm for IZO thin films deposited at the substrate temperature 200 °C and 0% oxygen atmosphere. [28] Benouis et al. found the In doping effect on electrical properties showing that the film resistivity decreases significantly until the In doping concentration is 2%. [29] Quang et al. studied the In doping effect on single crystal ZnO thin films obtained by a low temperature hydrothermal synthesis method. The carrier concentration increases as the result of In doping and the best conductivity was achieved at IZO (2%) thin film. [30] Gomez et al. reported IZO thin films with the sheet resistance of 36 Ω / □ by using zinc acetate dissolved in methanol and 3% indium acetate deposited at 450 °C. [31] Lucio-Lopez et al. studied the electrical properties as a function of deposition conductions and the thickness dependence of IZO thin films. The lowest electrical resistivity of 3×10^{-3} Ωcm was reported for the films deposited at 475 °C with a 0.5 mol / L precursor solution. The electrical resistivity decreases as the film thickness increases and the lowest value is 2×10^{-3} Ωcm. [32, 33] Olvera et al. have studied the aspects of the spray pyrolysis technique to deposit ZnO thin films including doping, annealing, and thickness effects. It has been reported that In is easier to incorporate into the host lattice than Al or Ga according to the electrical resistivity of as-deposited IZO, AZO, and GZO thin films. By annealing IZO thin films, a lowest resistivity of ~ 10^{-3} Ωcm was obtained. [34]

Film	Resistivity (Ωcm)	Transparency (%)	Thickness (nm)	Deposition method	Reference
IZO	6.2×10^{-4}	80	300	RF magnetron sputtering	Lee at al. [26]
In-N co-doped ZnO	16.1	-	120 - 150	DC reactive magnetron sputtering	Chen et al. [27]
IZO	4×10^{-4}	-	-	RF magnetron sputtering	Kim et al. [28]
IZO	6×10^{-3}	90	550	Spray pyrolysis	Benouis et al. [29]
IZO	2×10^{-3}	85	600	Spray pyrolysis	Gomez et al. [31]
IZO	3×10^{-3}	85	550	Spray pyrolysis	Lucio-Lopez et al. [32]
IZO	2×10^{-3}	77	2900	Spray pyrolysis	Lucio-Lopez et al. [33]
IZO	$\sim 10^{-3}$	87	200 - 2400	Spray pyrolysis	Olvera et al. [34]

Table 4.1: A summary of optical and electrical properties of reported IZO thin films.

Benouis et al. studied the optical properties of IZO thin films as a function of In doping percentage deposited by spray pyrolysis. It has been reported that the increased band gap is due to the increased carrier concentration resulting in a Burstein-Moss effect. The reported optical transmittance is more than 90% with the absorption edge of 350 - 360 nm. [29] Ushiro et al. reported the optical properties of thin films as a function of the substrate temperature deposited from a $Zn_3In_2O_6$ polycrystalline target by RF sputtering. The optical band gap is 3.2 eV for the film deposited below 290 °C, and the optical band gap is 3.4 eV for the film deposited above 320 °C. [35] Chang et al. pointed out that the optical absorption edge shifts to a shorter wavelength as the film thickness decreased. The optical transmittance increases as the film thickness decreases. The film surface roughness decreases from 0.270 nm to 0.169 nm as the film thickness decreases. [36] Peng et al. reported the optical transmittance in the visible range, which is over 85% for 600 nm-thick films. The energy band gap increases as the carrier concentration increases. [37] Lucio-Lopez et al. reported that both the optical transmittance and the band gap (3.21 - 3.44 eV) decrease as the film thickness increases. [33]

Lee et al. reported the IZO thin films had a high transmittance from 500 nm to 1000 nm and a low reflectance from 500 nm to 800 nm. [24] Caglar et al. found that the width of the localised state in the optical band is affected by the dopants. In the low photon energy range, the Urbach rule is expressed as $\alpha = \alpha_0 \exp(h\nu / E_U)$ where α_0 is a constant, and E_U is the Urbach energy, which characterises the slope of the exponential edge. The Urbach energy of dopants decreases as the order of In, Al and Sn while the band gap values of the dopants are 3.285, 3.289 and 3.295 eV respectively. [38] Hammarberg et al. made IZO nanocrystals which have a transmittance of 79.7% in the visible region and a band gap of 3.27 eV by microwave-assisted heating. [39] Lee et al. reported a transmittance of 80 - 85% in the visible region for IZO thin films made by using a sol-gel method where zinc acetate dihydrate, indium nitrate trihydrate, 2-methoxyethanol, and monoethanolamine were used as the precursors. [40] Machado et al. reported the band gap energy of 3.27 eV - 3.42 eV for IZO thin films varied as a function of In concentration in the precursors by using a co-electrodeposition method. [41] Ramamoorthy et al. successfully made IZO thin films by PLD with the average transmittances of 87% - 95% which are better and comparable to the commercial ITO films made by PLD. [42]

In this chapter, IZO as one type of singly doped ZnO thin films has been fully studied.

4.1.3 Co-Doped Thin Films

If a cation is successfully doped into a ZnO lattice, the electrical conductivity increases as the concentration of free carrier electrons increases. The different ionic radii between a cation dopant and a Zn^{2+} ion will distort the host ZnO lattice and change the unit cell constant, as well as lowering the crystallinity of ZnO. The solubility limit of a dopant in a lattice determines the limit of carrier concentration and the electrical resistivity. A method called co-doping or double doping is used by adding a second cation or anion in addition to the primary cation. [43-46] Cation-anion co-doping increases the free carrier electron concentration by substituting Zn^{2+} ions with cations and O^{2-} ions with anions. Generally, both

cation-cation and cation-anion co-doping can increase the conductivity of doped ZnO compared with singly doped ZnO.

One cation-cation co-doping approach is to use Al in combination with In. AIZO thin films can be prepared by many different techniques including RF sputtering, DC magnetron sputtering, PLD, and spray pyrolysis. These polycrystalline thin films have a wurtzite ZnO structure with the (002) preferred orientation in most cases. [47-54] The unit cell volume decreases when Al is introduced into the ZnO but increases when In is added. This is due to the different ionic radii of ions (ionic radii of tetrahedral coordinated Zn^{2+} is 0.6 Å, ionic radii of four coordinated In^{3+} is 0.62 Å, and ionic radii of four coordinated Al^{3+} is 0.39 Å. [48, 55, 56]). The co-doped ZnO has a lower 2θ for the (002) peak than the undoped ZnO in XRD patterns showing an enhanced out-of-plane lattice parameter. [54] Bae et al. made amorphous AlZO thin films at low substrate temperatures showing a broad and weak peak at around 2θ = 31° in the XRD patterns. [49] IZO is amorphous if 55% or more In is doped into the lattice. [57, 58]

The electrical properties of co-doped and singly doped ZnO thin films deposited by RF sputtering are shown in **Figure 4.1** as reported by Kirby and Dover [48] There is a significant improvement in the conductivity for co-doped ZnO thin films compared to Al or In singly doped ZnO thin films. Element contents were determined by EDX. AIZO (4% Al-1% In) thin films have a conductivity of one order magnitude compared with AZO (4%) or IZO (1%) thin films. At meantime, AIZO (4% Al-1% In) thin films have a carrier concentration value of twice compared with AZO (4%) or IZO (1%) thin films, whereas their mobility increase by three times compared with AZO (4%) or IZO (1%) thin films. However, the carrier concentration decreases for heavily co-doped ZnO thin films when Al and In concentrations are more than 4% and 1%, respectively. I wished to see the performance of co-doping with Si and In using spray pyrolysis as opposed to RF sputtering and similar techniques, and to explore a wide range of dopant concentrations.

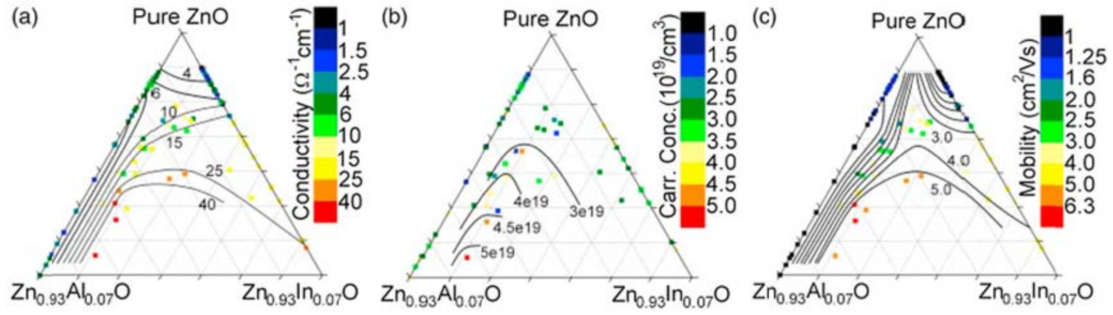

Figure 4.1: Electrical properties of $Zn_{1-x}Al_xO_y$ and $Zn_{1-x}In_xO_y$ thin films for various ZnO compositions. Conductivities, carrier concentrations, and mobilities are shown in diagram (a), (b), and (c), respectively. [10, 48] Reprinted from Kirby and Dover [48], with permission from Elsevier.

The electrical resistivity is given by the following relation. [59]

$$\sigma = \frac{1}{\rho} = ne\mu$$

Equation 4.1

Where σ is the electrical conductivity, ρ is the corresponding resistivity, n is the carrier concentration, e is the electron carrier charge, and μ is the carrier mobility. The electrical resistivity is inverse proportional to the carrier concentration and mobility. The mobility is restricted to as low as 1 cm^2 / Vs due to grain boundary scattering when the carrier concentration is less than 1×10^{20} cm^{-3}. Tohsophon et al. reported the lowest resistivity value of 7.9×10^{-4} Ωcm for AIZO thin films while Bae et al. reported the lowest resistivity value of 2.3×10^{-4} Ωcm for AIZO thin films. [47, 49] A thick film (509 nm) obtained by a wet chemical deposition method has the lowest resistivity value of 1.3×10^{-3} Ωcm. [53] It is obvious that the resistivity of AIZO thin films deposited by a wet chemical deposition method is about one order magnitude higher than those deposited by a sputtering method due to the oxygen rich film deposition conditions and fewer oxygen vacancies formed in the ZnO lattice. The films with improved conductivity can be obtained by annealing in argon at 350 °C due to the oxygen desorption from grain boundaries. [51] The AIZO thin film conductivity is generally dominated by the In concentration instead of the Al concentration. In other words, a

higher In concentration in the film has a higher conductivity, and vice versa. The Al concentration does not affect the film conductivity much if In is present in AIZO thin films. [49] The general visible transmittance of AIZO thin films is 80 - 85% and a lower visible transmittance of ~ 70% is observed for much thicker films. [52] Other novel cation-cation co-doping combinations include Al-B, Al-Ga, Al-Sn, and ln-Ga.

In this chapter, In-Si co-doping as one type of cation-cation co-doping ZnO thin films which has hitherto not been reported has now been fully studied.

4.2 Experimental

The correlation between optical and electrical properties is based on dielectric modelling. Electric susceptibility is a dimensionless proportionality constant relating the electric field in a material to the degree of polarisation. [60, 61] The free carrier electron conduction is described by Drude free electron model and represented by the equation below. [62, 63]

$$\chi(\omega) = \frac{\omega_p^2}{-\omega^2 + i\Gamma\omega}$$

Equation 4.2

Where $\chi(\omega)$ is the susceptibility generated by the Drude model, ω is the frequency, ω_p is the plasma frequency, and Γ is the damping constant (or the inverse of the relaxation time τ).

A Lorentz oscillator is used to model the band gap absorption as shown below. [64]

$$\chi_{Lor}(\omega) = \frac{\omega_{n,Lor}^2}{\omega_{0,Lor}^2 - \omega^2 + i\Gamma_{Lor}\omega}$$

Equation 4.3

Where $\chi_{Lor}(\omega)$ is the susceptibility generated by the Lorentz oscillator, ω is the frequency, $\omega_{n,Lor}$ is the Lorentz oscillator frequency, $\omega_{0,Lor}$ is the Lorentz resonant frequency, and Γ_{Lor} is the Lorentz damping constant.

The relative permittivity $\tilde{\varepsilon}(\omega)$ for a material due to both free electrons and band gap absorptions can be expressed as the following equation. [64]

$$\tilde{\varepsilon}(\omega) = \varepsilon_{\infty} + \frac{\omega_p^2}{-\omega^2 + i\Gamma\omega} + \frac{\omega_{n,Lor}^2}{\omega_{0,Lor}^2 - \omega^2 + i\Gamma_{Lor}\omega}$$

Equation 4.4

Where ε_{∞} is the high frequency dielectric constant of the material, and the other parameters have been explained as above.

However, the extended Drude model is used if the Drude damping constant is dependent on the incident light frequency. [65-67] The damping constant Γ(ω) varies from low frequencies to high frequencies and can be expressed as below. [68-70]

$$\Gamma(\omega) = \Gamma_{low} - \frac{\Gamma_{low} - \Gamma_{high}}{\pi}[\arctan(\frac{\omega - \Omega_{crossover}}{\Omega_{width}}) + \frac{\pi}{2}]$$

Equation 4.5

Where Γ_{low} and Γ_{high} are damping constants at low frequency (ω = 0) and high frequency (ω = ∞), respectively, $\Omega_{crossover}$ is the crossover frequency, Ω_{width} is the width of the function, and ω is the frequency.

The optical carrier concentration n_{opt} can be calculated from the Drude plasma frequency ω_p in the fitted model.

$$n_{opt} = \frac{m^* \varepsilon_0 \omega_p^2}{q^2}$$

Equation 4.6

Where q is the electron carrier charge, ε_0 is the permittivity of free space, and m* is the electron effective mass which is fixed as $0.3m_0$ for ZnO as reported from the literature. [68]

The optical mobility μ_{opt} is calculated from Drude damping constant $\Gamma(\omega_p)$ at the Drude plasma frequency ω_p.

$$\mu_{opt} = \frac{q}{m^* \Gamma(\omega_p)}$$

Equation 4.7

The dielectric modelling of optical spectra was simulated with the computer programme J.A. Woollam WVASE. The geometrical model and the 45° cross-section SEM image of a thin film used in the simulation process are shown in **Figure 4.2**. The model is based on three layers with the parameters of layer thickness and surface roughness. The glass substrate thickness is 0.17 mm, the TCO thin film thickness is calculated from the Swanepoel method, and the surface roughness is measured by AFM. These parameters, as well as those in **Equation 4.4** and **Equation 4.5**, are fitted with the experimental spectra to get best fitted values. Finally, the optical carrier concentration and optical mobility can be calculated from **Equation 4.6** and **Equation 4.7**, respectively.

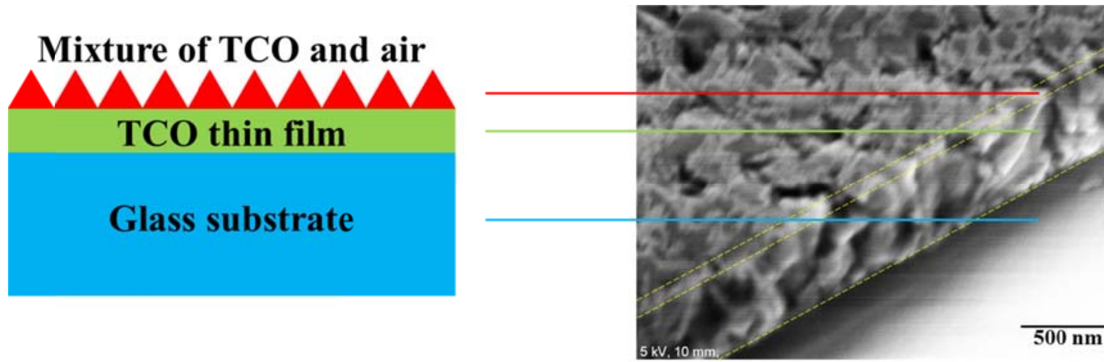

Figure 4.2: A thin film model for dielectric modelling.

4.3 Results and Discussion

4.3.1 Effect of Element Concentration

4.3.1.1 Singly Doped Thin Films: SiZO

The room temperature electrical properties of ZnO and SiZO thin films containing varying amounts of Si are shown in **Figure 4.3**. The Hall effect measurement of ZnO and SiZO thin films confirms that the variation tendency of the electrical resistivity with Si addition arises from the increase in the carrier concentration and carrier mobility. As the electrical resistivity is given by the relation as **Equation 4.1**, the electrical resistivity is inversely proportional to the carrier concentration and mobility. The carrier concentration and mobility increase to the maximum values when the Si concentration is 0.6% and then decrease as the Si concentration increases. The carrier concentration of SiZO thin films is more than ten times larger than undoped ZnO thin films, which suggests that Si acts as an n-type dopant to substitute Zn in the ZnO lattice to improve the conductivity. [71] The mobility or carrier electron transport ability can be affected by the film surface morphology observed in AFM and SEM as shown in **Chapter 6**. The best performance of SiZO thin films is made by doping 0.6% (i.e., $c_p = 3\%$) Si with a carrier concentration of 1.2×10^{20} cm^{-3}, a mobility of 8 cm^2 / Vs, and a resistivity of 7×10^{-3} Ωcm. It also has the visible transmittance of 86% corrected for the glass substrate as shown in **Chapter 5**. The increase in the resistivity and the decrease in the carrier concentration as more than 0.6% Si is doped indicate that adding more Si does not create yet

more free electrons and Si has reached the natural solid solubility limit as an n-type dopant in the ZnO lattice.

It can be confirmed by the investigations of lattice parameters in **Chapter 6**, which demonstrates a reduced unit cell volume for SiZO (0.6%) by the substitution of Zn^{2+} ions by smaller Si^{4+} ions and the expansion of the unit cell for heavily Si doped ZnO due to interstitial occupancy of Si in the lattice. The increased conductivity of doped ZnO thin films may also be contributed to the smoother surface morphology by doping with Si as shown in the AFM and SEM images. In addition to SiZO, IZO and InSiZO thin films also have the similar effect. At the same time, the increased oxygen vacancies introduced by the extrinsic Si doping are observed by XPS thus enhancing the conductivity of the films. The similar growth of oxygen vacancies is also shown in IZO thin films.

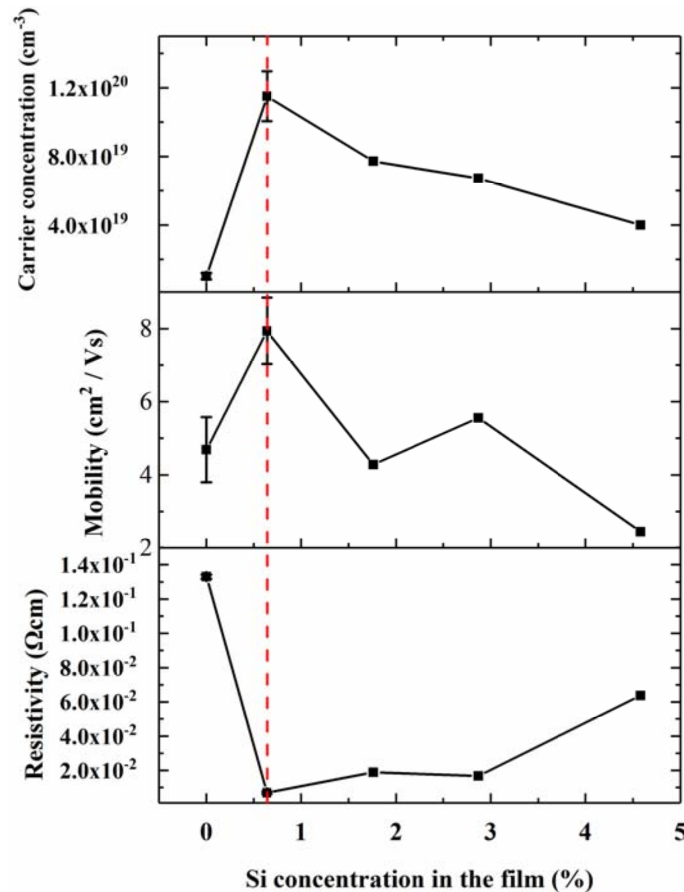

Figure 4.3: Electrical properties of ZnO and SiZO thin films containing varying amounts of Si.

The doping efficiency shows the ratio between the carrier concentration generated by the dopants in the film calculated from the Hall effect measurement and the dopant amount per volume in the film calculated from the ICP-MS data on the same film. The doping efficiency is calculated according to the following equation.

$$Doping\,efficiency = \frac{n - n_{undoped}}{a \times N_A \times N_{element} / V} \times 100\%$$

Equation 4.8

Where $N_{element}$ is the dopant quantity in the film calculated from the ICP-MS data, n is the carrier concentration in the film, $n_{undoped}$ is the carrier concentration of the undoped thin film, N_A is the Avogadro constant, V is the volume of the film, and a is the number of electrons generated by each dopant. The value of a is 2 or 1 when the dopant is Si or In, respectively.

The doping efficiencies and carrier concentrations of SiZO thin films containing varying amounts of Si are shown in **Figure 4.4**. The doping efficiency decreases as the Si concentration increases. All the doping efficiencies of SiZO thin films are less than 25% suggesting, importantly, that not all the dopants present in the film contribute two electrons per Si for electronic conduction, or part of these dopants present in the film is not contributing electrons to the conducting properties reflecting the fact that a certain amount of the dopants appear ‘electrically inactive’. However, I cannot distinguish these from the statistical results at present.

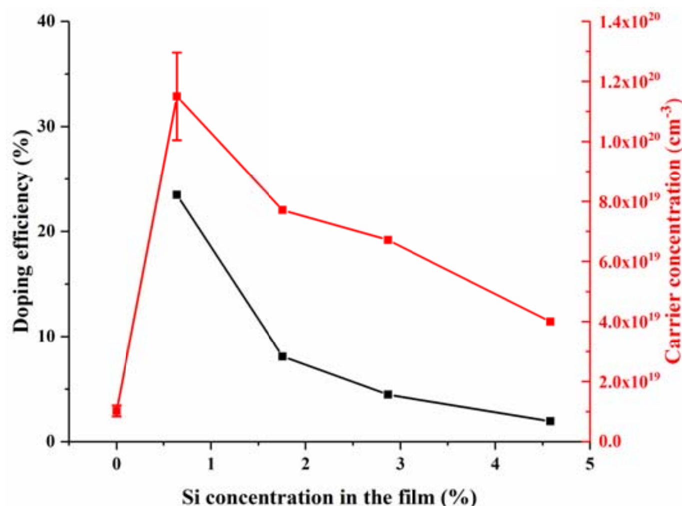

Figure 4.4: Doping efficiencies and carrier concentrations of SiZO thin films containing varying amounts of Si.

4.3.1.2 Singly Doped Thin Films: IZO

The room temperature electrical properties of ZnO and IZO films containing varying amounts of indium are shown in **Figure 4.5**. The relations among carrier concentrations, mobilities, and resistivities are similar to those of SiZO thin films as discussed before. The carrier concentration and mobility increase to the maximum values when the In concentration is 2 - 3% and then slightly decrease as the In concentration increases. The carrier concentration of IZO thin films is 10 - 30 times larger than ZnO thin films suggesting that In acts as an effective n-type dopant to substitute Zn in the ZnO lattice to produce extra free electrons for electronic conduction, and is more effective than Si. Similarly to SiZO thin films, the film surface roughness decreases significantly by doping In into ZnO and the smallest film surface roughness for IZO (3%) thin films is just one third compared to ZnO thin films as shown in **Chapter 6**. The best performance of IZO thin films is achieved by doping at 2 - 3% (i.e., c_p = 6 - 9%) In with a carrier concentration of 3.1×10^{20} cm^{-3}, a mobility of 15 cm^2 / Vs and a resistivity of 1.4×10^{-3} Ωcm. It obtains the visible transmittance of 80% corrected for the glass substrate as discussed in **Chapter 5**. The slight increase in resistivity and the slight decrease in carrier concentration beyond 3% In indicate, that adding more In cannot generate

more free electrons for conductivity and In has reached the solid solubility limit as an n-type dopant in the ZnO lattice. However, the turning point for IZO thin films is 3% which is larger than the value of 0.6% for SiZO thin films. It indicates that the solid solubility limit for In is much larger than Si, thus making In a better dopant than Si. Similar to SiZO thin films, the In incorporation is also consistent with the lattice parameters as shown in **Chapter 6** where a significant lattice expansion is observed as the In concentration increases which can be explained by the substitutional or the interstitial occupancy of larger In^{3+} ions compared with Zn^{2+} ions in the lattice.

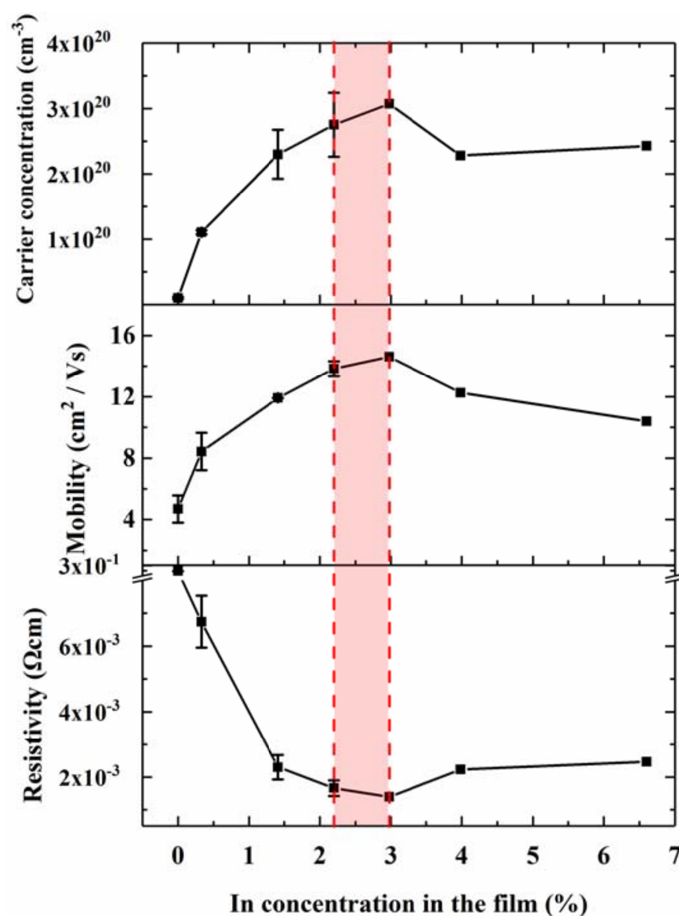

Figure 4.5: Electrical properties of ZnO and IZO thin films containing varying amounts of In.

According to **Equation 4.8**, the doping efficiencies and carrier concentrations of IZO thin films containing varying amounts of In are shown in **Figure 4.6**. Similarly to SiZO thin films, the doping efficiency decreases as the In concentration increases. However, the doping

efficiencies of In are 20 - 40%, which are higher than those (2 - 25%) of Si. It again suggests that In is a more effective dopant compared to Si.

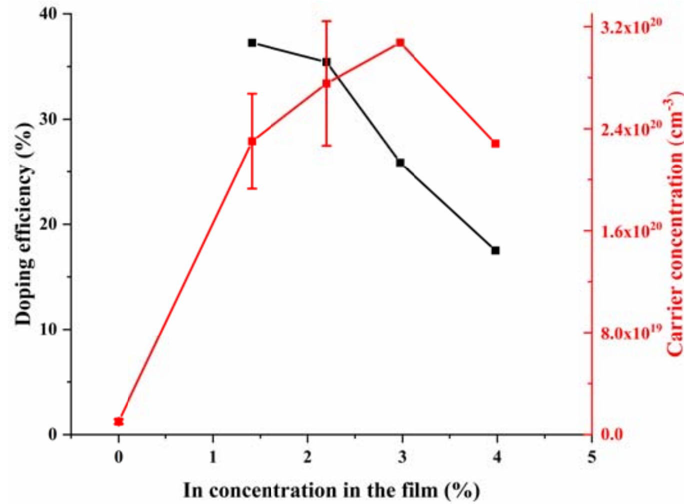

Figure 4.6: Doping efficiencies and carrier concentrations of IZO thin films containing varying amounts of In.

4.3.1.3 Co-Doped Thin Films: InSiZO

The room temperature electrical properties of InSiZO thin films containing varying amounts of In and a fixed value of 0.6% Si are shown in **Figure 4.7**. The carrier concentration and mobility increase to maximum values when the In concentration is 2% - 3% and then slightly decreases as the In concentration increases. The trend of the electrical properties is similar to those of IZO thin films. These findings indicate that the electrical properties of InSiZO thin films are generally dominated by the In concentrations. [49] The effects of Si concentration are discussed later. High In concentrations in the films give high conductivities while low In concentrations in films give low conductivities. There is a significant improvement in the conductivity for co-doped ZnO thin films compared with singly doped ZnO thin films when the In concentration is less than 2%. The conductivities of InSiZO (0.6% In-0.6% Si) thin films are more than twice as large as SiZO (0.6%) or IZO (0.3%) thin films. Moreover, InSiZO (0.6% In-0.6% Si) thin films have carrier concentration values of almost twice

compared to SiZO (0.6%) or IZO (0.3%) thin films, whereas their mobilities increase by almost twice compared to SiZO (0.6%) or IZO (0.3%) thin films. This suggests that the In acts as another n-type dopant in addition to Si to substitute Zn in the ZnO lattice to give extra free electrons for electronic conduction. The best performance of InSiZO thin films is achieved by doping 2% (i.e., c_p = 6%) In and 0.6% (i.e., c_p = 3%) Si with a carrier concentration of 2.6×10^{20} cm^{-3}, a mobility of 16 cm^2 / Vs, and a resistivity of 1.6×10^{-3} Ωcm. **Chapter 5** shows its visible transparency is 82% corrected for the glass substrate which is not lowered by co-doping compared with singly doped thin films. **Chapter 6** shows the lattice expansion of co-doped ZnO thin films due to the In incorporation which can be explained the same as IZO thin films and it is also consistent with the trend of electrical properties as discussed above.

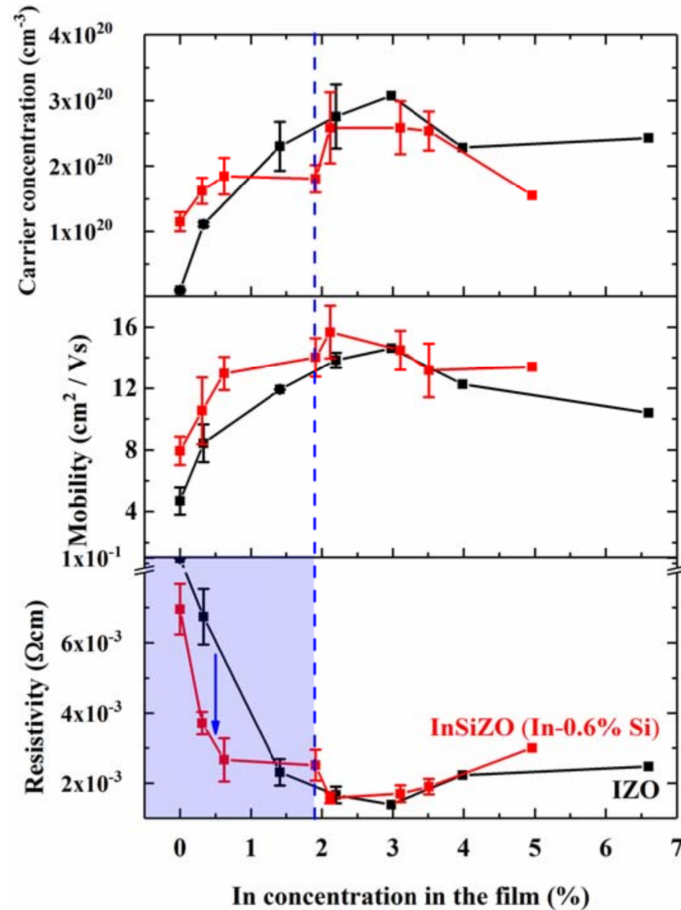

Figure 4.7: Electrical properties of InSiZO (red) thin films containing varying amounts of In and 0.6% Si. Electrical properties of IZO (black) thin films are plotted for comparisons. The blue area shows the superior performance of co-doped ZnO thin films.

Figure 4.8 shows the room temperature electrical properties of InSiZO thin films containing varying amounts of Si and 2% In. In theory, Si can act as another n-type dopant besides In to substitute Zn in the ZnO lattice to give out extra free electrons for electronic conduction. However, there is no improvement in electrical properties because the free electrons for conductivity have been saturated in InSiZO (2% In-Si) thin films and the second n-type dopant Si cannot provide extra free electrons for electronic conduction. The InSiZO (2% In-Si) thin films have conductivity values of more than 4 times compared to SiZO (0.6%) thin films, and meanwhile, their carrier concentrations and mobilities are more than twice compared to SiZO (0.6%) thin films. Co-doped thin films have advantages only at low doping levels. [49]

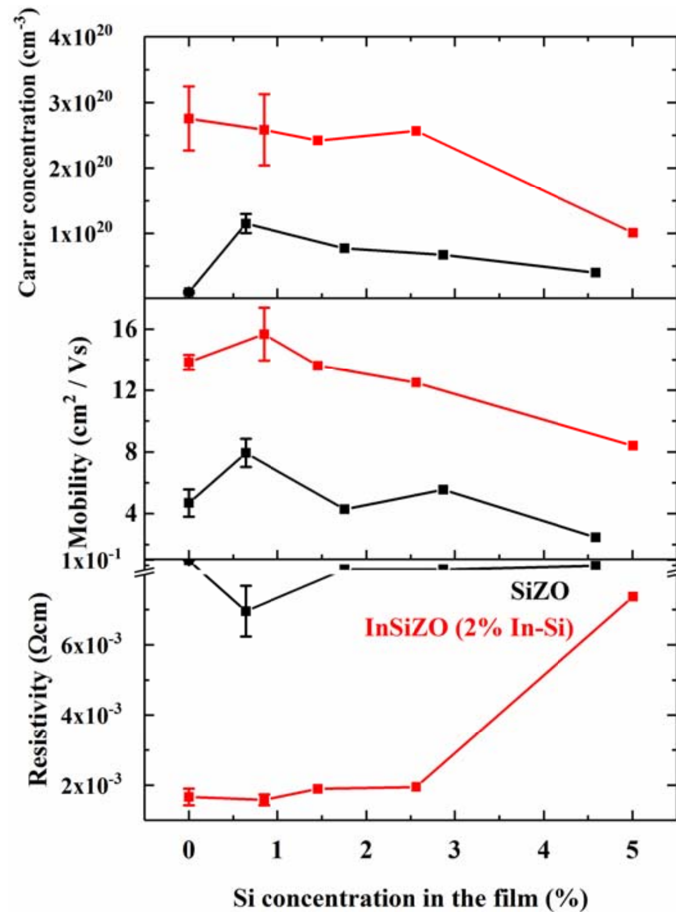

Figure 4.8: Electrical properties of InSiZO (red) thin films containing varying amounts of Si and 2% In. Electrical properties of SiZO (black) thin films are plotted for comparisons.

4.3.2 Effect of Film Thickness

The room temperature electrical properties of ZnO, SiZO (0.6%), and IZO (2%) thin films of various thicknesses are shown in **Figure 4.9**(a) - (c). Their carrier concentrations and mobilities increase as the film thicknesses increase; therefore, the resistivities decrease. However, the decrease of resistivities in IZO thin films is less significant than that in ZnO and SiZO thin films. What is more, the carrier concentrations of IZO thin films do not change much as a function of film thicknesses showing that IZO thin films have relatively high carrier concentrations even for very thin films. Their dominant factors in decreasing the resistivities are the increasing mobilities as a function of the film thicknesses.

Films with reduced thicknesses have smoother surfaces and smaller grain sizes as shown in the AFM and SEM images in **Chapter 6**. What is more, the TEM studies also show that the film structure is not the same and the elemental compositions are not uniform from the bottom to the top along the thickness direction within the film. These variations are consistent with the differences of electrical performance of the films.

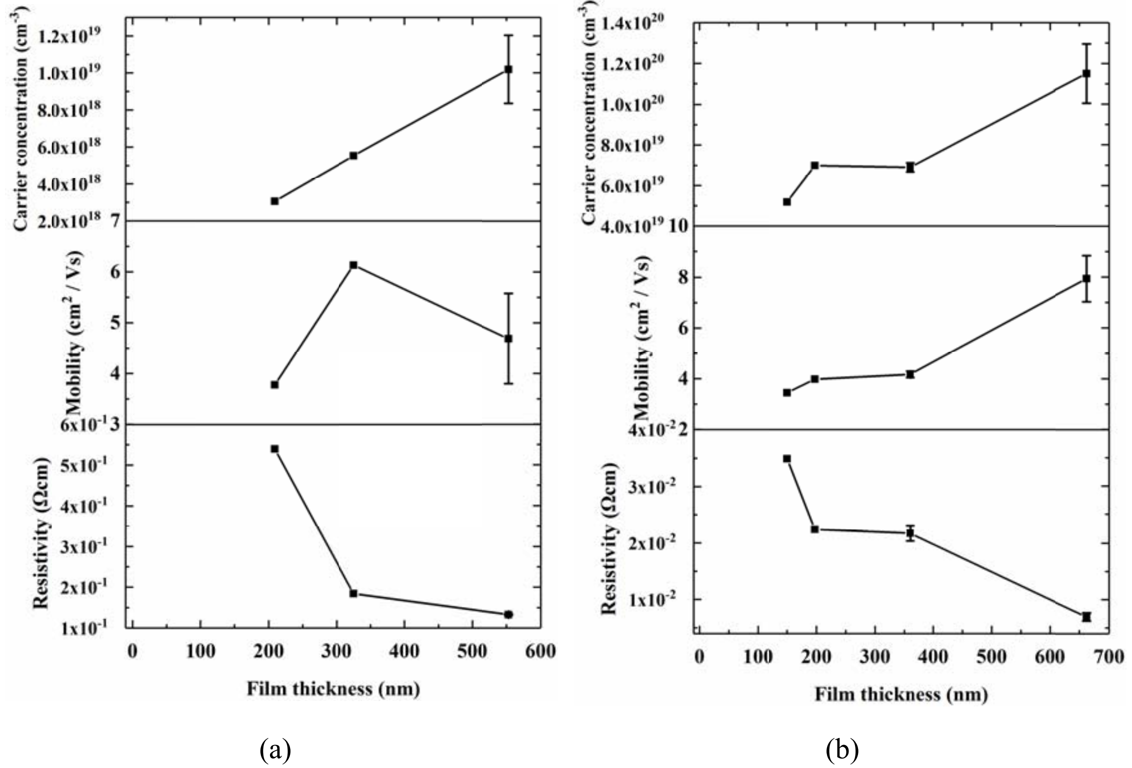

(a) (b)

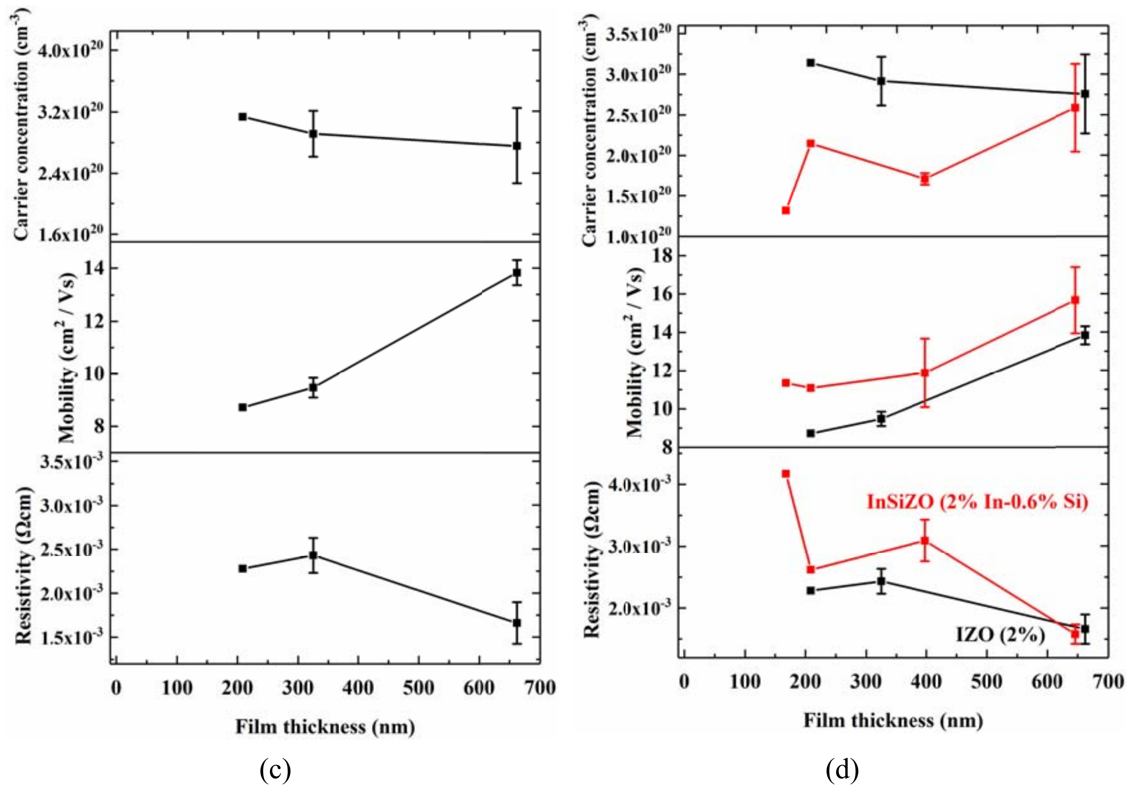

(c) (d)

Figure 4.9: Electrical properties of ZnO (a), SiZO (0.6%) (b), IZO (2%) (c), and InSiZO (2% In-0.6% Si) (d) thin films of various thicknesses.

The room temperature electrical properties of InSiZO thin films of various thicknesses are shown in **Figure 4.9**(d). The carrier concentrations, mobilities, and resistivities show similar trends as singly doped ZnO thin films. However, co-doping has no advantages over singly doping at small film thickness (< 600 nm), which is different from the comparisons of InSiZO and IZO thin films in **Figure 4.7**. As the mobilities of co-doped thin films are higher than singly doped thin films, the reason for the higher resistivities of InSiZO thin films is their smaller (almost one-half) carrier concentrations compared to IZO thin films.

4.4 Conclusions

Si and In are both suitable impurity elements to be doped into ZnO thin films and enhance the electrical properties of the semiconducting host ZnO. Effective doping is achieved when oxygen vacancies are created by achieving charge balance after the addition of a cation with a

charge other than 2+ for Zn^{2+} ions or an anion with a charge other than 2- for O^{2-} ions. Among our thin films deposited by the spray pyrolysis technique, the best performance of SiZO thin films is achieved by doping 0.6% (i.e., c_p = 3%) Si with a carrier concentration of 1.2×10^{20} cm^{-3}, a mobility of 8 cm^2 / Vs, and a resistivity of 7×10^{-3} Ωcm, and meanwhile, the best IZO thin films is made by doping 2 - 3% (i.e., c_p = 6 - 9%) In with a carrier concentration of 3.1×10^{20} cm^{-3}, a mobility of 15 cm^2 / Vs and a resistivity of 1.4×10^{-3} Ωcm. Importantly, they are comparable with most of the thin films deposited by vacuum techniques such as sputtering. However, the investigations on the electrical properties of SiZO and IZO thin films indicate that further additions of Si/In into ZnO thin films do not create more free electrons for electronic conduction and Si/In reaches a solid solubility limit as an n-type dopant in the ZnO lattice.

We can see the solubility limit of a dopant in a lattice is important in determining the limit in the carrier concentration and the electrical resistivity increase beyond a certain dopant concentration. In order to make the most of the dopant solubility limit, co-doping or double doping is used by adding a second cation to the primary cation or adding an anion into the primary doping cation. Therefore, co-doping can increase the free carrier electron concentration and conductivity. [72] In our case, Si and In are used for co-doping with comparisons with their singly doped ZnO thin films, which have not been much reported and fully studied before. The comparisons of co-doped and singly doped thin films show a significant improvement in the conductivity for co-doped ZnO thin films, which is observed for low dopant content, i.e., the In concentration is less than 2%. However, there is no significant improvement in electrical properties if beyond the doping level. It also indicates that the electrical properties of InSiZO thin films are generally dominated by the In concentrations, not the Si concentrations. [49]

As in the previous discussion, one of the advantages of the spray pyrolysis technique is the easy control of the film thickness by changing the precursor solution volume. The carrier concentrations and mobilities increase as the film thicknesses increase for singly and

co-doped ZnO thin films; therefore, the resistivities decrease. However, co-doping has no advantages over singly doping at small film thickness (< 600 nm). It suggests that the significant improvement in the conductivity for co-doped thin films is highly related to the film thickness. That is to say, co-doping is not always a better choice over singly doping in any case.

References

[1] Özgür, Ü., Alivov, Y. I., Liu, C., Teke, A., Reshchikov, M. A., Doğan, S., Avrutin, V., Cho, S. & Morkoç, H. 2005. A Comprehensive Review of ZnO Materials and Devices. *Journal of Applied Physics,* 98**,** 041301.

[2] Minami, T. 2008. Substitution of Transparent Conducting Oxide Thin Films for Indium Tin Oxide Transparent Electrode Applications. *Thin Solid Films,* 516**,** 1314-1321.

[3] Liu, Y., Li, Y. & Zeng, H. 2013. ZnO-Based Transparent Conductive Thin Films: Doping, Performance, and Processing. *Journal of Nanomaterials,* 2013**,** 9.

[4] Cheng, I. & Wagner, S. 2009. Overview of Flexible Electronics Technology. *In:* Wong, W. S. & Salleo, A. (eds.) *Flexible Electronics: Materials and Applications.* Boston, MA: Springer US.

[5] Shtereva, K., Tvarozek, V., Sutta, P., Kovac, J. & Novotny, I. 2009. Experimental Studies on Doped and Co-Doped ZnO Thin Films Prepared by RF Diode Sputtering. *Micro Electronic and Mechanical Systems.* London: InTech.

[6] Ginley, D. S. & Bright, C. 2011. Transparent Conducting Oxides. *MRS Bulletin,* 25**,** 15-18.

[7] Anderson, J. & Van de Walle, C. G. 2009. Fundamentals of Zinc Oxide as a Semiconductor. *Reports on Progress in Physics,* 72**,** 126501.

[8] Clatot, J., Campet, G., Jean, M., Nistor, M. & Rougier, A. 2011. Influence of Dopant Nature on the TCO Properties of ZnO:M (M=Al, Ga, Sn, Si, Ge) Thin Films. *MRS Proceedings,* 1328**,** mrss11-1328-h04-01.

[9] Tadatsugu, M., Hirotoshi, S., Hidehito, N. & Shinzo, T. 1986. Highly Conductive and Transparent Silicon Doped Zinc Oxide Thin Films Prepared by RF Magnetron Sputtering. *Japanese Journal of Applied Physics,* 25**,** L776.

[10] Mallick, A. & Basak, D. 2018. Revisiting the Electrical and Optical Transmission Properties of Co-Doped ZnO Thin Films as n-Type TCOs. *Progress in Materials Science,* 96**,** 86-110.

[11] Gordon, R. G. 2011. Criteria for Choosing Transparent Conductors. *MRS Bulletin,* 25**,** 52-57.

[12] Kim, S., Yoon, H., Kim, D. Y., Kim, S. & Leem, J. 2013. Optical Properties and Electrical Resistivity of Boron-Doped ZnO Thin Films Grown by Sol-Gel Dip-Coating Method. *Optical Materials,* 35**,** 2418-2424.

[13] Aragonès, A. C., Palacios-Padrós, A., Caballero-Briones, F. & Sanz, F. 2013. Study and Improvement of Aluminium Doped ZnO Thin Films: Limits and Advantages. *Electrochimica Acta,* 109**,** 117-124.

[14] Thambidurai, M., Kim, J. Y., Song, J., Ko, Y., Muthukumarasamy, N., Velauthapillai, D. & Lee, C. 2014. Nanocrystalline Ga-Doped ZnO Thin Films for Inverted Polymer Solar Cells. *Solar Energy,* 106**,** 95-101.

[15] Chen, K. J., Hung, F. Y., Chang, S. J. & Hu, Z. S. 2009. Microstructures, Optical and Electrical Properties of In-Doped ZnO Thin Films Prepared by Sol-Gel Method. *Applied Surface Science,* 255**,** 6308-6312.

[16] Minami, T., Sato, H., Sonohara, H., Takata, S., Miyata, T. & Fukuda, I. 1994.

Preparation of Milky Transparent Conducting ZnO Films with Textured Surface by Atmospheric Chemical Vapour Deposition Using Zn (C5H7O2)2. *Thin Solid Films,* 253, 14-19.

[17] Bel-Hadj-Tahar, R. & Mohamed, A. B. 2014. Sol-Gel Processed Indium-Doped Zinc Oxide Thin Films and Their Electrical and Optical Properties. *New Journal of Glass and Ceramics,* 4, 55-65.

[18] Lo, C., Hsu, C., Yu, Q., Lee, H. & Lee, C. 2002. Investigation of Transparent and Conductive Undoped Zn2In2O5-x Films Deposited on n-Type GaN Layers. *Journal of Applied Physics,* 92, 274-280.

[19] Zhang, X., Lee, H., Kwon, J., Kim, E. & Park, J. 2017. Low-Concentration Indium Doping in Solution-Processed Zinc Oxide Films for Thin-Film Transistors. *Materials,* 10, 880.

[20] Ramamoorthy, K., Kumar, K., Chandramohan, R. & Sankaranarayanan, K. 2006. Review on Material Properties of IZO Thin Films Useful as Epi-N-TCOs in Opto-Electronic (SIS Solar Cells, Polymeric LEDs) Devices. *Materials Science and Engineering: B,* 126, 1-15.

[21] Ito, N., Sato, Y., Song, P. K., Kaijio, A., Inoue, K. & Shigesato, Y. 2006. Electrical and Optical Properties of Amorphous Indium Zinc Oxide Films. *Thin Solid Films,* 496, 99-103.

[22] Jung, Y. S., Seo, J. Y., Lee, D. W. & Jeon, D. Y. 2003. Influence of DC Magnetron Sputtering Parameters on the Properties of Amorphous Indium Zinc Oxide Thin Film. *Thin Solid Films,* 445, 63-71.

[23] Naghavi, N., Rougier, A., Marcel, C., Guéry, C., Leriche, J. B. & Tarascon, J. M. 2000. Characterization of Indium Zinc Oxide Thin Films Prepared by Pulsed Laser Deposition Using a Zn3In2O6 Target. *Thin Solid Films,* 360, 233-240.

[24] Lee, W. J., Fang, Y. K., Ho, J. J., Chen, C. Y., Chiou, L. H., Wang, S. J., Dai, F., Hsieh, T., Tsai, R. Y., Huang, D. & Ho, F. C. 2002. Organic Light-Emitting Diode on Indium Zinc Oxide Film Prepared by Ion Assisted Deposition Dc Sputtering System. *Solid-State Electronics,* 46, 477-480.

[25] Hu, G., Kumar, B., Gong, H., Chor, E. F. & Wu, P. 2006. Transparent Indium Zinc Oxide Ohmic Contact to Phosphor-Doped n-Type Zinc Oxide. *Applied Physics Letters,* 88, 101901.

[26] Lee, C., Park, A., Cho, Y., Park, M., Lee, W. I. & Kim, H. W. 2008. Influence of ZnO Buffer Layer Thickness on the Electrical and Optical Properties of Indium Zinc Oxide Thin Films Deposited on PET Substrates. *Ceramics International,* 34, 1093-1096.

[27] Chen, L. L., Ye, Z. Z., Lu, J. G., He, H. P., Zhao, B. H., Zhu, L. P., Chu, P. K. & Shao, L. 2006. Co-Doping Effects and Electrical Transport in In-N Doped Zinc Oxide. *Chemical Physics Letters,* 432, 352-355.

[28] Kim, C. E., Soo Shin, H., Moon, P., Jae Kim, H. & Yun, I. 2009. Modeling of In2O3-10 wt% ZnO Thin Film Properties for Transparent Conductive Oxide Using Neural Networks. *Current Applied Physics,* 9, 1407-1410.

[29] Benouis, C. E., Benhaliliba, M., Sanchez Juarez, A., Aida, M. S., Chami, F. & Yakuphanoglu, F. 2010. The Effect of Indium Doping on Structural, Electrical Conductivity, Photoconductivity and Density of States Properties of ZnO Films.

Journal of Alloys and Compounds, 490**,** 62-67.
[30] Quang, L. H., Lim, S. K. & Goh, K. L. G. 2010. Structural and Electrical Properties of Single Crystal Indium Doped ZnO Films Synthesized by Low Temperature Solution Method. *Journal of Crystal Growth,* 312**,** 437-442.
[31] Gómez, H., Maldonado, A., Asomoza, R., Zironi, E. P., Cañetas-Ortega, J. & Palacios-Gómez, J. 1997. Characterization of Indium-Doped Zinc Oxide Films Deposited by Pyrolytic Spray with Different Indium Compounds as Dopants. *Thin Solid Films,* 293**,** 117-123.
[32] Lucio-López, M., Luna-Arias, M., Maldonado, A., Olvera, M. de la L. & Acosta, D. 2006. Preparation of Conducting and Transparent Indium-Doped ZnO Thin Films by Chemical Spray. *Solar Energy Materials and Solar Cells,* 90**,** 733-741.
[33] Lucio-López, M. A., Maldonado, A., Castanedo-Pérez, R., Torres-Delgado, G. & Olvera, M. de la L. 2006. Thickness Dependence of ZnO:In Thin Films Doped with Different Indium Compounds and Deposited by Chemical Spray. *Solar Energy Materials and Solar Cells,* 90**,** 2362-2376.
[34] Olvera, M. de la L., Gómez, H. & Maldonado, A. 2007. Doping, Vacuum Annealing, and Thickness Effect on the Physical Properties of Zinc Oxide Films Deposited by Spray Pyrolysis. *Solar Energy Materials and Solar Cells,* 91**,** 1449-1453.
[35] Ushiro, T., Tsuji, D., Fukushima, A., Moriga, T., Nakabayashi, I., Murayama, K. & Tominaga, K. 2001. Structural Variation of Thin Films Deposited from Zn3In2O6 Target by RF-Sputtering. *Materials Research Bulletin,* 36**,** 1075-1082.
[36] Chang, S.-C. & Shiao, M.-H. 2007. Smooth Indium Zinc Oxide Film Prepared by Sputtering a In2O3:ZnO=95:5 Target. *Microelectronics Journal,* 38**,** 1202-1206.
[37] Peng, L. P., Fang, L., Yang, X. F., Ruan, H. B., Li, Y. J., Huang, Q. L. & Kong, C. Y. 2009. Characteristics of ZnO:In Thin Films Prepared by RF Magnetron Sputtering. *Physica E: Low-dimensional Systems and Nanostructures,* 41**,** 1819-1823.
[38] Caglar, Y., Ilican, S., Caglar, M. & Yakuphanoglu, F. 2007. Effects of In, Al and Sn Dopants on the Structural and Optical Properties of ZnO Thin Films. *Spectrochimica Acta Part A: Molecular and Biomolecular Spectroscopy,* 67**,** 1113-1119.
[39] Hammarberg, E., Prodi-Schwab, A. & Feldmann, C. 2009. Microwave-Assisted Polyol Synthesis of Aluminium- and Indium-Doped ZnO Nanocrystals. *Journal of Colloid and Interface Science,* 334**,** 29-36.
[40] Lee, S. & Park, B. 2005. Electrical and Optical Properties of In2O3-ZnO Thin Films Prepared by Sol-Gel Method. *Thin Solid Films,* 484**,** 184-187.
[41] Machado, G., Guerra, D. N., Leinen, D., Ramos-Barrado, J. R., Marotti, R. E. & Dalchiele, E. A. 2005. Indium Doped Zinc Oxide Thin Films Obtained by Electrodeposition. *Thin Solid Films,* 490**,** 124-131.
[42] Ramamoorthy, K., Kumar, K., Chandramohan, R., Sankaranarayanan, K., Saravanan, R., Kityk, I. V. & Ramasamy, P. 2006. High Optical Quality IZO (In2Zn2O5) Thin Films by PLD - A Novel Development for III-V Opto-Electronic Devices. *Optics Communications,* 262**,** 91-96.
[43] Dutta, M., Ghosh, T. & Basak, D. 2009. N Doping and Al-N Co-Doping in Sol-Gel ZnO Films: Studies of Their Structural, Electrical, Optical, and Photoconductive Properties. *Journal of Electronic Materials,* 38**,** 2335-2342.

[44] Suja, M., Bashar, S. B., Morshed, M. M. & Liu, J. 2015. Realization of Cu-Doped p-Type ZnO Thin Films by Molecular Beam Epitaxy. *ACS Applied Materials & Interfaces,* 7**,** 8894-8899.

[45] Kim, K., Kim, H., Hwang, D., Lim, J. & Park, S. 2003. Realization of p-Type ZnO Thin Films via Phosphorus Doping and Thermal Activation of the Dopant. *Applied Physics Letters,* 83**,** 63-65.

[46] Kumar, M., Kim, T., Kim, S. & Lee, B. 2006. Growth of Epitaxial p-Type ZnO Thin Films by Codoping of Ga and N. *Applied Physics Letters,* 89**,** 112103.

[47] Tohsophon, T., Wattanasupinyo, N., Silskulsuk, B. & Sirikulrat, N. 2011. Effect of Aluminum and Indium Co-Doping on Zinc Oxide Films Prepared by DC Magnetron Sputtering. *Thin Solid Films,* 520**,** 726-729.

[48] Kirby, S. D. & van Dover, R. B. 2009. Improved conductivity of ZnO through codoping with In and Al. *Thin Solid Films,* 517**,** 1958-1960.

[49] Bae, J. H. & Kim, H. K. 2008. Characteristics of Al Doped ZnO Co-Sputtered InZnO Anode Films Prepared by Direct Current Magnetron Sputtering for Organic Light-Emitting Diodes. *Thin Solid Films,* 516**,** 7866-7870.

[50] Teehan, S., Efstathiadis, H. & Haldar, P. 2011. Enhanced Power Factor of Indium Co-Doped ZnO:Al Thin Films Deposited by RF Sputtering for High Temperature Thermoelectrics. *Journal of Alloys and Compounds,* 509**,** 1094-1098.

[51] Hadri, A., Taibi, M., hat, A. E. & Mzerd, A. 2016. Transparent and Conductive Al/F and in Co-Doped ZnO Thin Films Deposited by Spray Pyrolysis. *Journal of Physics: Conference Series,* 689**,** 012024.

[52] Jayaraman, V. K., Maldonado-Álvarez, A., Jimenez-Gonzalez, A. E. & Olvera-Amador, M. de la L. 2016. Influence of Precursor Ball Milling in Enhancing the Structural, Morphological, Optical and Electrical Properties of AIZO Thin Films. *Materials Letters,* 181**,** 52-55.

[53] Jayaraman, V. K., Álvarez, A. M., Kuwabara, Y. M., Koudriavstev, Y. & Olvera-Amador, M. de la L. 2016. Effect of Co-Doping Concentration on Structural, Morphological, Optical and Electrical Properties of Aluminium and Indium Co-Doped ZnO Thin Films Deposited by Ultrasonic Spray Pyrolysis. *Materials Science in Semiconductor Processing,* 47**,** 32-36.

[54] Nehra, K. S., Dhar, R. & Mohan, D. 2016. Synthesis and Characterization of Aluminium and Indium Co-Doped Zinc Oxide Thin Films Prepared by Pulsed Laser Deposition. *2016,* 4**,** 4.

[55] Shannon, R. D. 1976. Revised Effective Ionic Radii and Systematic Studies of Interatomic Distances in Halides and Chalcogenides. *Acta Crystallographica Section A,* 32**,** 751-767.

[56] Cullity, B. D. & Stock, S. R. 2014. *Elements of X-Ray Diffraction,* London, Pearson Education.

[57] Taylor, M. P., Readey, D. W., Teplin, C. W., Van Hest, M. F. A. M., Alleman, J. L., Dabney, M. S., Gedvilas, L. M., Keyes, B. M., To, B., Parilla, P. A., Perkins, J. D. & Ginley, D. S. 2004. Combinatorial Growth and Analysis of the Transparent Conducting Oxide ZnO/In (IZO). *Macromolecular Rapid Communications,* 25**,** 344-347.

[58] Taylor, M. P., Readey, D. W., Van Hest, M. F., Teplin, C. W., Alleman, J. L., Dabney, M. S., Gedvilas, L. M., Keyes, B. M., To, B. & Perkins, J. D. 2008. The Remarkable Thermal Stability of Amorphous In‐Zn‐O Transparent Conductors. *Advanced Functional Materials,* 18**,** 3169-3178.

[59] Neamen, D. A. 1997. *Semiconductor Physics and Devices,* New York, McGraw-Hill.

[60] Griffiths, D. J. 1999. *Introduction to Electrodynamics,* Upper Saddle River, N.J., Prentice Hall.

[61] Purcell, E. M. 1965. *Electricity and Magnetism,* New York, McGraw-Hill.

[62] Drude, P. 1900. Zur Elektronentheorie der Metalle. *Annalen der Physik,* 306**,** 566-613.

[63] Drude, P. 1900. Zur Elektronentheorie der Metalle; II. Teil. Galvanomagnetische und Thermomagnetische Effecte. *Annalen der Physik,* 308**,** 369-402.

[64] Tompkins, H. & Irene, E. A. 2005. *Handbook of Ellipsometry,* New York, William Andrew.

[65] Hamberg, I. & Granqvist, C. G. 1986. Evaporated Sn‐Doped In2O3 Films: Basic Optical Properties and Applications to Energy‐Efficient Windows. *Journal of Applied Physics,* 60**,** R123-R160.

[66] Ehrmann, N. & Reineke-Koch, R. 2010. Ellipsometric Studies on ZnO:Al Thin Films: Refinement of Dispersion Theories. *Thin Solid Films,* 519**,** 1475-1485.

[67] Pflug, A., Sittinger, V., Ruske, F., Szyszka, B. & Dittmar, G. 2004. Optical Characterization of Aluminum-Doped Zinc Oxide Films by Advanced Dispersion Theories. *Thin Solid Films,* 455-456**,** 201-206.

[68] Vai, A. T. 2015. *Performance Limitations in Practical Transparent Conducting Oxide Thin Films.* University of Oxford.

[69] Mergel, D. & Qiao, Z. 2002. Dielectric Modelling of Optical Spectra of Thin In2O3 : Sn Films. *Journal of Physics D: Applied Physics,* 35**,** 794.

[70] Solieman, A. & Aegerter, M. A. 2006. Modeling of Optical and Electrical Properties of In2O3:Sn Coatings Made by Various Techniques. *Thin Solid Films,* 502**,** 205-211.

[71] Wang, R., Sleight, A. W., Platzer, R. & Gardner, J. A. 1996. Nonstoichiometric Zinc Oxide and Indium-Doped Zinc Oxide: Electrical Conductivity and111In-TDPAC Studies. *Journal of Solid State Chemistry,* 122**,** 166-175.

[72] Zhang, J., Tse, K., Wong, M., Zhang, Y. & Zhu, J. 2016. A Brief Review of Co-Doping. *Frontiers of Physics,* 11**,** 117405.

Chapter 5

Optical Properties

5.1 Results and Discussion

5.1.1 Effect of Element Concentration

5.1.1.1 Singly Doped Thin Films: SiZO

The UV-Vis-NIR optical transmittance and reflectance spectra of ZnO and SiZO thin films ranging from 250 to 2500 nm containing varying amounts of Si are shown in **Figure 5.1**. Most of the films have a high transmittance of over 85% in the visible range (400 - 750 nm) of the spectra corrected for the glass substrate. The optical transmittance (> 83 % - 85%) of these spray pyrolysed SiZO, as well as IZO and InSiZO thin films discussed later, can compete with the doped ZnO thin films (> 80%) deposited by PLD as shown in **Table 1.1** in **Chapter 1.**

The dense interference fringes in the infrared region are due to the multiple reflections in the glass substrate. The thin films exhibit a decrease in the transmittance in the near-infrared region when the Si is doped into ZnO thin films. The decrease in the transmittance in the near-infrared region is associated with an increase in reflectance. [1] According to the plasma frequency dependence in **Equation 4.6**, a larger carrier concentration gives a higher plasma frequency thus leading to a higher reflectance in the near-infrared region. An increase in near-infrared reflectance occurs as the carrier concentration increases when the Si concentration increases to 0.6%. However, a decrease in the near-infrared reflectance occurs as the carrier concentration decreases for SiZO thin films with the Si concentration increases from 0.6% to 4.6%.

The absorption coefficient α in the near-infrared region is related to the carrier concentration n and the mobility μ, which can be expressed as below. [2, 3]

$$\alpha = \frac{Cn\lambda^2}{\mu}$$

Equation 5.1

Where C is a constant, and λ the wavelength of incident light. The increase in absorption coefficient is attributed to the increase in carrier concentration and the decrease in mobility, thus reducing the transmittance. This is shown in **Figure 5.1**.

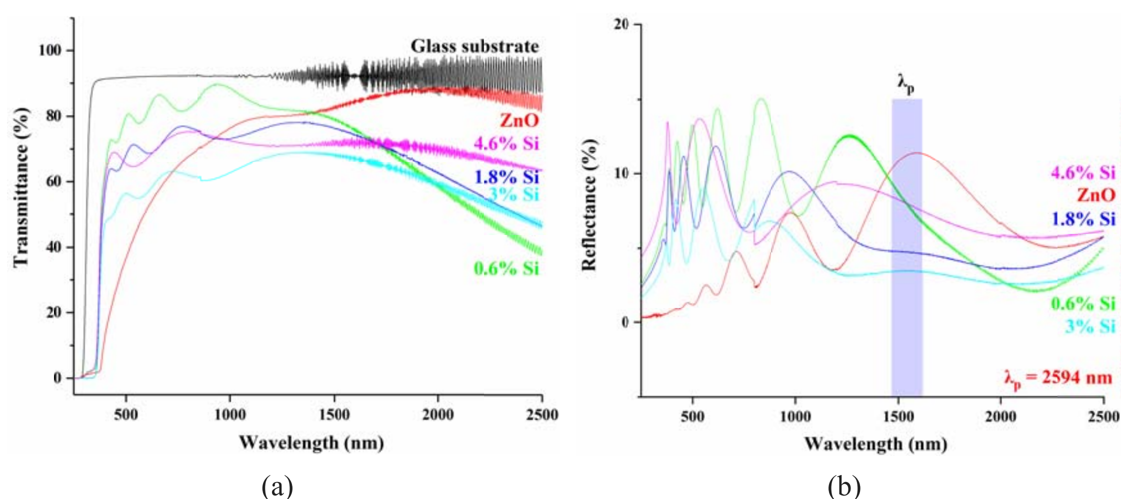

(a) (b)

Figure 5.1: UV-Vis-NIR optical transmittance (a) and reflectance (b) spectra of ZnO and SiZO thin films containing varying amounts of Si. The data is not corrected for the glass substrate to show the comparisons with the glass substrate. The plasma wavelengths λ_p calculated from the dielectric modelling of optical spectra are shown as the straight line and the area.

The graph of $(\alpha h\nu)^2$ as a function of photon energies and the graph of derived band gaps for ZnO and SiZO thin films containing varying amounts of Si are shown in **Figure 5.2**. A Burstein-Moss widening [4, 5] of the optical band gap (calculated by Tauc relation) occurs as the Si concentration increases to 0.6%. An increasing carrier concentration with the Si addition (as noted in **Chapter 4**) results in a blue shift of the plasma edge in the near-infrared and a widening of the optical band gap when the Si concentration is 0.6%. The film has the best electrical performance with a carrier concentration of 1.2×10^{20} cm^{-3}, a mobility of 8 cm^2 / Vs, and a resistivity of 7×10^{-3} Ωcm. The decreasing carrier concentration with the Si

addition results in a red shift of the plasma edge in the near-infrared and a narrowing of the optical band gap [6] when the Si concentration increases from 0.6% to 4.6% leading to a decrease in carrier concentration as discussed in **Chapter 4**. There is a significant absorption edge in the optical transmittance spectra at ~ 380 nm consistent with the intrinsic band gap (~ 3.2 eV) of ZnO (**Figure 5.1**).

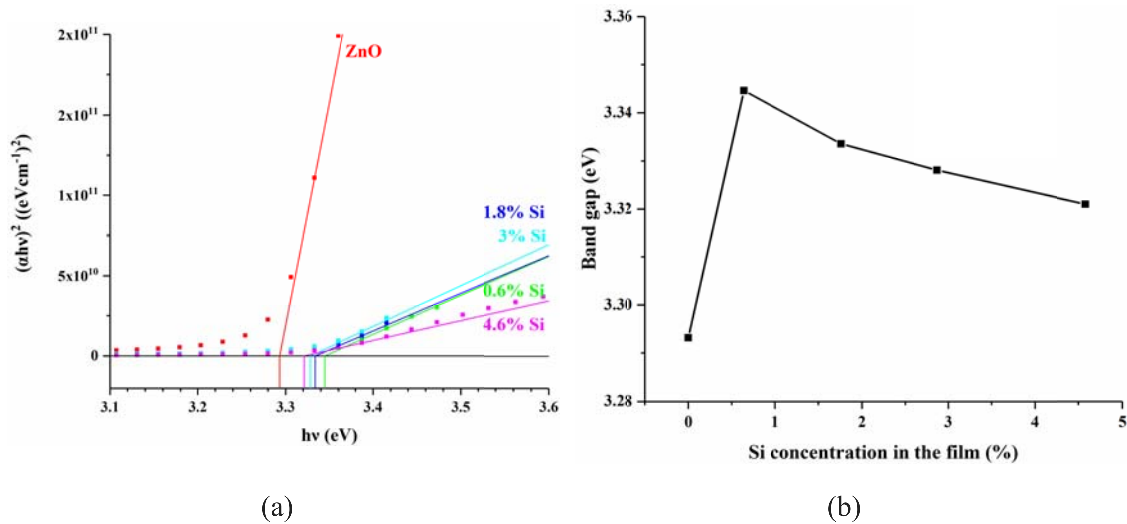

(a) (b)

Figure 5.2: Graph of $(\alpha h\nu)^2$ as a function of photon energies (a) and band gaps (b) for ZnO and SiZO thin films containing varying amounts of Si. It shows a maximum value of the band gap corresponding to the highest carrier concentration.

5.1.1.2 Singly Doped Thin Films: IZO

Figure 5.3 shows the UV-Vis-NIR optical transmittance and reflectance spectra of ZnO and IZO thin films containing varying amounts of In ranging from 250 to 2500 nm. Most of the films have a high transmittance of over 83% in the visible range of the spectra corrected for the glass substrate. Similarly to SiZO thin films, the thin films exhibit a decrease in transmittance in the near-infrared region when doped with In. A substantial increase in near-infrared reflectance occurs with increasing In to 2 - 3% as the carrier concentration increases, [1] where the carrier concentration is 3.1×10^{20} cm^{-3}, the mobility is 15 cm^2 / Vs and the resistivity is 1.4×10^{-3} Ωcm. Both the transmittance and the reflectance then keep as

constant values with the In concentration higher than 2 - 3% due to the In substitution limit in the ZnO lattice as no more free electrons are generated for electronic conduction which is consistent with the almost constant value of the carrier concentration as shown in **Chapter 4**.

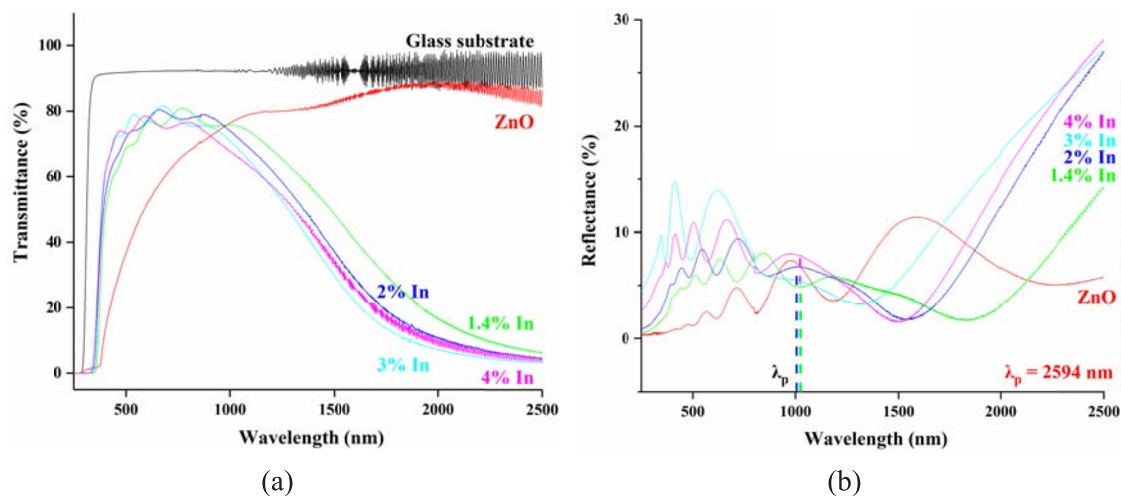

(a) (b)

Figure 5.3: UV-Vis-NIR optical transmittance (a) and reflectance (b) spectra of ZnO and IZO thin films containing varying amounts of In.

Figure 5.4 shows the graph of $(\alpha h\nu)^2$ as a function of photon energies and the graph of band gaps for ZnO and IZO thin films containing varying amounts of In. Similarly, a Burstein-Moss widening of the optical band gap occurs with increasing In to 3% as the carrier concentration increases. The increasing carrier concentration with In addition results in a blue shift of the plasma edge in the near-infrared and a widening of the optical band gap. However, not much additional increase in optical band gap occurs with the In concentrations higher than 3% and the carrier concentration actually decreases slightly.

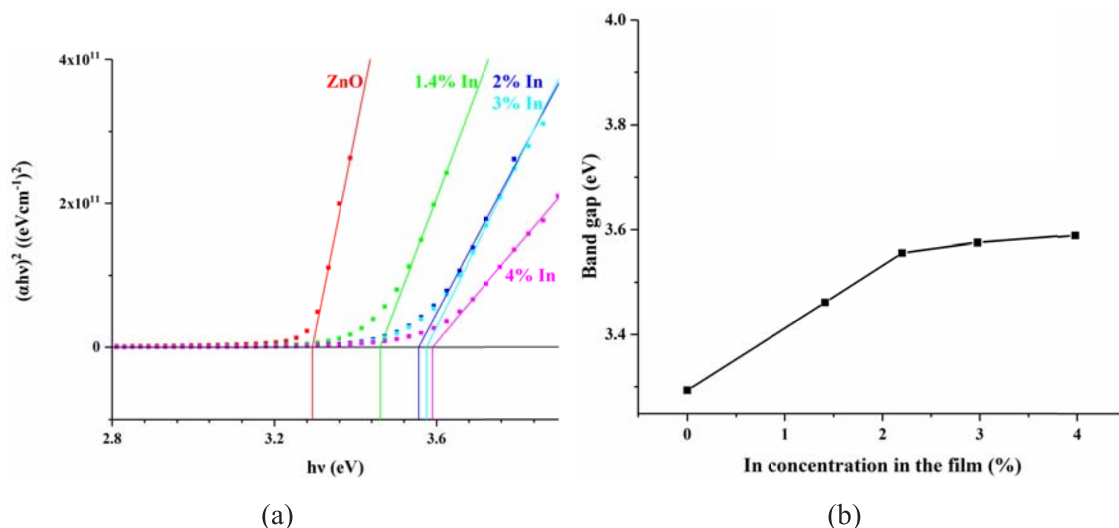

(a) (b)

Figure 5.4: Graph of $(\alpha h\nu)^2$ as a function of photon energies (a) and band gaps (b) for ZnO and IZO thin films containing varying amounts of In.

5.1.1.3 Co-Doped Thin Films: InSiZO

A high transmittance of over 83% is observed in most of the InSiZO (In-0.6% Si) thin films in the visible range of the spectra corrected for the glass substrate. (**Figure 5.5**) Similarly to IZO thin films, the transmittance decreases in the near-infrared region as In is doped into SiZO thin films and then keeps a constant value at the In concentration of 2 - 3.5%, whereas the near-infrared reflectance increases to the maximum value with the In increases to 2% - 3.5% as the carrier concentration increases. There is little change beyond this point and doping saturation has occurred.

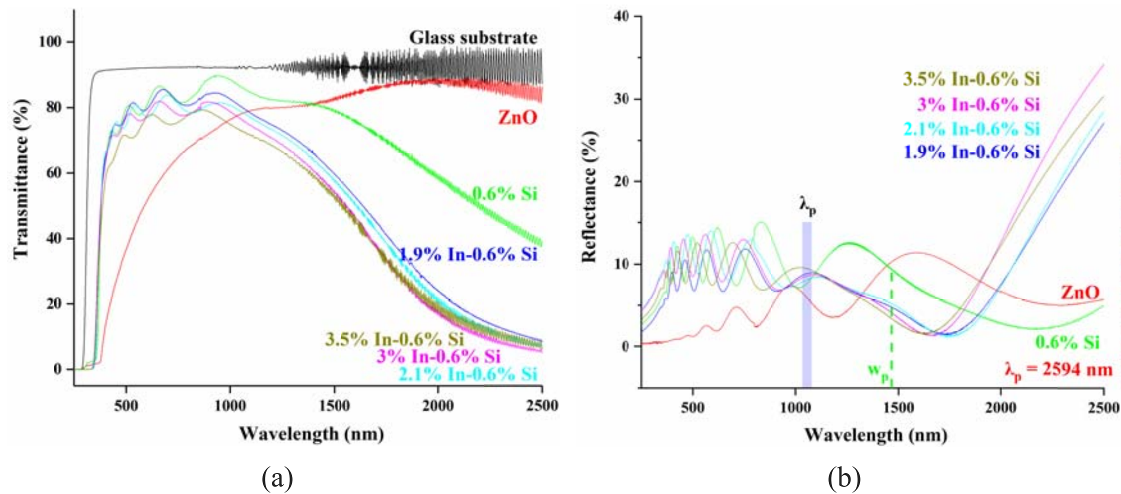

(a) (b)

Figure 5.5: UV-Vis-NIR optical transmittance (a) and reflectance (b) spectra of InSiZO thin films containing varying amounts of In and 0.6% Si.

Similarly, a Burstein-Moss widening of the optical band gap is observed as the In concentration increases, i.e., the carrier concentration increases. (**Figure 5.6**) The blue shift of the plasma edge in the near-infrared and the widening of the optical band gap for InSiZO thin films are due to the increasing carrier concentration. [7] The optical band gap maintains a constant value with the In concentration of 2% - 3.5%. As I have discussed in **Chapter 4** that the electrical properties of InSiZO thin films are generally dominated by the In concentrations. [8] A significant improvement in the conductivity for co-doped ZnO thin films compared with singly doped ZnO thin films is observed when the In concentration is less than 2%. The average visible transmittance does not become lower for InSiZO thin films compared to singly doped ZnO thin films, which suggests that the co-doping can enhance the conductivity with no negative effect on the visible transmittance at the low doping levels.

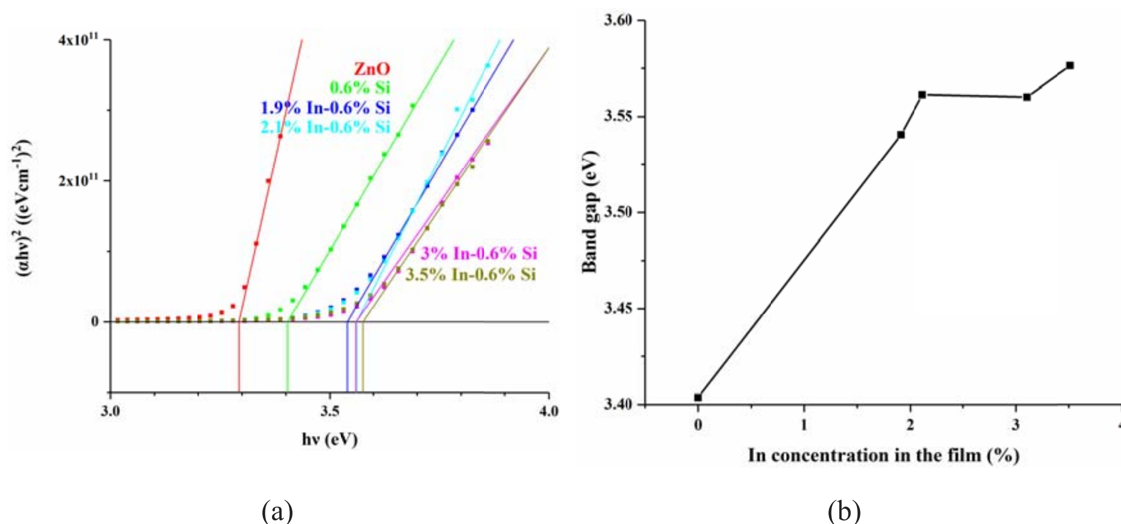

(a) (b)

Figure 5.6: Graph of $(\alpha h\nu)^2$ as a function of photon energies (a) and band gaps (b) for InSiZO thin films containing varying amounts of In and 0.6% Si.

As discussed in **Chapter 4**, the extra free electrons for electronic conduction should be generated due to the substitution of Zn with Si in the ZnO lattice, which acts as the second n-type dopant in addition to In. [9] However, the saturation of free electrons in InSiZO (2% In-Si) thin films limits the improvement of the conductivity. The decrease in the band gap with the addition of the second dopant Si is due to the decreasing carrier concentration. (**Figure 5.7** and **Figure 5.8**) It confirms that Si concentrations do not affect the optical properties much if In is present in InSiZO thin films and Si concentrations are not too high (< 5%). [8] However, there is a big drop off for high Si concentrations - just like SiZO, which indicate here that adding Si is quite different to adding In.

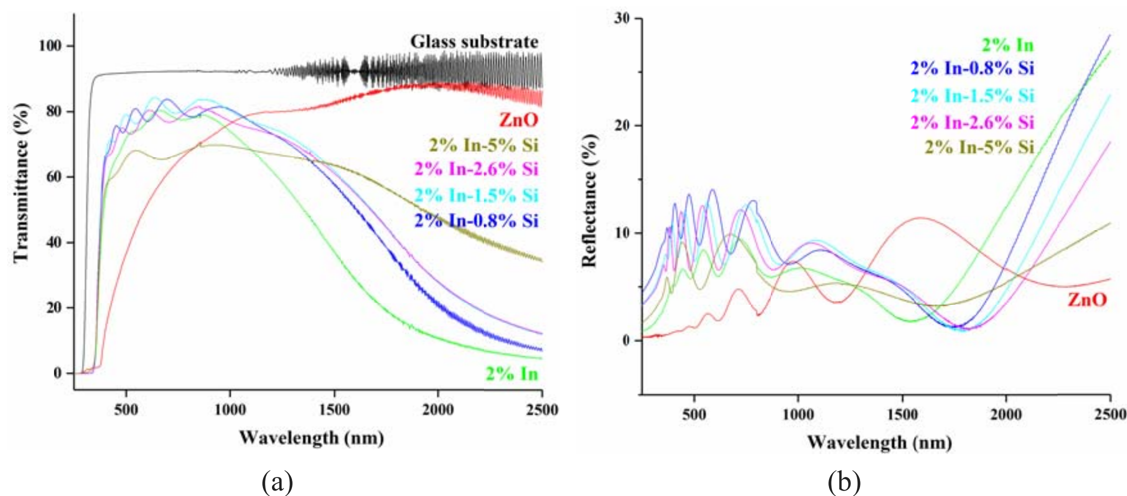

Figure 5.7: UV-Vis-NIR optical transmittance (a) and reflectance (b) spectra of InSiZO thin films containing varying amounts of Si and 2% In.

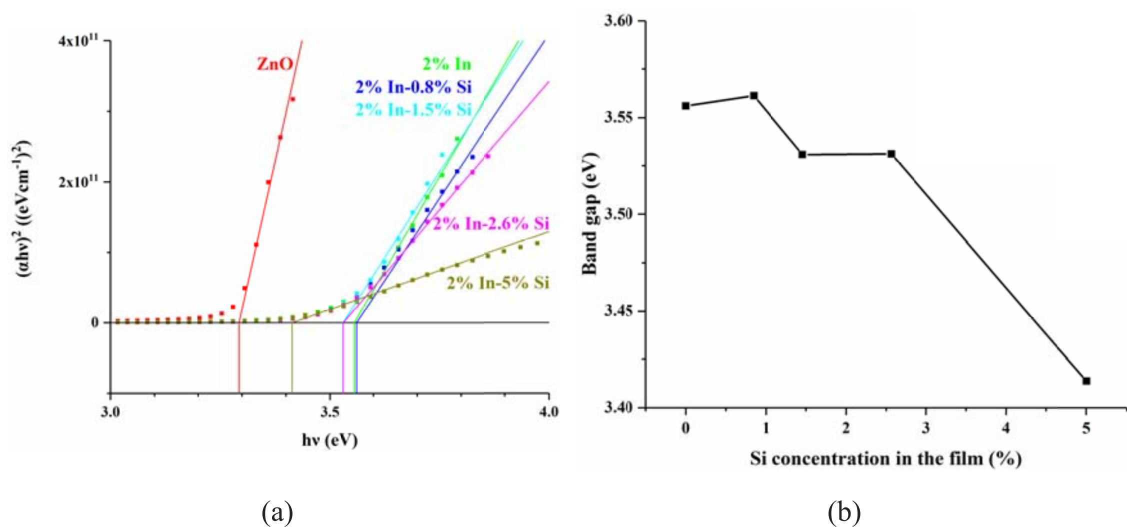

Figure 5.8: Graph of $(\alpha h\nu)^2$ as a function of photon energies (a) and band gaps (b) for InSiZO thin films containing varying amounts of Si and 2% In.

5.1.2 Effect of Film Thickness

5.1.2.1 Singly Doped Thin Films: SiZO

UV-Vis-NIR optical transmittance and reflectance spectra of ZnO thin films of various thicknesses ranging from 250 to 2500 nm are shown in **Figure 5.9**. Most of the films have a high visible transmittance of ~ 80% (especially 97% for very thin films) in the visible range

(400 - 750 nm) of the spectra corrected for the glass substrate (except for 550 nm-thick films). The thin films exhibit a decrease in transmittance in the near-infrared region when the film thickness increases. The decrease in transmittance as the film thickness increases can be explained by the Beer-Lambert Law. [10] The absorbance of light is enhanced as the light path length increases when the film thickness increases.

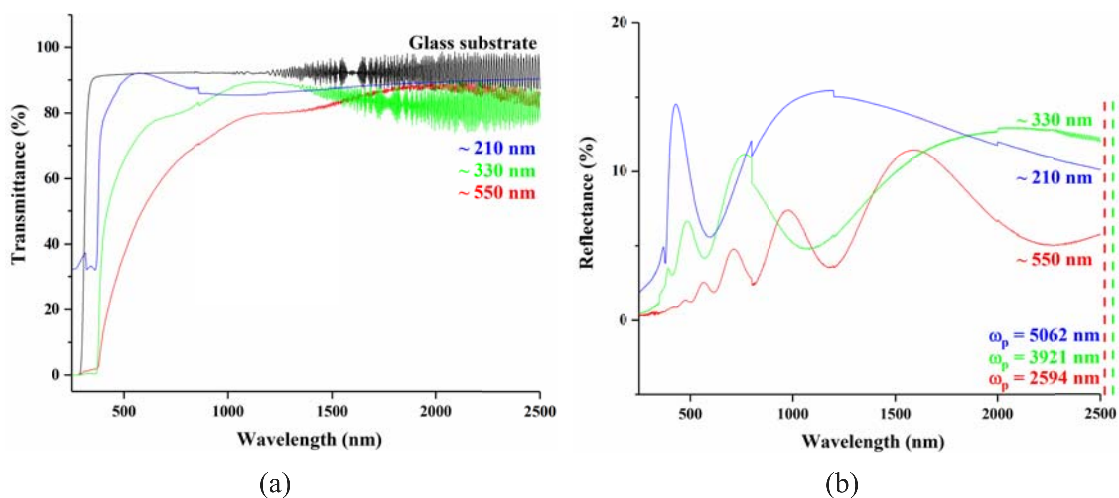

(a) (b)

Figure 5.9: UV-Vis-NIR optical transmittance (a) and reflectance (b) spectra of ZnO thin films of various thicknesses.

The graph of $(\alpha h\nu)^2$ as a function of photon energies for ZnO thin films of various thicknesses is shown in **Figure 5.10**(a). The decreasing film thickness results in a widening of the optical band gap in the range of 3.29 - 3.33 eV calculated from the Tauc relation (**Figure 5.10**(b)). The loss of the preferential orientation and stress relaxation induce the defects to absorb the light, thus reducing the transmittance in the ultraviolet region. [11] The increase of the optical band gap is attributed to the increasing density of defects. For the case of ZnO thin films, the defects are Zn in interstitial positions and oxygen vacancies. Gonçalves et al. [11] observed the contraction of lattice parameter c and the reduction of interatomic distances due to stress relaxation for thinner films. It makes electrons more tightly bound; therefore, the energy to excite electrons to conduction bands becomes higher. [12]

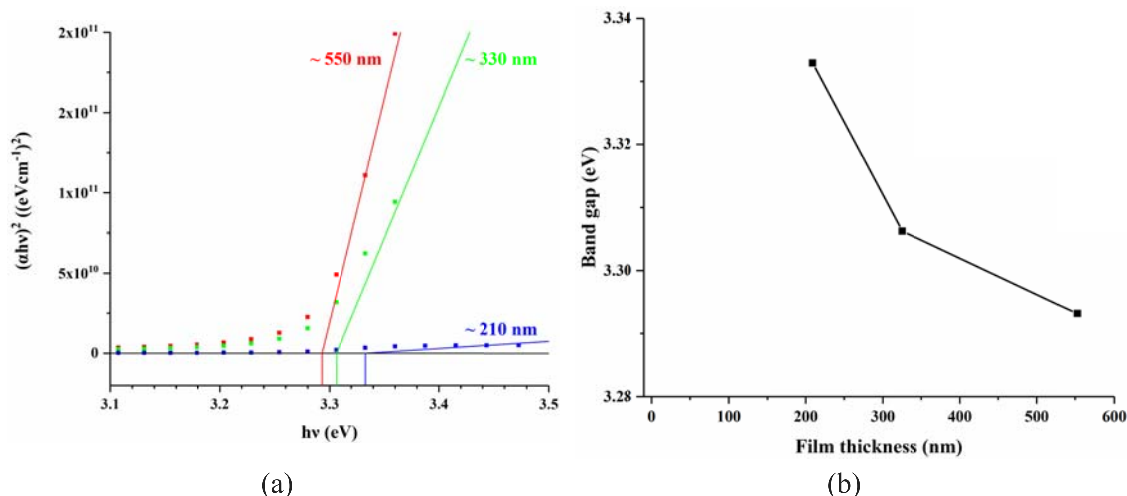

(a) (b)

Figure 5.10: Graph of $(\alpha h\nu)^2$ as a function of photon energies (a) and band gaps (b) for ZnO thin films of various thicknesses.

The majority of SiZO thin films of various thicknesses have a high visible transmittance of ~ 90% (especially 92% for very thin films) in the visible range corrected for the glass substrate. Similarly to ZnO thin films, a decrease in transmittance and an increase in reflectance in the near-infrared region are observed as the film thickness increases. A widening of the optical band gap also occurs in the range of 3.34 - 3.42 eV as the film thickness decreases. Please refer to the figures in **Appendix A5.1**. **Figure 5.11** shows an example of how reproducible the results are for the UV-Vis-NIR optical transmittance spectra of four identical SiZO (0.6%) thin films with the thickness of 197 nm. The average visible optical transmittance corrected for the glass substrate is in a narrow range of 90% - 92% thus showing good reproducibility.

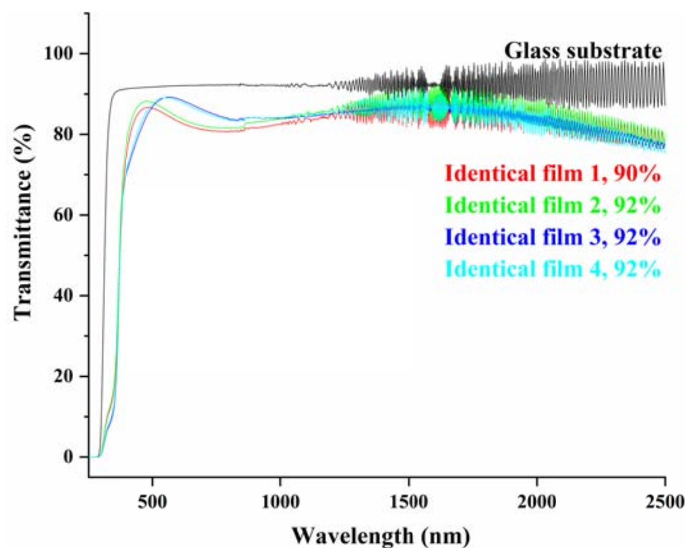

Figure 5.11: UV-Vis-NIR optical transmittance spectra of four identical SiZO (0.6%) thin films with the thickness of 197 nm showing the reproducibility. The average visible optical transmittance corrected for the glass substrate is also labeled.

Figure 5.12 shows the graph of band gaps and crystallite sizes of SiZO (0.6%) thin films of various thicknesses. The optical band gap increases as the crystallite size calculated from XRD decreases. Furthermore, the negative relationship between the optical band gap and the crystallite size may be attributed to the quantum confinement effect in nanocrystalline materials. [13] A classical model called effective mass approximation (EMA) [14] can be used to theoretically estimate the quantum confinement effect on the relationship between the optical band gap and the crystallite size. In all these thin films, the weak confinement regime for size calculation is used because the crystallite size is much larger than the exciton Bohr radius of bulk ZnO (~ 2.34 nm). [15] For the weak confinement regime for the size calculation, the electron and the hole are treated as a correlated pair. The quantisation of the exciton motion occurs while the dominant energy term is the Coulomb term. [16] The equation to express the quantum confinement effect in the weak confinement regime is described in **Equation 5.2**. [17, 18]

$$E = E_{bulk} + \frac{\hbar^2 \pi^2}{2R^2}\left(\frac{1}{m_e^*} + \frac{1}{m_h^*}\right)$$

Equation 5.2

Where E_{bulk} is the band gap of the bulk material, ħ is the reduced Planck constant equal to the Planck constant divided by 2π, m_e^* and m_h^* are the effective mass of the electron ($0.28m_0$) and the hole ($0.59m_0$), respectively for ZnO, and R is the crystallite size.

The crystallite size calculated from EMA is very small, which suggests that the various band gaps cannot be completely attributed to the quantum confinement effect alone. The local strain in the thin films may also contribute to the change in the optical band gap. [19] The optical band gap is corresponds to electronic transitions between the top of the valence band and the bottom of the conduction band. [20] The valence bands and the conduction bands for SiZO thin films are continuous. Kubo theory [18, 21] shows that the equation to calculate the nearest electronic level δ is as follows.

$$\delta = \frac{4}{3}\frac{E_F}{N} \propto \frac{1}{R^3}$$

Equation 5.3

Where E_F is the Fermi level, N is the total atoms, and R is the crystallite size.

The nearest electronic level δ increases as the crystallite size decreases. The larger separation of valence bands and conduction bands results in larger optical band gaps. As the crystallite size increases as the film thickness increases, the optical band gap decreases as the film thickness increases. Thinner films have larger optical band gaps and vice versa. In addition to the crystallite sizes calculated by EMA, the AFM and SEM images visualise the smaller grain sizes and smoother surfaces with decreased film thicknesses thus supporting the explanations of EMA and Kubo theory.

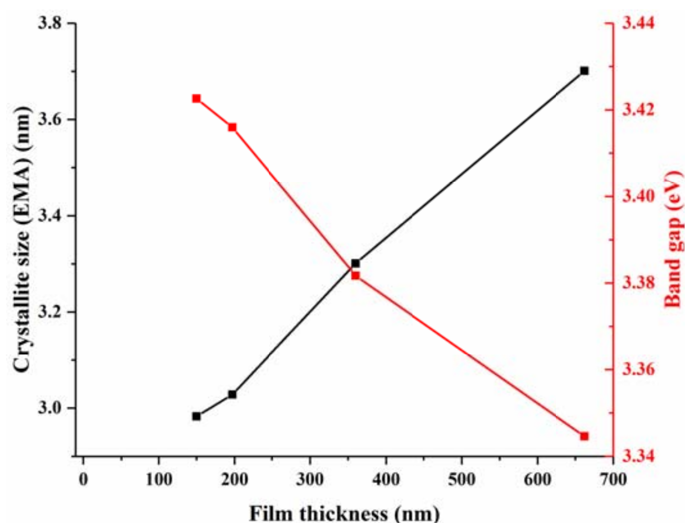

Figure 5.12: Graph of band gaps and crystallite sizes calculated from EMA of SiZO (0.6%) thin films of various thicknesses.

The graph of the average visible optical transmittance of ZnO and SiZO (0.6%) thin films of various thicknesses is shown in **Figure 5.13**. Smaller volumes of precursor solutions deposit thinner films thus improving the average visible optical transmittance of films. The highest average visible optical transmittance of ZnO thin films is 97% with the thickness of ~ 210 nm deposited using 2 mL of the precursor solution. The highest average visible optical transmittance of SiZO (0.6%) thin films is 92% with the thickness of ~ 200 nm deposited by using 2 mL of the precursor solution.

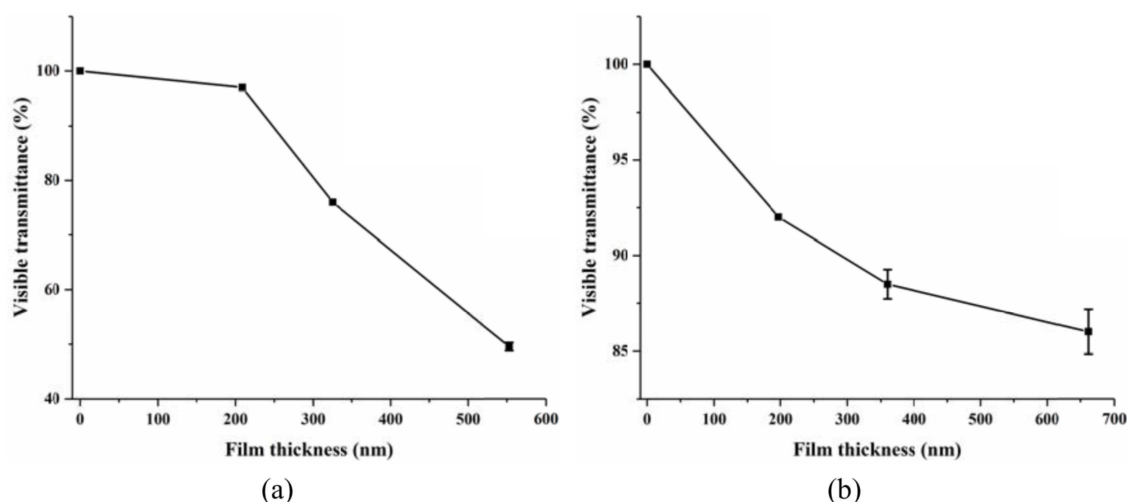

Figure 5.13: Average visible optical transmittance (400 - 750 nm) corrected for the glass substrate of ZnO (a) and SiZO (0.6%) (b) thin films of various thicknesses.

5.1.2.2 Singly Doped Thin Films: IZO

A high visible transmittance of over 80% (95% for very thin films) is observed for all IZO thin films of various thicknesses. The transmittance decreases and the reflectance increases as the film thickness increases more significantly for SiZO thin films. These variations are attributed to the increase in the free carrier concentration. The decrease in film thickness leads to an increase in optical band gap, which is similar to SiZO thin films.

Similarly, the crystallite size of IZO thin films increases as the film thickness increases, thus decreasing the optical band gap. These correlations can be explained by the EMA model [14] and Kubo theory [18, 21] as described in **Equation 5.2** and **Equation 5.3**, respectively.

The visible transmittance is improved by depositing thinner films using less precursor solution, which is the same as SiZO thin films. 2 mL of the precursor solution can deposit a ~ 210 nm-thick IZO (2%) film with a highest average visible optical transmittance of 95%. Please refer to the figures in **Appendix A5.2**.

5.1.2.3 Co-Doped Thin Films: InSiZO

A high visible transmittance of over 83% is observed for all InSiZO thin films of various thicknesses. The highest value is 95% for very thin films. The addition of the second dopant has no negative effect on the visible transmittance compared to singly doped thin films either for SiZO or IZO thin films (**Figure 5.14**). The transmittance decreases and the reflectance increases as the film thickness increases, which are similar to those of singly doped ZnO thin films. The reduced film thickness leads to an enlarged optical band gap, which is similar to IZO thin films. Similarly to the explanation for singly doped thin films by the EMA model [14] and Kubo theory [18, 21], the crystallite size of InSiZO thin films increases as the film thickness increases; therefore the optical band gap becomes narrow.

The improvement of the visible transmittance is due to the usage of smaller volumes of precursor solutions to make thinner films, which is the same case as SiZO and IZO thin films. A highest average visible optical transmittance of 95% is obtained by depositing a ~ 170 nm-thick InSiZO (2% In-0.6% Si) film with 2 mL of the precursor solution. Please refer to the figures in **Appendix A5.3**.

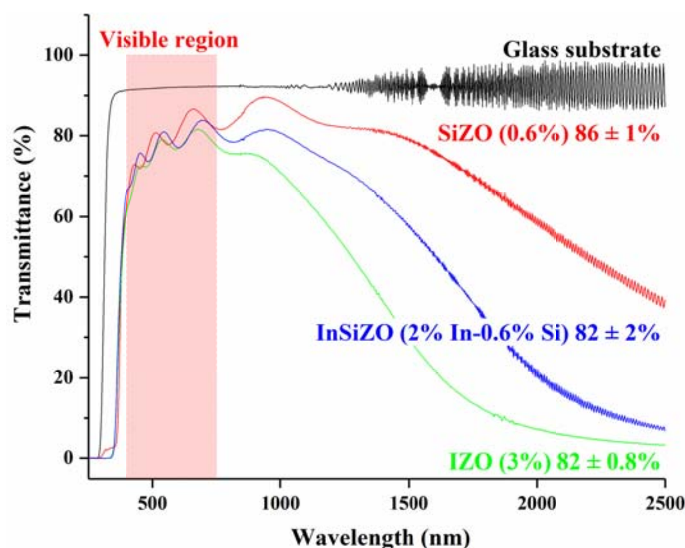

Figure 5.14: UV-Vis-NIR optical transmittance spectra of selected SiZO, IZO, and InSiZO thin films with the best electrical performance. Their average visible transmittances are labelled.

5.2 Conclusions

A high electrical conductivity and a good visible transmittance are two key properties for TCO thin films. In **Chapter 4**, I have found that Si and In are both suitable impurity elements to be doped into ZnO thin films to enhance their electrical properties. However, an acceptable visible transmittance determines whether the films are applicable for applications. The visible transmittance for the best SiZO thin films with a resistivity of 7×10^{-3} Ωcm is 86% corrected for the glass substrate. Meanwhile, the best IZO thin films have a resistivity of 1.4×10^{-3} Ωcm and a visible transmittance of 80% corrected for the glass substrate. Both of the conductivities and the transparencies are comparable with most of the thin films deposited by vacuum techniques such as sputtering. The optical investigations indicate that the decrease in the transmittance in the near-infrared region and the increase of the reflectance are determined by the carrier concentration. [1] The plasma frequency dependence equation suggests that a larger carrier concentration gives a higher plasma frequency thus leading to a higher reflectance in the near-infrared region. A Burstein-Moss shift occurs as the carrier concentration increases leading to a larger optical band gap. The carrier concentration is positively correlated with the dopant content leading to a decrease of the transmittance in the near-infrared region as well as an increasing band gap until reaching the solid solubility limit. However, the transmittance in the near-infrared region and the band gap moves the opposite way as the further dopant is added, which cannot create more free electrons for conductivity beyond the solubility limit.

The advantages of co-doping over singly doping on the electrical conductivity improvement have been discussed in **Chapter 4**. The best InSiZO thin films have a resistivity of 1.6×10^{-3} Ωcm and a visible transparency of 82% corrected for the glass substrate. In the dopant content limit region (In concentration < 2%) where the conductivity for co-doping is better than singly doping, the typical co-doped thin films InSiZO (0.6% In-0.6% Si) with a resistivity of 2.7×10^{-3} Ωcm have a visible transparency of 85% corrected by the substrate, which is not lower than the singly doped thin films. It shows that adding a second dopant to make

co-doped thin films has no negative effect on the visible transmittance.

The studies on the thickness dependence of optical properties indicate that it is possible to make TCO thin films with extremely high transparencies by using small volumes of the precursor solution. I can obtain ZnO thin films with a visible transparency of 97% corrected for the glass substrate. Both the decrease in transmittance and the increase in reflectance in the near-infrared region as the film thickness increases are due to the increase of the free carriers. The increase of the optical band gap is attributed to the increasing density of defects. The energy to excite electrons to conduction bands increases because of the tightly bound electrons attributed to the reduction of interatomic distances inside the lattice. [11, 12]

The EMA model is introduced to correlate optical band gaps and crystallite sizes. It shows that the various band gaps cannot be completely attributed to the quantum confinement effect alone. The local strain in the thin films may also attribute to the change of the optical band gap. [19] Kubo theory [18, 21] shows that the larger separation of valence and conduction bands results in larger optical band gaps. As the crystallite size increases as the film thickness increases, the optical band gap decreases as the film thickness increases.

References

[1] Dressel, M. & Scheffler, M. 2006. Verifying the Drude Response. *Annalen der Physik,* 15, 535-544.

[2] Singh, A. V., Mehra, R. M., Yoshida, A. & Wakahara, A. 2004. Doping Mechanism in Aluminum Doped Zinc Oxide Films. *Journal of Applied Physics,* 95, 3640-3643.

[3] Smith, R. A. 1978. *Semiconductors,* Cambridge, Cambridge University Press.

[4] Zeng, H., Cai, W., Hu, J., Duan, G., Liu, P. & Li, Y. 2006. Violet Photoluminescence from Shell Layer of Zn / ZnO Core-Shell Nanoparticles Induced by Laser Ablation. *Applied Physics Letters,* 88, 171910.

[5] Zeng, H., Duan, G., Li, Y., Yang, S., Xu, X. & Cai, W. 2010. Blue Luminescence of ZnO Nanoparticles Based on Non‐Equilibrium Processes: Defect Origins and Emission Controls. *Advanced Functional Materials,* 20, 561-572.

[6] Tauc, J. 1968. Optical Properties and Electronic Structure of Amorphous Ge and Si. *Materials Research Bulletin,* 3, 37-46.

[7] Zhou, X. H., Hu, Q. H. & Fu, Y. 2008. First-Principles LDA+U Studies of the In-Doped ZnO Transparent Conductive Oxide. *Journal of Applied Physics,* 104, 063703.

[8] Bae, J. H. & Kim, H. K. 2008. Characteristics of Al Doped ZnO Co-Sputtered InZnO Anode Films Prepared by Direct Current Magnetron Sputtering for Organic Light-Emitting Diodes. *Thin Solid Films,* 516, 7866-7870.

[9] Wu, H., Peng, Y. & Shen, T. 2012. Electronic and Optical Properties of Substitutional and Interstitial Si-Doped ZnO. *Materials,* 5, 2088.

[10] Calloway, D. 1997. Beer-Lambert Law. *Journal of Chemical Education,* 74, 744.

[11] Gonçalves, R. S., Barrozo, P., Brito, G. L., Viana, B. C. & Cunha, F. 2018. The Effect of Thickness on Optical, Structural and Growth Mechanism of ZnO Thin Film Prepared by Magnetron Sputtering. *Thin Solid Films,* 661, 40-45.

[12] Sun, Y., Thompson, S. E. & Nishida, T. 2007. Physics of Strain Effects in Semiconductors and Metal-Oxide-Semiconductor Field-Effect Transistors. *Journal of Applied Physics,* 101, 104503.

[13] Ramana, C. V., Vemuri, R. S., Fernandez, I. & Campbell, A. L. 2009. Size-Effects on the Optical Properties of Zirconium Oxide Thin Films. *Applied Physics Letters,* 95, 231905.

[14] Brus, L. E. 1984. Electron-Electron and Electron-Hole Interactions in Small Semiconductor Crystallites: The Size Dependence of the Lowest Excited Electronic State. *The Journal of Chemical Physics,* 80, 4403-4409.

[15] Lin, K., Cheng, H., Hsu, H., Lin, L. & Hsieh, W. 2005. Band Gap Variation of Size-Controlled ZnO Quantum Dots Synthesized by Sol-Gel Method. *Chemical Physics Letters,* 409, 208-211.

[16] Trwoga, P. F., Kenyon, A. J. & Pitt, C. W. 1998. Modeling the Contribution of Quantum Confinement to Luminescence from Silicon Nanoclusters. *Journal of Applied Physics,* 83, 3789-3794.

[17] Lee, E. J. H., Ribeiro, C., Giraldi, T. R., Longo, E., Leite, E. R. & Varela, J. A. 2004. Photoluminescence in Quantum-Confined SnO2 Nanocrystals: Evidence of Free

Exciton Decay. *Applied Physics Letters,* 84**,** 1745-1747.

[18] Wang, Y., Tang, W. & Zhang, L. 2015. Crystalline Size Effects on Texture Coefficient, Electrical and Optical Properties of Sputter-Deposited Ga-Doped ZnO Thin Films. *Journal of Materials Science & Technology,* 31**,** 175-181.

[19] Giri, P. K., Bhattacharyya, S., Singh, D. K., Kesavamoorthy, R., Panigrahi, B. K. & Nair, K. G. M. 2007. Correlation Between Microstructure and Optical Properties of ZnO Nanoparticles Synthesized by Ball Milling. *Journal of Applied Physics,* 102**,** 093515.

[20] Imai, Y. & Watanabe, A. 2004. Comparison of Electronic Structures of Doped ZnO by Various Impurity Elements Calculated by a First-Principle Pseudopotential Method. *Journal of Materials Science: Materials in Electronics,* 15**,** 743-749.

[21] Kubo, R. 1962. Electronic Properties of Metallic Fine Particles. I. *Journal of the Physical Society of Japan,* 17**,** 975-986.

Chapter 6

Structural Studies

6.1 XRD Studies

6.1.1 Effect of Element Concentration

6.1.1.1 Singly Doped Thin Films: SiZO

Figure 6.1 shows the XRD patterns of ZnO and SiZO thin films containing varying amounts of Si. The XRD patterns only show peaks consistent with the wurtzite ZnO structure with no evidence for other phases such as SiO_2 or Zn_2SiO_4. Undoped ZnO and all SiZO thin films have the highest peak intensities for the (002) peaks which mean a (002) preferred plane orientation with the c axis perpendicular to the surface of the substrate.

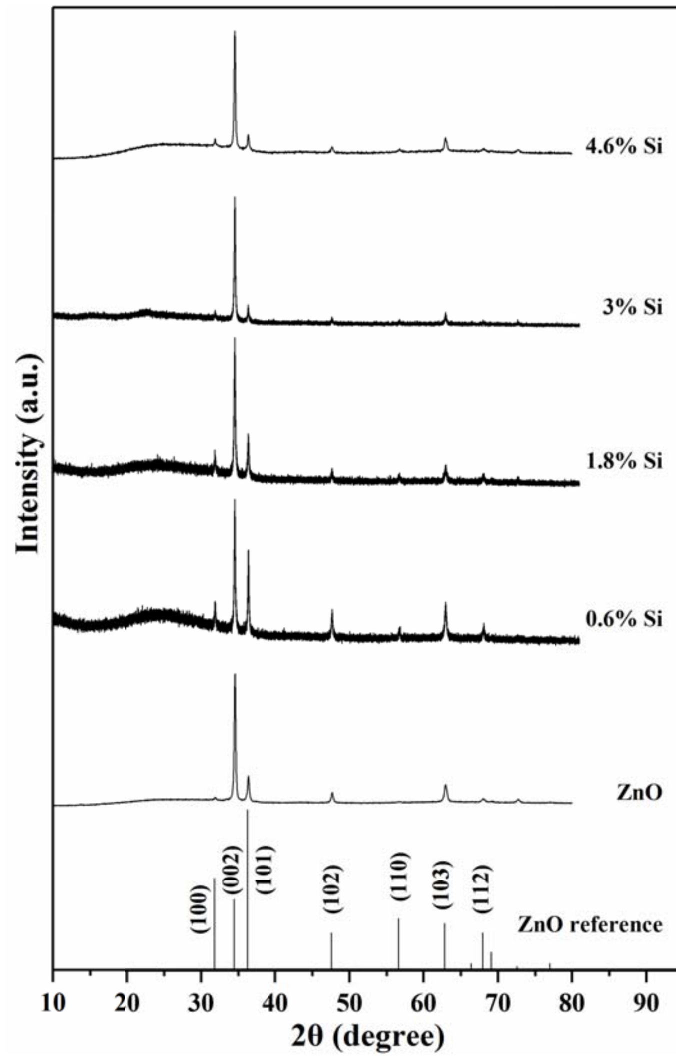

Figure 6.1: XRD patterns of ZnO and SiZO thin films containing varying amounts of Si.

The texture coefficient shows the texture of a specific plane and a preferred film growth direction. The texture coefficient of the (hkl) plane is calculated from the XRD data according to the following equation. [1]

$$TC_{(hkl)} = \frac{I_{(hkl)} / I_{0(hkl)}}{(1/N)[\sum_N I_{(hkl)} / I_{0(hkl)}]}$$

Equation 6.1

Where $TC_{(hkl)}$ is the texture coefficient of the (hkl) plane, $I_{(hkl)}$ is the intensity of the (hkl) diffraction peak in the XRD patterns, $I_{0(hkl)}$ is the intensity of (hkl) plane on a randomly

oriented bulk taken from a PDF card, and N is the number of diffractions taken into analysis. The (100), (002), and (101) XRD reflections are the three main XRD peaks for the preferred orientation analysis. In our XRD analysis, a series of texture coefficient equations deduced from the above equation is showing as follows.

$$TC_{(100)} = \frac{I_{(100)}}{I_{(100)} + I_{(002)} + I_{(101)}}$$

$$TC_{(002)} = \frac{I_{(002)}}{I_{(100)} + I_{(002)} + I_{(101)}}$$

$$TC_{(101)} = \frac{I_{(101)}}{I_{(100)} + I_{(002)} + I_{(101)}}$$

Equation 6.2

Where $TC_{(100)}$, $TC_{(002)}$, and $TC_{(101)}$ are the texture coefficients of the (100), (002), and (101) XRD reflections. $I_{(100)}$, $I_{(002)}$, and $I_{(101)}$ are the intensities of the (100), (002), and (101) XRD reflections, respectively. A higher value of TC (maximum value = 1) means that a film has a higher degree of orientation along a specific plane.

The texture coefficients of the (100), (002), and (101) XRD reflections for ZnO and SiZO thin films as a function of Si concentration are shown in **Figure 6.2**. The high $TC_{(002)}$ value confirms the domination of the (002) preferred orientation in all the series of SiZO thin films. The $TC_{(100)}$ value is very small across all the series of SiZO thin films, which shows relatively little (100) orientation. The obvious $TC_{(101)}$ value means most of the SiZO thin films have a (002) preferred orientation with some (101) character. The preferred orientation depends on the balance between the kinetic and thermodynamic processes involved in the film deposition. The texture is mainly affected by the minimisation of surface free energy which depends on the hybridisation of the atoms in the films. [2-6] Hexagonal wurtzite ZnO has a tetrahedral coordination of Zn with sp^3 hybridised orbitals. The (002) plane has a minimum surface free energy in a hexagonal structure for sp^3 hybridised orbitals. [7] Similarly, the (111) plane has a minimum surface free energy in a cubic structure for sp^3 hybridised orbitals. This is why the

(002) plane is preferred for the growth of undoped ZnO and all SiZO thin films. [8]

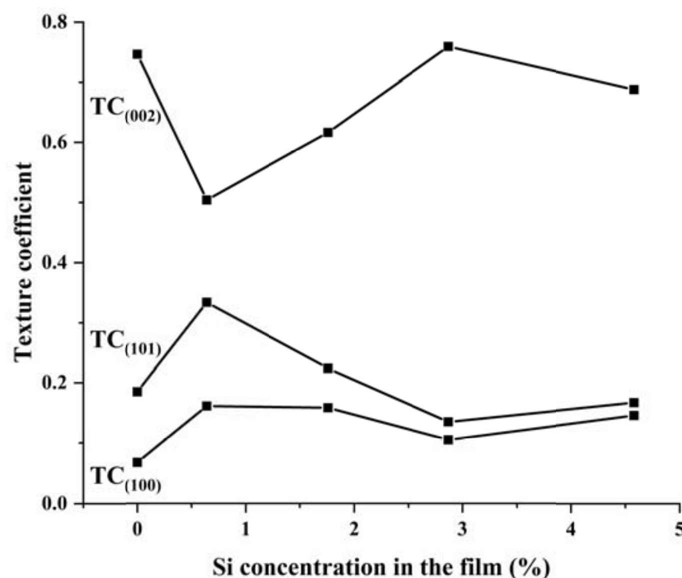

Figure 6.2: $TC_{(100)}$, $TC_{(002)}$, and $TC_{(101)}$ values for ZnO and SiZO thin films containing varying amounts of Si.

The lattice parameters of ZnO and SiZO thin films containing varying amounts of Si are shown in **Figure 6.3**. The lattice parameters a and b keep in the range of 3.248 (± 0.006) - 3.251 (± 0.003) Å as the Si concentration increases. Therefore effectively there are no significant changes for the lattice parameters a and b. The lattice parameter c increases from 5.191 (± 0.001) to 5.200 (± 0.003) Å as the Si concentration increases from 0 to 4.6%. The unit cell volumes follow the same trend of the lattice parameter c. However, I can observe a reduced unit cell volume for SiZO (0.6%) thin films. It may contribute to the substitution of Zn^{2+} ions by smaller Si^{4+} ions resulting in a lattice contraction. Nevertheless, this reduced unit cell volume can also be due to the errors in calculating the lattice parameters a, b, and c. Therefore, I can hardly tell which case it should be at the moment.

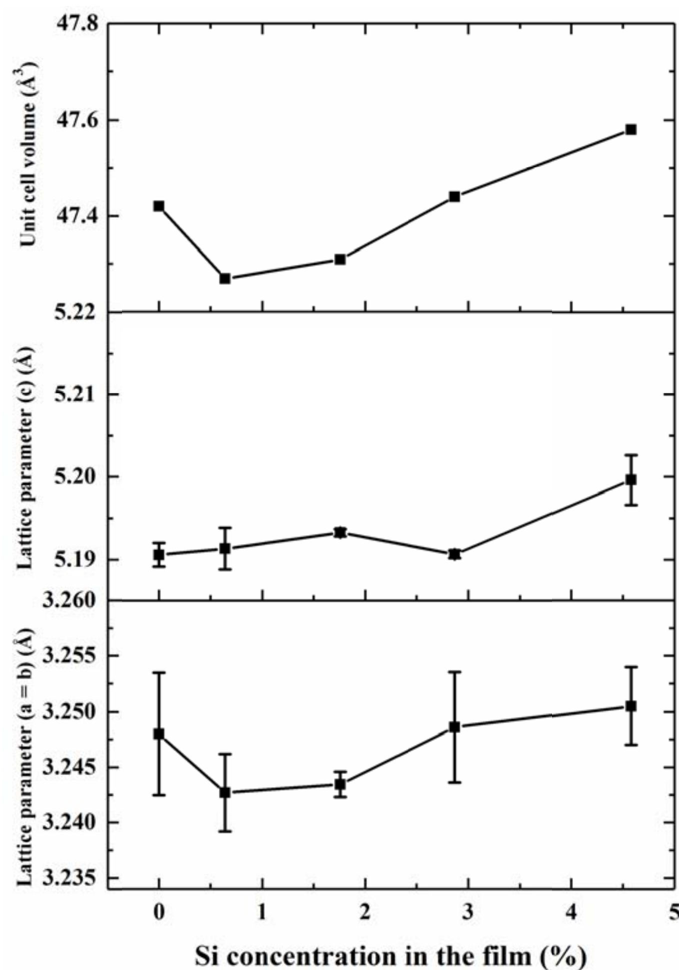

Figure 6.3: Lattice parameters of ZnO and SiZO thin films containing varying amounts of Si.

Wu et al. calculated the formation energy for SiZO indicating the incorporation of Si into substitutional sites of ZnO lattice is thermodynamically favourable (see **Figure 1.25** in **Chapter 1**). [9] The formation energies of substitutional and interstitial Si defects indicate the interstitial occupancy of Si is unfavourable compared to substitution. [9, 10] If the ZnO lattice contracts due to the Si doping, the slight contraction of the unit cell is due to the substitution of Zn^{2+} ions by smaller Si^{4+} ions for low Si doped ZnO (ionic radii of tetrahedral coordinated Zn^{2+} and Si^{4+} are 0.60 Å and 0.26 Å, respectively [11]). The lattice does not show a large expansion at low doping levels. However, the expansion of the unit cell for heavily Si doped ZnO may well be due to interstitial occupancy of Si in the lattice.

6.1.1.2 Singly Doped Thin Films: IZO

Figure 6.4 shows the XRD patterns of ZnO and IZO thin films containing varying amounts of In. Similarly to SiZO thin films, no peaks for other phases (e.g., In_2O_3 or $In_2Zn_2O_5$) are seen. IZO thin films do not always have a (002) preferred plane orientation like SiZO thin films. A low In content (< 2%) leads to a (002) preferred plane orientation, whereas, a (101), or a mixture character of (100) and (101), preferred plane orientation occurs with a high In content (> 2%). Vai also reported the changes in the preferred plane orientation as a function of the In concentration. [12]

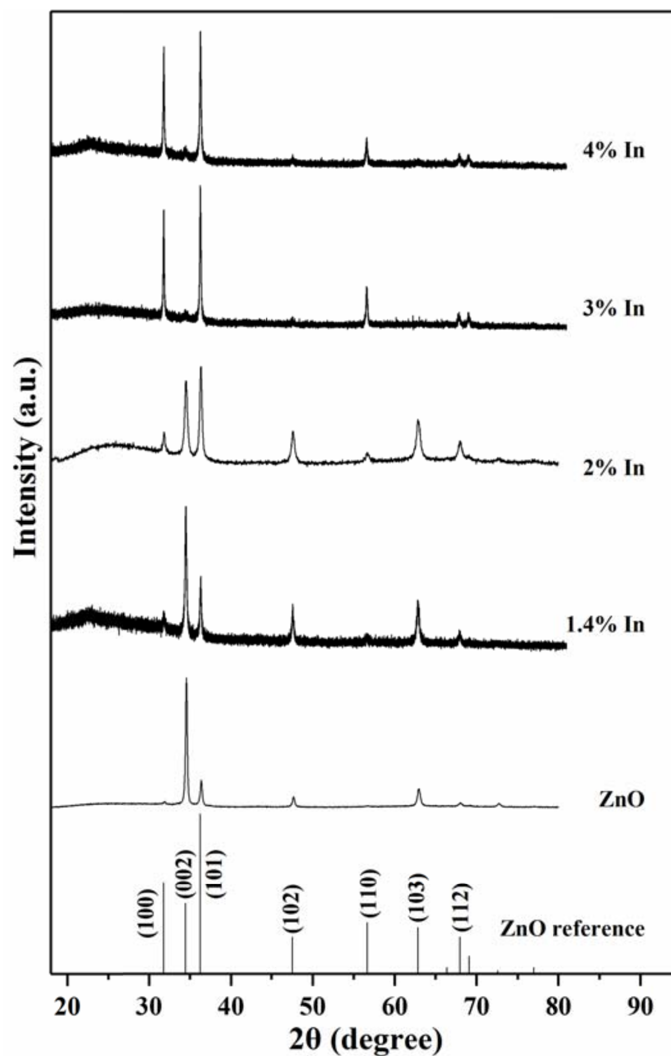

Figure 6.4: XRD patterns of ZnO and IZO thin films containing varying amounts of In.

Figure 6.5 shows the texture coefficients of the (100), (002), and (101) XRD reflections for ZnO and IZO thin films containing varying amounts of In. Unlike SiZO thin films, the (002) preferred orientation loses its domination (i.e., $TC_{(002)}$ value < 0.1) as the In concentration is higher than 2%. The $TC_{(100)}$ and $TC_{(101)}$ values increase to ~ 0.5 for heavily In (> 2%) doped ZnO thin films showing an increased character of the (100) and (101) preferred plane orientations. Heavily In (> 3%) doped ZnO thin films have a (101) preferred plane orientation but it is mixed with a significant amount of a (100) preferred plane orientation character because the values of $TC_{(100)}$ and $TC_{(101)}$ are very close to each other.

The dominant structure for both SiZO and IZO thin films is hexagonal wurtzite. However, SiZO thin films retain a (002) preferred orientation while IZO thin films change the preferred orientation to (101). Clearly, the In presence causes a shift in the growth pattern and changes the film deposition kinetics. Joseph et al. [13] reported that the preferred orientation of IZO thin films is due to the combined effect of Zn/In incorporation, growth rate and reorientational effect. Goyal et al. [14] found that the ZnO lattice can retain its original preferred orientation (002) at a low In concentration (< 2%). However, the film growth is along the (100) or (101) direction if excess In is incorporated into the ZnO lattice. Hadri et al. [15] pointed out that In doping lower the degree of the film crystallinity especially for a heavily In doping [16] and change the preferred orientation from (002) to (100) or (101) [17]. Nevertheless, it is still not understood completely whether the preferred orientation is affected by the In in the film or the excess In in the precursor solution. Further investigations are needed.

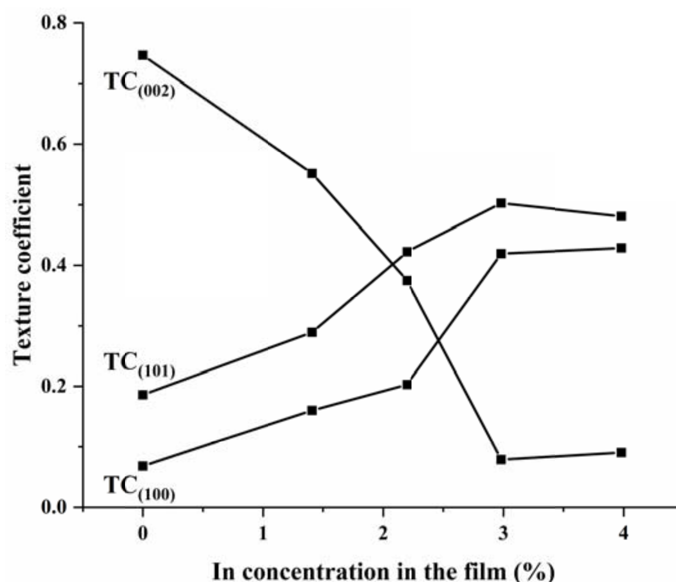

Figure 6.5: $TC_{(100)}$, $TC_{(002)}$ and $TC_{(101)}$ values for ZnO and IZO thin films containing varying amounts of In.

Figure 6.6 shows the lattice parameters of ZnO and IZO thin films containing varying amounts of In. Similarly to SiZO thin films, the lattice parameters a and b remain at an almost constant value in the range of 3.248 (± 0.006) - 3.250 (± 0.003) Å as the In concentration increases from 0 to 4%. The lattice parameter c increases from 5.191 (± 0.001) Å to 5.204 (± 0.004) Å as the In concentration increases from 0 to 4%. The unit cell volume follows the same trend observed for the lattice parameter c. I can observe a significant lattice expansion from 47.42 $Å^3$ to 47.6 $Å^3$ as the In concentration increases from 0 to 4%. The IZO unit cell parameters are determined by (1) the substitution of Zn^{2+} ions by larger In^{3+} ions (ionic radii of tetrahedral coordinated Zn^{2+} is 0.60 Å while ionic radii of four coordinated In^{3+} is 0.62 Å. [11]) in the ZnO lattice during the formation of IZO thin films which contributes to the lattice expansion, and (2) the interstitial occupancy of In in the lattice for heavily In doped ZnO. As in the case of SiZO thin films, the interstitial occupancy of In is unfavourable compared with substitutional sites. [9, 10] Therefore, a significant expansion of the unit cell occurs for IZO thin films as the In concentration increases.

It suggests there is a limit for In substitution of Zn in the lattice at ~ 2% In and beyond this any added In does not generate further free carrier electrons. These variations in the lattice

parameters are consistent with the electrical properties, where the best carrier concentrations and conductivities are achieved at ~ 2% In.

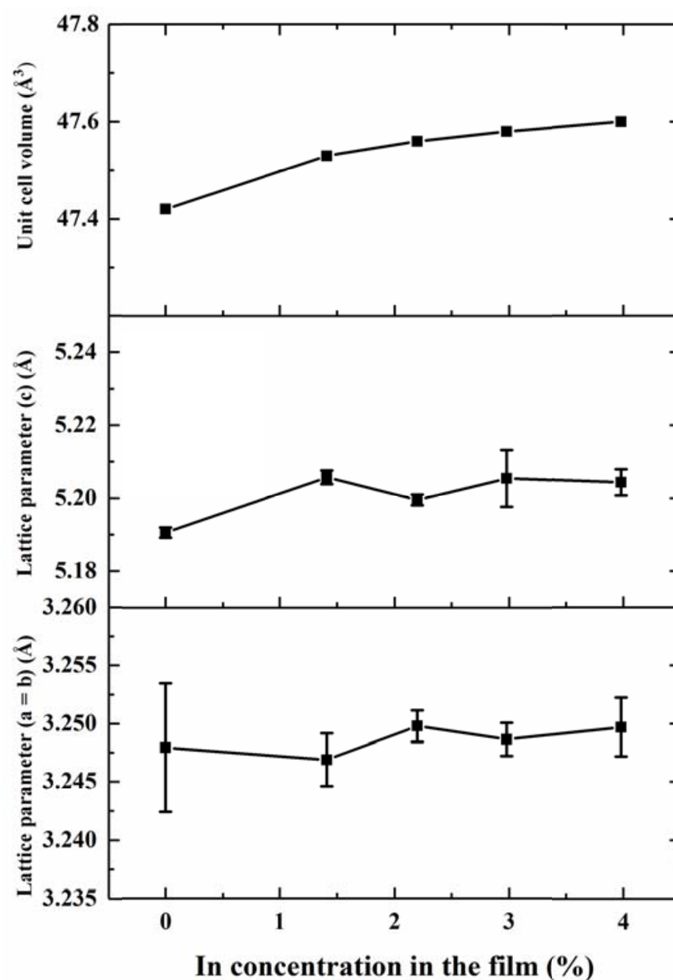

Figure 6.6: Lattice parameters of ZnO and IZO thin films containing varying amounts of In.

6.1.1.3 Co-Doped Thin Films: InSiZO

The XRD patterns of InSiZO thin films containing varying amounts of In and 0.6% Si are shown in **Figure 6.7**. No peaks for other phases (e.g., SiO_2, Zn_2SiO_4, In_2O_3 or $In_2Zn_2O_5$) except wurtzite ZnO are shown. InSiZO thin films have the similar preferred plane orientation to the IZO thin films. However, the (002) orientation is not observed in any of the co-doped thin films. Adding a little In (< 2%) leads to the transformation of the preferred orientation from (002) to (101). As the In concentration continues to increase, the domination of a (100) or (101) preferred plane orientation occurs, but the peak intensities are very close. The close

values of $TC_{(100)}$ and $TC_{(101)}$ indicate the preferred orientation is a mixture of (100) and (101), neither of them has the absolute predominance (**Figure 6.8**). It suggests that the texture of co-doped thin films is dominated by In not Si.

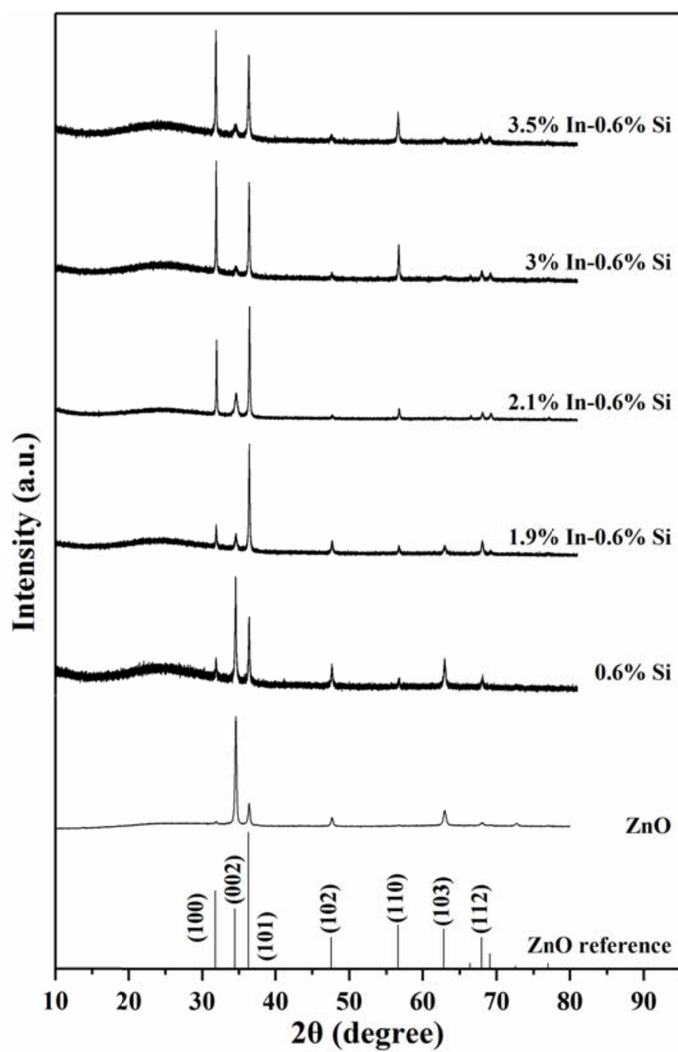

Figure 6.7: XRD patterns of InSiZO thin films containing varying amounts of In and 0.6% Si.

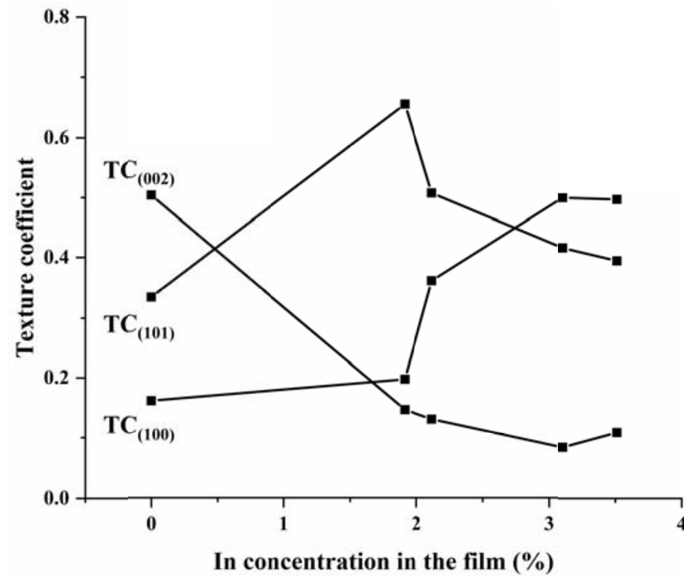

Figure 6.8: $TC_{(100)}$, $TC_{(002)}$ and $TC_{(101)}$ values for InSiZO thin films containing varying amounts of In and 0.6% Si.

Figure 6.9 shows the lattice parameters of InSiZO thin films containing varying amounts of In and 0.6% Si. The lattice parameters and unit cell volumes show similar trends as a function of In concentrations to those of IZO thin films. The unusual decreased unit cell volume for InSiZO (3.5% In-0.6% Si) thin films may be due to the errors in calculating the lattice parameters a, b, and c. The reasons for the expansions of the lattice and the limits of electrical properties can be explained in an analogous manner to IZO thin films as discussed above. InSiZO thin films with the highest carrier concentrations and conductivities are achieved with ~ 2% In as shown and discussed in **Section 4.3.1** of **Chapter 4**.

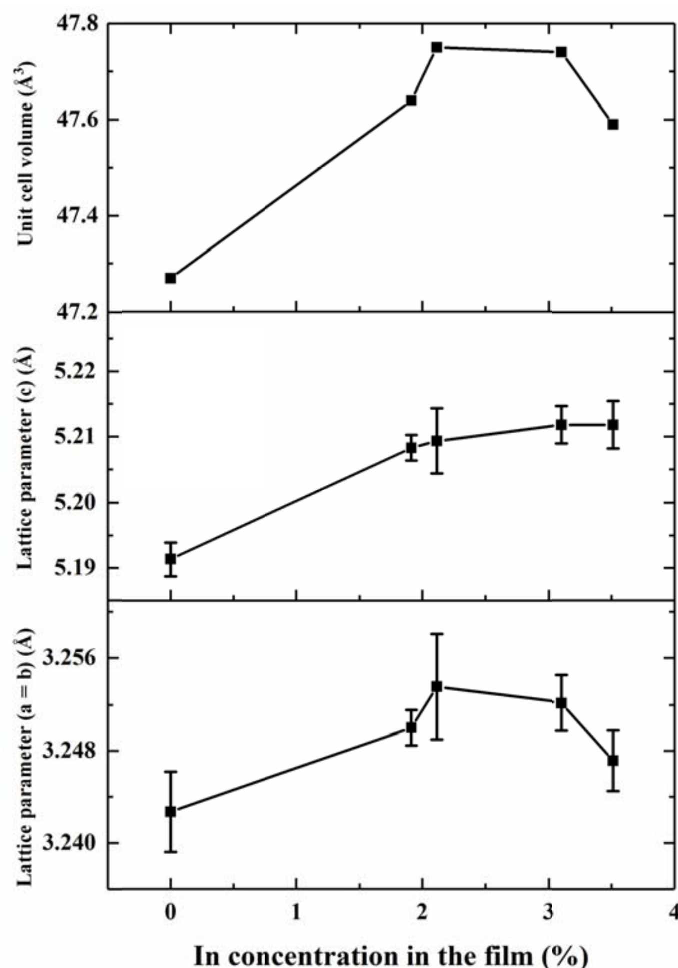

Figure 6.9: Lattice parameters of InSiZO thin films containing varying amounts of In and 0.6% Si.

6.1.2 Effect of Film Thickness

The XRD patterns of ZnO, SiZO, IZO, and InSiZO thin films of various thicknesses are shown in **Figure 6.10** and **Figure 6.11**. Only peaks consistent with the wurtzite ZnO structure are observed. However, the intensities of the characteristic peaks of the wurtzite ZnO structure decrease significantly as the film thickness decreases, since thinner films have less atomic layers to diffract X-rays. [18-21] The broad diffraction peaks below 30° are produced by the amorphous glass substrate. As the film thickness decreases, the overall XRD patterns are produced by a mixture which is a sum of the diffraction patterns of each individual phase including the characteristic peaks of the wurtzite ZnO structure with decreased intensities and the broad diffraction peaks produced by the amorphous glass substrate. Film thickness does

not affect the preferred orientation for all the films. The film performance for various thickness can be attributed to a misalignment of the grains along the preferred orientation due to the competition in the growth of neighbouring crystals as reported by Barna et al. [22] Shewale et al. pointed out the higher peak intensity is attributed to the better crystallite alignment as the thickness increases. The increased thickness provides more space for the thermal motion of particles, which leads to a better crystallite alignment. [23-25]

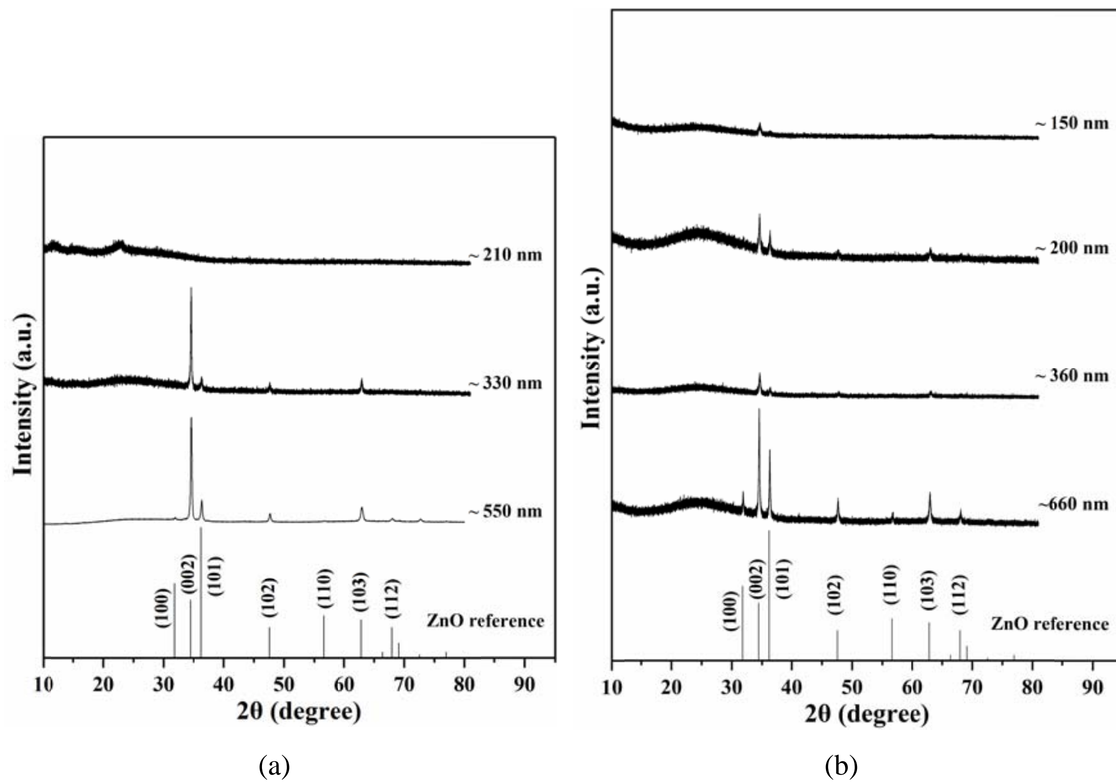

Figure 6.10: XRD patterns of ZnO (a) and SiZO (0.6%) (b) thin films of various thicknesses.

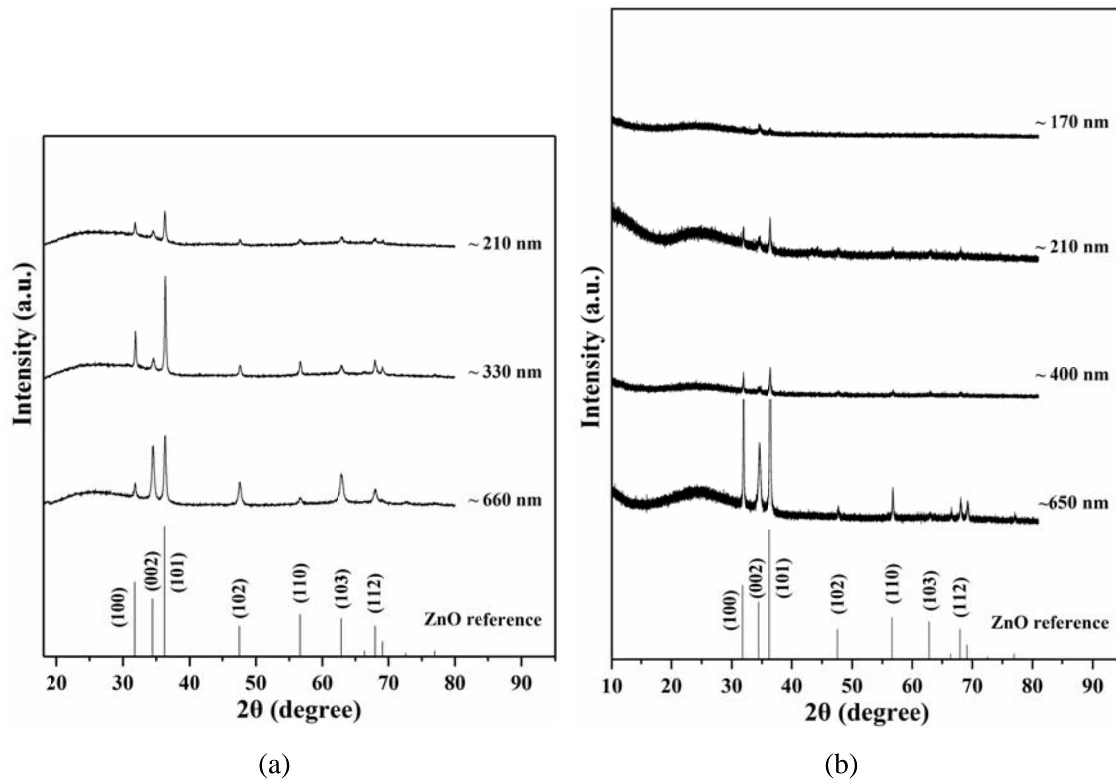

Figure 6.11: XRD patterns IZO (2%) (a) and InSiZO (2% In-0.6% Si) (b) thin films of various thicknesses.

Al-Khawaja et al. [20] found that the smaller stress values are concurring with increased thicknesses. The contact between the amorphous glass substrate and the films leads to a higher stress value for thinner films since amorphous glass substrate cannot be a good template for the crystal growth. However, the stress in thicker films is smaller attributed to the contact as a buffer, i.e., the initial layer growing on the glass substrate acts as a highly crystalline template for the further film growth. [18]

6.2 AFM and SEM Studies

6.2.1 Effect of Element Concentration

6.2.1.1 Singly Doped Thin Films: SiZO

The AFM images and surface roughnesses of ZnO and SiZO thin films containing varying amounts of Si are shown in **Figure 6.12** and **Figure 6.13**. The surface roughness decreases from ~ 60 nm for undoped ZnO thin films to ~ 20 nm for SiZO (0.6%) thin films. The surface roughness then keeps almost as a constant as the Si concentration continue to increase. It indicates that increasing Si concentrations can smooth thin films. The AFM images show that the grain size decreases as the Si concentration increases, which is also proved by the SEM images (**Figure 6.14**). The grain size decreases from ~ 490 nm to ~ 280 nm as the Si concentration increases from 0 to 4.6% (**Figure 6.15**). The highly crystalline grains are distributed uniformly to make good contacts for electrical conductivities. [26] The SEM grain sizes are much larger than the crystallites calculated from XRD data. This is because of the different definitions of 'grain size' attributed to different measurement methods. The SEM grain size means the distance of adjacent visible grain boundaries, whereas for the crystallite size determined by XRD it means the coherent X-ray diffracting distance in the crystal lattice, which is a smaller scale than that of SEM. [20] The observed SEM grains are more likely to be clusters composed of small crystallites.

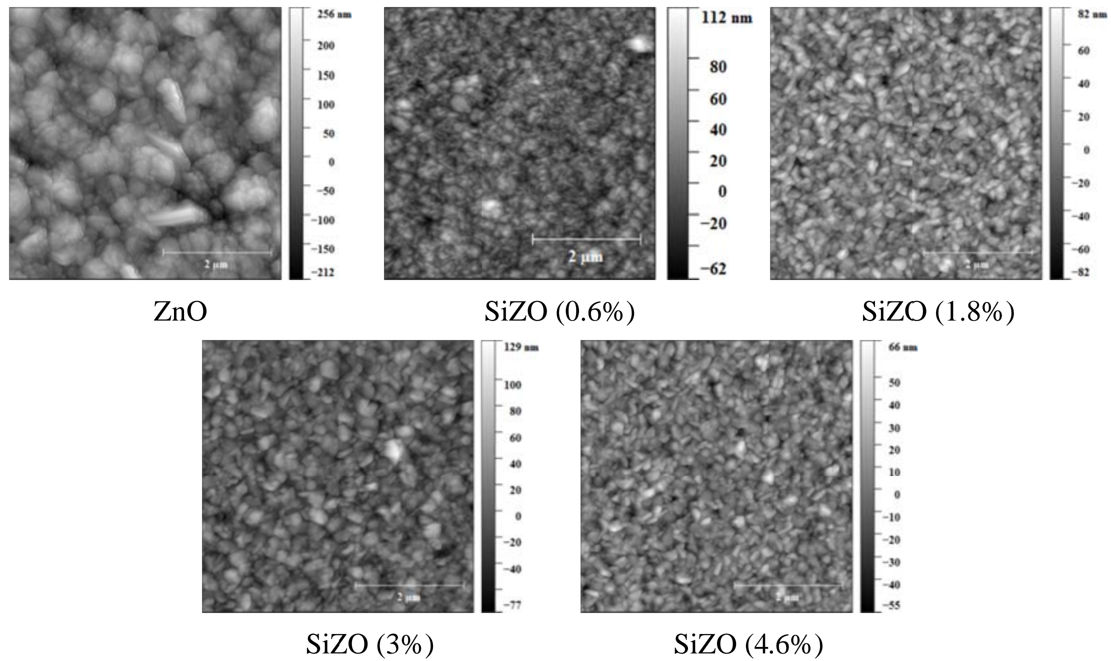

Figure 6.12: AFM images of ZnO and SiZO thin films containing varying amounts of Si.

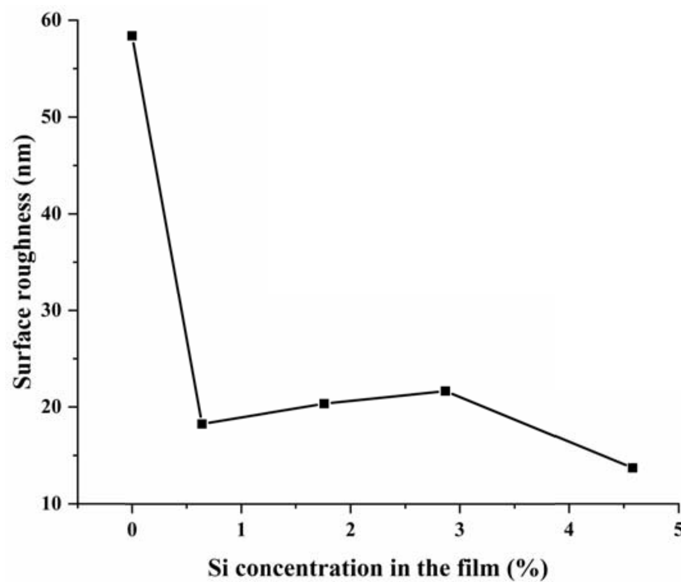

Figure 6.13: RMS surface roughnesses of ZnO and SiZO thin films containing varying amounts of Si calculated from the AFM data.

Figure 6.14 shows the SEM images of ZnO and SiZO thin films containing varying amounts of Si. ZnO and all SiZO thin films have the (002) preferred orientation and the c axis orientated structure as shown in XRD patterns. The schematic diagram for crystal growth orientations of ZnO thin films grown on a glass substrate is shown in **Figure 6.16**. ZnO thin

films have hexagonal cylindrical structures showing flake-like sheets parallel to the surface of the substrate, while SiZO (0.6%) thin films have pyramidal-like structures showing the mixing character of (002) with (101) orientations, which is consistent with XRD patterns. The other SiZO thin films still have hexagonal cylindrical structures showing flake-like sheets, which are smaller than those of ZnO thin films.

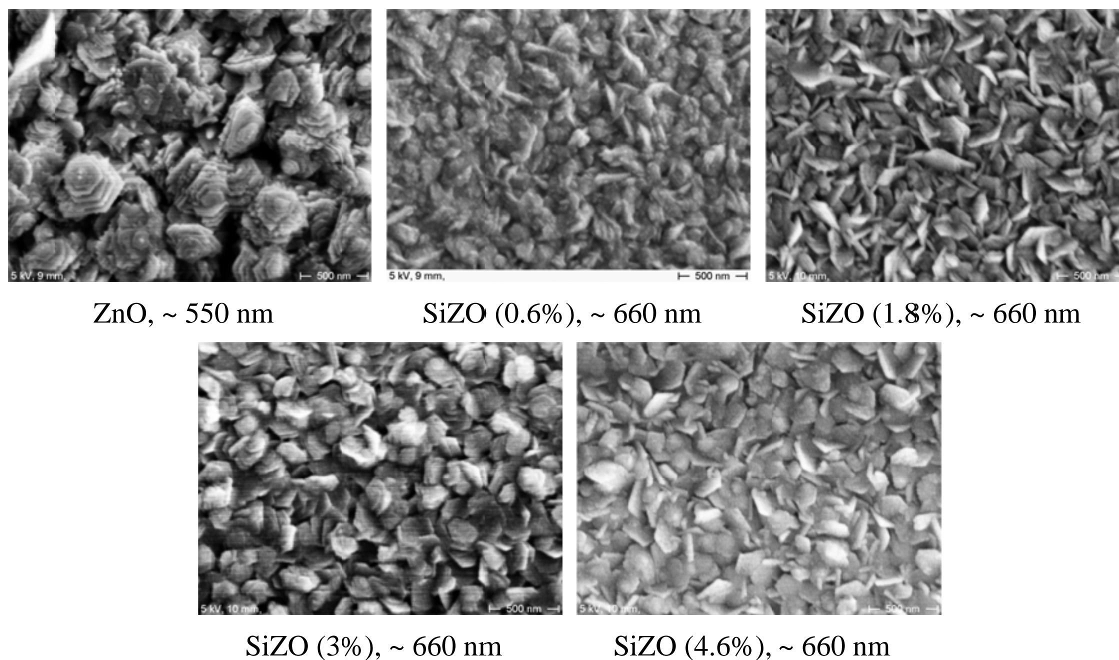

Figure 6.14: SEM images of ZnO and SiZO thin films containing varying amounts of Si.

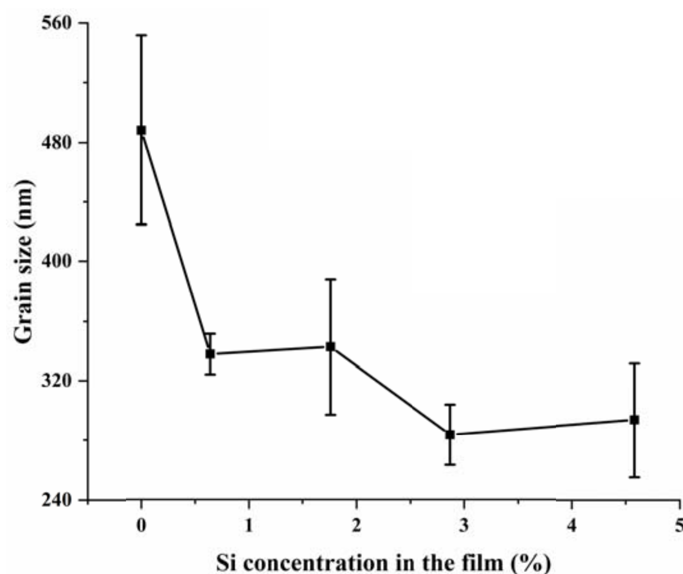

Figure 6.15: Grain sizes of ZnO and SiZO thin films containing varying amounts of Si calculated from SEM images.

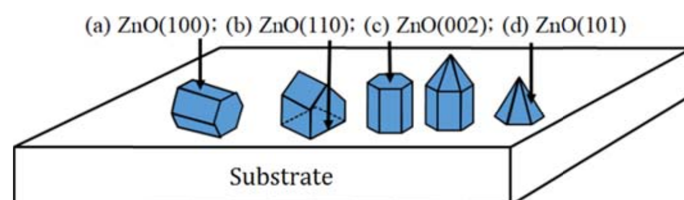

Figure 6.16: Schematic diagram for crystal growth orientations of ZnO (undoped or doped) thin films grown on a glass substrate. (a) A polygonal structure; (b) A ridge-like structure; (c) a pyramidal-like structure (hexagonal cylindrical with a pyramidal tip or not); (d) A pyramidal tip structure. Reproduced from Tsai et al. [27] with permission from Beilstein-Institut.

6.2.1.2 Singly Doped Thin Films: IZO

The variation in the surface roughness for IZO thin films is similar to that of SiZO thin films, and decreases from ~ 60 nm for undoped ZnO thin films to 16 - 23 nm for IZO thin films as the In concentration increases to 4%. It suggests that either In or Si can smooth thin films at higher concentrations. However, SiZO thin films are smoother than IZO thin films at low dopant levels (< 3%). The AFM images also show the negative correlation between the grain sizes and the In concentration, which is consistent with the SEM images. The grain size

decreases from ~ 490 nm to ~ 190 nm with increased In concentration in the range of 0 - 4%. The difference between SEM grain sizes and those of XRD has been discussed in SiZO thin films. [20]

The hexagonal cylindrical structures showing flake-like sheets are only observed for IZO (1.4%) thin films showing a (002) preferred orientation consistent with XRD patterns. The (100) preferred orientation dominates for IZO (2%) thin films, which have polygonal structures. Such structures make the film surface closely and densely packed, with a smooth surface and a small grain size. [28] Both the (100) and (101) orientations have equal contributions to the overall film structures for heavily In (> 3%) doped ZnO thin films. These are likely to be polygonal mixed with pyramidal tip structures showing almost disordered structures, thus reducing the film roughness and grain size. Please refer to the figures in **Appendix A6.1**.

6.2.1.3 Co-Doped Thin Films: InSiZO

Figure 6.17 and **Figure 6.18** show the AFM images and surface roughnesses of InSiZO thin films containing varying amounts of In and 0.6% Si. Adding 2% In into SiZO (0.6%) thin films increases the surface roughness from 18 nm to 37 nm. However, the surface roughness decreases to 21 nm for a further increase in In concentration, which shows the similar trend as that of IZO thin films. It indicates that co-doped films are still as smooth as singly doped thin films. The correlation between the grain size and the In concentration is more complicated compared to singly doped thin films, which is shown in the AFM and SEM images (**Figure 6.17** and **Figure 6.19**). The grain size of InSiZO thin films has the similar size as SiZO thin films at low In doping levels (< 2%). Nevertheless, it increases rapidly from ~ 320 nm to a maximum value of 560 nm for the In concentration of 2% - 3%. Finally, it decreases to the same grain size as SiZO thin films at an In concentration value of 3.5%.

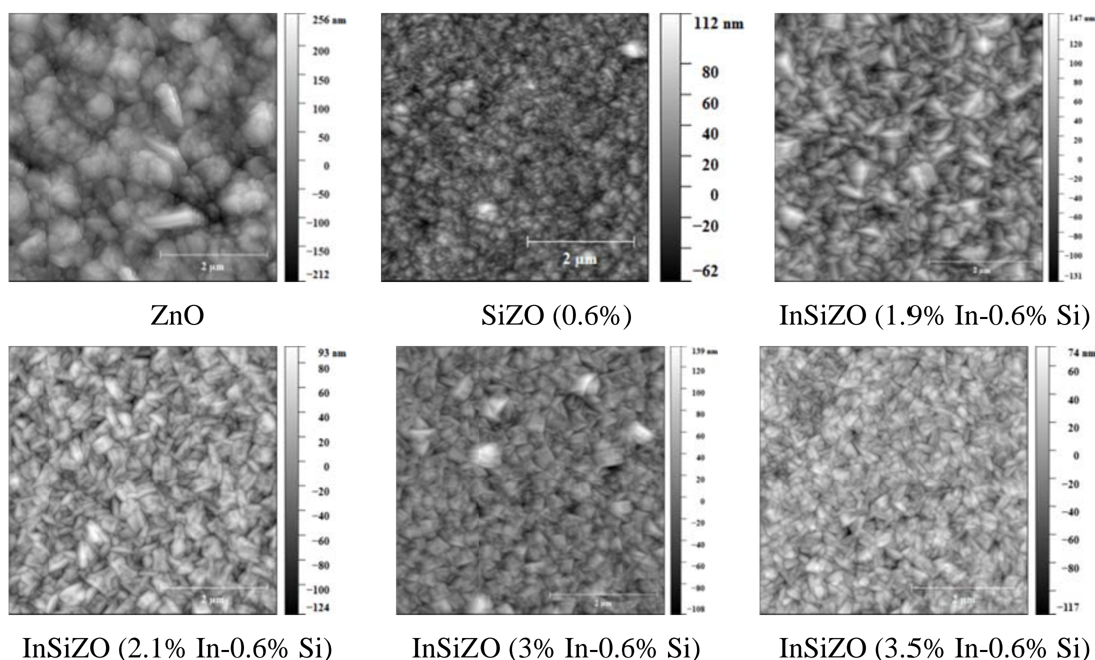

Figure 6.17: AFM images of InSiZO thin films containing varying amounts of In and 0.6% Si.

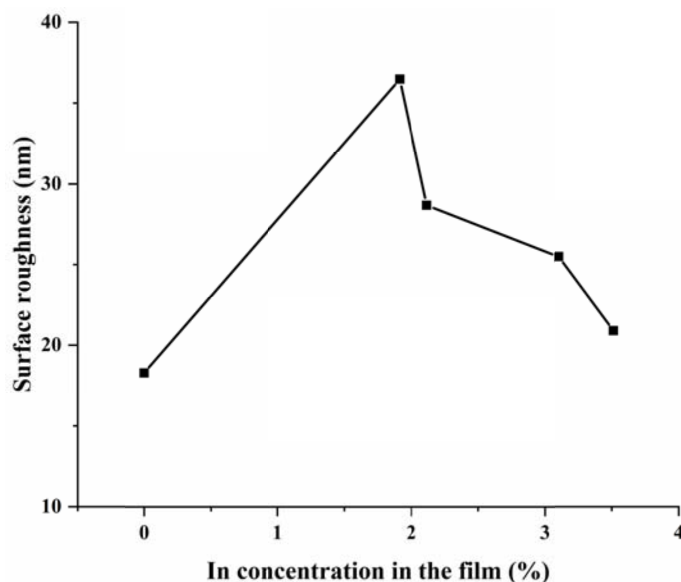

Figure 6.18: RMS surface roughnesses of InSiZO thin films containing varying amounts of In and 0.6% Si calculated from the AFM data.

The SEM images of InSiZO thin films containing varying amounts of In and 0.6% Si are shown in **Figure 6.19**. These films have pyramidal tip structures consistent with (101) preferred orientations. For In concentrations higher than 2%, films comprise almost equal mixtures of (100) and (101) preferred orientations. The morphology differences indicate that a

second dopant can alter structures of the crystal growth orientations of singly doped thin films. Fox example, SiZO (0.6%) thin films have pyramidal-like structures characteristic of a blend of (002) and (101) orientations, and IZO (2%) thin films have polygonal structures dominated by (100) preferred orientations. Both InSiZO (1.9% In-0.6% Si) and InSiZO (2.1% In-0.6% Si) thin films have very different structures to the two singly doped thin films as shown in **Figure 6.19**. The morphological changes that occur on singly doping and co-doping have a significant effect on electrical properties and while they are reproducible the precise factors that drive the changes are unknown at present.

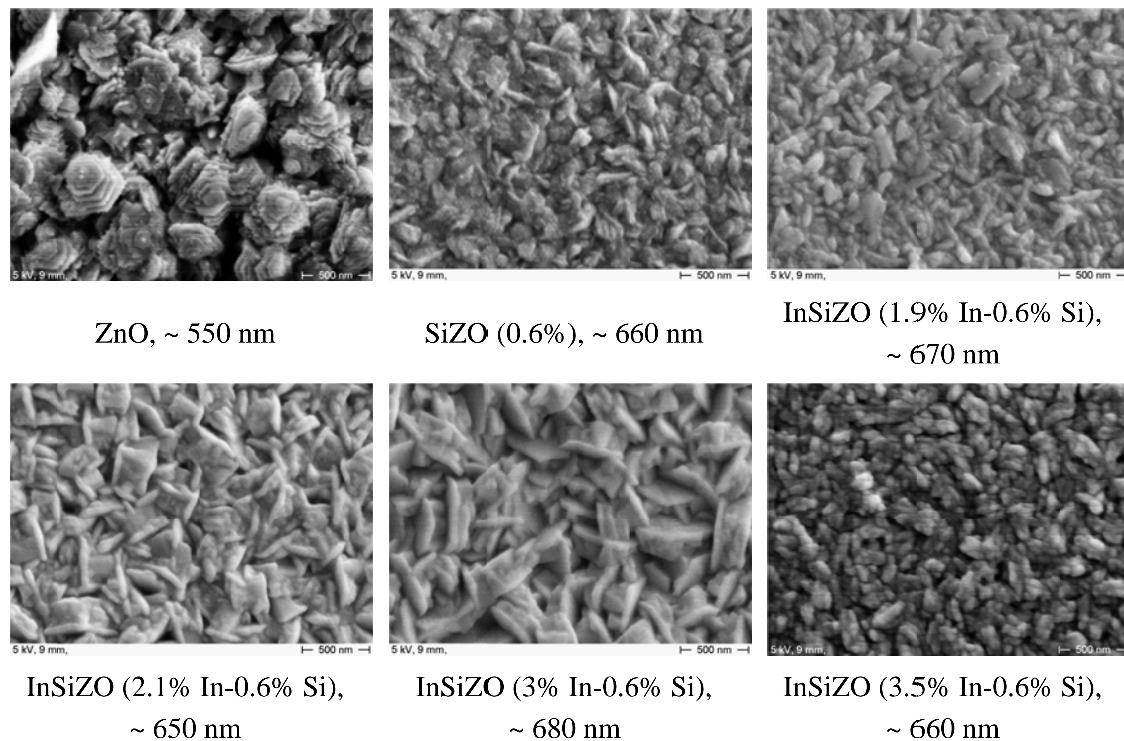

Figure 6.19: SEM images of InSiZO thin films containing varying amounts of In and 0.6% Si.

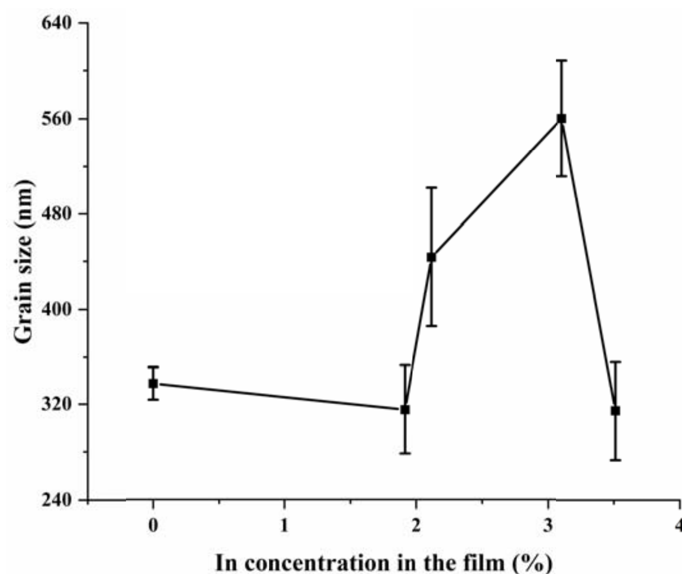

Figure 6.20: Grain sizes of InSiZO thin films containing varying amounts of In and 0.6% Si calculated from SEM images.

6.2.2 Effect of Film Thickness

Figure 6.21 and **Figure 6.22** show the AFM images and surface roughnesses of ZnO thin films of various thicknesses. They show the films become smoother as the film thickness decreases, which shows up in the reduced peak intensities of XRD patterns. The grain size also becomes smaller as the film thickness decreases as shown in **Figure 6.21**, **Figure 6.23**, and **Figure 6.24**. ZnO thin films of various thicknesses have hexagonal cylindrical structures showing flake-like sheets parallel to the surface of the substrate, which are consistent with (002) preferred orientations as shown in the XRD patterns. The increased surface roughness can be attributed to the asymmetric growth of the crystals, which was also observed by Gonçalves et al. [18] and Bang et al. [29] The grains can only grow in two dimensions for thinner films, whereas they have a possibility to grow in the third dimension where a space is available for thicker films. The increased dimension leads to an increased grain size for thicker films. [23, 25] The positive correlation between surface roughnesses and film thicknesses is mainly due to the grain size variations. [30]

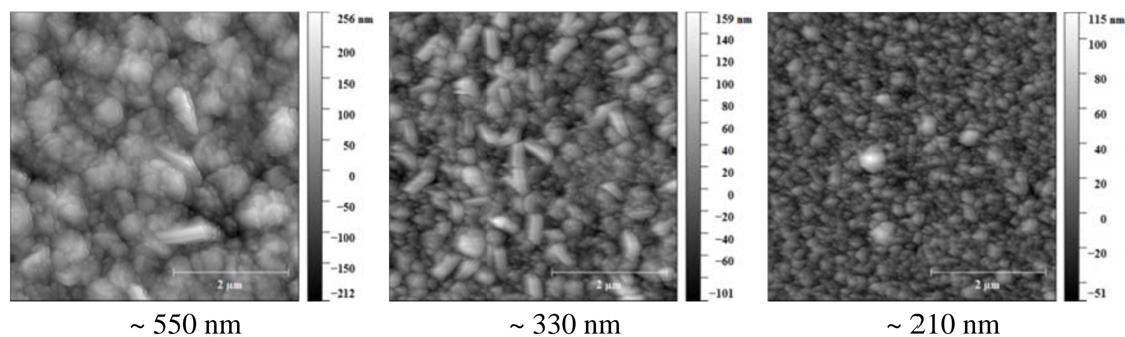

Figure 6.21: AFM images of ZnO thin films of various thicknesses.

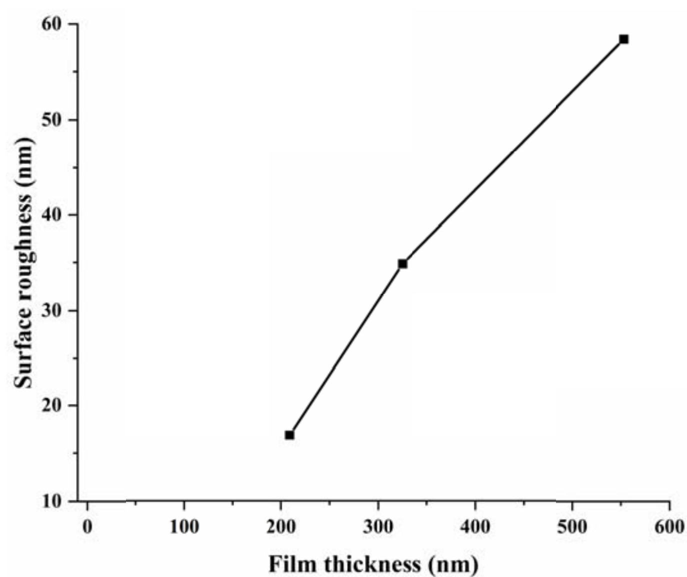

Figure 6.22: RMS surface roughnesses of ZnO thin films of various thicknesses calculated from the AFM data.

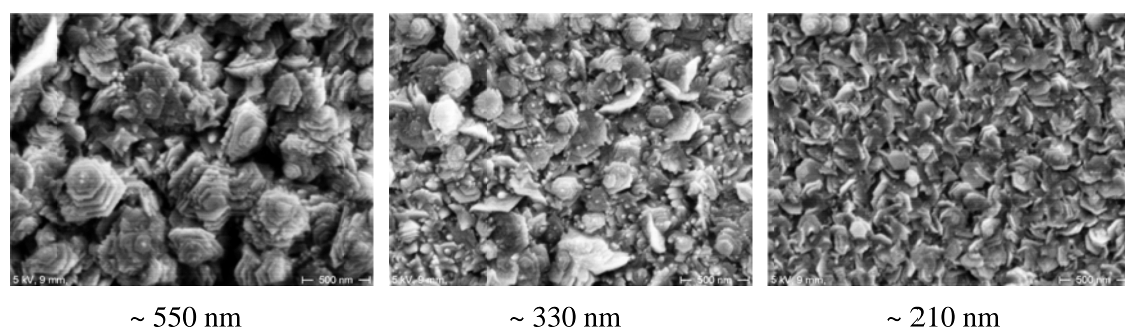

Figure 6.23: SEM images of ZnO thin films of various thicknesses.

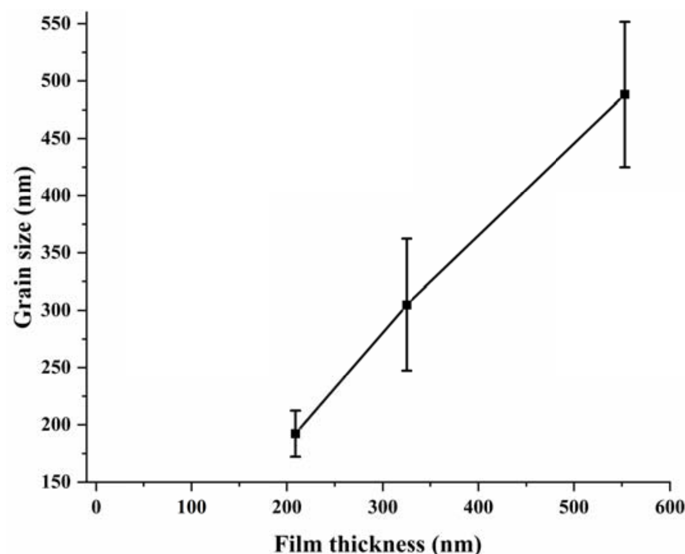

Figure 6.24: Grain sizes of ZnO thin films of various thicknesses calculated from SEM images.

The AFM images and surface roughnesses of SiZO thin films of various thicknesses are shown in **Figure 6.25** and **Figure 6.26**. Similarly to ZnO thin films, thinner films are smoother. The grain size is also smaller for thinner films (**Figure 6.25**, **Figure 6.27**, and **Figure 6.28**. All of these SiZO thin films have pyramidal-like structures comprising mixed (002) with (101) orientations, which is consistent with XRD patterns. At very small thicknesses such as ~ 150 nm, the films become nearly 'amorphous' with no evidence in the SEM of crystallite edges and very broad XRD peaks. This is presumably as the early stages of film deposition largely reflect the amorphous structure of the glass substrate.

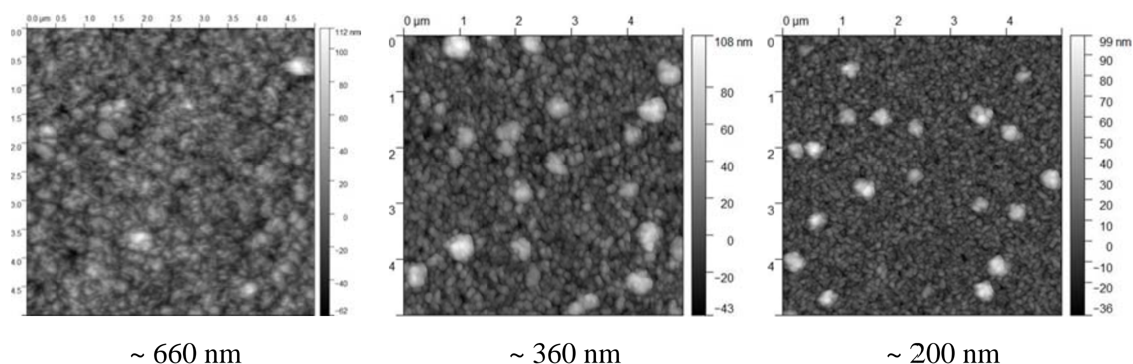

Figure 6.25: AFM images of SiZO (0.6%) thin films of various thicknesses.

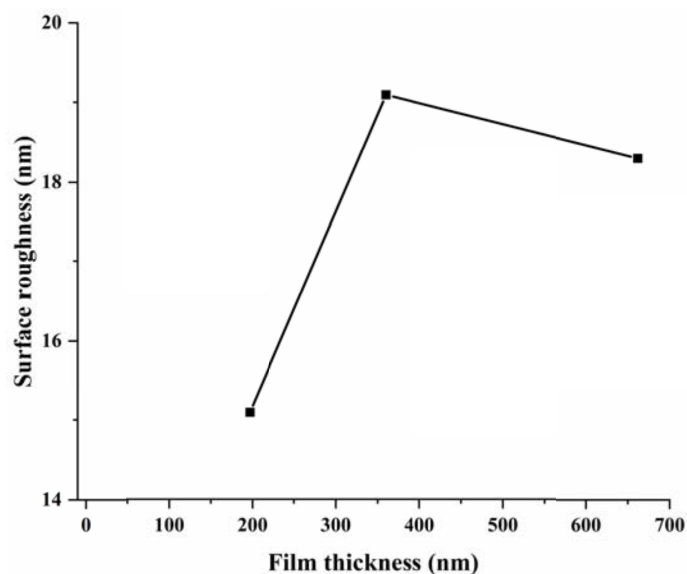

Figure 6.26: RMS surface roughness of SiZO (0.6%) thin films of various thicknesses calculated from the AFM data. The deviation of the middle point is due to experimental errors in AFM measurements.

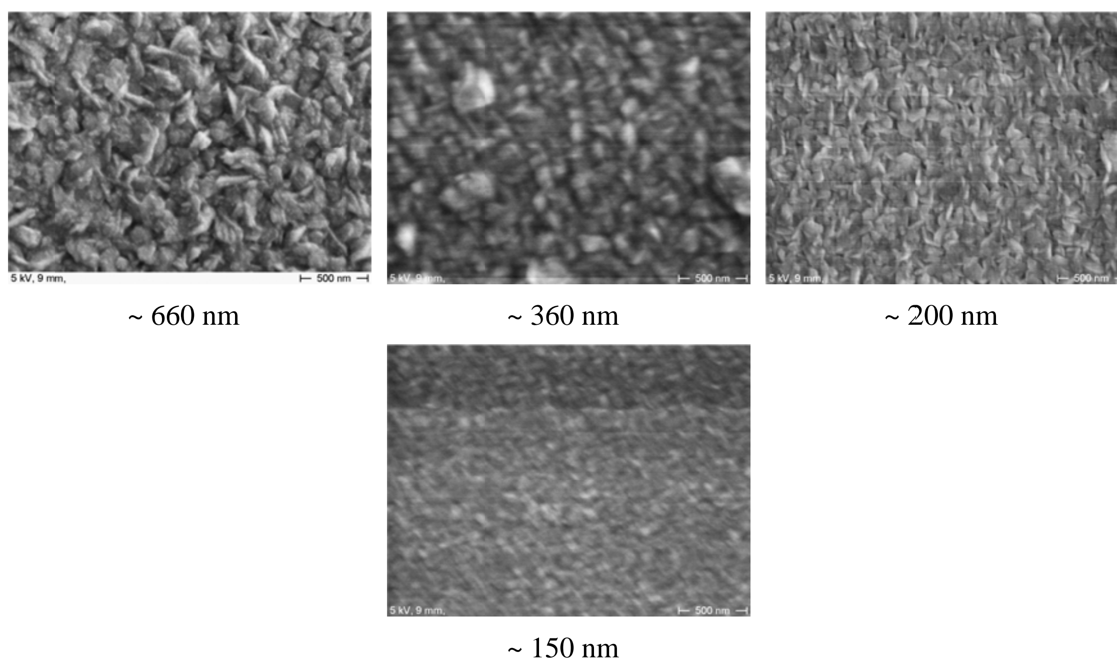

Figure 6.27: SEM images of SiZO (0.6%) thin films of various thicknesses.

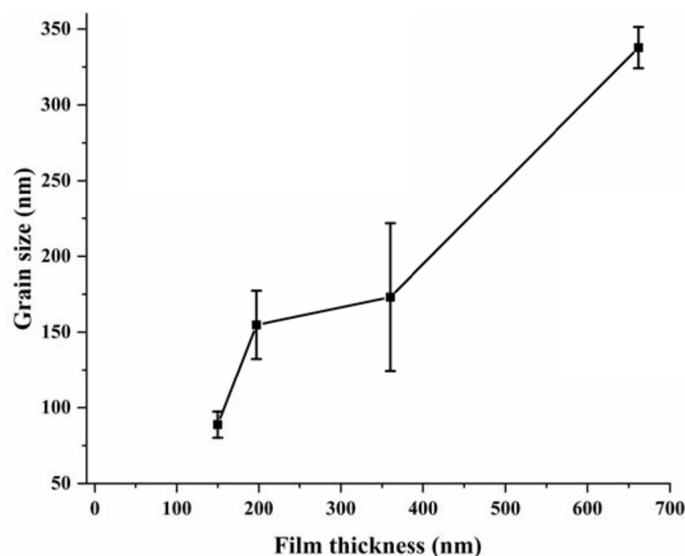

Figure 6.28: Grain sizes of SiZO (0.6%) thin films of various thicknesses calculated from SEM images.

Similarly to SiZO thin films, thinner IZO films are smoother. The grain size is also smaller for thinner films. ~ 660 nm-thick films have polygonal structures showing a (100) preferred orientation, which is consistent with XRD patterns. However, thinner films (~ 330 nm and ~ 210 nm) are a mixture of polygonal and pyramidal tip structures characteristic of (100) and (101) orientations; and therefore are much different from thicker films. Please refer to the figures in **Appendix A6.2**.

Thinner films are again smoother with smaller grain sizes becoming a rule for either singly doped or co-doped films. All InSiZO thin films of various thicknesses have polygonal mixed with pyramidal tip structures showing a mixture of (100) and (101) orientations. These structures are much like those observed in IZO films. Please refer to the figures in **Appendix A6.3**.

6.3 TEM Studies

ZnO, SiZO, IZO, and InSiZO films comprise polycrystalline wurtzite ZnO. The films are

reasonably compact, with crystal grains abutting each other without an amorphous intergranular phase. Voids are present at triple and quadruple-grain junctions. All films bar one, InSiZO, show large irregular prismatic grains with large degrees of concavity. InSiZO thin films are the only ones exhibiting stable growth of individual grains that thread the film entirely, i.e., from nucleating layer to top surface. These 'super grains' grow steadily throughout the film leading to large hillocks of single crystal at the top surface. All diffraction patterns concur with the wurtzite polytype of ZnO.

6.3.1 The Microstructure of ZnO, SiZO, and IZO

These films are 680 ± 20, 580 ± 20, 570 ± 30 nm thick, which were imaged via a cross-section, for ZnO, SiZO, and IZO, respectively. The BF image of ZnO in **Figure 6.29**(a) shows a reasonably densely packed film with some voids between grains. The grains in the film are quite irregular, with a high degree of concavity, which are similar to those of SiZO, and IZO. (**Appendix A6.4**)

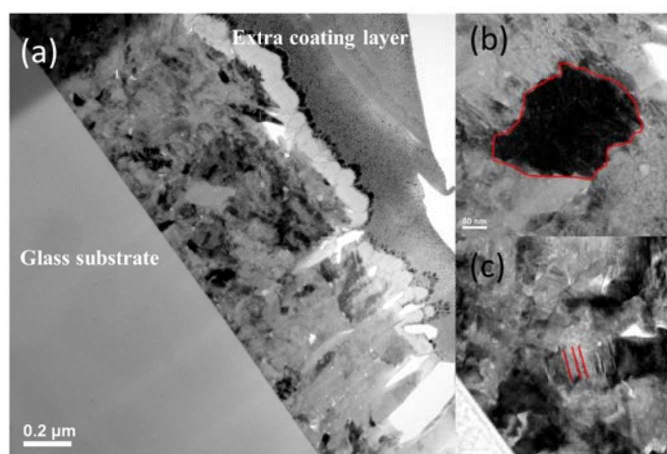

Figure 6.29: ZnO: The overall microstructure (a) and example of an irregular grain, strongly diffracting (b) which displays the boundary of the grain. A grain containing planar faults is seen in (c). The black spots are the voids. The red lines draw the outlines of the key structures.

The nucleation layer for ZnO indicates grains growing directly on the glass (**Figure 6.30**(a)).

There is no transition region, i.e., a distinct height above the interface that marks a change in the crystal grain size or shape. The white lines between grains in **Figure 6.30**(a) show that the grains are as irregular here as they are in the upper reaches of the film. The space between the grains (the grain boundaries) appears to be abrupt with no glassy film or interfacial phase of significance (**Figure 6.30**(b)). Lattice fringes are seen right up to the boundaries of the grain. Often a switch of lattice contrast is seen within a few angstroms, suggesting sharp crystallographic termination. No particular grain orientation is seen either.

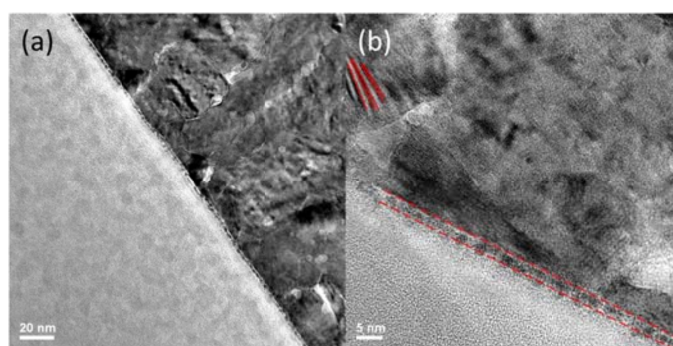

Figure 6.30: ZnO: An under-focused BF image shows white lines delineating the grain boundaries (a). HRTEM images show the dense network of crystalline material with no evidence of glassy films between grains (b). FIB artefacts are seen as 3 - 5 nm 'blobs' just below the interface (these have been seen on other films with glass substrates).

SiZO is similar to ZnO. (**Appendix A6.5**) However, the grain boundaries for IZO appear straighter and the mottling within the grains of ZnO and SiZO is largely missing. The nucleating region shows more regular prismatic grains (**Figure 6.31**). There are some dark patches within the grains, suggesting strain or defects, but not to the same extent as before. The HRTEM images show lattice fringes with reasonable good contrast and without too much fine-scale contrast, again suggesting good clean crystals. No amorphous phase is seen between grains. It shows IZO has 'better' grain boundaries than SiZO, which suggests improved electrical transport and electrical mobility for free carrier electrons. The better electrical resistivity of IZO compared to SiZO is consistent with the difference in grain boundaries. It may suggest why In is a superior to Si as a dopant to improve the conductivity

of ZnO.

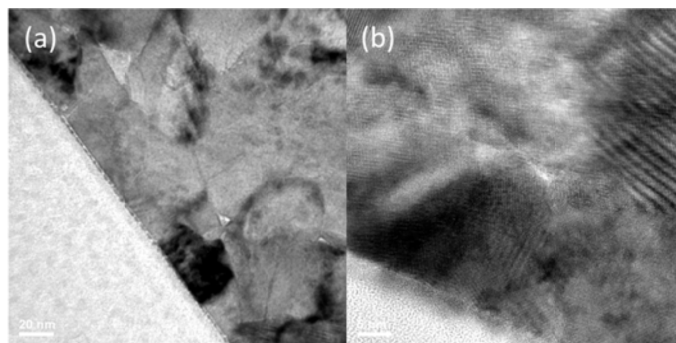

Figure 6.31: IZO: Under-focused BF image showing the boundaries between grains (a). HRTEM image of the nucleating interface shows good clear lattice contrast (b).

No orientational order between neighbouring grains is apparent either at the nucleating film (**Figure 6.30**(b)) or in the diffraction pattern of the bulk of the film (**Figure 6.32**) for ZnO. The spotted rings indicate that the material is, most likely, a single phase, but randomly oriented. If crystallographic correlations were present in the film, the diffraction pattern should show arcs made up many grains at slightly different orientations. However, this is not seen. SiZO and IZO are similar to ZnO. **(Appendix A6.6**)

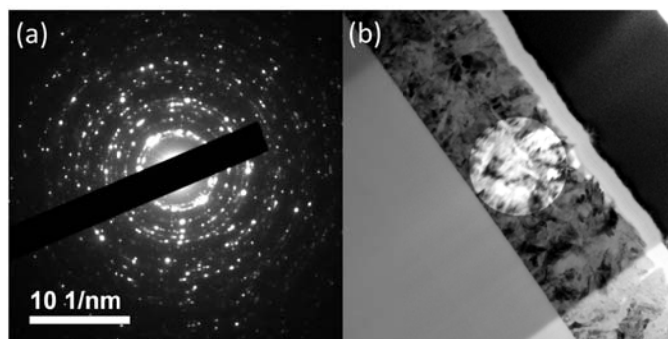

Figure 6.32: Selected area diffraction pattern (a) taken from a 1070 nm diameter patch in the thicker part of the FIB lamella of ZnO (b).

6.3.2 The Microstructure of InSiZO

The thickness of InSiZO (2% In-0.6% Si) thin films is 530 ± 30 nm. Like the earlier films, InSiZO is a densely packed polycrystalline film, but with one significant difference. Several large grains appeared as 'inverted cones' with the cone tip located at, or close to, the nucleating interface (**Figure 6.33**(b)).

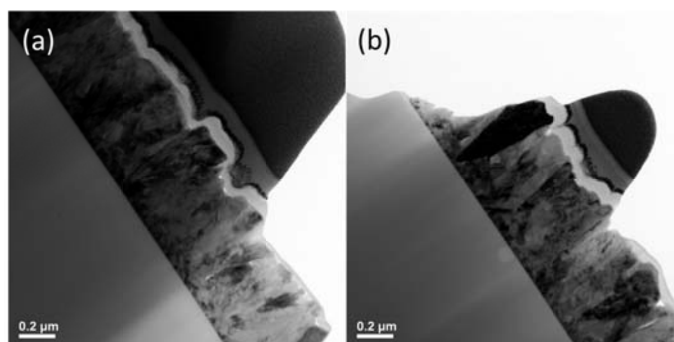

Figure 6.33: BF images of the thicker part (a) and thin part (b) of the lamella of InSiZO. Over-milling between these two regions results in a film-free window between them.

Like IZO, InSiZO has reasonably regular prismatic grains in the nucleating layer. Further, there is a change in the film behaviour at about 50 nm above the nucleating interface (**Figure 6.34**(a)), where the smaller grains either terminate or emerge as larger grains. This behaviour is seen in both the thick (a) and thin (b) parts of the film in **Figure 6.34**. Again, the under-focused image shows white lines where the grain boundaries are. Some mottling within the grains exists, but the grains appear reasonably uniform, suggesting good crystallinity.

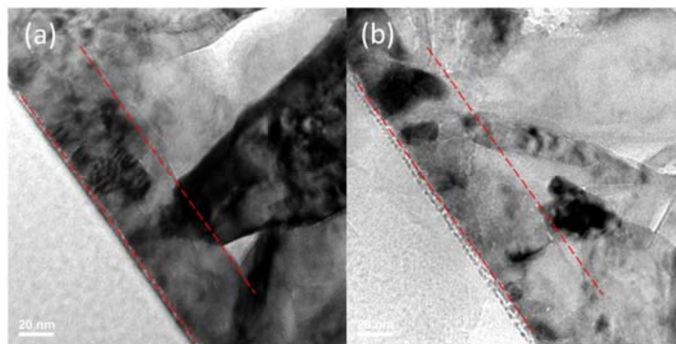

Figure 6.34: Under-focused BF images showing the grain boundaries in the nucleating layer for a thicker area (a) corresponding to the upper left of **Figure 6.33**(b) and thin area (beyond the lower right corner of previous **Figure 6.33**(b)).

The HRTEM images show very good crystallinity at the nucleating interface with no sign of amorphous intergranular films. The grains in the nucleating layer are regular polygonal structures with reasonably straight edges. Some of the grains have a 'V' shape suggesting an expanding growth front from the interface (**Figure 6.35**(a) and (b)).

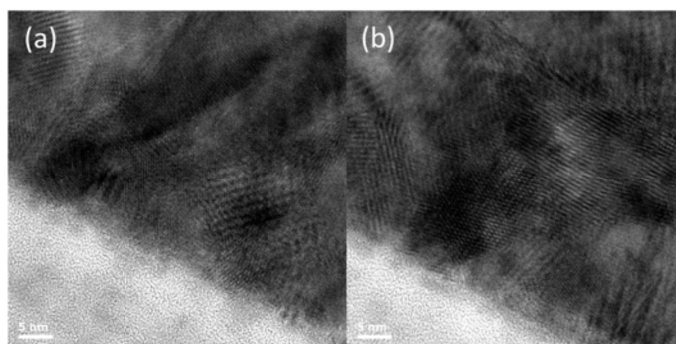

Figure 6.35: HRTEM images of the grains at the nucleating layers at different sites of the interface seen in **Figure 6.33**(b). Note the divergent triangular profile of the grains in (b).

Details of the grain structure of a percolating grain are shown in **Figure 6.36**. The grain shows a linear lateral expansion through the film (**Figure 6.36**(a)) and emerges at the top as a 300 - 400 nm wide grain. The grain shows strong expansion within the nucleating layer (first ~ 50 nm of the film, **Figure 6.36**(b)) before settling to a slower growth rate above it. This successful grain is one of many within the nucleating layer (**Figure 6.36**(c)) but it is hard to

see exactly where its lattice fringes originate.

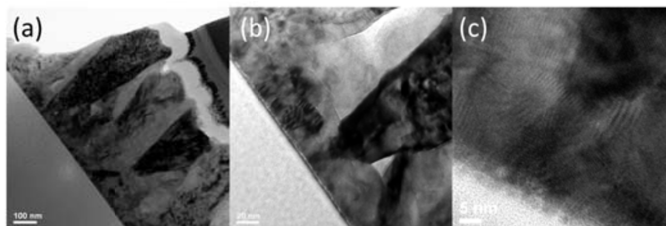

Figure 6.36: Structure of a percolating grain at large scale (a) and finer scales within 200 nm of the interface (b) and within 50 nm of the interface (c).

In summary, InSiZO differs significantly from ZnO, SiZO, and IZO in two respects. First, the nucleating layer shows a distinct change at about 50 nm from the film-glass interface. Second, the film contains large grains whose growth is stable and steadily increases in lateral extension as growth proceeds, constituting an increasing fraction of the growth front.

6.3.5 Chemistry of Films Measured with EDX Spectra

The distribution of elements along the normal direction of the films was characterised by EDX. EDX spectra taken from the films at bottom, middle, and top from the initial interfaces are shown in **Figure 6.37**.

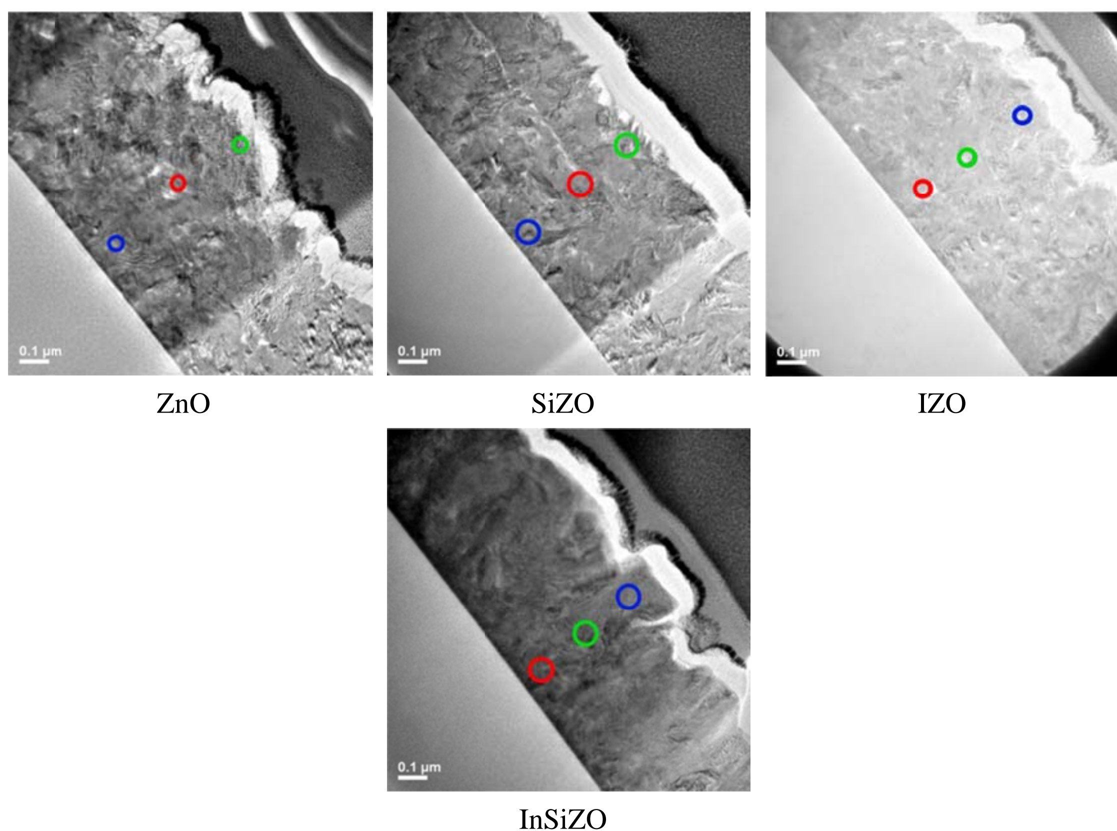

Figure 6.37: EDX spectra taken from ZnO, SiZO, IZO, and InSiZO thin films at the points indicated in images at roughly bottom, middle, and top from the initial interfaces.

Table 6.1 shows the element contents in ZnO, SiZO, IZO, and InSiZO thin films determined by EDX and ICP-MS. IZO and InSiZO show a reasonably constant level of Si or In throughout the films, whereas, the distribution of Si is uneven along the normal direction of the films for SiZO. It indicates that the distribution of elements in the films is not always uniform.

The comparisons of element contents measured by ICP-MS and EDX show that these two methods do not always give consistent results since ICP-MS measures elements in the whole films while EDX just measures specified chosen spots. I must be very careful when using solid state detection methods such as EDX and XPS because the spots they measured do not necessarily represent the whole information of a sample.

		ZnO			SiZO			IZO			InSiZO		
C_p	Si (%)	0			3			6			3		
	In (%)	0			0			0			6		
ICP-MS	Si (%)	0			0.6			0			0.8		
	In (%)	0			0			2.2			2.1		
EDX		Top	Middle	Bottom	Top	Middle	Bottom	Top	Middle	Bottom	Top	Middle	Bottom
	Si (%)	0	0	0	3.1	3.5	1.5	0	0	0	0.8	0.9	0.8
	In (%)	0	0	0	0	0	0	2.5	2.1	2.4	1.4	1.9	1.8

Table 6.1: Element contents in ZnO, SiZO, IZO, and InSiZO thin films determined by EDX and ICP-MS. The compositions of elements in the films at the three locations: top, middle, and bottom are determined by EDX. Please refer to the detailed EDX analysis in **Appendix A6.7**.

6.3.6 Crystallography

Diffraction patterns of all the films were acquired and calibrated against polycrystalline gold films (**Figure 6.38**). Diffraction patterns for SiZO and IZO were from relatively thick areas and the number of reflections in the pattern mirror that (**Figure 6.38**(a)) - both ZnO and InSiZO shows a smaller number of very bright reflections, suggesting fewer, thinner grains contributing.

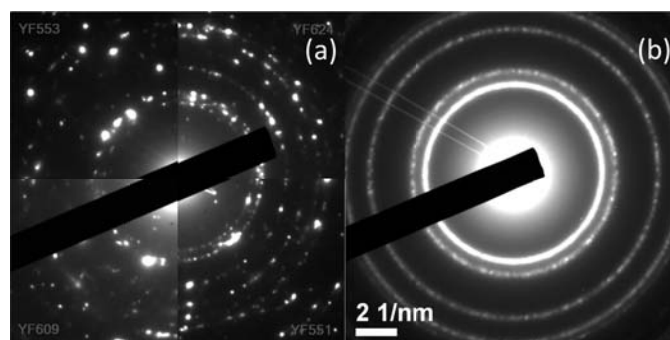

Figure 6.38: Montage of the 40 cm camera length diffraction patterns of the four films (a), working clockwise from top left: InSiZO, IZO, SiZO and ZnO. The calibration pattern from gold under identical conditions (b).

Comparison of the four patterns in above **Figure 6.38**(a) shows no extra reflections or rings that might suggest a change in crystallographic phase. In fact, all the reflections can be

accounted for by using a wurtzite ZnO unit cell for the all the allowed reflections. Please refer to **Appendix A.6.8** for details.

6.4 XPS Studies

The XPS wide survey spectra of ZnO, SiZO, IZO, and InSiZO thin films are shown in **Figure 6.39** showing the elemental compositions and the surrounding chemical environment on the surface of the films. The detected carbon C 1s peak is due to the absorption of carbon on the film surface when exposed to the ambient atmosphere. [31] The Zn $2p_{3/2}$ and Zn $2p_{1/2}$ peaks indicate the oxidation state of Zn is +2 for all these films. [32-34] The binding energies of Zn $2p_{3/2}$ and O 1s show the formation of ZnO. [35, 36] The incorporation of In is observed for IZO and InSiZO thin films with In $3d_{5/2}$ and In $3d_{3/2}$ peaks. [36-38] A small amount of Si is detected as Si 2p peaks for SiZO and InSiZO thin films. Meanwhile, Cl 2p peaks are also present in the XPS spectra for IZO and InSiZO thin films because Cl comes from $InCl_3$ in the starting materials dissolved into the precursor solutions.

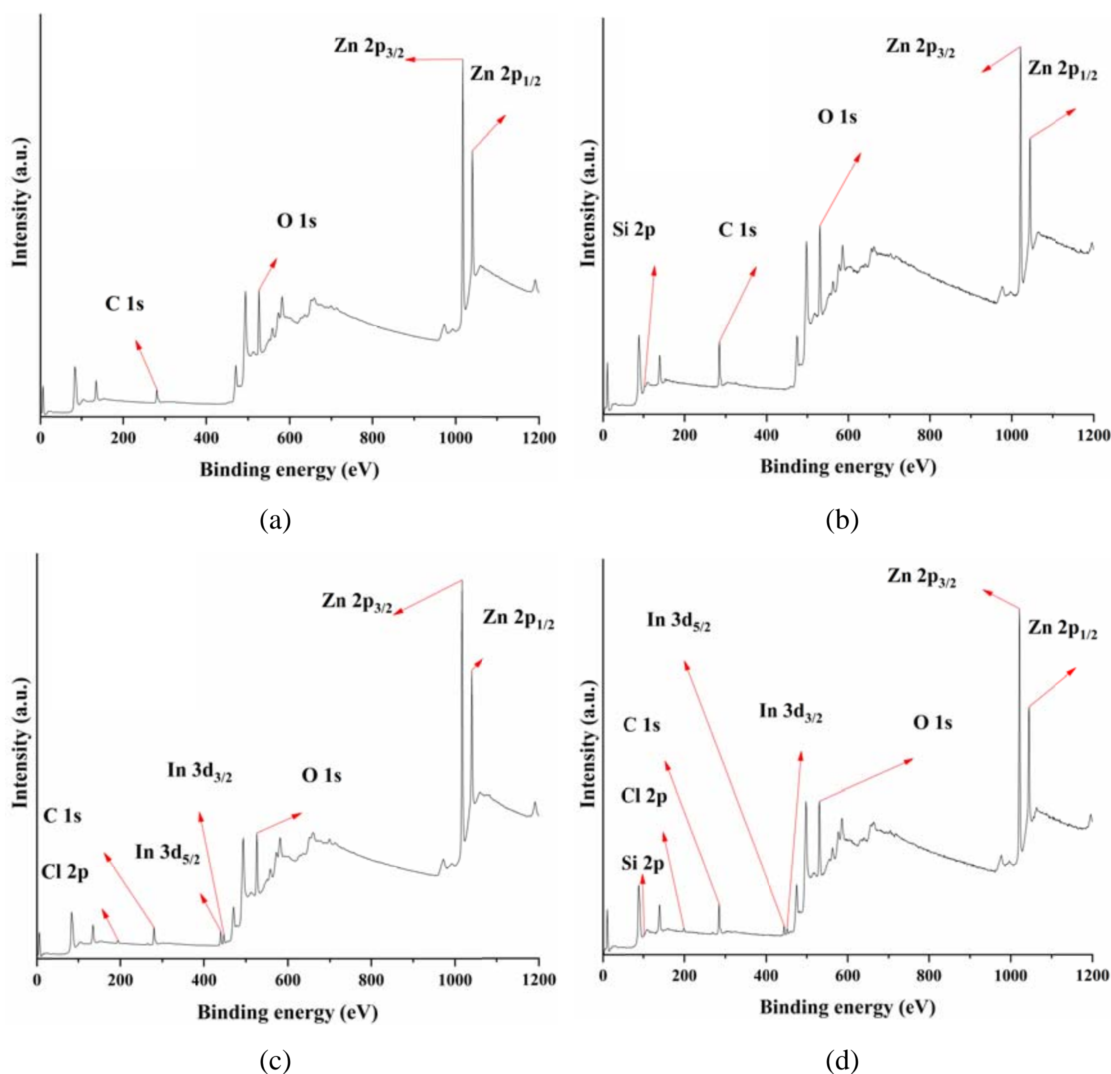

Figure 6.39: XPS wide survey spectra of ZnO (a), SiZO (0.6%) (b), IZO (2%) (c), and InSiZO (2% In-0.6% Si) (d) thin films.

The Si 2p peaks confirm the presence of Si in SiZO and InSiZO thin films, and the existence of In in IZO and InSiZO thin films is also indicated by the In 3d peaks in the XPS high resolution spectra (**Figure 6.40** and **Figure 6.41**). The Si 2p peaks are very weak but detectable in the range 101 - 103 eV, which correspond to oxidised Si. [39-42] The In $3d_{5/2}$ and In $3d_{3/2}$ peaks and their energy difference indicate the +3 oxidation state of In. [43, 44] The Si 2p/In 3d peaks are observed in all doped ZnO thin films containing Si/In.

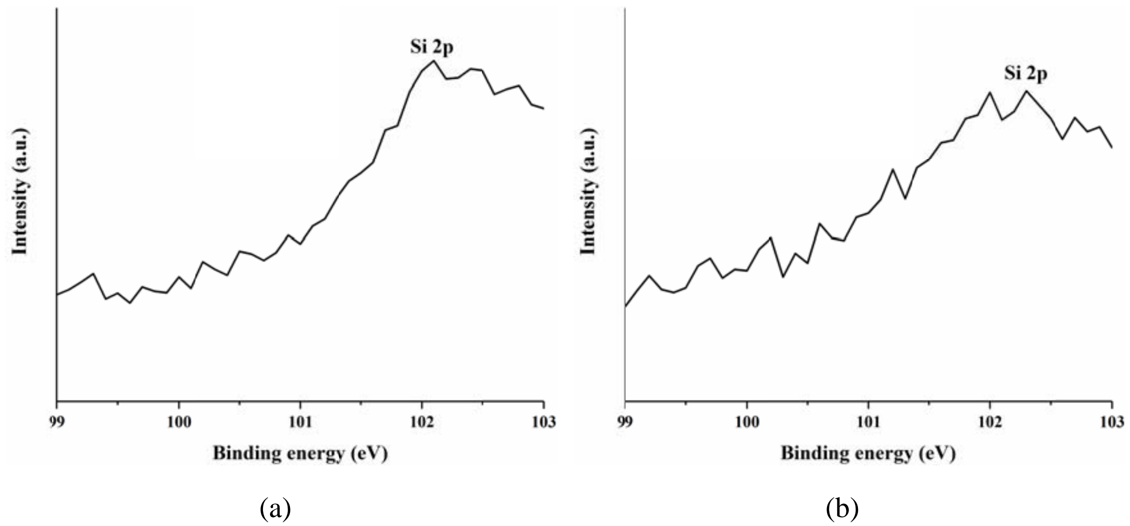

(a) (b)

Figure 6.40: XPS high resolution Si 2p spectra of SiZO (0.6% Si) (a) and InSiZO (2% In-0.6% Si) (b) thin films.

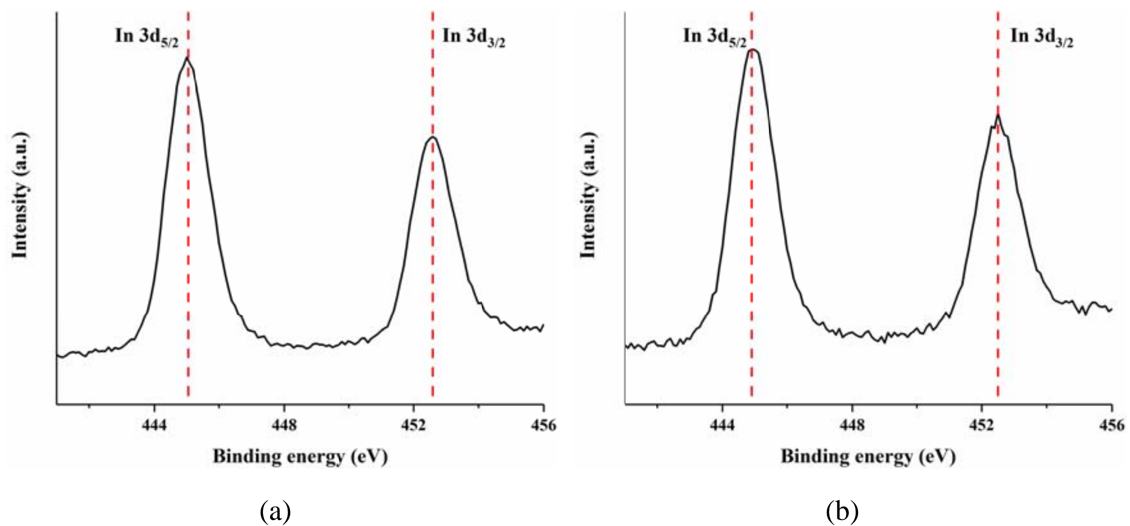

(a) (b)

Figure 6.41: XPS high resolution In 3d spectra of IZO (2% In) (a) and InSiZO (2% In-0.6% Si) (b) thin films.

The shifts of Zn $2p_{3/2}$, Zn $2p_{1/2}$, and O 1s peaks to higher binding energies for both singly and co-doped ZnO thin films are observed, compared to undoped ZnO thin films (**Figure 6.42**). The binding energy shifts are reliable since the XPS measurement error of binding energy is less than 0.1 eV. [45, 46] The shifts of these binding energies can be explained by the different electronegativity of Zn (1.65), Si (1.9), and In (1.78). [47] The valence electron density of Zn in the Zn-O-Si or Zn-O-In bond for singly or co-doped ZnO thin films is lower than that in

the Zn-O-Zn bond for undoped ZnO thin films when Si/In accepts electrons from Zn; therefore, the screening effect of electrons is weakened for Zn and strengthened for Si/In. Consequently, the binding energies of Zn $2p_{3/2}$, Zn $2p_{1/2}$ and O 1s become higher. [44, 48, 49] The binding energy shift for Zn 2p due to doping is also observed by Ahmad et al. [44], Zhu et al. [48], and Bae et al. [49]

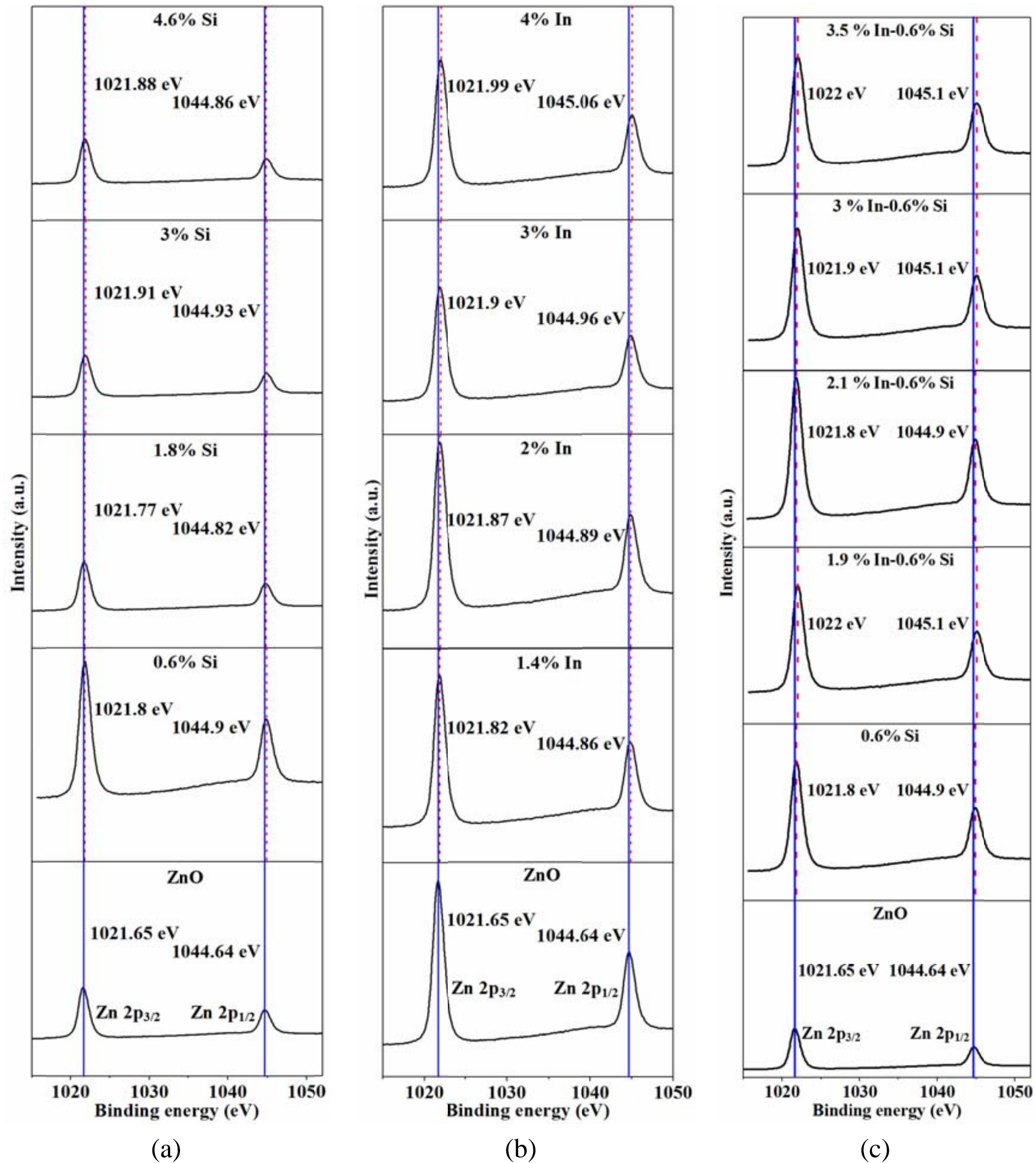

Figure 6.42: XPS high resolution Zn 2p spectra of SiZO (a), IZO (b), and InSiZO (In-0.6% Si) (c) thin films. Zn $2p_{3/2}$ and Zn $2p_{1/2}$ peaks are shown as blue and red lines for ZnO and doped ZnO thin films, respectively. Their binding energies are also labelled.

The O 1s deconvoluted spectra of ZnO, SiZO, and IZO thin films are shown in **Figure 6.43**. The O 1s peak is fitted according to four components. The lowest binding energy peak O_I is the O^{2-} directly linked to metal ions in the ZnO. [31, 34] The medium energy peak O_{II} is the oxygen near vacancies (oxygen deficiency region) in the ZnO. The highest two peaks O_{III} and O_{IV} are chemisorbed species such as the hydroxyls oxygen [50] and the carbonyl oxygen, respectively. [48, 51] The shifts of O 1s peaks to higher binding energies for doped thin films compared to undoped ZnO thin films are due to the different electronegativity of Zn, Si, and In as discussed before, which are also observed by Zhu et al. [48] The area ratio of O_{II} / O_{total} is obtained to investigate the oxygen vacancies in the films as shown in **Table 6.2**. The values are 17% and more than 20% for ZnO and SiZO/IZO thin films, respectively. It indicates that doped thin films have more oxygen vacancies than undoped ZnO thin films. [48, 52]

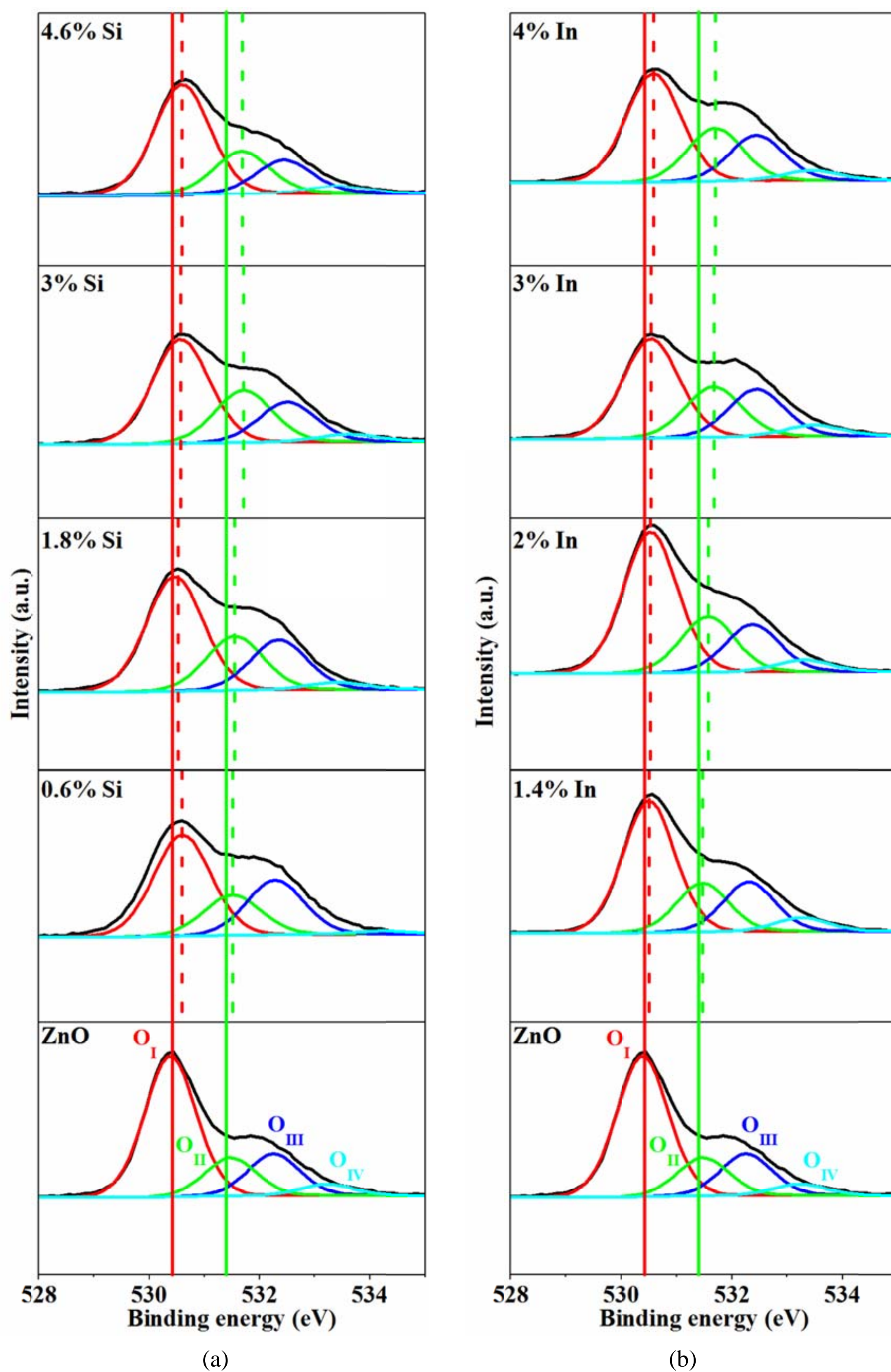

Figure 6.43: XPS high resolution O 1s spectra of SiZO (a) and IZO (b) thin films. O_I and O_{II} peaks are shown as red and green straight lines for all the films, respectively.

	ZnO	SiZO (0.6%)	SiZO (1.8%)	SiZO (3%)	SiZO (4.6%)
O_{II} / O_{total} (%)	17	20	24	26	24
	ZnO	IZO (1.4%)	IZO (2%)	IZO (3%)	IZO (4%)
O_{II} / O_{total} (%)	17	20	22	24	24

Table 6.2: The ratio of O_{II} area to the total area ($O_I + O_{II} + O_{III} + O_{IV}$) for ZnO, SiZO, and IZO thin films calculated from XPS high resolution spectra.

We can observe the presence of Cl in the XPS wide survey spectra of IZO and InSiZO thin films. The XPS high resolution Cl 2p spectra of one example of IZO thin films are shown in **Figure 6.44** to investigate the Cl compounds. Cl 2p represents inorganic chlorine with a binding energy of < 199 eV and represents an organic chlorine bond with a value of > 200 eV (C-Cl). [53-55] In our samples, it is likely to be inorganic chlorine (metal chloride) with peaks around 199 eV. The similar Cl 2p peaks are observed in all doped IZO and InSiZO thin films.

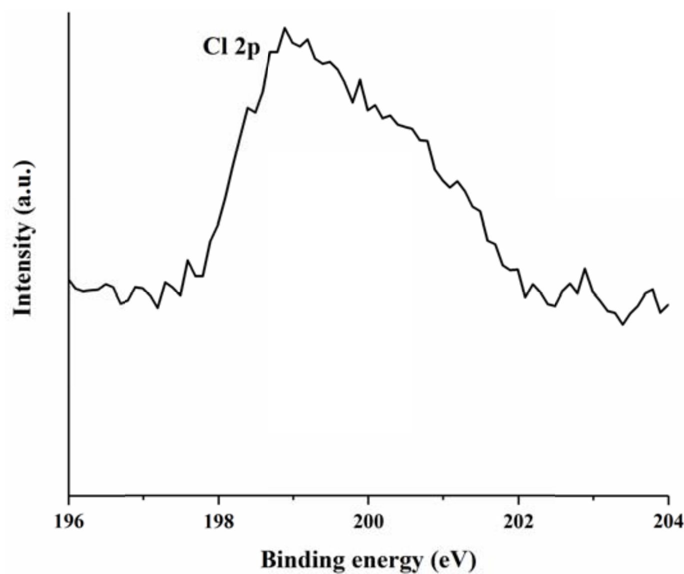

Figure 6.44: XPS high resolution Cl 2p spectra of IZO (2%) thin films.

6.5 Conclusions

In **Chapter 4** and **Chapter 5**, I have found that Si and In are both suitable elements for doping into ZnO thin films to enhance their electrical properties and to maintain good visible transparencies. These two key properties are dependent on their structures including elemental compositions, morphologies, grain growths, etc. XRD data shows that the preferred orientation or the texture of a film is highly affected by the impurity dopants. The preferred orientation depends on the balance between the kinetic and thermodynamic processes involved in the film deposition. The texture is affected by the minimisation of surface free energy which depends on the hybridisation of the atoms in the films. [2-6] Si does not change the preferred orientation of ZnO thin films; therefore, SiZO thin films keep the (002) preferred orientation of ZnO thin films. However, In changes the preferred orientation from (002) to (100) or (101) for IZO or InSiZO thin films. It indicates that the preferred orientations of InSiZO thin films are dominated by the In concentrations and not the Si concentrations, which is similar to that of electrical properties as discussed in **Chapter 4**. [56] Rashidi [57] reported the contraction of the ZnO lattice due to the Si doping into ZnO at low Si doping levels (< 0.6%). However, the expansion of the unit cell occurs for SiZO with the Si concentration higher than 0.6%. Wu et al. calculated the formation energy for SiZO showing that Si^{4+} ions prefer to substitute Zn^{2+} sites instead of occupying interstitial sites. [9, 10] The contraction of the unit cell is due to the substitution of Zn ions by smaller Si ions for low Si doped ZnO [11]. However, the expansion of the unit cell may due to the interstitial occupancy of Si in the lattice for heavily Si doped ZnO. The case of In is similar to that of Si, whereas, the substitution of Zn^{2+} ions by larger In^{3+} ions [11] in the ZnO lattice contributes to the lattice expansion. In^{3+} ions prefer to substitute Zn^{2+} sites instead of occupying interstitial sites. [9, 10] Therefore, the significant expansion of the unit cell happens for IZO thin films. The expansion of the InSiZO lattice can be explained in way for of IZO thin films. The parameters of the ZnO lattice suggest a limit of In substitution with Zn in the lattice which in turn limit the increase in free carrier electrons for conductivity if higher amounts of In occupy interstitial rather than substitutional sites. The best carrier concentrations and conductivities

are also achieved at 2% In for IZO and InSiZO thin films.

The thickness dependence of the film structures is interesting because it is possible to make very thin ZnO films by the spray pyrolysis technique with a visible transmittance of 97% corrected for the glass substrate. Film thickness does not affect the preferred orientation for all the films. The film performance for various thickness can be attributed to a misalignment of the grains along the preferred orientation due to the competition in the growth of neighbouring crystals as reported by Barna et al. [22] Thinner films have smaller crystallite sizes for either singly doped or co-doped ZnO thin films. [20] Al-Khawaja et al. [20] found that the stress values decrease with increased thicknesses, which are consistent with increased gain sizes; therefore, the smaller stress values correspond to larger grain sizes. The contact between the amorphous glass substrate and the films leads to a higher stress value for thinner films. The stress in thicker films is smaller attributed to the contact as a buffer. [18]

AFM images show that increasing Si/In concentrations can smooth singly doped thin films. The AFM and SEM images also indicate that the grain size decreases as the Si/In concentration increases for singly doped thin films. Co-doped thin films are still as smooth as singly doped thin films. However, the correlation between the grain size and the dopant concentration is more complicated compared to singly doped thin films. It should be emphasised that the different definitions of 'grain size' is attributed to different measurement methods. The SEM grain size means the distance of adjacent visible grain boundaries, whereas it means the coherent X-ray diffracting distance in the crystal lattice for the XRD crystallite size, which is a smaller scale than that of SEM. [20] The observed SEM grains are more likely to be clusters composed of small crystallites. Therefore, the variation tendencies of these two types of grain sizes do not need to be necessarily the same. These crystal growth structures are related to the preferred orientations of the crystallites but not determined by the crystallites (**Figure 6.16**). The crystal growth structures observed by SEM show the clusters or the packing of crystallites, not the small crystallites themselves. The clusters or the packing can directly reflect the crystallite structures only when the crystallites are packed in a highly

ordered way.

AFM and SEM images show the films become smoother and their grain sizes become smaller for reduced film thicknesses for both singly doped and co-doped films. The increased surface roughness for thicker films can be attributed to the asymmetric growth of the crystals, which is also observed by Gonçalves et al. [18] and Bang et al. [29] The grains can only grow in two dimensions for thinner films, whereas they have a possibility to grow in the third dimension where a space is available for thicker films. The increased dimension leads to an increased grain size for thicker films. [23, 25] The positive correlation between surface roughnesses and film thicknesses is mainly due to the grain size variations. [30] Some films can be almost amorphous such as SiZO (0.6%) thin films with the thickness of ~ 150 nm.

TEM studies show that undoped, singly doped, and co-doped ZnO thin films are comprised of polycrystalline wurtzite ZnO. The films are reasonably compact, with crystal grains abutting each other without an amorphous intergranular phase. Voids are present at triple and quadruple-grain junctions. All the three films show large irregular prismatic grains with large degrees of concavity except for co-doped ZnO thin films. Co-doped films alone exhibit stable growth of individual grains that thread the film entirely, i.e., from nucleating layer to top surface. These ‘super grains’ grow steadily throughout the film leading to large hillocks of single crystal at the top surface. All diffraction patterns concur with the wurtzite polytype of ZnO. IZO and InSiZO show a reasonably constant level of Si or In throughout the films, whereas, the distribution of Si is uneven along the normal direction of the films for SiZO as shown by EDX. It indicates that the distribution of elements in the films is not always uniform.

XPS studies confirm the formation of ZnO in all the films. SiZO and InSiZO thin films contain Si, and In exists in IZO and InSiZO thin films. Cl is also present in IZO and InSiZO thin films, which comes from $InCl_3$ in the starting materials dissolved into the precursor solutions. The XPS high resolution Cl 2p spectra show that metal chloride can possibly exist

on the surface of IZO as well as InSiZO thin films. [33, 38, 53-55] The Zn $2p_{3/2}$, Zn $2p_{1/2}$, and O 1s peaks for singly doped and co-doped ZnO thin films shift to higher binding energies, in contrast to undoped ZnO thin films, which can be explained by the different electronegativity of Zn, Si, and In as discussed in this chapter. [44, 47-49] The area ratio of O_{II} / O_{total} indicates that doped thin films have more oxygen vacancies than undoped ZnO thin films. [48, 52]

References

[1] Barrett, C. S. 1980. *Structure of Metals : Crystallographic Methods, Principles and Data,* Oxford; New York, Pergamon.

[2] Pinot, Y., Tuilier, M. H., Pac, M. J., Rousselot, C., Thiaudière, D. & Ulhaq-Bouillet, C. 2018. Influence of Film Thickness on the Structural Transition Cubic/Hexagonal Within Ti0.38Al0.62N Films. *Thin Solid Films,* 649**,** 160-166.

[3] Zhou, H., Wu, L., Wang, H., Zheng, J., Zhang, L., Kisslinger, K., Li, Y., Wang, Z., Cheng, H., Ke, S., Li, Y., Kang, J. & Zhu, Y. 2017. Interfaces Between Hexagonal and Cubic Oxides and Their Structure Alternatives. *Nature Communications,* 8**,** 1474.

[4] Al-Kuhaili, M. F., Durrani, S. M. A., Bakhtiari, I. A. & Saleem, M. 2012. Optical Constants of Vacuum Annealed Radio Frequency (RF) Magnetron Sputtered Zinc Oxide Thin Films. *Optics Communications,* 285**,** 4405-4412.

[5] Mahmood, A., Ahmed, N., Raza, Q., Khan, T. M., Mehmood, M., Hassan, M. M. & Mahmood, N. 2010. Effect of Thermal Annealing on the Structural and Optical Properties of ZnO Thin Films Deposited by the Reactive E-Beam Evaporation Technique. *Physica Scripta,* 82**,** 065801.

[6] Bouderbala, M., Hamzaoui, S., Adnane, M., Sahraoui, T. & Zerdali, M. 2009. Annealing Effect on Properties of Transparent and Conducting ZnO Thin Films. *Thin Solid Films,* 517**,** 1572-1576.

[7] Fusella, M. A., Schreiber, F., Abbasi, K., Kim, J. J., Briseno, A. L. & Rand, B. P. 2017. Homoepitaxy of Crystalline Rubrene Thin Films. *Nano Letters,* 17**,** 3040-3046.

[8] Fujimura, N., Nishihara, T., Goto, S., Xu, J. & Ito, T. 1993. Control of Preferred Orientation for ZnOx Films: Control of Self-Texture. *Journal of Crystal Growth,* 130**,** 269-279.

[9] Wu, H., Peng, Y. & Shen, T. 2012. Electronic and Optical Properties of Substitutional and Interstitial Si-Doped ZnO. *Materials,* 5**,** 2088.

[10] Körner, W. & Elsässer, C. 2011. Density Functional Theory Study for Polycrystalline ZnO Doped with Si or Nb. *Physical Review B,* 83**,** 205306.

[11] Shannon, R. D. 1976. Revised Effective Ionic Radii and Systematic Studies of Interatomic Distances in Halides and Chalcogenides. *Acta Crystallographica Section A,* 32**,** 751-767.

[12] Vai, A. T. 2015. *Performance Limitations in Practical Transparent Conducting Oxide Thin Films.* University of Oxford.

[13] Joseph, B., Manoj, P. K. & Vaidyan, V. K. 2005. Studies on Preparation and Characterization of Indium Doped Zinc Oxide Films by Chemical Spray Deposition. *Bulletin of Materials Science,* 28**,** 487-493.

[14] Goyal, D. J., Agashe, C., Takwale, M. G., Marathe, B. R. & Bhide, V. G. 1992. Development of Transparent and Conductive ZnO Films by Spray Pyrolysis. *Journal of Materials Science,* 27**,** 4705-4708.

[15] Hadri, A., Nassiri, C., Chafi, F., Loghmarti, M., Fares, B., Laanab, L., Chraibi, F., Bensitel, M. & Mzerd, A. 2014. Indium Doping Effect on Structural, Optical and Electrical Properties of Sprayed ZnO Thin Films. *Sensors & Transducers,* 178**,** 63.

[16] Ilican, S., Caglar, Y., Caglar, M. & Demirci, B. 2008. Polycrystalline Indium-Doped

ZnO Thin Films: Preparation and Characterization. *Journal of Optoelectronics and Advanced Materials,* 10**,** 2592-2598.

[17] Ilican, S., Caglar, Y., Caglar, M. & Yakuphanoglu, F. 2006. Electrical Conductivity, Optical and Structural Properties of Indium-Doped ZnO Nanofiber Thin Film Deposited by Spray Pyrolysis Method. *Physica E: Low-dimensional Systems and Nanostructures,* 35**,** 131-138.

[18] Gonçalves, R. S., Barrozo, P., Brito, G. L., Viana, B. C. & Cunha, F. 2018. The Effect of Thickness on Optical, Structural and Growth Mechanism of ZnO Thin Film Prepared by Magnetron Sputtering. *Thin Solid Films,* 661**,** 40-45.

[19] Shariffudin, S. S., Salina, M., Herman, S. H. & Rusop, M. 2012. Effect of Film Thickness on Structural, Electrical, and Optical Properties of Sol-Gel Deposited Layer-By-Layer ZnO Nanoparticles. *Transactions on Electrical and Electronic Materials,* 13**,** 102-105.

[20] Al-Khawaja, S., Abdallah, B., Abou Shaker, S. & Kakhia, M. 2015. Thickness Effect on Stress, Structural, Electrical and Sensing Properties of (0 0 2) Preferentially Oriented Undoped ZnO Thin Films. *Composite Interfaces,* 22**,** 221-231.

[21] Lin, S. & Huang, J. 2004. Effect of Thickness on the Structural and Optical Properties of Zno Films by R.F. Magnetron Sputtering. *Surface and Coatings Technology,* 185**,** 222-227.

[22] Barna, P. B. & Adamik, M. 1998. Fundamental Structure Forming Phenomena of Polycrystalline Films and the Structure Zone Models. *Thin Solid Films,* 317**,** 27-33.

[23] Shewale, P. S., Agawane, G. L., Shin, S. W., Moholkar, A. V., Lee, J. Y., Kim, J. H. & Uplane, M. D. 2013. Thickness dependent H2S sensing properties of nanocrystalline ZnO thin films derived by advanced spray pyrolysis. *Sensors and Actuators B: Chemical,* 177**,** 695-702.

[24] Sharma, M. & Mehra, R. M. 2008. Effect of Thickness on Structural, Electrical, Optical and Magnetic Properties of Co and Al Doped ZnO Films Deposited by Sol–Gel Route. *Applied Surface Science,* 255**,** 2527-2532.

[25] Bouderbala, M., Hamzaoui, S., Amrani, B., Reshak, A. H., Adnane, M., Sahraoui, T. & Zerdali, M. 2008. Thickness Dependence of Structural, Electrical and Optical Behaviour of Undoped ZnO Thin Films. *Physica B: Condensed Matter,* 403**,** 3326-3330.

[26] Vijayan, T. A., Chandramohan, R., Valanarasu, S., Thirumalai, J., Venkateswaran, S., Mahalingam, T. & Srikumar, S. R. 2008. Optimization of Growth Conditions of ZnO Nano Thin Films by Chemical Double Dip Technique. *Science and Technology of Advanced Materials,* 9**,** 035007.

[27] Tsai, C., Lai, J., Feng, S., Huang, C., Chen, C., Yang, F., Wang, H. & Tu, L. 2017. Growth and Characterization of Textured Well-Faceted ZnO on Planar Si(100), Planar Si(111), and Textured Si(100) Substrates for Solar Cell Applications. *Beilstein Journal of Nanotechnology,* 8**,** 1939-1945.

[28] Lee, J. & Park, B. 2003. Transparent Conducting ZnO:Al, In and Sn Thin Films Deposited by the Sol-Gel Method. *Thin Solid Films,* 426**,** 94-99.

[29] Bang, K., Hwang, D. & Myoung, J. 2003. Effects of ZnO Buffer Layer Thickness on Properties of ZnO Thin Films Deposited by Radio-Frequency Magnetron Sputtering.

Applied Surface Science, 207**,** 359-364.

[30] Liang, G., Fan, P., Cai, X., Zhang, D. & Zheng, Z. 2011. The Influence of Film Thickness on the Transparency and Conductivity of Al-Doped ZnO Thin Films Fabricated by Ion-Beam Sputtering. *Journal of Electronic Materials,* 40**,** 267-273.

[31] Al-Gaashani, R., Radiman, S., Daud, A. R., Tabet, N. & Al-Douri, Y. 2013. XPS and Optical Studies of Different Morphologies of ZnO Nanostructures Prepared by Microwave Methods. *Ceramics International,* 39**,** 2283-2292.

[32] Zheng, J. H., Jiang, Q. & Lian, J. S. 2011. Synthesis and Optical Properties of Flower-Like ZnO Nanorods by Thermal Evaporation Method. *Applied Surface Science,* 257**,** 5083-5087.

[33] Moulder, J. F., Chastain, J. & King, R. C. 1995. *Handbook of X-Ray Photoelectron Spectroscopy: A Reference Book of Standard Spectra for Identification and Interpretation of XPS Data,* Eden Prairie, Physical Electronics.

[34] Das, J., Pradhan, S. K., Sahu, D. R., Mishra, D. K., Sarangi, S. N., Nayak, B. B., Verma, S. & Roul, B. K. 2010. Micro-Raman and XPS Studies of Pure ZnO Ceramics. *Physica B: Condensed Matter,* 405**,** 2492-2497.

[35] Inamdar, A. I., Mujawar, S. H., Barman, S. R., Bhosale, P. N. & Patil, P. S. 2008. The Effect of Bath Temperature on the Electrodeposition of Zinc Oxide Thin Films via an Acetate Medium. *Semiconductor Science and Technology,* 23**,** 085013.

[36] Kyaw, A. K. K., Wang, Y., Zhao, D. W., Huang, Z. H., Zeng, X. T. & Sun, X. W. 2011. The Properties of Sol-Gel Processed Indium-Doped Zinc Oxide Semiconductor Film and Its Application in Organic Solar Cells. *Physica Status Solidi (A),* 208**,** 2635-2642.

[37] Maira, G. K., Orton, B. R. & Riviere, J. C. 1987. An XPS Study of Indium Through the Melting Point. *Journal of Physics F: Metal Physics,* 17**,** 1999.

[38] Lee, D. Y. & Chung, C. W. 2009. Etch Characteristics of Indium Zinc Oxide Thin Films Using Inductively Coupled Plasma of A Cl2/Ar gas. *Thin Solid Films,* 517**,** 4047-4051.

[39] Alfonsetti, R., Lozzi, L., Passacantando, M., Picozzi, P. & Santucci, S. 1993. XPS Studies on SiOx Thin Films. *Applied Surface Science,* 70-71**,** 222-225.

[40] Lin, J., Chiu, H., Lin, Y., Wen, T., Patil, R. A., Devan, R. S., Chen, C., Shiu, H., Liou, Y. & Ma, Y. 2013. Electrical and Chemical Characteristics of Probe-Induced Two-Dimensional SiOx Protrusion Layers. *Applied Physics Letters,* 102**,** 031603.

[41] He, J. W., Xu, X., Corneille, J. S. & Goodman, D. W. 1992. X-Ray Photoelectron Spectroscopic Characterization of Ultra-Thin Silicon Oxide Films on a Mo(100) Surface. *Surface Science,* 279**,** 119-126.

[42] Thøgersen, A., Selj, J. H. & Marstein, E. S. 2012. Oxidation Effects on Graded Porous Silicon Anti-Reflection Coatings. *Journal of the Electrochemical Society,* 159**,** D276-D281.

[43] Bae, S. Y., Na, C. W., Kang, J. H. & Park, J. 2005. Comparative Structure and Optical Properties of Ga-, In-, and Sn-Doped ZnO Nanowires Synthesized via Thermal Evaporation. *The Journal of Physical Chemistry B,* 109**,** 2526-2531.

[44] Ahmad, M., Zhao, J., Xie, L., Mo, R., Zhu, J., Iqbal, J. & Miao, W. 2009. Conductivity Enhancement by Slight Indium Doping in ZnO Nanowires for Optoelectronic Applications. *Journal of Physics D: Applied Physics,* 42**,** 7.

[45] Deshkovskaya, A. & Shchukarev, A. XPS Study of Fluorine Implantation Induced Centres in Fused Silica. Interaction of Radiation with Solids Proceedings of the 10th International Conference, 2013 Belarus. 384.

[46] Radnik, J., Mohr, C. & Claus, P. 2003. On the Origin of Binding Energy Shifts of Core Levels of Supported Gold Nanoparticles and Dependence of Pretreatment and Material Synthesis. *Physical Chemistry Chemical Physics,* 5**,** 172-177.

[47] Emsley, J. 1995. *The Elements Oxford Chemistry Guides,* New York, Oxford University Press.

[48] Zhu, Z., Li, B., Wen, J., Chen, Z., Chen, Z., Zhang, R., Ye, S., Fang, G. & Qian, J. 2017. Indium-Doped Zno Horizontal Nanorods for High On-Current Field Effect Transistors. *RSC Advances,* 7**,** 54928-54933.

[49] Bae, S. Y., Choi, H. C., Na, C. W. & Park, J. 2005. Influence of in Incorporation on the Electronic Structure of Zno Nanowires. *Applied Physics Letters,* 86**,** 033102.

[50] Zhou, H. & Li, Z. 2005. Synthesis of Nanowires, Nanorods and Nanoparticles of ZnO Through Modulating the Ratio of Water to Methanol by Using a Mild and Simple Solution Method. *Materials Chemistry and Physics,* 89**,** 326-331.

[51] Forget, A., Tucker, R. T., Brett, M. J., Limoges, B. & Balland, V. 2015. Tuning the reactivity of nanostructured indium tin oxide electrodes toward chemisorption. *Chemical Communications,* 51**,** 6944-6947.

[52] Han, Y., Yan, H., Tsai, Y., Li, Y., Zhang, Q. & Shieh, H. D. 2016. Influences of Nitrogen Doping on the Electrical Characteristics of Indium-Zinc-Oxide Thin Film Transistors. *IEEE Transactions on Device and Materials Reliability,* 16**,** 642-646.

[53] Yang, B., Cao, Y., Qi, F., Li, X. & Xu, Q. 2015. Atrazine Adsorption Removal with Nylon6/Polypyrrole Core-Shell Nanofibers Mat: Possible Mechanism and Characteristics. *Nanoscale Research Letters,* 10**,** 207.

[54] Binner, E., Facun, J., Chen, L., Ninomiya, Y., Li, C. & Bhattacharya, S. 2011. Effect of Coal Drying on the Behavior of Inorganic Species during Victorian Brown Coal Pyrolysis and Combustion. *Energy & Fuels,* 25**,** 2764-2771.

[55] Jamil, K., Hayashi, J. & Li, C. 2004. Pyrolysis of a Victorian Brown Coal and Gasification of Nascent Char in CO2 Atmosphere in a Wire-Mesh Reactor. *Fuel,* 83**,** 833-843.

[56] Bae, J. H. & Kim, H. K. 2008. Characteristics of Al Doped ZnO Co-Sputtered InZnO Anode Films Prepared by Direct Current Magnetron Sputtering for Organic Light-Emitting Diodes. *Thin Solid Films,* 516**,** 7866-7870.

[57] Rashidi-Alavijeh, N. 2015. *Cation and Anion Doping of ZnO Thin Films by Spray Pyrolysis.* University of Oxford.

Chapter 7

Summary Discussion and Conclusions

7.1 Summary Discussion

7.1.1 The Metal-Insulator Transition

The metal-insulator transition (MIT) reflects a natural process in which highly conducting metals can be transformed into low conductivity insulators, also called non-metals, and vice versa. A letter from Sir Nevill Mott to Professor Peter P. Edwards stated the fact, '*...a metal conducts, and a non-metal doesn't*' [1] - albeit, at the absolute zero of temperature. By following the ideas of Mott, and also Edwards[1], the conductivity of metals tends to a finite value approaching the absolute zero of temperature, while the conductivity of non-metals tends to zero at the limit of the absolute zero of temperature. However, substantial differences can also be observed even at room temperature. **Figure 7.1** shows a wide range of 28 orders of magnitude in the variations of electrical conductivities for metals and non-metals.

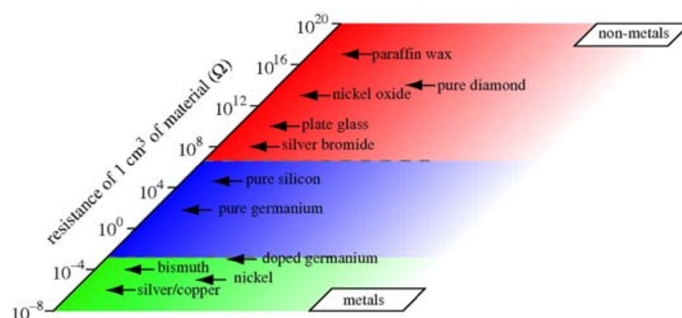

Figure 7.1: The room temperature electrical resistivities of materials including metals and non-metals. Republished with permission from Edwards [1] et al. and Ehrenreich [2]; permission conveyed through Copyright Clearance Center, Inc.

A MIT can occur through changes in temperature, pressure and - the main subject of this work - by changes in the chemical composition of intentionally doped TCOs. These changes can be viewed in the context of an increasing impurity or dopant concentration which increases the current-carrying electron concentration.

Figure 7.2 is taken from the work of Vai et al. [3] which attempts to summarise the two

essential aspects. Thus, electrons can be thermally excited into the conduction band from impurity states at high (typically room) temperature where the impurity or donor states lie close to the conduction band (within $k_B\mathbf{T}$ of the band). Thus in this case all donor states lying close to the conduction band (so-called ‘shallow donors’) are ionised by thermal energy into the host (ZnO) conduction band. However, a dramatically different situation occurs at low temperatures. There, the associated impurity or donor wavefunctions can be localised at a low donor concentration. but then delocalised at a high donor concentration through the concentration-induced MIT occurring exclusively in an ‘impurity band’ derived from the direct (or indirect) overlap of the donor state wavefunctions. In this situation electronic conduction within the impurity band occurs when electrons hop from the constituent impurity states by quantum-mechanical tunnelling. The overlap of the wavefunctions of impurity states is of course highly sensitive to the donor/impurity concentration.

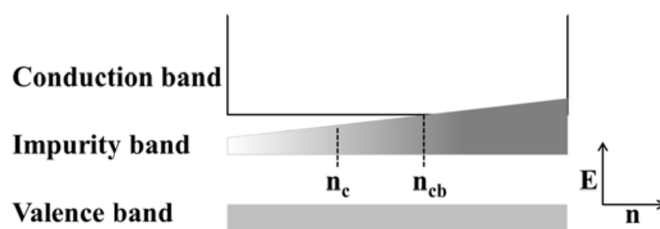

Figure 7.2: Schematic of impurity band conduction for various carrier concentrations. n_c is the critical carrier concentration where a MIT occurs, and n_{cb} is the carrier concentration where impurity band merges with the conduction band. Republished with permission from Vai et al. [3]; permission conveyed through Copyright Clearance Center, Inc.

Mott suggested that the free carriers become completely delocalised by increasing the impurity concentration in this way, resulting in a MIT. The venerable Mott criterion [4, 5] describes the critical carrier concentration $n_c^{1/3}$ where a MIT occurs, which is expressed as below.

$$n_c^{1/3} a_H^* \approx 0.26$$

Equation 7.1

Where a_H^* is the effective Bohr radius of the isolated impurity state at low concentrations. The value 0.26 is suggested by the extensive analysis of the Mott criterion by Edwards and Sienko and compiled here as a so-called Mott-Edwards-Sienko plot [6], which summarises a wide range of materials which undergo a MIT with changes in electron concentration. (**Figure 7.3**)

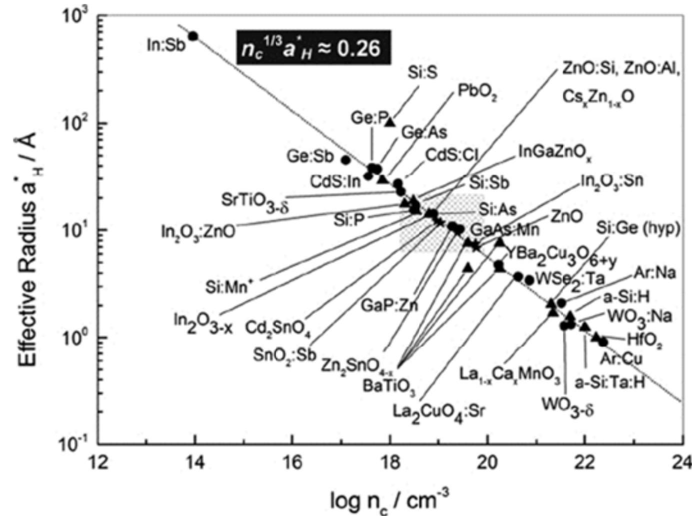

Figure 7.3: Mott-Edwards-Sienko plot showing the relationship between the effective Bohr radius a_H^* and the critical carrier concentration n_c for MIT. The shaded region includes the surveyed TCOs. The data are from [3, 7-16]. The plot is republished with permission from Vai et al. [3]; permission conveyed through Copyright Clearance Center, Inc. which originates from Edwards and Sienko. [16]

We have not carried out extensively low temperature measurements, but the variable temperature Hall effect measurements of typical undoped and doped ZnO thin films in this thesis are shown in **Figure 7.4**. The carrier concentrations of the films increase with increasing temperature when $n_{RT} = 1.1 \times 10^{19}$ cm^{-3}, i.e., $< 1 \times 10^{20}$ cm^{-3}.

These data are consistent with the thermal excitation of electrons into delocalised conduction band states. The fact that the carrier concentrations remains constant with increasing temperature for higher n_{RT} values points to the fact that in this concentration regime, and over this temperature range, all carriers are ionised into the host (ZnO) conduction band. [17] It

shows that the donor electrons can be easily delocalised resulting in electronic conduction.

The mobilities of these films increase with increasing temperature, whereas the magnitudes of the change are larger for smaller n_{RT} values. (**Figure 7.4**(b)) This behaviour I attribute to the grain boundary effects in these polycrystalline thin films will be discussed later.

The overall contributions of both carrier concentrations and mobilities as a function of temperature show as resistivities in **Figure 7.4**(c). The magnitudes of the change are larger for smaller n_{RT} values. Importantly, the difference of resistivity values between the least conductive films (i.e., ZnO) and other doped films is magnified at lower temperature compared with higher temperature.

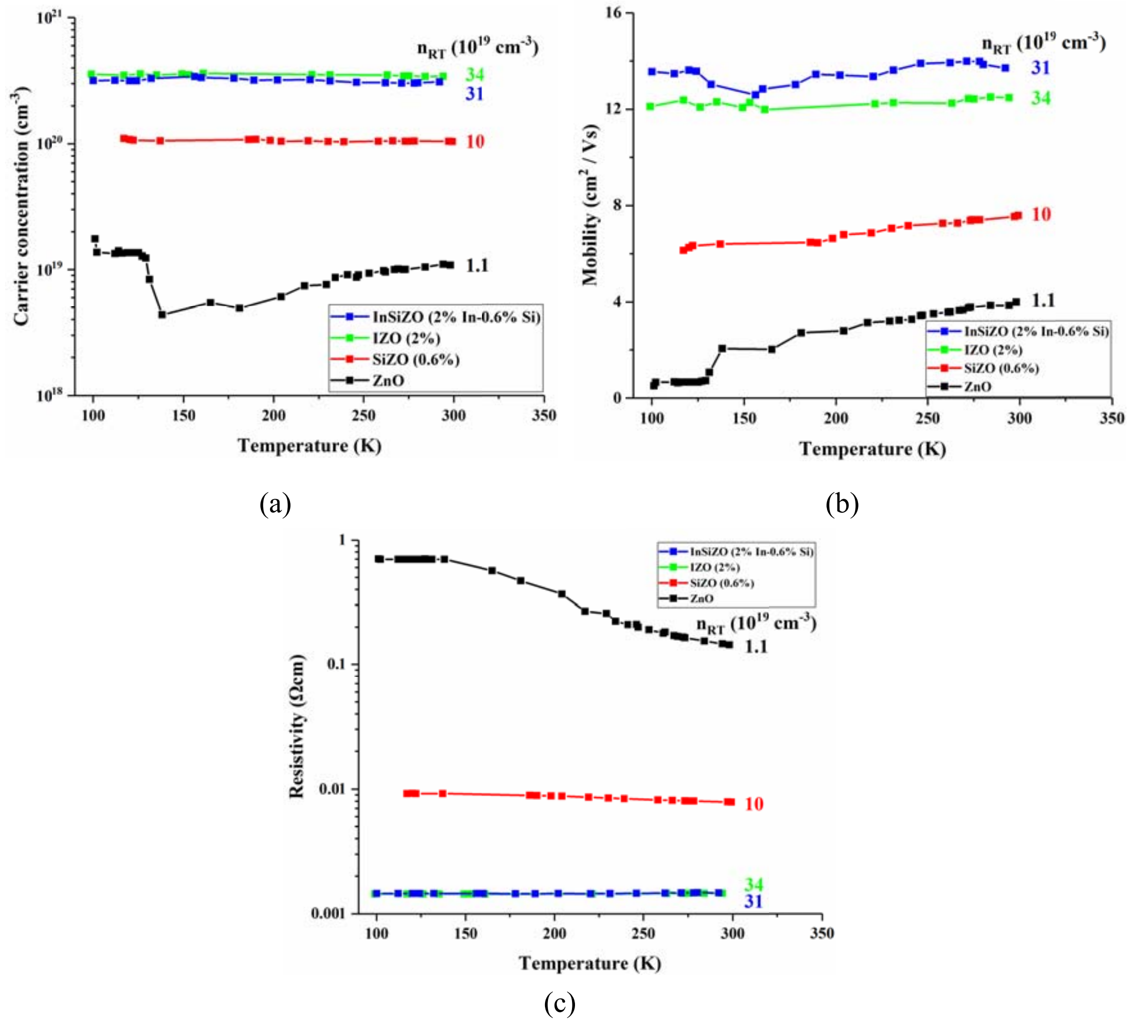

Figure 7.4: Hall effect carrier concentrations (a), mobilities (b), and resistivities (c) as a function of temperature for undoped and doped ZnO thin films with the indicated carrier concentrations n_{RT} at room temperature.

Ioffe and Regel [18] argued that the mean free path of current carriers l_e must be larger than the interatomic spacing for the carriers transporting through a material; therefore the classical picture of electronic conduction fails when the mean free path of carriers approaches the typical values of the interatomic spacing. It is generally assumed that the electrons become delocalised and a MIT occurs when $k_F l_e = 1$, [19] which is known as Ioffe-Regel criterion [20] and can be expressed as below.

$$k_F l_e = \frac{\hbar(3\pi^2)^{2/3}}{e^2 \rho n^{1/3}}$$

Equation 7.2

Where k_F is the Fermi wavenumber, ħ is the reduced Planck constant, e is the electron carrier charge, and ρ and n are the resistivity and carrier concentration at a given temperature, respectively. I can estimate the critical carrier concentration n at $k_F l_e = 1$ where a MIT occurs. However, the electron states are localised when $k_F l_e \ll 1$.

The Ioffe-Regel criterion expressed in **Equation 7.2** does not take extrinsic limits such as grain boundary effects into account. **Figure 7.5** shows the Ioffe-Regel parameters $k_F l_e$ as a function of carrier concentrations of zinc-based samples in this thesis. The critical carrier concentration for these doped ZnO thin films is then predicted to be 0.71 - 1.2 × 10^{20} cm^{-3} when a MIT occurs. The similar values were also observed by Vai and Rashidi in zinc-based TCOs. [21, 22] However, the critical carrier concentration deduced from the Ioffe-Regel criterion is an overestimate since the data are collected in room temperature. In addition, as I will illustrate, grain boundary effects can also increase the measured resistivity for any given carrier concentration.

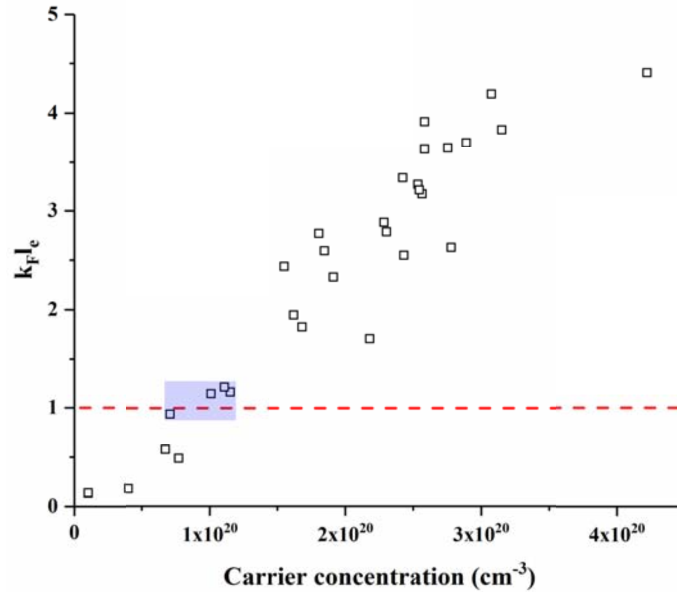

Figure 7.5: The Ioffe-Regel parameters k_Fl_e as a function of carrier concentrations of ZnO, SiZO, IZO, and InSiZO thin films at room temperature. The red dash line shows k_Fl_e = 1 where a MIT occurs. The blue area shows the critical carrier concentration for a MIT.

A combination of my data in this thesis with the literature data of various TCOs is shown in **Figure 7.6**. It shows a clear transition from metallic states to insulating states at low temperature driven by dopant/impurity concentration (77 K). The significant transition from low temperature to high temperature indicates that the electrons are thermally excited into the conduction band from impurity states at high temperature. Therefore, the continuous evolution of the metallic state is due to the continuous increase in conductivity with carrier concentration, i.e., $\sigma = ne\mu$.

However, the discontinuous MIT at low temperature is due to the overlap of the wavefunctions of impurity states within the donor impurity band. Therefore, it is highly sensitive to the donor/impurity concentration. This transition from localised to delocalised donor state wavefunctions shows the critical carrier concentration which is consistent with the Mott-Edwards-Sienko plot (**Figure 7.3**).

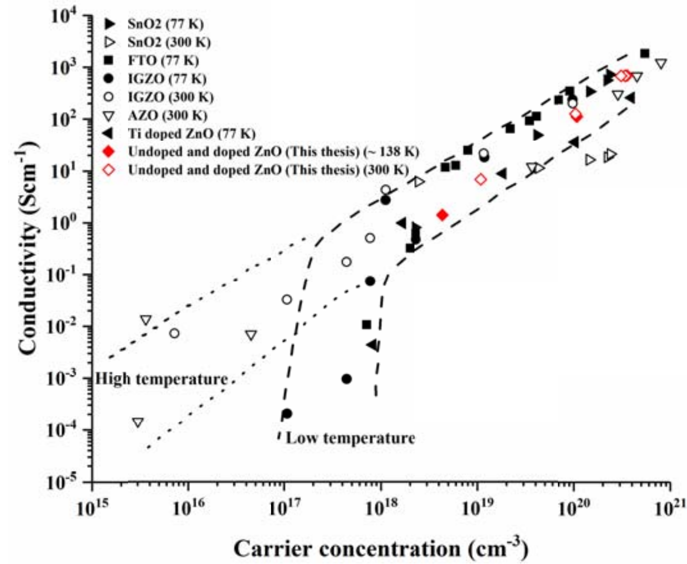

Figure 7.6: Conductivity as a function of carrier concentration for various TCOs at high temperature (300 K) and low temperature (77 K). The plot is adapted with permission from Vai et al. [3]; permission conveyed through Copyright Clearance Center, Inc. The literature data are from [23-28].

7.1.2 Grain Boundary Effects

When the carrier electrons attempt to transport across the grain boundaries of individual crystallites within a thin film, the electron mobility is reduced due to so-called grain boundary scattering. Importantly, this scattering may also be affected by the carrier concentration in the film (**Figure 7.7**). Thus the carriers can traverse the potential barrier height of the grain boundary either by a thermionic emission process or by a quantum mechanical tunnelling process. [29]

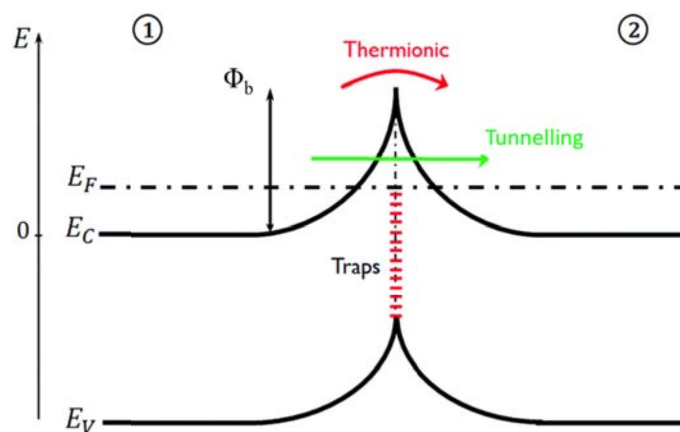

Figure 7.7: Schematic band diagram near a grain boundary of a TCO thin film. Φ_b is the potential barrier height, E_F is the Fermi level energy, E_C is the bottom of the conduction band, and E_V is the top of the valence band. Reproduced from Nguyen et al. [29] with permission from the Royal Society of Chemistry.

Thus, a comparison of the optically derived mobility (i.e., high frequency) and the transport Hall mobility (a DC measurement) is a most effective way to study the grain boundary scattering effect. The optical mobility is calculated from **Equation 4.7** by simulating the reflectance spectra with the dielectric model. [30] One of the UV-Vis-NIR optical reflectance spectra with its simulation spectrum is shown in **Figure 7.8**. It shows that the fringes are well fitted with a small mean square error of less than 1. Please refer to **Appendix A7.1** for IZO (2%) and InSiZO (2% In-0.6% Si) thin films.

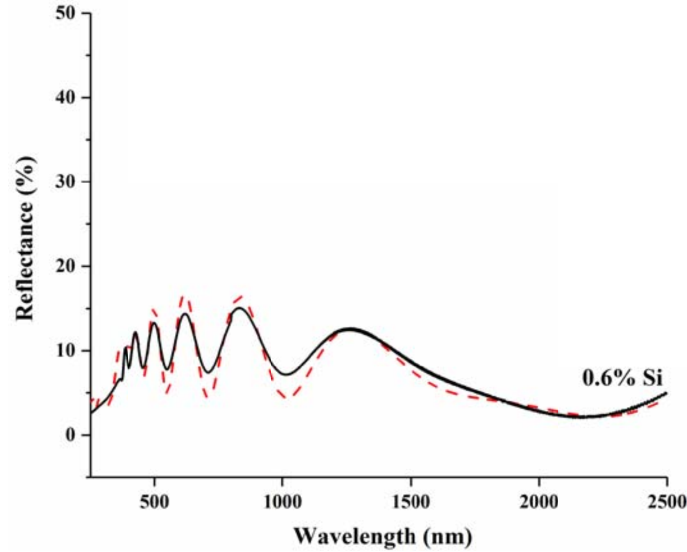

Figure 7.8: A typical UV-Vis-NIR optical reflectance spectra of SiZO (0.6%) thin films. The simulation spectrum is shown as the red curve.

The resulting optical and Hall mobility properties of SiZO, IZO, and InSiZO thin films are shown in **Figure 7.9**. It shows that the optical carrier concentrations and mobilities are much higher than those of Hall effect measurements.

We focus on the mobilities as their magnitudes are closely related to the grain boundary scattering effect. The Hall mobilities are affected by both in-grain (intra-grain) and grain boundary scatterings which can be expressed in the following equation derived from Matthiessen's rule. [31, 32]

$$\frac{1}{\mu_{Hall}} = \frac{1}{\mu_{in-grain}} + \frac{1}{\mu_{gb}}$$

Equation 7.3

Where μ_{Hall} is the Hall mobility, $\mu_{in\text{-}grain}$ is the in-grain mobility, and μ_{gb} is the mobility across the grain boundary. It is obvious that $\mu_{in\text{-}grain}$ equals to the optical mobility μ_{opt}. Furthermore, the electron carriers must overcome the potential barrier height at the grain boundary to transport across grains inside thin films. The different values of optical and Hall mobilities are

attributed to the grain boundary scattering effect. [31] The mobility at the grain boundary μ_{gb} shows how the carriers transport across the grain boundary is primarily by a thermionic emission.

Importantly, the number of trapped electrons at grain boundaries and the potential barrier height increase as the doping level increases, thus obstructing the transport of carriers. In contrast, an increasing electron concentration also raises the Fermi energy within the particles. The charge can saturate if the grain boundary states are fully filled with trapped electrons by further doping.

If the doping level continues to increase, the carrier trap density increases at the grain boundary, thus reducing the mobility at the grain boundary. [31, 33-35] What is more, the electron effective mass increases significantly as the doping level exceeds the substitutional solubility limit, thus contributing a reduced mobility at the grain boundary. The large differences between optical and Hall carrier concentrations in **Figure 7.9** indicate the presence of the trapped electrons, or other such impeding processes, at the grain boundaries.

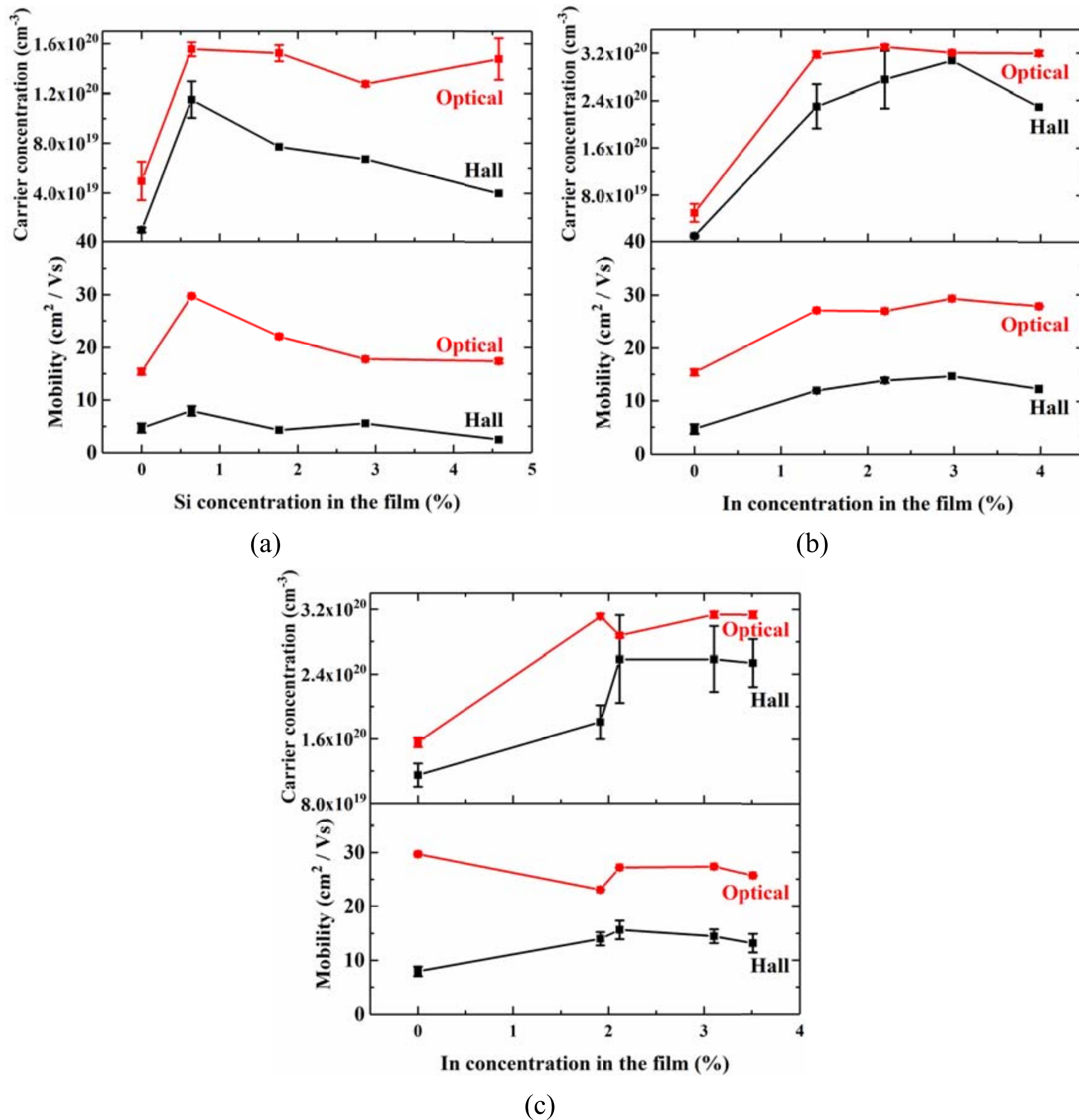

Figure 7.9: Optical (red) and Hall (black) electrical properties of SiZO, IZO, and InSiZO (In-0.6% Si) thin films.

We note that the optical carrier concentrations and mobilities are consistently much higher than those of Hall effect measurements for either singly doped or co-doped thin films of various thicknesses. Please refer to **Appendix A7.1** for further details.

For modelling the grain boundary limited mobility, the mobility at the grain boundary μ_{gb} shows how the carriers transport across the grain boundary by a thermionic emission, which can be expressed as below. [36, 37]

$$\mu_{gb} = Le(\frac{1}{2\pi m^* k_B T})^{1/2} \exp(-\frac{\Phi_b}{k_B T})$$

Equation 7.4

Where L is the effective grain size, e is the electron carrier charge, m* is the electron effective mass, k_B is the Boltzmann's constant, T is the temperature, and Φ_b is the potential barrier height. **Equation 7.4** can be written as below.

$$ln(\mu_{gb} T^{1/2}) = -\frac{\Phi_b}{k_B}\frac{1}{T} + ln(Le(\frac{1}{2\pi m^* k_B})^{1/2})$$

Equation 7.5

We can draw a linear plot of $\ln(\mu_{gb}T^{1/2})$ against 1 / T and deduce Φ_b and L from the slope and the intercept of the plot. (**Figure 7.10**) The data for T > 160 K is used for fitting because the grain boundary scatterings, i.e., thermionic emissions, dominate at higher temperature.

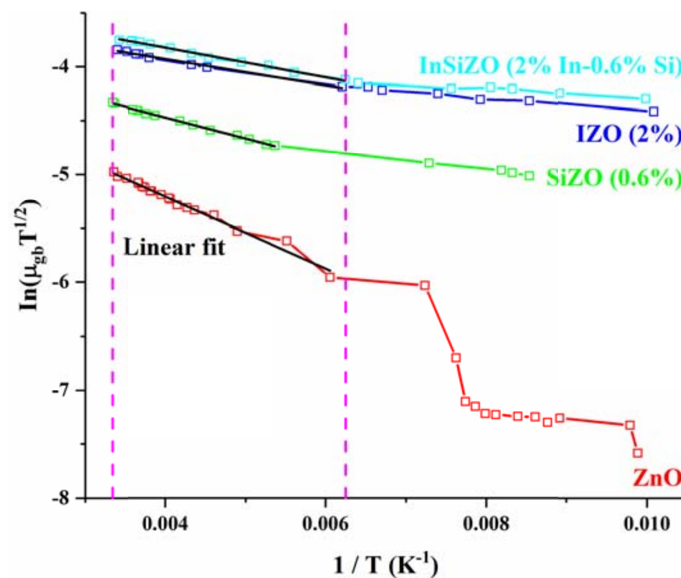

Figure 7.10: Plots of $\ln(\mu_{gb}T^{1/2})$ against 1 / T for ZnO, SiZO (0.6%), IZO (2%), and InSiZO (2% In-0.6% Si) thin films. The linear fitted curves are shown as black solid lines and the magenta lines show the range of data for fitting.

The significantly different electrical properties of undoped and doped ZnO thin films are highly related to the potential barrier height Φ_b. (**Table 7.1**) Both singly and co-doped films have remarkably smaller Φ_b values of 10.4 - 16.7 meV than those (28.8 meV) of undoped ZnO thin films. This is consistent with the improved conductivity for doped ZnO films. IZO (2%) and InSiZO (2% In-0.6% Si) thin films have similar Φ_b values of ~ 11 meV which are smaller than those (16.7 meV) of SiZO (0.6%) thin films. Therefore these trends also well correspond with electrical properties as discussed in **Chapter 4**. The effective grain size L is calculated by assuming m* = $0.3m_0$ [38, 39] with a value of ~ 1 nm for all the samples.

Samples	Φ_b (meV)	L (nm)
ZnO	28.8	0.63
SiZO (0.6%)	16.7	0.76
IZO (2%)	10.4	0.97
InSiZO (2% In-0.6% Si)	11.8	1.1

Table 7.1: The values of Φ_b and L derived from the fitted curves for the samples. The electron effective mass m* = $0.3m_0$ is used in the calculation. [38, 39]

7.1.3 The Co-Doping Mechanism

The conductivity of an n-type doped ZnO thin film is positively correlated to the impurity levels generated from the occupation of the substitutional Zn sites by the impurities such as Si and In. However, it is established that the interstitial defect reduces both the carrier concentration and the mobility due to the increased effective mass of the carriers thus giving lower conductivity as discussed in **Section 1.13** of **Chapter 1** (**Figure 1.25**). For this ZnO defect model, substitutional sites are known to be energetically more favourable than interstitial sites; therefore the substitutional Zn sites are preferentially occupied. [40]

Figure 7.11 shows the electrical properties of SiZO, IZO, and InSiZO thin films in **Chapter 4**. I can observe the lowest resistivities and their corresponding dopant concentrations, i.e., the substitutional solubility limit in the ZnO lattice. The values are 0.6% Si, 2 - 3% In, and 2 - 3% In + 0.6% Si for SiZO, IZO, and InSiZO thin films, respectively. The values for Si are much smaller than those for In because of the following reasons.

1. The representative oxidation states for Si and In are +4 and +3, respectively. Therefore, more In^{3+} ions are required if Zn^{2+} ions are substituted to generate the same amount of free electrons compared with Si^{4+} ions.

2. Si^{4+} (0.26 Å) has a much smaller ionic radius than Zn^{2+} (0.6 Å) while the ionic radius of In^{3+} (0.62 Å) is close to that of Zn^{2+} [41]. The ZnO lattice experiences more contraction, stress, and distortion for Si doping compared with In doping, thus resulting a higher formation energy. Consequently, Si doping appears not as effective as In doping.

3. The resulting band structures for Si doping and In doping are different. The dominant contribution to the conducting band near the Fermi level in SiZO is Si 3s and 3p orbitals [40] while that in IZO is In 5s orbitals [42]. Both of the donor states near the Fermi level can provide n-type carriers to improve the conductivities. However, the energy of In 5s orbitals is much lower than that of Si 3s and 3p orbitals, thus In is easier than Si to promote electrons to enhance the conductivity. [40, 42] In addition, the spatial characteristics of In 5s orbitals are clearly more conducive to direct overlap of the donor states (which themselves can also contribute to the local make-up of the host conduction band).

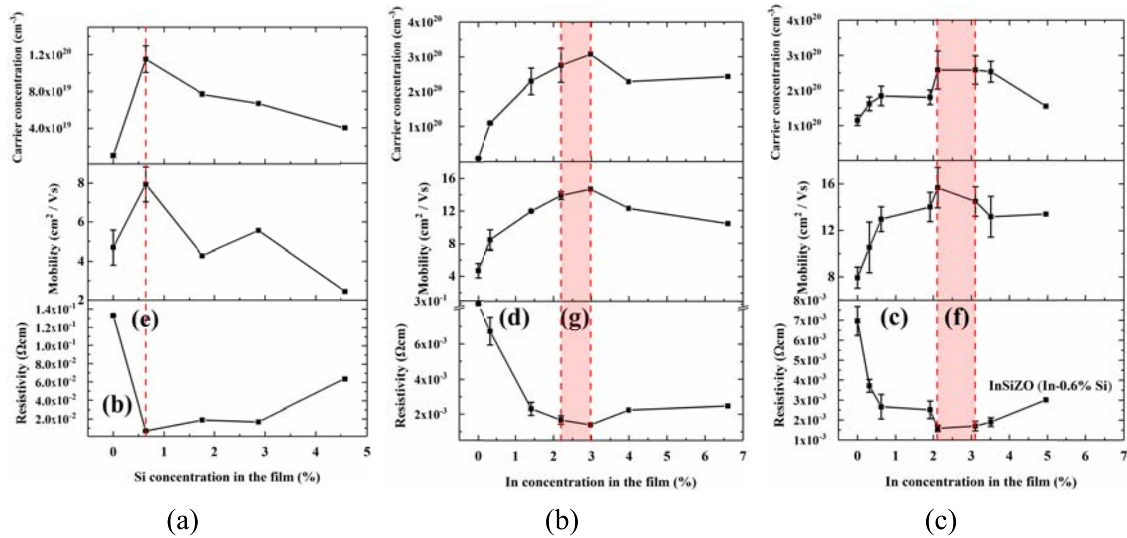

(a) (b) (c)

Figure 7.11: Electrical properties of SiZO (a), IZO (b), and InSiZO (c) thin films. The red lines and red area show the substitutional limits of the dopants. The inserted labels (b) - (g) are the corresponding models in **Figure 7.12**.

In an attempt to visualise the different, competing substitutional processes, in **Figure 7.12**, I show the substitutional doping models for singly doped and co-doped ZnO thin films. Since the number of the substitutional Zn sites is limited, which is also known as the solubility limit, the electrical conductivity of doped ZnO thin films is determined by the combination of Si and In occupations. (g) has the best electrical conductivity among all the films as In is a better dopant than Si. (f) is the saturated co-doping case which shows the similar electrical performance. (d) is the IZO thin film at a low In concentration (< 2%). (e) has the best electrical conductivity among SiZO thin films. (b) is the SiZO thin film at a low Si concentration (< 0.6%). (c) is the co-doping case below the solubility limit. **Figure 7.11** shows the corresponding regions of electrical properties for the models (b) - (g).

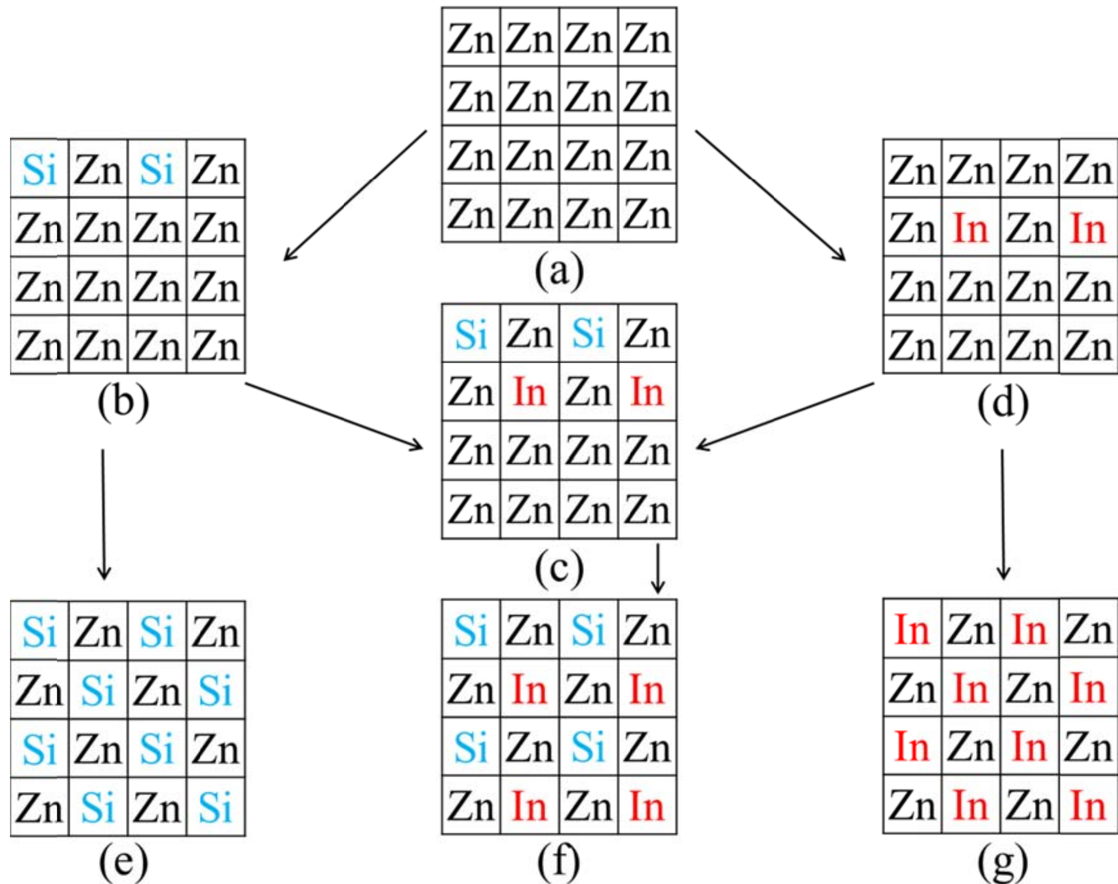

Figure 7.12: Substitutional doping models for singly doped and co-doped ZnO thin films. Each empty small pane represents a substitutional Zn site and each filled small pane represents a substitutional Si or In defect. These models are just schematic and do not represent any geometry information (e.g., they are two-dimensional rather than three-dimensional.). Initial Zn sites (a), part of sites occupied by Si (b), part of sites occupied by Si and In (c), part of sites occupied by In (d), solubility limit of Si (e), solubility limit of Si and In (f), and solubility limit of In (g). The solubility limits of Si and In are 0.6% and 2%, respectively.

The electrical resistivities and average visible transmittances as a function of In and Si concentrations for doped ZnO thin films in this thesis is shown in **Figure 7.13**. The idea of the co-doping is to obtain appropriate electrical and optical properties by using significantly reduced amounts of In by replacing In with inexpensive and more available Si. The plots in **Figure 7.14** illustrate how the electrical and optical properties InSiZO thin films vary with the Si and In contents. Optimal electrical performance (dark red areas) is obtained with

concentrations in the films of 0 - 0.6% for Si and 0.3 - 2% for In. When optimising the electrical performance, the visible transmittance never becomes an issue of concern as it remains a very high value (> 80%). Further increase in the In content causes no improvement and higher Si content causes an increase in resistivity. This type of plot is important as it enables the precise selection of doping concentrations to give a required conductivity and/or optical properties. Moreover, the Si/In balance can be adjusted to minimise the In content and therefore cost.

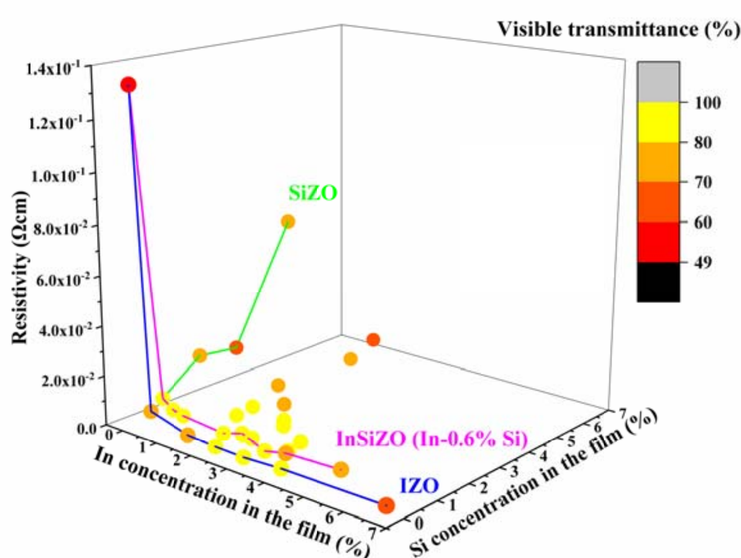

Figure 7.13: Electrical resistivities and average visible transmittances as a function of In and Si concentrations for singly doped and co-doped ZnO thin films. The examples of SiZO (green), IZO (blue), and InSiZO (In-0.6% Si) (magenta) thin films are also shown.

For example, if cost is not a primary issue, one could select IZO (1.4%) thin films with a resistivity of ~ 2.3×10^{-3} Ωcm. However, if the objective is to reduce cost of the TCO films by utilising less In, one might select InSiZO (0.6% In-0.6% Si) thin films which have a resistivity of ~ 2.7×10^{-3} Ωcm, which is close to that of pure IZO (1.4%) thin films.

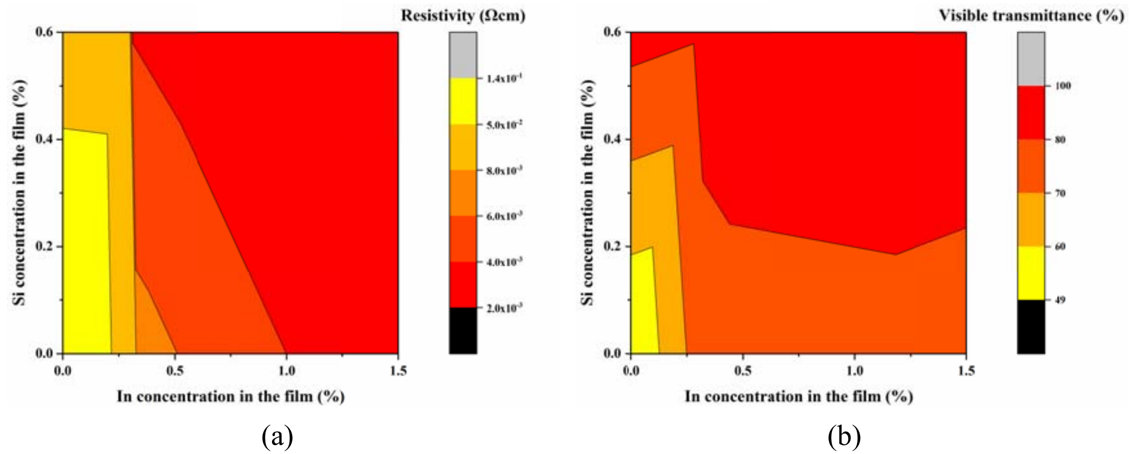

(a) (b)

Figure 7.14: Co-doping design model for InSiZO thin films for electrical (a) and optical (b) properties. The visible transmittance values are corrected for the glass substrate.

7.1.4 The Figure of Merit

Ideally, both of the optical and electrical performance of a thin film should be as large as possible to be an excellent TCO material. However, it is difficult to achieve the best transmittance and electrical performance simultaneously. A Figure of Merit ϕ_{TC} is a useful tool, therefore, to compare the performance of TCOs and can be expressed as the following equation proposed by Haacke [43].

$$\phi_{TC} = T^{10} / R_S = T^{10} / (\rho / d)$$

Equation 7.6

Where T is the optical transmittance, R_S is the electrical sheet resistance, ρ is the electrical resistivity, and d is the film thickness.

The Figure of Merit nicely illustrates the balance between the optical transmittance and electrical performance. A better TCO material should have a large as possible Figure of Merit, which is due to a larger transmittance and smaller sheet resistance, and vice versa. The dopant concentrations for the highest Figure of Merit values of both singly doped and co-doped ZnO

thin films (**Figure 7.15**) are consistent with those for the best electrical performance as shown in **Section 4.3.1** of **Chapter 4**. The In concentrations are also consistent with those for the best electrical performance when co-doped ZnO thin films have superior Figure of Merit values to singly doped thin films (**Figure 7.16**). These results show again that neither singly doping nor co-doping has a negative effect on the visible transmittance of ZnO thin films.

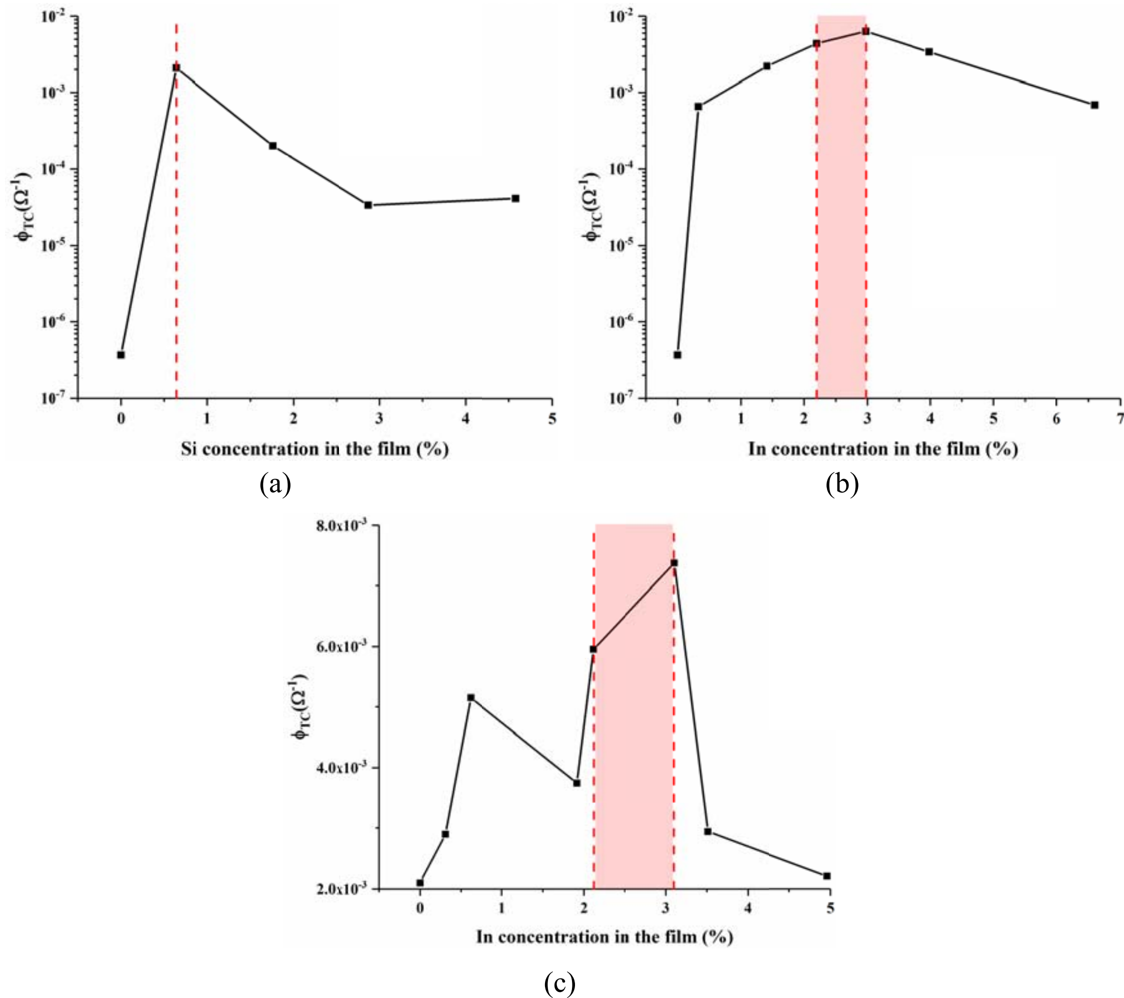

Figure 7.15: Figure of Merits as a function of dopant concentrations for SiZO (a), IZO (b), and InSiZO (c) thin films.

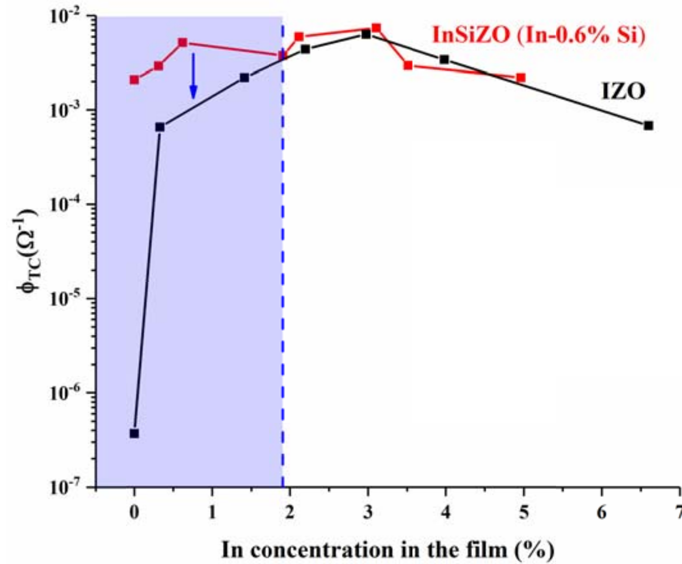

Figure 7.16: Figure of Merits as a function of In concentrations for the comparisons of IZO and InSiZO thin films. The blue area shows the superior performance of co-doped ZnO thin films.

The primary advantage of zinc-based over indium-based TCOs is the cost of raw materials. The In price is \$605 / kg while the Zn price is only \$2 / kg in 2015. [44] The difference between these prices is ~ 300 times; thus the cost of TCOs depends on the amount of In to be used. If I take the cost into account when the Figure of Merit is used, a term called cost-based Figure of Merit (CFOM) ϕ_{CFOM} can be expressed as below.

$$\phi_{CFOM} = \phi_{TC} / x = T^{10} / R_S / x$$

Equation 7.7

Where x is the In content in the TCOs.

Most of the IZO and InSiZO thin films have superior ϕ_{CFOM} values to the commercial ITO thin films. (**Figure 7.17**) It shows that these zinc-based TCOs are competitive candidates to be substituted for commercial ITOs based on the balance between the performance and costs.

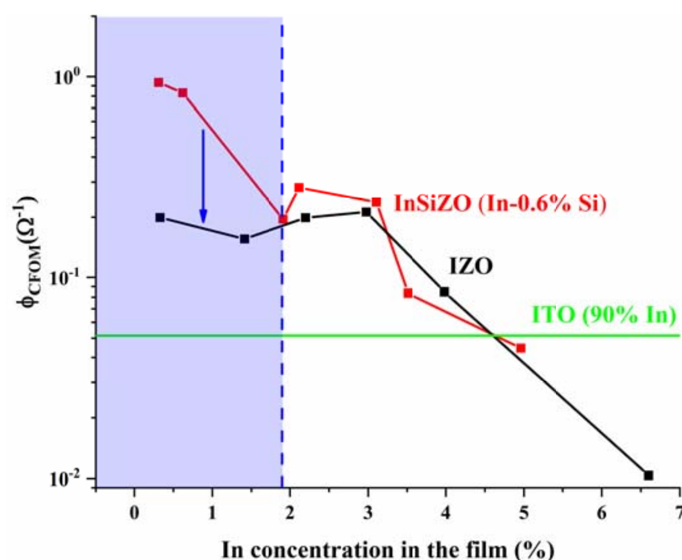

Figure 7.17: Cost-based Figure of Merits as a function of In concentrations for the comparisons of IZO and InSiZO thin films. The blue area shows the superior performance of co-doped ZnO thin films. The commercial ITO (90%) value is shown as reference.

7.2 Conclusions

Due to the cost and global scarcity of In, the search for TCOs that have reduced In content or indeed no In is an important goal. [45] Our strategy in this project has been to use inexpensive doped zinc-based TCOs to replace ITOs and related indium-based TCOs. Moreover, the synthesis technique used has been spray pyrolysis, which is a lower cost method compared to physical deposition methods such as vacuum sputtering. Using films made by the spray pyrolysis technique, I have investigated the origins of the properties of both indium-containing and indium-free TCOs, thereby finding more efficient routes to develop the next-generation TCOs with superior optoelectronic performances. As a result, I have established a co-doping protocol using both Si and In to obtain films with both good optical transparencies and electrical conductivities. This co-doping strategy can dramatically reduce the usage of the expensive element In while retaining acceptable optoelectronic performances compared to singly doped ZnO thin films, i.e., SiZO and IZO. A summary of the properties of deposited thin films in this thesis, reported sputtered thin films, and commercially supplied

ITO thin films is shown in **Table 7.2**. To our knowledge it is the first time that co-doped InSiZO thin films have been successfully synthesised with both high optical and electrical performances, thus giving a basis for a further development in co-doping and material design. It is also the first time that the total chemical composition of elements in the bulk of a TCO material has been investigated. The crystal structure growths along the film thickness direction have also been explored; therefore, I explain fundamental questions in a microscopic view to see limitations or restrictions in doping. This has provided a high resolution picture of precisely how doping affects the optoelectronic properties.

Film	Resistivity (Ωcm)	Thickness (nm)	Deposition method	Reference
SiZO	7×10^{-3}	662	Spray pyrolysis	This thesis
IZO	1.4×10^{-3}	628	Spray pyrolysis	This thesis
InSiZO	1.6×10^{-3}	646	Spray pyrolysis	This thesis
SiZO	3.8×10^{-4}	445	RF magnetron sputtering	Minami et al. [46]
ITO	1.5×10^{-4}	121	Sputtering	Sigma-Aldrich, 703192

Table 7.2: A summary of thin films with best resistivities from the thesis and the literatures.

One of the advantages of the spray pyrolysis technique is the easy control of the film thickness by changing the precursor solution volume. The relationships between the thicknesses of thin films and the precursor solution volumes are linear. The impurity dopant concentrations in the films are much lower than the nominal ones in the precursor solutions. The preferred orientation, the surface morphology, the optical band gap, and the electrical properties are highly determined by the species and quantity of the dopant.

The investigation of films of various thicknesses indicates the electrical mobility values of these films are not independent of film thicknesses. Therefore, the film is not uniform throughout its thickness direction. This is confirmed by the TEM analysis, which shows

different crystal structures and element distributions from the bottom of the film to the top of the film. This non-uniform feature points out the possible limitation in the conventional electrical property measurement, which makes four ohmic contacts on the film surface. [47] Therefore in the future would be worthwhile to see the electrical performance when the probe contacts the whole depth of a film rather than the surface. The non-uniform feature of the film may give different results at varying film depths.

7.3 Further Work

The effect of Cl in thin films introduced from $InCl_3$ in the starting materials needs to be further investigated. Does it have a positive or a negative effect on optoelectronic properties? Is it necessary to deposit chloride-free thin films by using other starting materials? What are the chemical environment and the structure of Cl in the films? These are all important questions for us to optimise the TCO materials. I could use $InBr_3$ instead of $InCl_3$ to deposit thin films to study the effects of halogen anions.

Either for singly doped or co-doped ZnO thin films, the investigation of the defects, including substitutional occupations, interstitial occupations, and vacancies, is important to understand the fundamental cause of the optoelectronic properties of TCOs. It is really necessary to 'see' the environment of defects and the arrangements of atoms in the lattice. High resolution X-ray diffraction, neutron diffraction, and X-ray absorption spectroscopy including extended X-ray absorption fine structure (EXAFS) and X-ray absorption near edge structure (XANES) could be used to establish these.

The elemental content in the precursor solution can be analysed by using ICP-MS, thus giving the whole picture of the element transfer efficiencies both from the starting materials to the precursor solutions and from the precursor solutions to the films. Therefore, I can clearly know where the starting materials are lost during the whole synthesis process and the actual

elemental content of the films.

In order to reduce the non-uniform feature of the films, which limits the optoelectronic performance, a highly crystalline substrate can be used to replace the amorphous glass. I may also deposit a very thin highly crystalline layer as a template on the glass substrate before depositing the desired TCO film.

Since the incorporation of dopants is limited by the spray pyrolysis technique, other deposition techniques such as sputtering and PLD could be explored to enhance the doping levels in the ZnO lattice, thus possibly improving the electrical conductivity.

There are various parameters in the spray pyrolysis technique including substrate, precursor solution (dopant, solvent, pH, solution chemistry, etc.), deposition temperature, atmosphere, gas flow rate, reaction time, post-annealing, etc. [48] Each of these can be optimised to get a better film performance. As discussed before, the low transfer efficiencies (< 2%) indicate that the synthesis of thin films by using spray pyrolysis is wasteful in terms of the precursors. The spray pyrolysis apparatus could be reconfigured to reduce the aerosol splashing, thus reducing the waste.

The relatively high temperature used to deposit thin films is one of the limitations of the spray pyrolysis technique. [49] Some polymer or plastic substrates cannot tolerate the high temperature when placing on a heating platform such as that in the current system. If microwaves are used to just heat the precursor solutions near the top of the substrate and the substrate remains cool, it may be possible to deposit TCO thin films on a heat-labile substrate.

Spray pyrolysis has high potential to transfer from lab synthesis to industrial scale manufacture due to its cheap starting materials, non-vacuum condition, easy operating and quick synthesis process, etc. The future optimised key points for scale-up include the filter of the starting materials, the aerosol generator, the heating system, the oxygen-free reaction

environment, and quality control. [50] A preliminary agreement was signed between Edwards group, Oxford University Innovation, and a company in Suzhou on the research industrial scale-up production of ZnO-based TCOs years ago. I believe I will see the dawn of hope eventually by overcoming these obstacles.

References

[1] Edwards, P. P., Lodge, M. T. J., Hensel, F. & Redmer, R. 2010. '… a metal conducts and a non-metal doesn't'. *Philosophical Transactions of the Royal Society A: Mathematical, Physical and Engineering Sciences,* 368**,** 941-965.

[2] Ehrenreich, H. 1967. The Electrical Properties of Materials. *Scientific American,* 217**,** 194-209.

[3] Vai, A. T., Kuznetsov, V. L., Jain, H., Slocombe, D., Rashidi, N., Pepper, M. & Edwards, P. P. 2014. The Transition to the Metallic State in Polycrystalline n-Type Doped ZnO Thin Films. *Zeitschrift für Anorganische und Allgemeine Chemie,* 640**,** 1054-1062.

[4] Mott, N. F. 1961. The Transition to the Metallic State. *The Philosophical Magazine: A Journal of Theoretical Experimental and Applied Physics,* 6**,** 287-309.

[5] Mott, N. F. 1972. Conduction in Non-Crystalline Systems IX. The Minimum Metallic Conductivity. *The Philosophical Magazine: A Journal of Theoretical Experimental and Applied Physics,* 26**,** 1015-1026.

[6] Edwards, P. P. & Sienko, M. J. 1978. Universality Aspects of the Metal-Nonmetal Transition in Condensed Media. *Physical Review B,* 17**,** 2575-2581.

[7] Winkler, M. T., Recht, D., Sher, M.-J., Said, A. J., Mazur, E. & Aziz, M. J. 2011. Insulator-To-Metal Transition in Sulfur-Doped Silicon. *Physical Review Letters,* 106**,** 178701.

[8] Scanlon, D. O., Kehoe, A. B., Watson, G. W., Jones, M. O., David, W. I. F., Payne, D. J., Egdell, R. G., Edwards, P. P. & Walsh, A. 2011. Nature of the Band Gap and Origin of the Conductivity of PbO2 Revealed by Theory and Experiment. *Physical Review Letters,* 107**,** 246402.

[9] Rashidi, N., Kuznetsov, V. L., Dilworth, J. R., Pepper, M., Dobson, P. J. & Edwards, P. P. 2013. Highly Conducting and Optically Transparent Si-Doped ZnO Thin Films Prepared by Spray Pyrolysis. *Journal of Materials Chemistry C,* 1**,** 6960-6969.

[10] Lai, K., Zhu, Y., Dai, Y. & Huang, B. 2012. Intrinsic Defect in BiNbO4: A Density Functional Theory Study. *Journal of Applied Physics,* 112**,** 043706.

[11] Hu, S., Han, P., Liang, P., Xing, Y. & Lou, S. 2014. Metallic Conduction Behavior in Selenium-Hyperdoped Silicon. *Materials Science in Semiconductor Processing,* 17**,** 134-137.

[12] Robertson, J. 2012. Properties and Doping Limits of Amorphous Oxide Semiconductors. *Journal of Non-Crystalline Solids,* 358**,** 2437-2442.

[13] Robertson, J. & Gillen, R. 2013. Defect Densities Inside the Conductive Filament of RRAMs. *Microelectronic Engineering,* 109**,** 208-210.

[14] Kolodiazhnyi, T. 2008. Insulator-Metal Transition and Anomalous Sign Reversal of the Dominant Charge Carriers in Perovskite BaTiO3-δ. *Physical Review B,* 78**,** 045107.

[15] Makise, K., Shinozaki, B., Asano, T., Mitsuishi, K., Yano, K., Inoue, K. & Nakamura, H. 2012. Relationship Between Variable Range Hopping Transport and Carrier Density of Amorphous In2O3-10 wt. % ZnO Thin Films. *Journal of Applied Physics,*

112, 033716.

[16] Edwards, P. P., Porch, A., Jones, M. O., Morgan, D. V. & Perks, R. M. 2004. Basic Materials Physics of Transparent Conducting Oxides. *Dalton Transactions*, 2995-3002.

[17] Shanthi, E., Dutta, V., Banerjee, A. & Chopra, K. L. 1980. Electrical and Optical Properties of Undoped and Antimony‐Doped Tin Oxide Films. *Journal of Applied Physics,* 51, 6243-6251.

[18] Ioffe, A. & Regel, A. 1960. Non-Crystalline, Amorphous and Liquid Electronic Semiconductors. *Progress in Semiconductors,* 4, 89.

[19] Mark, R. G., Adkins, C. J., Haim, B. & Ralph, R. 1998. Experimental Study of the Ioffe-Regel Criterion for Amorphous Indium Oxide Films. *Journal of Physics: Condensed Matter,* 10, 809.

[20] Ioffe, A. F. & Regel, A. R. 1960. Non-Crystalline, Amorphous, and Liquid Electronic Semiconductors. *Progress in Semiconductors,* 4, 237-291.

[21] Vai, A. T. 2015. *Performance Limitations in Practical Transparent Conducting Oxide Thin Films.* University of Oxford.

[22] Rashidi-Alavijeh, N. 2015. *Cation and Anion Doping of ZnO Thin Films by Spray Pyrolysis.* University of Oxford.

[23] Bruneaux, J., Cachet, H., Froment, M. & Messad, A. 1991. Correlation Between Structural and Electrical Properties of Sprayed Tin Oxide Films with and Without Fluorine Doping. *Thin Solid Films,* 197, 129-142.

[24] Nomura, K., Kamiya, T., Ohta, H., Ueda, K., Hirano, M. & Hosono, H. 2004. Carrier Transport in Transparent Oxide Semiconductor with Intrinsic Structural Randomness Probed Using Single-Crystalline InGaO3(ZnO)5 Films. *Applied Physics Letters,* 85, 1993-1995.

[25] Takagi, A., Nomura, K., Ohta, H., Yanagi, H., Kamiya, T., Hirano, M. & Hosono, H. 2005. Carrier Transport and Electronic Structure in Amorphous Oxide Semiconductor, A-InGaZnO4. *Thin Solid Films,* 486, 38-41.

[26] Kim, I. H., Ko, J. H., Kim, D., Lee, K. S., Lee, T. S., Jeong, J. h., Cheong, B., Baik, Y. J. & Kim, W. M. 2006. Scattering Mechanism of Transparent Conducting Tin Oxide Films Prepared by Magnetron Sputtering. *Thin Solid Films,* 515, 2475-2480.

[27] Lu, J. J., Lu, Y. M., Tasi, S. I., Hsiung, T. L., Wang, H. P. & Jang, L. Y. 2007. Conductivity Enhancement and Semiconductor-Metal Transition in Ti-Doped ZnO Films. *Optical Materials,* 29, 1548-1552.

[28] Lu, J. G., Ye, Z. Z., Zeng, Y. J., Zhu, L. P., Wang, L., Yuan, J., Zhao, B. H. & Liang, Q. L. 2006. Structural, Optical, and Electrical Properties of (Zn,Al)O Films over a Wide Range of Compositions. *Journal of Applied Physics,* 100, 073714.

[29] Nguyen, V. H., Gottlieb, U., Valla, A., Muñoz, D., Bellet, D. & Muñoz-Rojas, D. 2018. Electron Tunneling Through Grain Boundaries in Transparent Conductive Oxides and Implications for Electrical Conductivity: The Case of ZnO:Al Thin Films. *Materials Horizons,* 5, 715-726.

[30] 2008. *Guide to Using WVASE 32: Spectroscopic Ellipsometry Data Acquisition and Analysis Software,* Lincoln, NE, J. A. Woollam Company, Incorporated.

[31] Yamada, T., Makino, H., Yamamoto, N. & Yamamoto, T. 2010. Ingrain and Grain

Boundary Scattering Effects on Electron Mobility of Transparent Conducting Polycrystalline Ga-Doped ZnO Films. *Journal of Applied Physics,* 107**,** 123534.

[32] Matthiessen, A. & Vogt, C. 1864. On the Influence of Temperature on the Electric Conducting-Power of Alloys. *Philosophical Transactions of the Royal Society of London,* 154**,** 167-200.

[33] Jiang, Y., Pillai, S. & Green, M. A. 2016. Grain boundary effects on the optical constants and Drude relaxation times of silver films. *Journal of Applied Physics,* 120**,** 233109.

[34] Rossetti, F. F., Reviakine, I. & Textor, M. 2003. Characterization of Titanium Oxide Films Prepared by the Template-Stripping Method. *Langmuir,* 19**,** 10116-10123.

[35] Vai, A. T., Rashidi, N., Fang, Y., Kuznetsov, V. L. & Edwards, P. P. 2016. Contrasting the Grain Boundary-Affected Performance of Zinc and Indium Oxide Transparent Conductors. *Journal of Physics: Condensed Matter,* 28**,** 224003.

[36] Romanyuk, V., Dmitruk, N., Karpyna, V., Lashkarev, G., Popovych, V., Dranchuk, M., Pietruszka, R., Godlewski, M., Dovbeshko, G. & Timofeeva, I. 2016. Optical and Electrical Properties of Highly Doped ZnO: Al Films Deposited by Atomic Layer Deposition on Si Substrates in Visible and near Infrared Region. *Acta Physica Polonica A,* 129.

[37] Nguyen, V. H., Gottlieb, U., Valla, A., Muñoz, D., Bellet, D. & Muñoz-Rojas, D. 2018. Electron Tunneling Through Grain Boundaries in Transparent Conductive Oxides and Implications for Electrical Conductivity: The Case of ZnO: Al Thin Films. *Materials Horizons*.

[38] Preissler, N., Bierwagen, O., Ramu, A. T. & Speck, J. S. 2013. Electrical Transport, Electrothermal Transport, and Effective Electron Mass in Single-Crystalline In2O3 Films. *Physical Review B,* 88**,** 085305.

[39] Morkoç, H. & Özgür, Ü. 2008. *Zinc Oxide: Fundamentals, Materials and Device Technology,* Weinheim, John Wiley & Sons.

[40] Wu, H., Peng, Y. & Shen, T. 2012. Electronic and Optical Properties of Substitutional and Interstitial Si-Doped ZnO. *Materials,* 5**,** 2088.

[41] Shannon, R. D. 1976. Revised Effective Ionic Radii and Systematic Studies of Interatomic Distances in Halides and Chalcogenides. *Acta Crystallographica Section A,* 32**,** 751-767.

[42] Zhou, X. H., Hu, Q. H. & Fu, Y. 2008. First-Principles LDA+U Studies of the In-Doped ZnO Transparent Conductive Oxide. *Journal of Applied Physics,* 104**,** 063703.

[43] Haacke, G. 1976. New Figure of Merit for Transparent Conductors. *Journal of Applied Physics,* 47**,** 4086-4089.

[44] Tolcin, A. C. 2015. *2015 Minerals Yearbook,* USA, U.S. Department of the Interior, U.S. Geological Survey.

[45] Shtereva, K., Tvarozek, V., Sutta, P., Kovac, J. & Novotny, I. 2009. Experimental Studies on Doped and Co-Doped ZnO Thin Films Prepared by RF Diode Sputtering. *Micro Electronic and Mechanical Systems.* London: InTech.

[46] Tadatsugu, M., Hirotoshi, S., Hidehito, N. & Shinzo, T. 1986. Highly Conductive and Transparent Silicon Doped Zinc Oxide Thin Films Prepared by RF Magnetron

Sputtering. *Japanese Journal of Applied Physics,* 25**,** L776.

[47] 2018. *Hall Effect Measurements*. NIST. Available: https://www.nist.gov/pml/engineering-physics-division/popular-links/hall-effect [Accessed 10 March 2019].

[48] Messing, G. L., Zhang, S. & Jayanthi, G. V. 1993. Ceramic Powder Synthesis by Spray Pyrolysis. *Journal of the American Ceramic Society,* 76**,** 2707-2726.

[49] Nehru, L., Umadevi, M. & Sanjeeviraja, C. 2012. Studies on Structural, Optical and Electrical Properties of ZnO Thin Films Prepared by the Spray Pyrolysis Method. *International Journal of Materials Engineering,* 2**,** 12-17.

[50] Matula, G., Bogovic, J., Stopic, S. & Friedrich, B. 2013. Scale-Up of the Ultrasonic Spray Pyrolysis (USP) Process for Nanopowder Production (Part 1). *Powder Injection Moulding International,* 7**,** 75-78.

Appendices

Chapter 2

A2.1 Swanepoel Calculator

Swanepoel Calculator is the programme written in Python by Yiwen Fang. It has a graphical interface and makes a semi-automatic calculation of the film thickness and the average visible transmittance based on the Swanepoel method in **Chapter 2**. The Python code is as follows.

```
#!/usr/bin/env python3
# -*- coding: utf-8 -*-

# Software info
# Swanepoel Calculator
# Made by Yiwen Fang, Peter Edwards FRS Group, University of Oxford
# Last Update: December 2017

# Tkinter Open File
from tkinter import filedialog
from tkinter import *

root = Tk()
root.withdraw()
root.filename =  filedialog.askopenfilename(initialdir = "/",title = "Select file",filetypes = (("csv files","*.csv"),("all files","*.*")))
print (root.filename)
# Close tkinter window
root.destroy()
# Tkinter Open File end

# Data import
```

```
import csv
with open(root.filename, 'r') as f:
    reader = csv.reader(f)
    data_list = list(reader)
x = []
y = []
for (x0,y0) in data_list:
    x.append(float(x0))
    y.append(float(y0))
# Data import end

# Plots
import matplotlib.pyplot as plt
import numpy as np

# Figure 1: Import original plots
plt.figure(num=1, figsize=(10,6))
plt.title('Draw Tmax plots')
plt.plot(x,y, linewidth=1.0)
plt.xlim((198, 2500))
plt.ylim((0, 100))
plt.xlabel('Wavelength (nm)')
plt.ylabel('T (%)')
plt.draw()

# Draw TM
TM=plt.ginput(n=int(),timeout=0)
TM_x = []
TM_y = []
```

```
for (x1,y1) in TM:
    TM_x.append(x1)
    TM_y.append(y1)
plt.close()

# Figure 2: Figure 1: Import original plots
plt.figure(num=2, figsize=(10,6))
plt.title('Draw Tmin plots')
plt.plot(x,y, linewidth=1.0)
plt.xlim((198, 2500))
plt.ylim((0, 100))
plt.xlabel('Wavelength (nm)')
plt.ylabel('T (%)')
plt.draw()

# Draw Tm
Tm=plt.ginput(n=int(),timeout=0)
Tm_x = []
Tm_y = []
for (x2,y2) in Tm:
    Tm_x.append(x2)
    Tm_y.append(y2)
plt.close()

# Figure 3: Tex1 plots (Max and Min extrema in order)
plt.figure(num=3, figsize=(10,6))
plt.title('Select extrema (both max & min) in order (at least 2)')
plt.plot(x,y, linewidth=1.0)
plt.plot(TM_x,TM_y, color='red', linewidth=1.0)
```

```
plt.plot(Tm_x,Tm_y, color='red', linewidth=1.0)
plt.xlim((198, 2500))
plt.ylim((0, 100))
plt.xlabel('Wavelength (nm)')
plt.ylabel('T (%)')
plt.draw()

# Choose points: Tex1
Tex1=plt.ginput(n=int(),timeout=0)
Tex1_x = []
Tex1_y = []
for (x3,y3) in Tex1:
    Tex1_x.append(x3)
    Tex1_y.append(y3)
plt.close()

# Figure 4: Tex2 plots (Max and Min extrema pairing in order)
plt.figure(num=4, figsize=(10,6))
plt.title('Select extrema paired points in order')
plt.plot(x,y, linewidth=1.0)
plt.plot(TM_x,TM_y, color='red', linewidth=1.0)
plt.plot(Tm_x,Tm_y, color='red', linewidth=1.0)
plt.scatter(Tex1_x,Tex1_y, marker = '+', color='black')
plt.xlim((198, 2500))
plt.ylim((0, 100))
plt.xlabel('Wavelength (nm)')
plt.ylabel('T (%)')
plt.draw()
```

```
# Choose points: Tex2
Tex2=plt.ginput(n=int(),timeout=0)
Tex2_x = []
Tex2_y = []
for (x4,y4) in Tex2:
    Tex2_x.append(x4)
    Tex2_y.append(y4)
plt.close()

# Figure 5: Plots all
plt.figure(num=5, figsize=(10,6))
plt.title('Results')
plt.plot(x,y, linewidth=1.0)
plt.plot(TM_x,TM_y, color='red', linewidth=1.0)
plt.plot(Tm_x,Tm_y, color='red', linewidth=1.0)
plt.scatter(Tex1_x,Tex1_y, marker = '+', color='black')
plt.scatter(Tex2_x,Tex2_y, marker = '+', color='black')
plt.xlim((198, 2500))
plt.ylim((0, 100))
plt.xlabel('Wavelength (nm)')
plt.ylabel('T (%)')
plt.draw()

# Swanepoel calculation
s=1.51
m=0
dlist = []
if len(Tex1_x) == len(Tex2_x) and len(Tex1_y) == len(Tex2_y) and len(Tex1_x) > 1: #
Check the same number of points
```

```
    while m < len(Tex1_x) - 1:
        N1 = 2 * s * abs(Tex1_y[m] - Tex2_y[m]) / Tex1_y[m] / Tex2_y[m] + ( s ** 2 + 1 )
/ 2
        N2 = 2 * s * abs(Tex1_y[m+1] - Tex2_y[m+1]) / Tex1_y[m+1] / Tex2_y[m+1] + ( s
** 2 + 1 ) / 2
        n1 = (N1 + (abs(N1 ** 2 - s **2))**0.5 ) ** 0.5
        n2 = (N2 + (abs(N2 ** 2 - s **2))**0.5 ) ** 0.5
        d = abs(0.5 * Tex1_x[m] * Tex1_x[m+1] / 2 / (Tex1_x[m] * n2 - Tex1_x[m+1] *
n1))
        dlist.append(d)
        m = m + 1
        d_avg = sum(dlist) / len(dlist)
        d_std = np.std(dlist)
else: # Choose points again
    d_avg = 0
    d_std = 0

# Average transparency 400 ~ 750nm
x_t = []
y_t = []
for (x_t0,y_t0) in data_list:
    if float(x_t0) < 400 or float(x_t0) > 750:
        continue
    x_t.append(float(x_t0))
    y_t.append(float(y_t0))
t_avg = sum(y_t) / len(y_t)

# Output
plt.text(1000,5, r'''Average Thickness (nm): {}
```

```
Standard Deviation (nm): {}
Average Trans of 400 ~ 750nm (%): {}'''.format('%.0f' % d_avg,'%.0f' % d_std,'%.0f' % t_avg))
fontdict={'size': 16, 'color': 'black'}
plt.show()
```

A2.2 Film Thickness Measurement

The film thicknesses of the samples are measured by using the Swanepoel method based on the interference fringes in the transmittance spectra. [1, 2] However, it has not been discussed in details how reliable this method is. It is straightforward to observe the film thickness from the TEM cross-sectional image of the film. **Table A.1** shows that the differences between these two methods are acceptable. Swanepoel method is an acceptable calculation method to determine the film thickness.

	Swanepoel Thickness (nm)	TEM Thickness (nm)	Ratio (Swanepoel vs TEM)
ZnO	553 ± 30	680 ± 20	0.8
SiZO (0.6%)	662 ± 35	580 ± 20	1.1
IZO(2%)	662 ± 30	570 ± 30	1.2
InSiZO (2% In-0.6% Si)	646 ± 14	530 ± 30	1.2

Table A.1: Comparisons of film thicknesses measured by Swanepoel method and TEM.

Chapter 3

A3.1 Thermal Distribution on the Heating Platform

A glass substrate is heated to a required temperature during a spray pyrolysis process. **Figure A.1** shows that the thermal distribution on the heating platform is not uniform ranging from 20 °C to 40 °C at a set temperature of ~ 40 °C. The central area is closer to the set temperature while the temperature near the edges is much lower. The temperature differences are due to the design of the heating platform since two cartridge heaters are inserted into two holes of the heating block. Therefore, the film performance and its properties may be affected by the non-uniform thermal distribution. Further optimisation of the synthesis kit can avoid this problem.

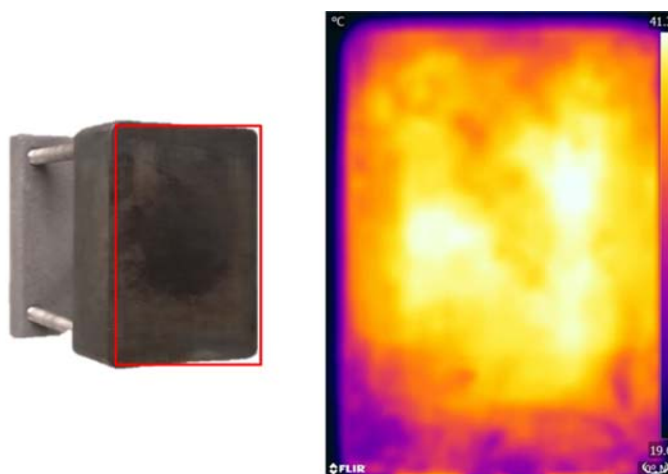

Figure A.1: Thermal distribution on the Heating Platform with a set temperature of ~ 40 °C observed by a thermal camera. The iron heating platform is also shown.

Chapter 5

A5.1 Effect of Film Thickness: SiZO

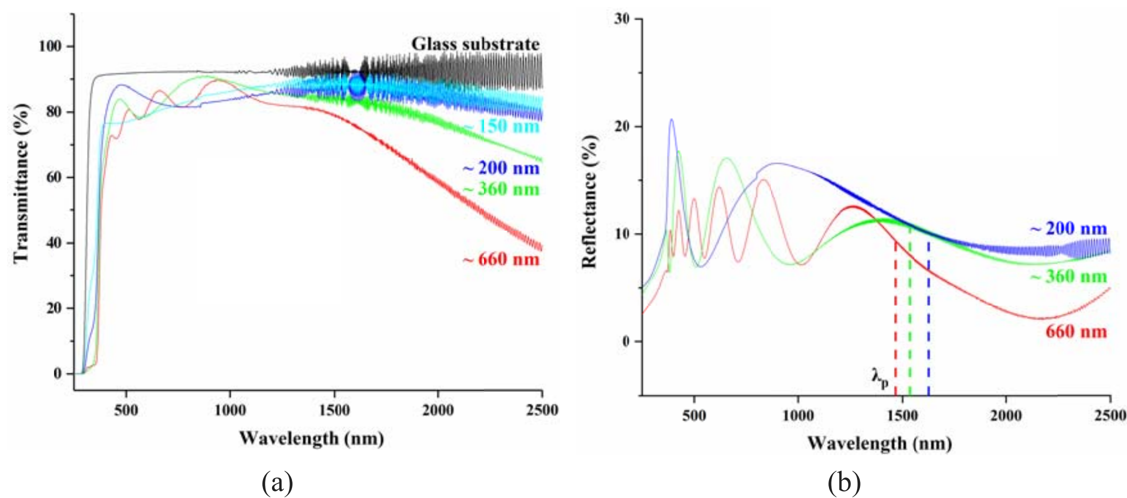

(a) (b)

Figure A.2: UV-Vis-NIR optical transmittance (a) and reflectance (b) spectra of SiZO (0.6%) thin films of various thicknesses.

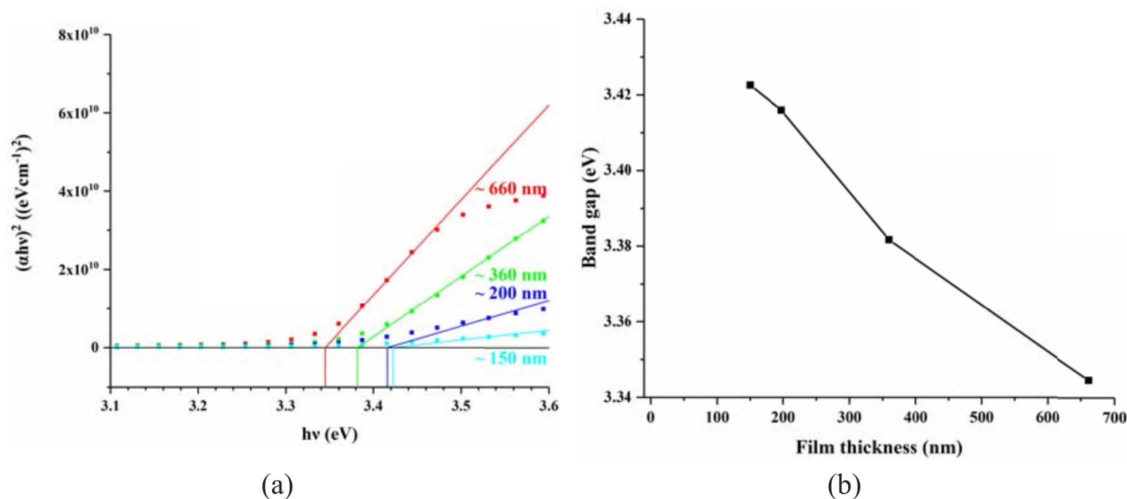

(a) (b)

Figure A.3: Graph of $(\alpha h\nu)^2$ as a function of photon energies (a) and band gaps (b) for SiZO (0.6%) thin films of various thicknesses.

A5.2 Effect of Film Thickness: IZO

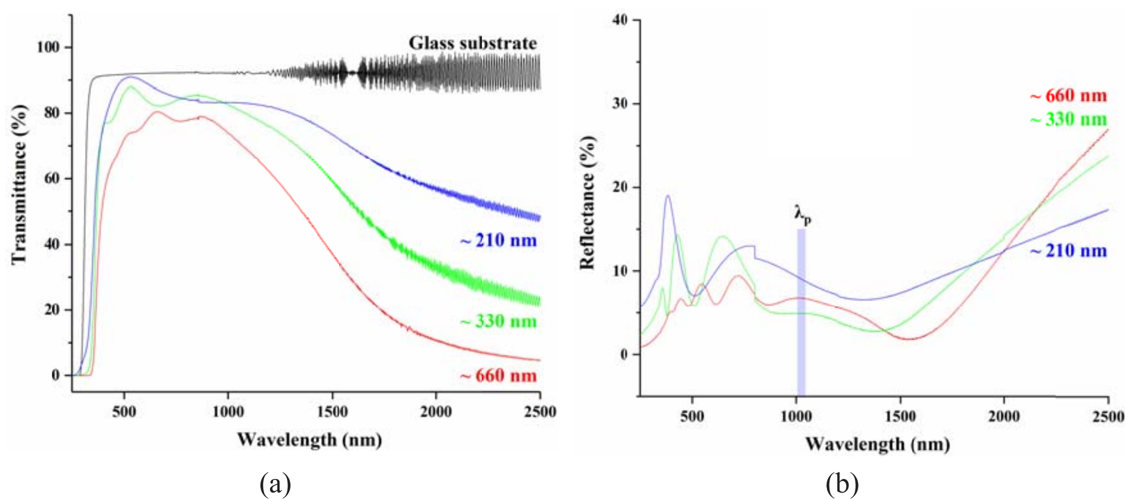

Figure A.4: UV-Vis-NIR optical transmittance (a) and reflectance (b) spectra of IZO (2%) thin films of various thicknesses.

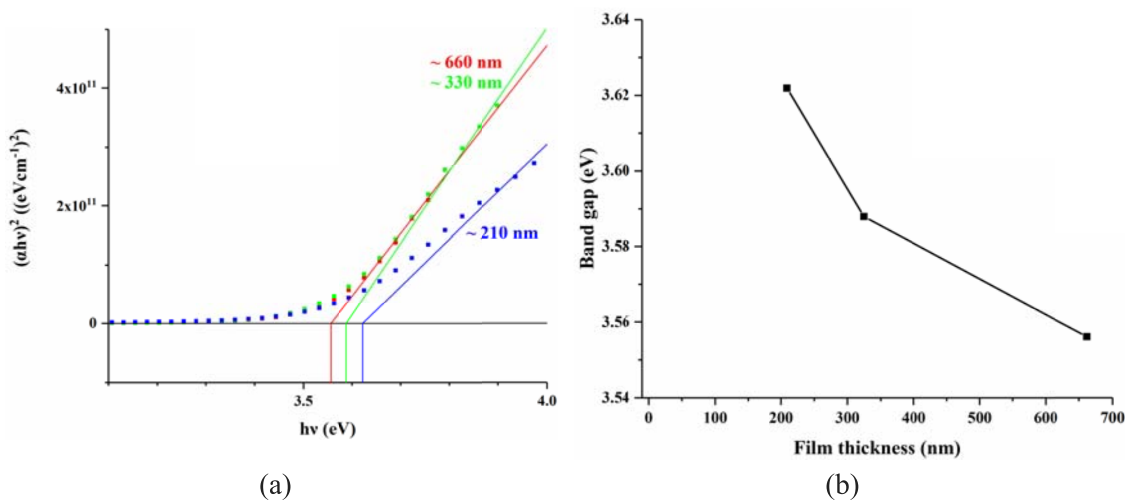

Figure A.5: Graph of $(\alpha h\nu)^2$ as a function of photon energies (a) and band gaps (b) for IZO (2%) thin films of various thicknesses.

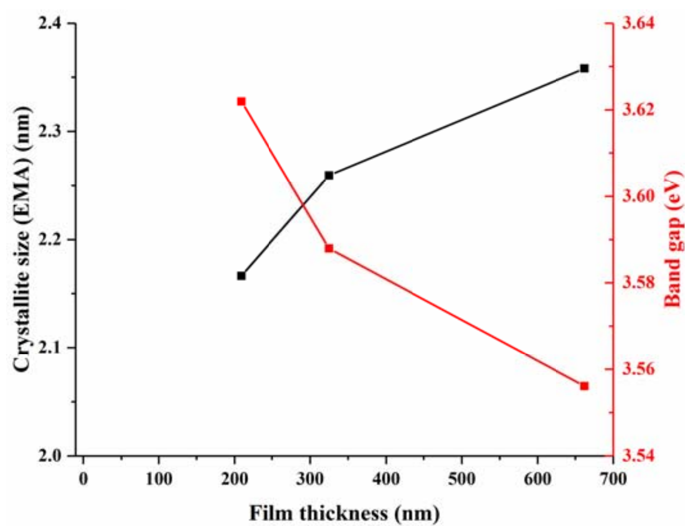

Figure A.6: Graph of band gaps and crystallite sizes calculated from EMA of IZO (2%) thin films of various thicknesses.

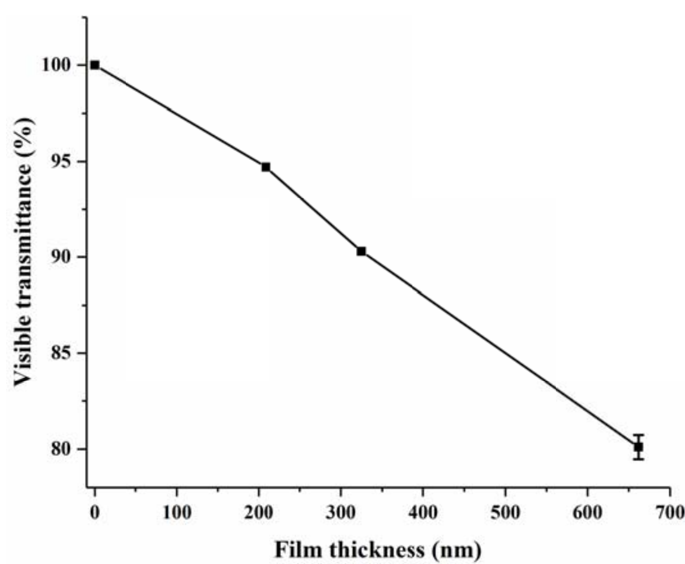

Figure A.7: Average visible optical transmittance (400 - 750 nm) corrected for the glass substrate of IZO (2%) thin films of various thicknesses.

A5.3 Effect of Film Thickness: InSiZO

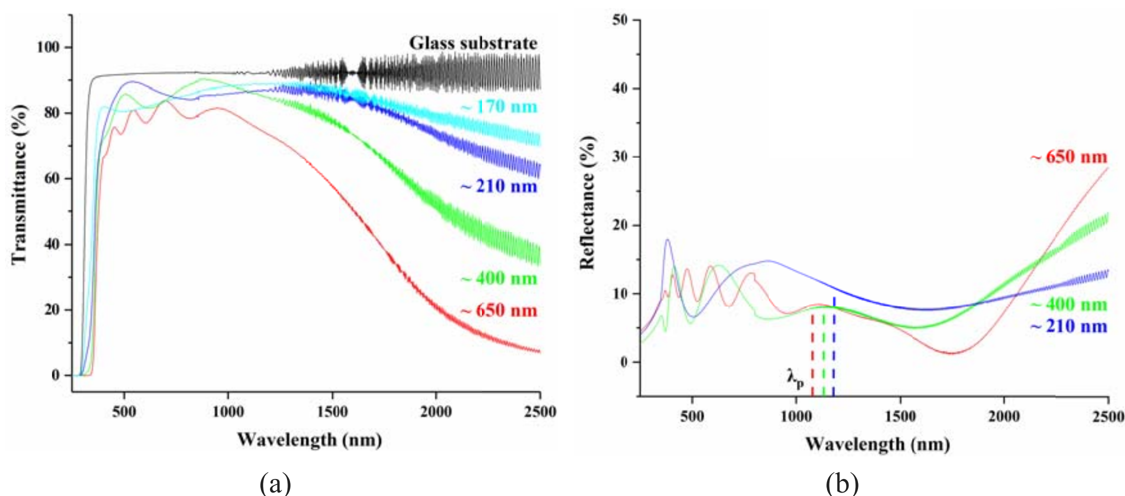

(a) (b)

Figure A.8: UV-Vis-NIR optical transmittance (a) and reflectance (b) spectra of InSiZO (2% In-0.6% Si) thin films of various thicknesses.

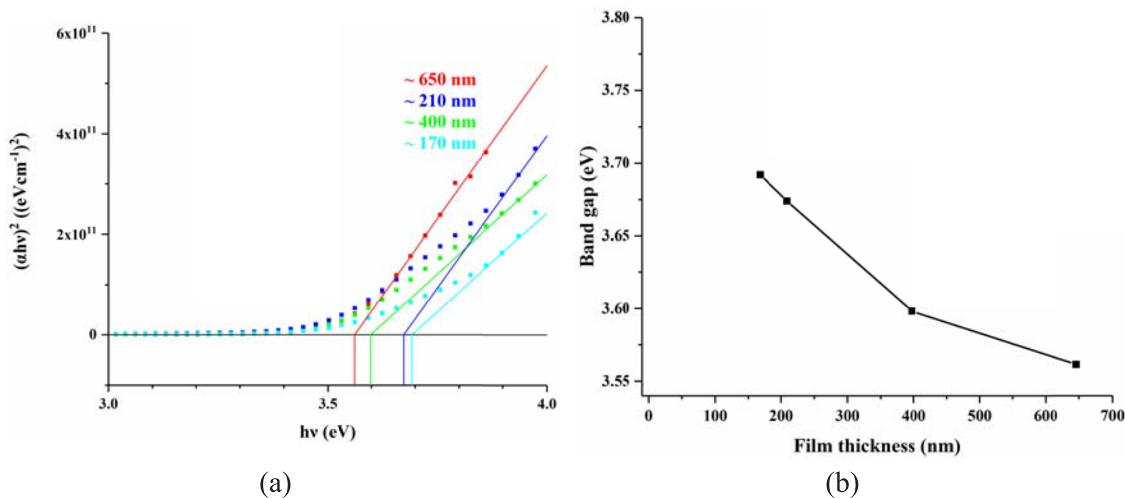

(a) (b)

Figure A.9: Graph of $(\alpha h\nu)^2$ as a function of photon energies (a) and band gaps (b) for InSiZO (2% In-0.6% Si) thin films of various thicknesses.

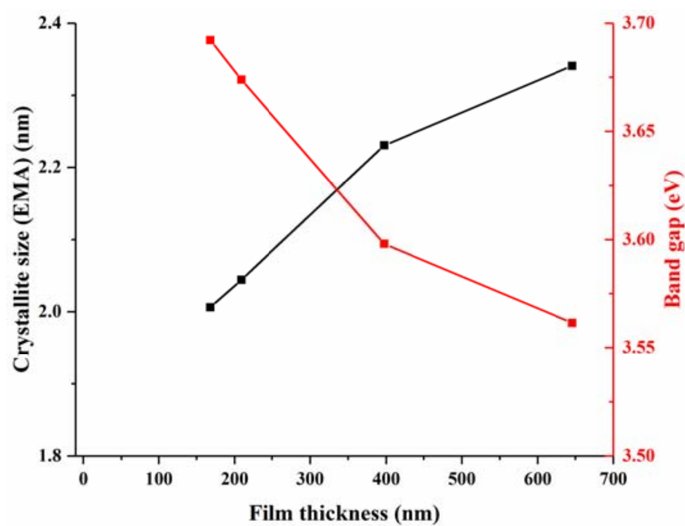

Figure A.10: Graph of band gaps and crystallite sizes calculated from EMA of InSiZO (2% In-0.6% Si) thin films of various thicknesses.

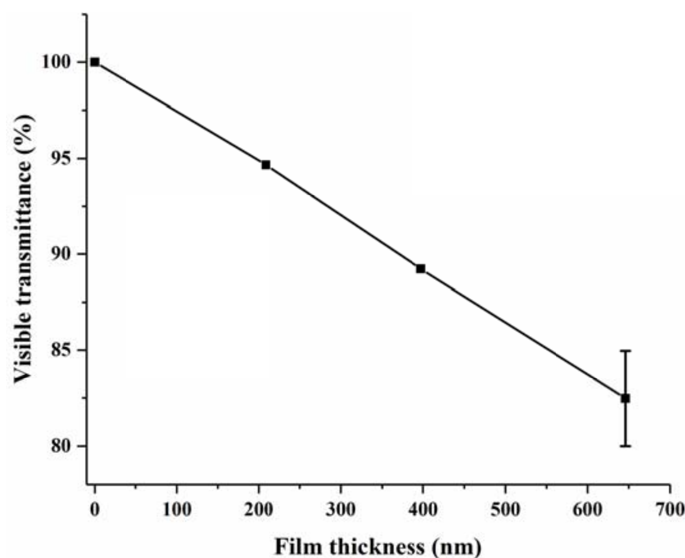

Figure A.11: Average visible optical transmittance (400 - 750 nm) corrected for the glass substrate of InSiZO (2% In-0.6% Si) thin films of various thicknesses.

Chapter 6

A6.1 AFM and SEM Studies: IZO

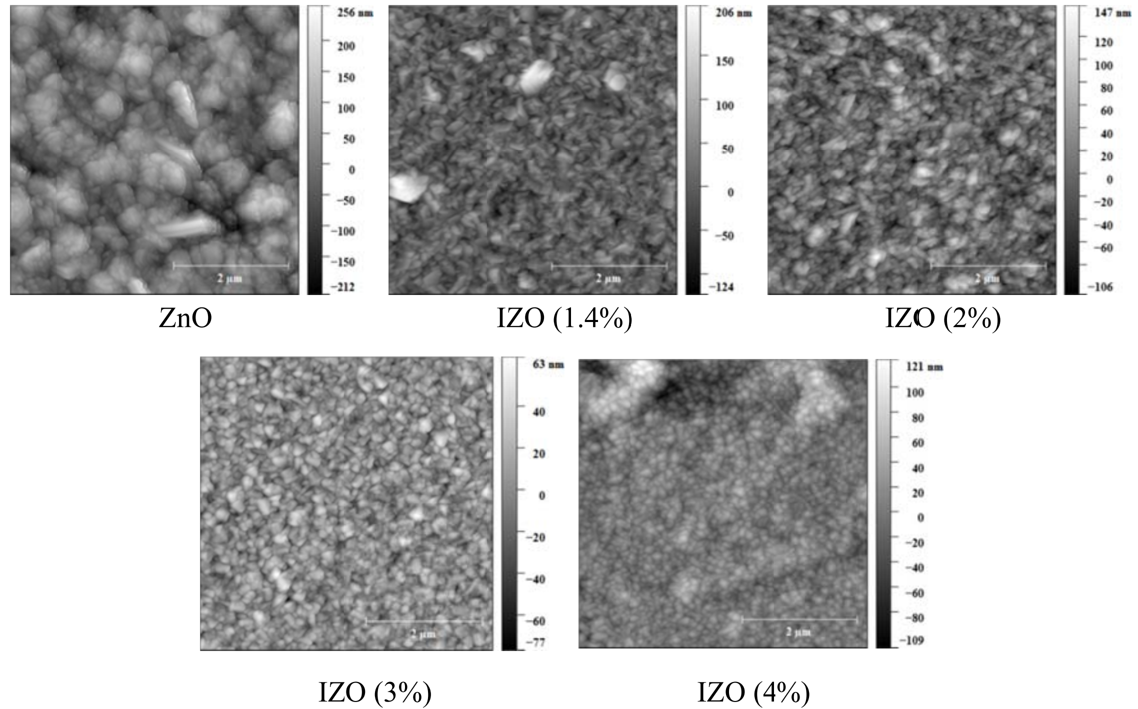

Figure A.12: AFM images of ZnO and IZO thin films containing varying amounts of In.

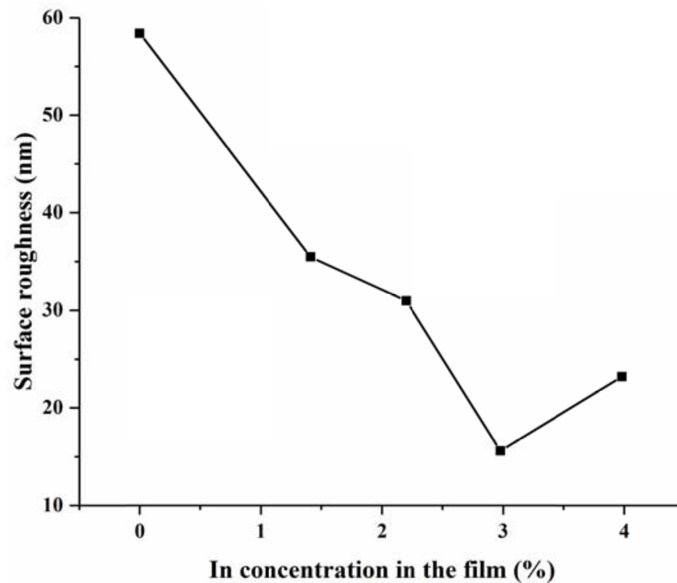

Figure A.13: RMS surface roughnesses of ZnO and IZO thin films containing varying amounts of In calculated from the AFM data.

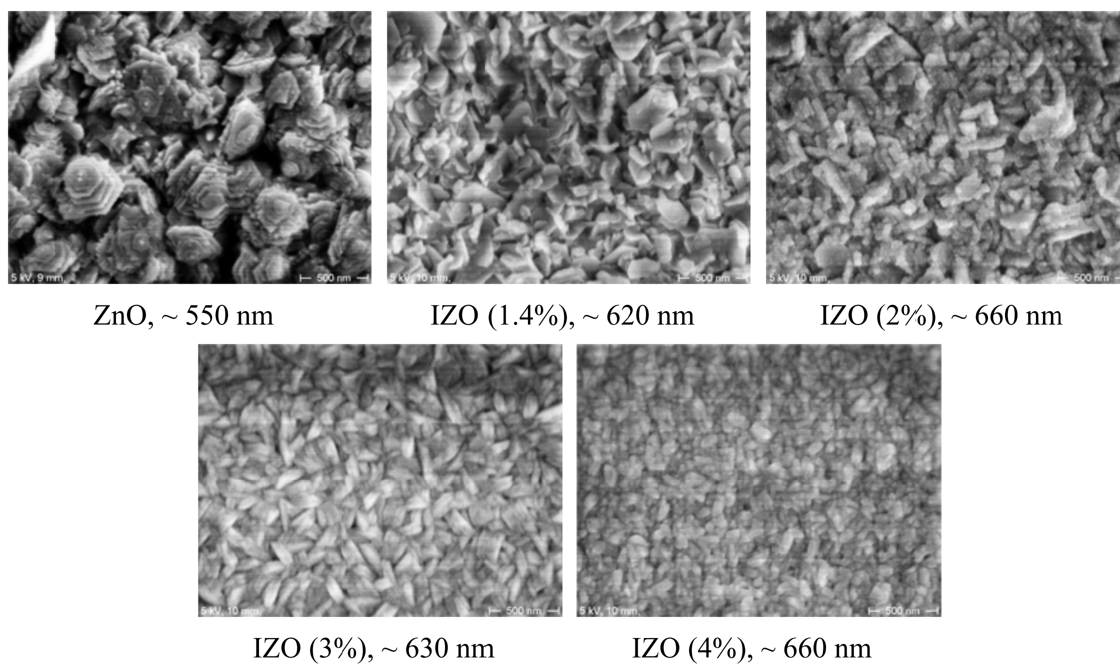

Figure A.14: SEM images of ZnO and IZO thin films containing varying amounts of In.

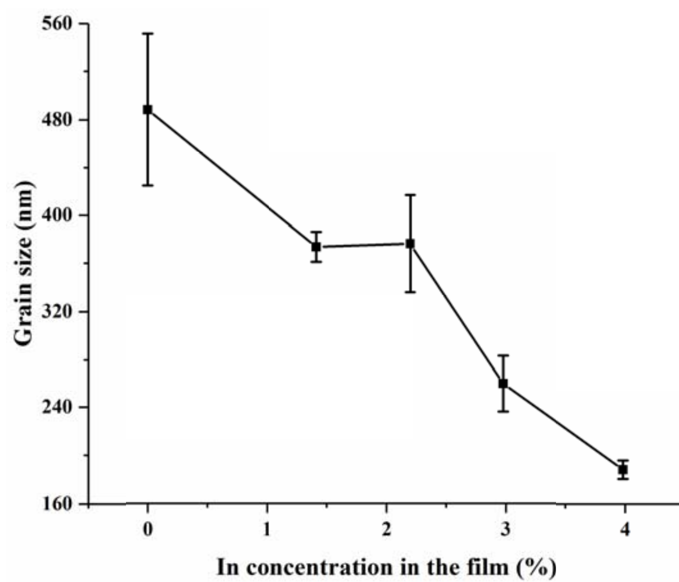

Figure A.15: Grain sizes of ZnO and IZO thin films containing varying amounts of In calculated from SEM images.

A6.2 Effect of Film Thickness: IZO

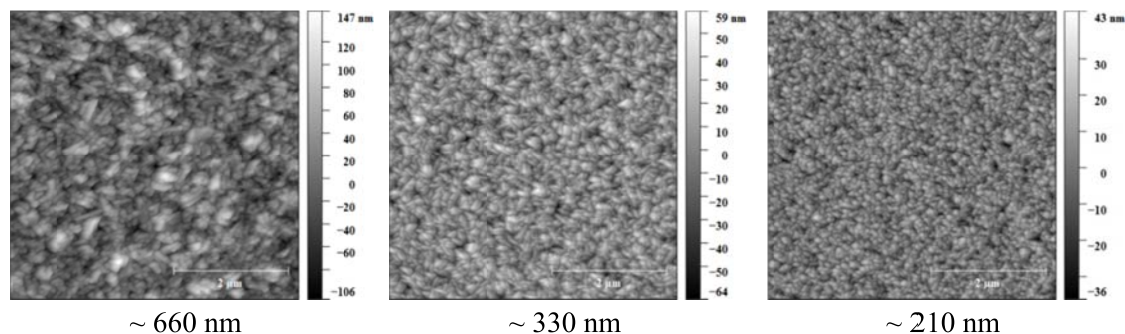

Figure A.16: AFM images of IZO (2%) thin films of various thicknesses.

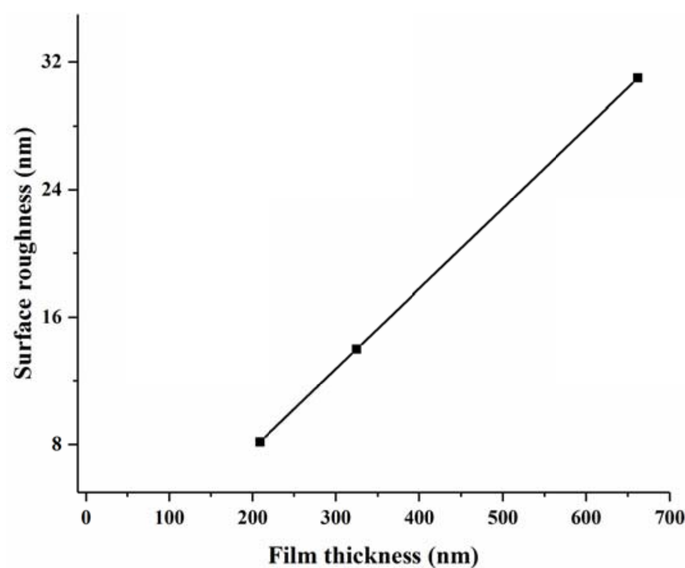

Figure A.17: RMS surface roughness of IZO (2%) thin films of various thicknesses calculated from the AFM data.

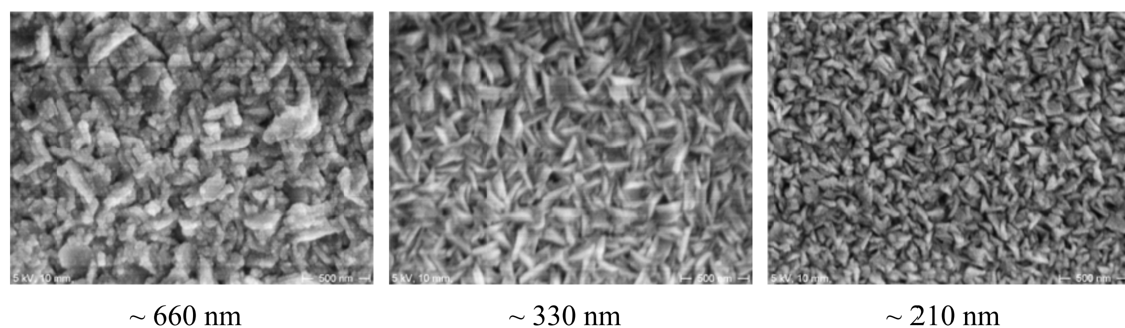

Figure A.18: SEM images of IZO (2%) thin films of various thicknesses.

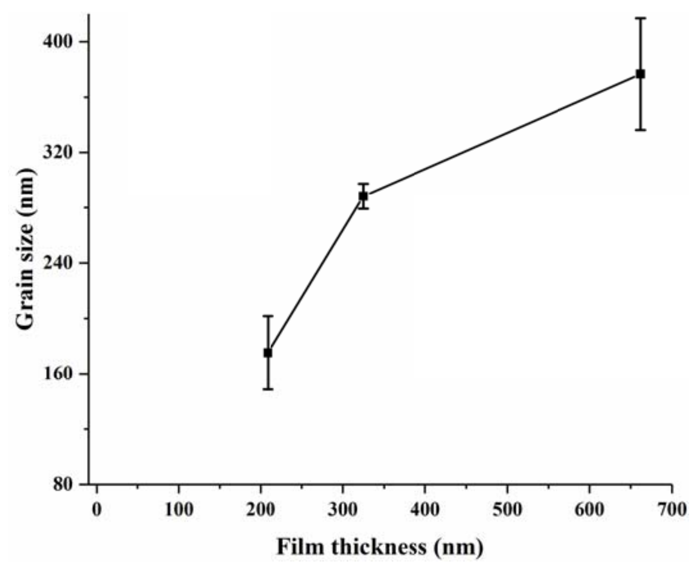

Figure A.19: Grain sizes of IZO (2%) thin films of various thicknesses calculated from SEM images.

A6.3 Effect of Film Thickness: InSiZO

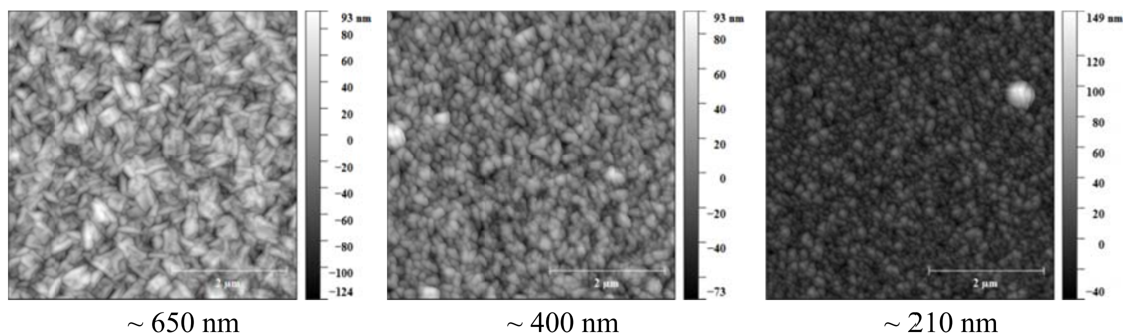

Figure A.20: AFM images of InSiZO (2% In-0.6% Si) thin films of various thicknesses.

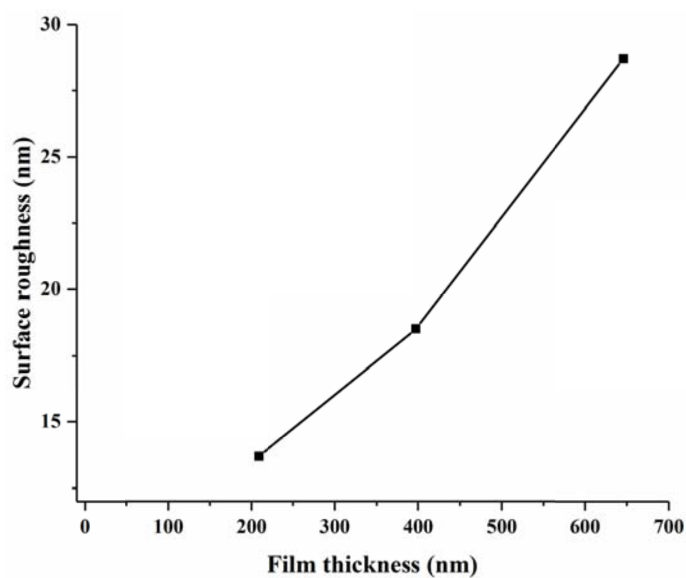

Figure A.21: RMS surface roughness of InSiZO (2% In-0.6% Si) thin films of various thicknesses calculated from the AFM data.

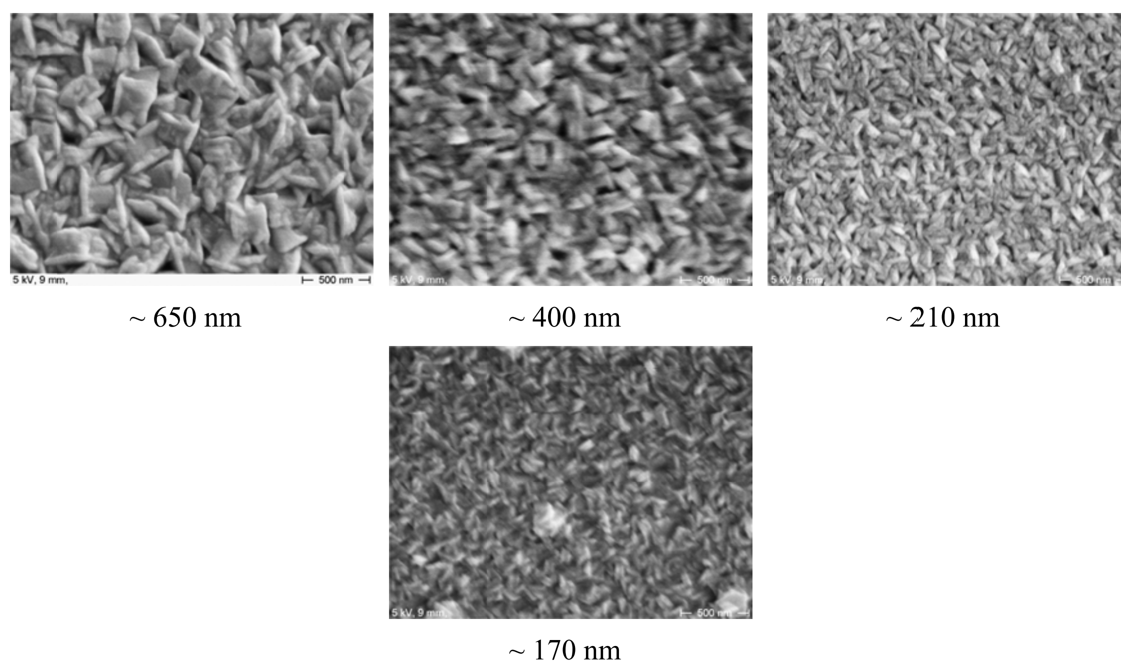

Figure A.22: SEM images of InSiZO (2% In-0.6% Si) thin films of various thicknesses.

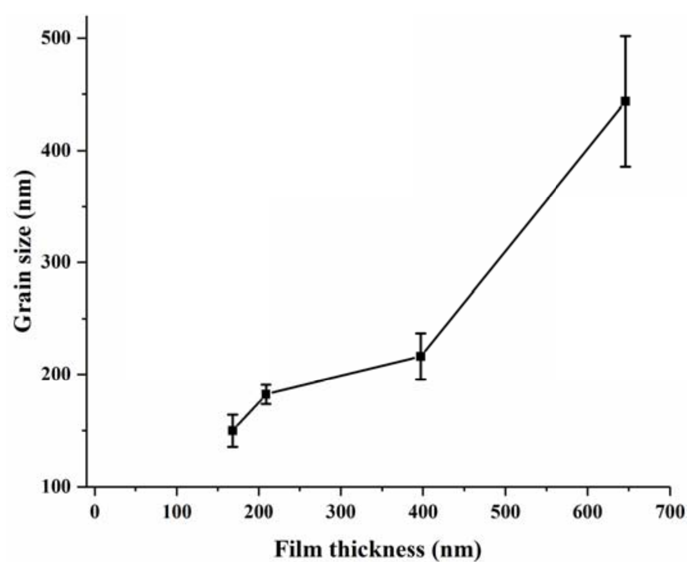

Figure A.23: Grain sizes of InSiZO (2% In-0.6% Si) thin films of various thicknesses calculated from SEM images.

A6.4 TEM 1

The thickness of SiZO (0.6%) thin films is 580 ± 20 nm (**Figure A.24**). The thicker part of the lamella suggests a surface roughness like that of ZnO, while the thinner part suggests a smoother film, especially with the good coverage carbon-Pt/Pd-Pt layers (**Figure A.24**(b)). Like ZnO, voids are seen in the film. In the thicker part of the lamella a rough boundary approximately 500 nm above the initial interface, is apparent, suggesting poor grain contact (**Figure A.24**(a)). The absence of a boundary in **Figure A.24**(b) suggests a local variation in the microstructure.

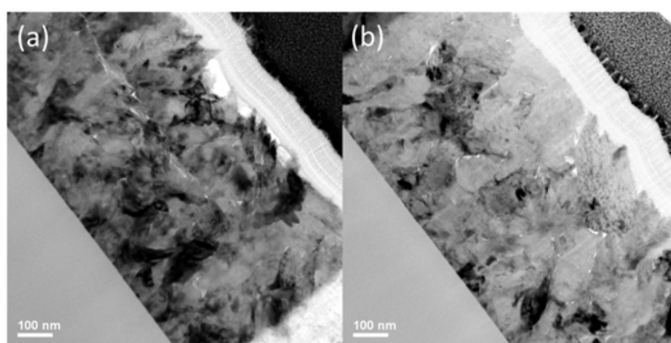

Figure A.24: SiZO: BF images of the thicker part of the lamella (a) and the thinner (b).

The thickness of IZO (2%) thin films is 570 ± 30 nm (**Figure A.25**). The BF images of the film (**Figure A.25**) show a densely packed polycrystalline film. Some voiding is seen, especially in the thinner part of the lamella (**Figure A.25**(b)).

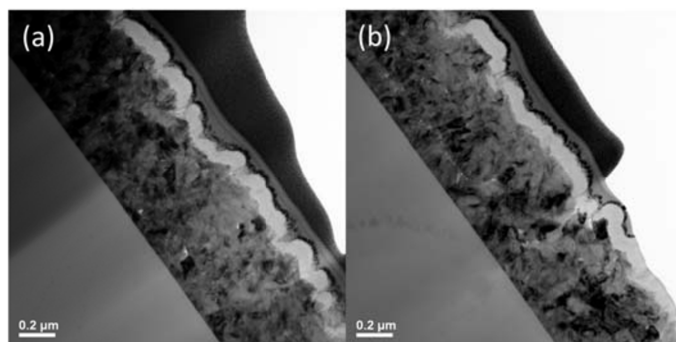

Figure A.25: Thick (a) and thin (b) parts of the lamella for IZO. Substantial thinning of the protective Pt strip is seen at the bottom right of both images.

A6.5 TEM 2

The structure of the nucleating region shows small crystallites between 10 and 20 nm thick, which show some fine-scale irregularity, but reasonably rounded grain morphology (**Figure A.26**(a)). Voids decorate the triple junctions between grains and persist right up to the upper-right of the image, suggesting this was a feature throughout the film. The HRTEM image (**Figure A.26**(b)) shows, like ZnO, the grains are crystalline with no amorphous boundary between them. No orientational order is seen in the nucleating region in the HRTEM image.

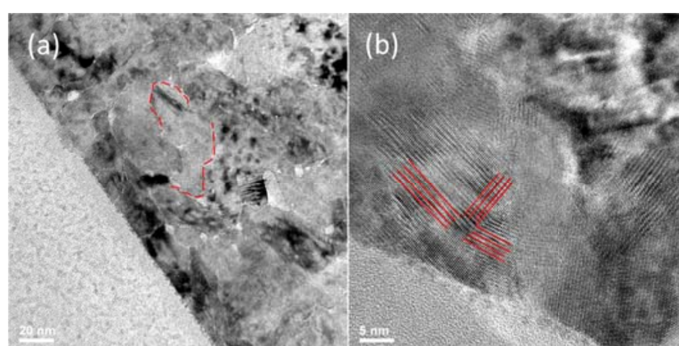

Figure A.26: Under-focused BF image of SiZO, showing grain boundaries as white lines (a). HRTEM images of the boundary show clear crystalline lattice fringes right down to the glass boundary (b).

A6.6 TEM 3

DF images of the brighter spots in the diffraction patterns are shown in **Figure A.27**(a) and (c). **Figure A.27**(a) shows a mixture of grain sizes, from very small at the nucleating interface and first 300 nm of film, to larger (> 100 nm grains) that emerge after ~ 100 nm of film growth. Large grains (> 100 nm) show complex, irregular shapes which span the majority of the film, but do not percolate it. The BF image in **Figure A.27**(b) and its DF counterpart in **Figure A.27**(c) show a grain with tapered geometry. The complementarity between images suggests that dark polygonal patches in the BF images are reasonably accurate representations of the grains.

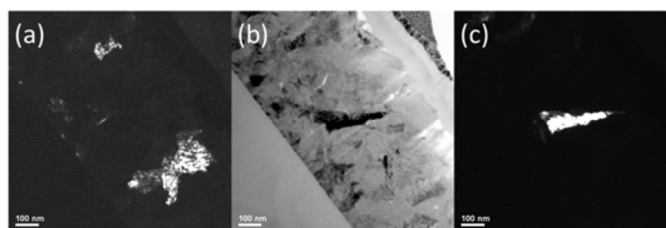

Figure A.27: DF image of SiZO (a) and (c) showing the large irregular morphology of the bigger grains that thread through the film. The BF image in (b) is the counterpart to (c).

The overall crystallographic structure of the film is essentially random (**Figure A.28**(a)). The spotted rings indicate that the material is, most likely, a single phase, but randomly oriented. The bright spots (not arcs or rings) indicate good crystallinity within the grains without too much short-range disorder, i.e., the film is primarily a polycrystalline film, with good short-range order within grains and no overall order in the film.

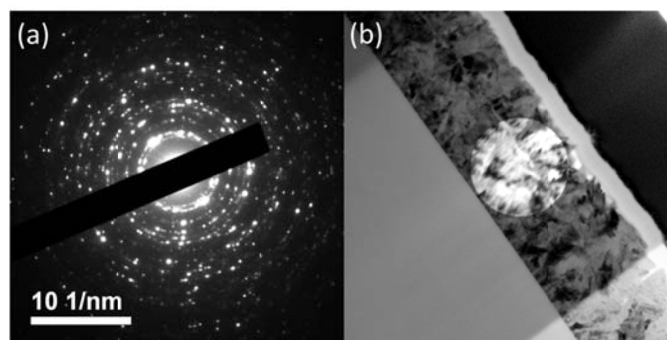

Figure A.28: The selected area diffraction pattern from ~ 1 μm diameter patch of the thicker area of SiZO (a). The BF image of the area with the area recorded indicated (b).

No orientational order of the grains is seen, either in the HRTEM images or in the diffraction pattern of the film (**Figure A.29**(b)). The diffraction pattern is comprised of discrete spots around several clearly defined rings. DF images using two of the brighter spots show that the grains are polygonal prismatic grains. Note that the smaller grains are in the lower half of the film and the bigger grains in the upper half.

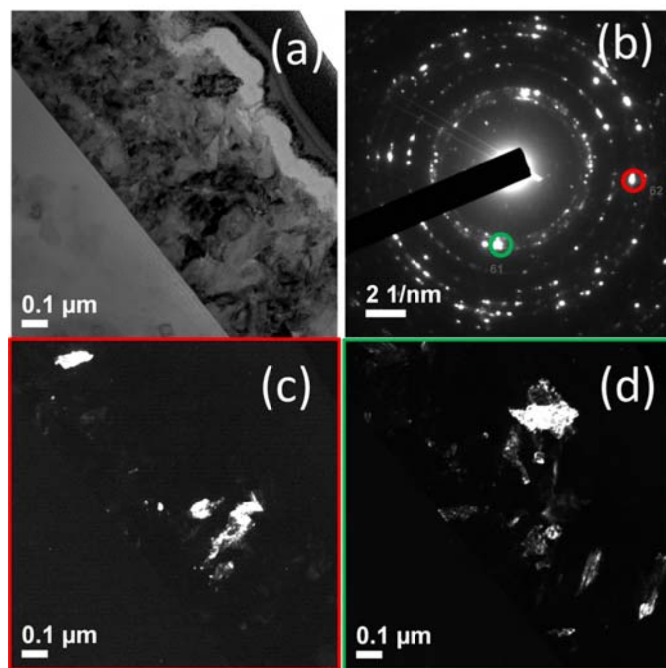

Figure A.29: BF image of IZO (a) with the corresponding diffraction pattern (b). Two DF images were taken with the objective aperture positions shown by coloured circles (diameters are roughly correct). The DF image from the fourth ring (c) shows their corresponding diffracting grains. In (d) the aperture spans the first three rings.

A6.7 EDX

The EDX spectrum of ZnO has dominated peaks for O (K = 0.525 keV) and Zn (L_{α}, K_{α}, and K_{β} = 1.01, 8.63, and 9.57 keV respectively). SiZO shows the same strong peaks for O, Zn, and Si (K = 1.74 keV). The incorporation of Si into the film is slow at first and peaks at the middle and falls a little at the top. IZO shows a consistent In L-signal ($L_{\alpha 1}$ = 3.29, $L_{\beta 1}$ = 3.49 keV), which appears to remain constant throughout the film. InSiZO shows little or no signs of Si (K = 1.74 keV). The In L line is observed, again, with a reasonably constant visibility in the film. (**Figure A.30 - Figure A.33**)

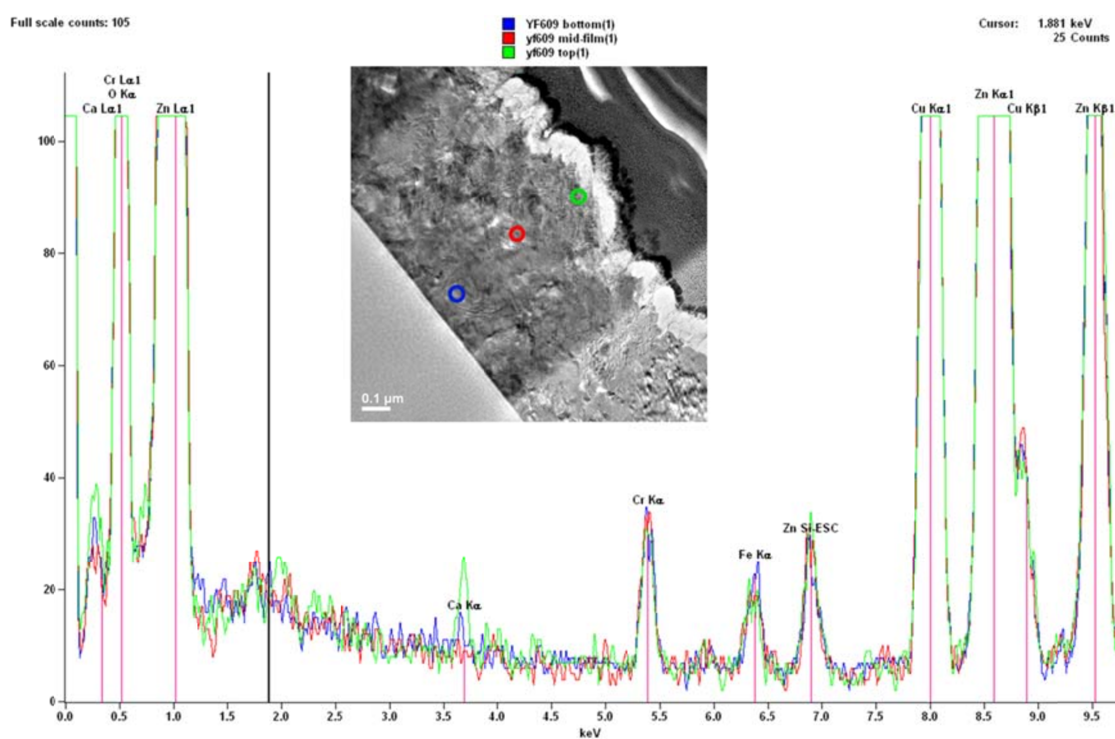

Figure A.30: EDX spectra taken from ZnO at the points indicated in the image at roughly 100 nm (blue), 350 nm (red), and 500 nm (green) from the initial interface.

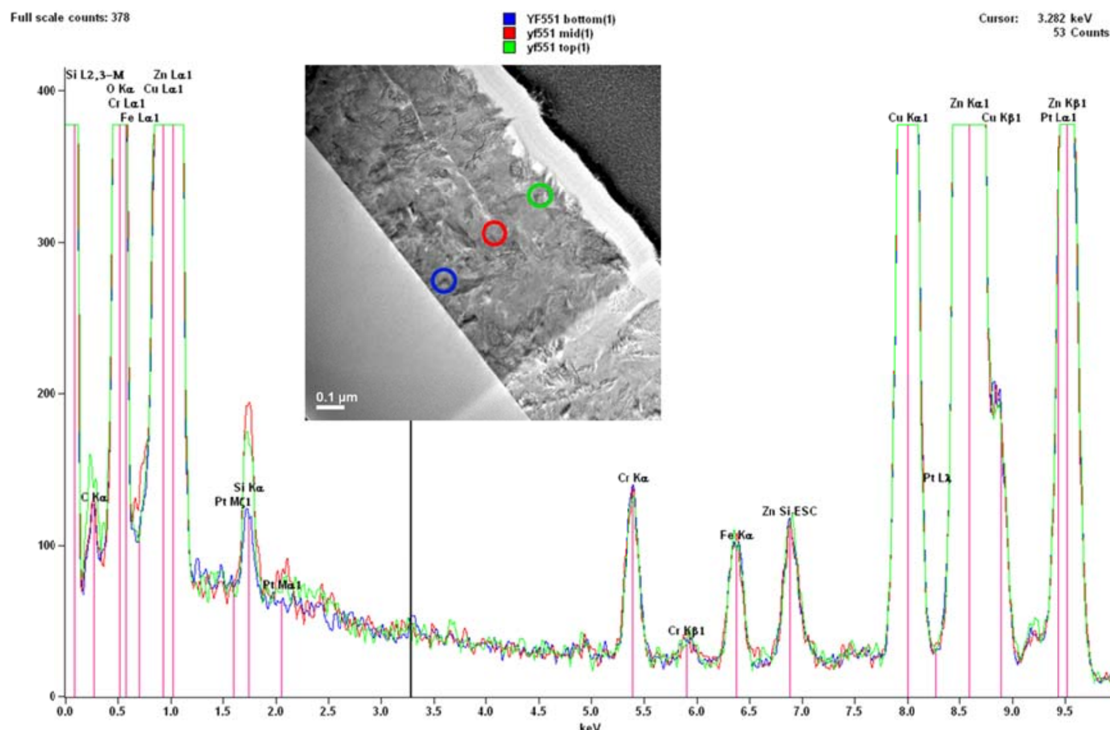

Figure A.31: EDX spectra taken from SiZO (0.6%) at the points indicated in the image at roughly 100 nm (blue), 300 nm (red), and 500 nm (green) from the initial interface.

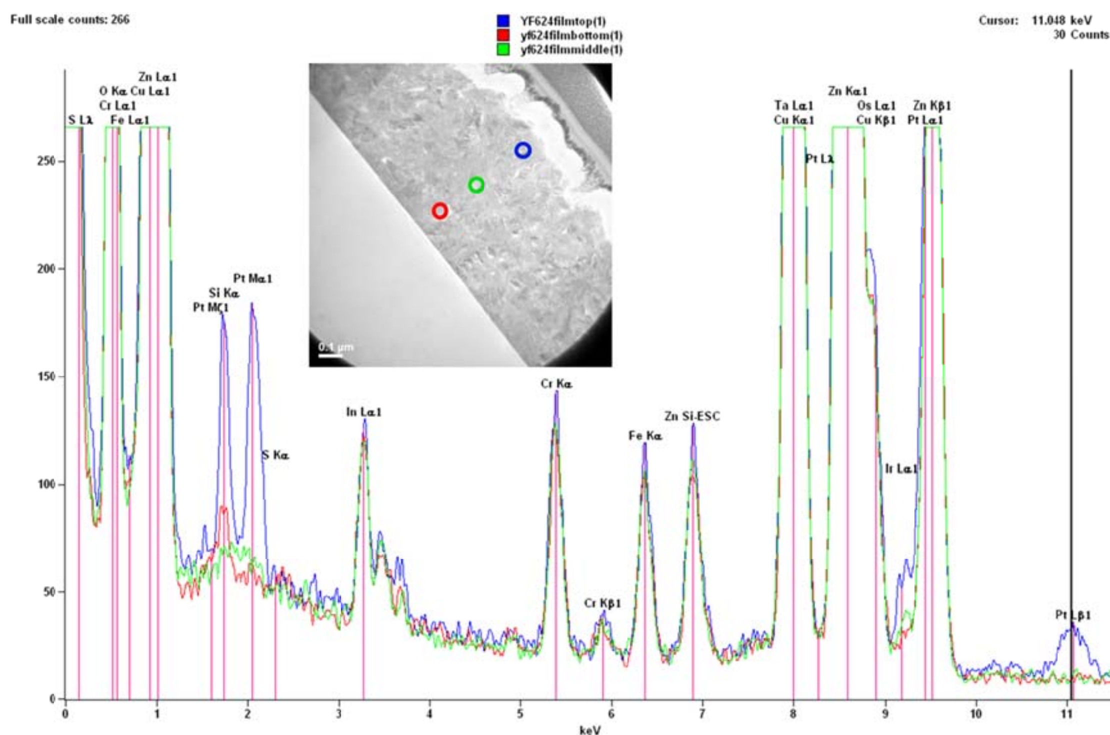

Figure A.32: EDX spectra taken from IZO (2%) at the points indicated in the image at roughly 100 nm (red), 300 nm (green), and 500 nm (blue) from the initial interface.

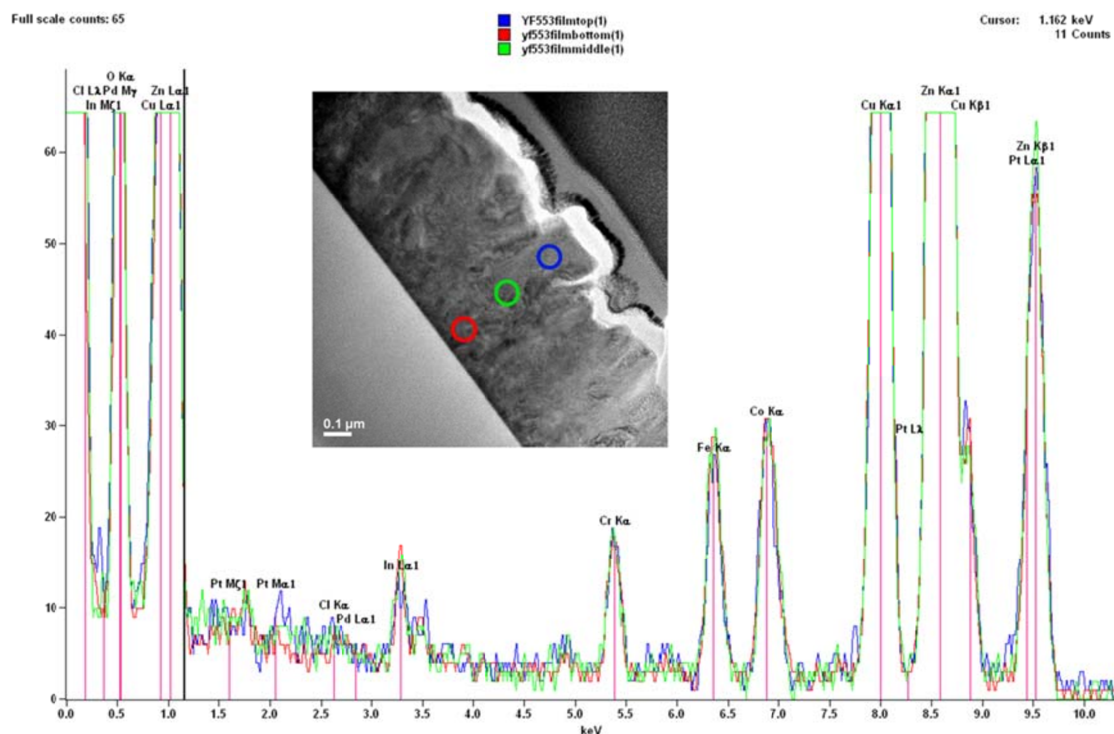

Figure A.33: EDX spectra taken from InSiZO (2% In-0.6% Si) at the points indicated along the 'super grain' in the image at roughly 100 nm (red), 350 nm (green), and 500 nm (blue) from the initial interface.

A6.8 Crystallography

All the strong reflections are accounted for by assuming lattice parameters of a = 0.329 nm and c = 0.5241 nm with the Space Group $P6_3mc$ (No. 186). Forbidden reflections include {0001} and {0003}, but may be seen with double-diffraction, which may account for weak spots close to the beam stop in **Figure A.34**.

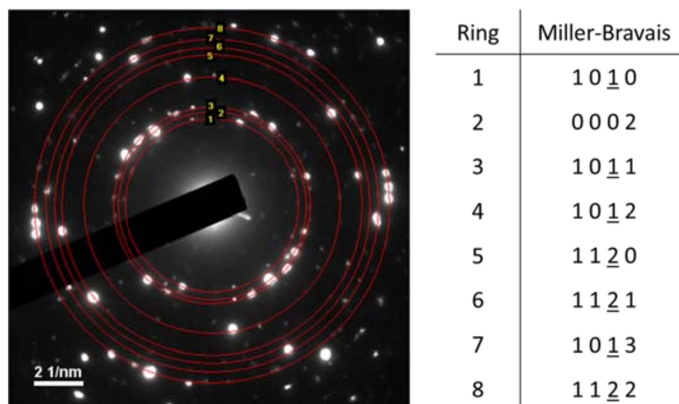

Ring	Miller-Bravais
1	$1 0 \underline{1} 0$
2	0 0 0 2
3	$1 0 \underline{1} 1$
4	$1 0 \underline{1} 2$
5	$1 1 \underline{2} 0$
6	$1 1 \underline{2} 1$
7	$1 0 \underline{1} 3$
8	$1 1 \underline{2} 2$

Figure A.34: The diffraction pattern of InSiZO with the predicted rings for hexagonal ZnO ($P6_3mc$) assuming lattice parameters a = 0.329 nm, c = 0.5241 nm. Note: the reflections {0001} and {0003} are forbidden, but may be excited by double diffraction, i.e., they are weak.

Chapter 7

A7.1 Grain Boundary Effects

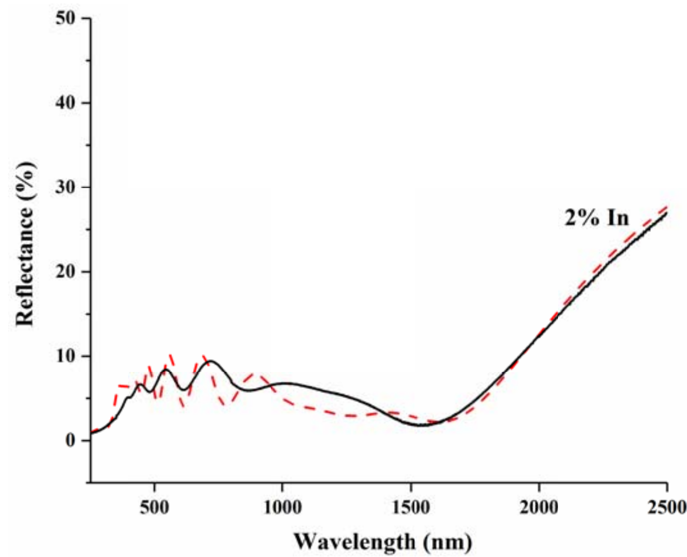

Figure A.35: UV-Vis-NIR optical reflectance spectra of IZO (2%) thin films. The simulation spectrum is shown as the red curve.

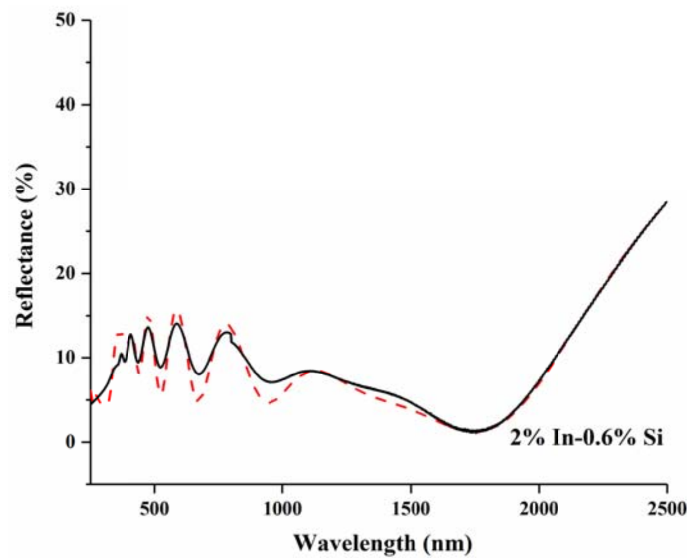

Figure A.36: UV-Vis-NIR optical reflectance spectra of InSiZO (2% In-0.6% Si) thin films. The simulation spectrum is shown as the red curve.

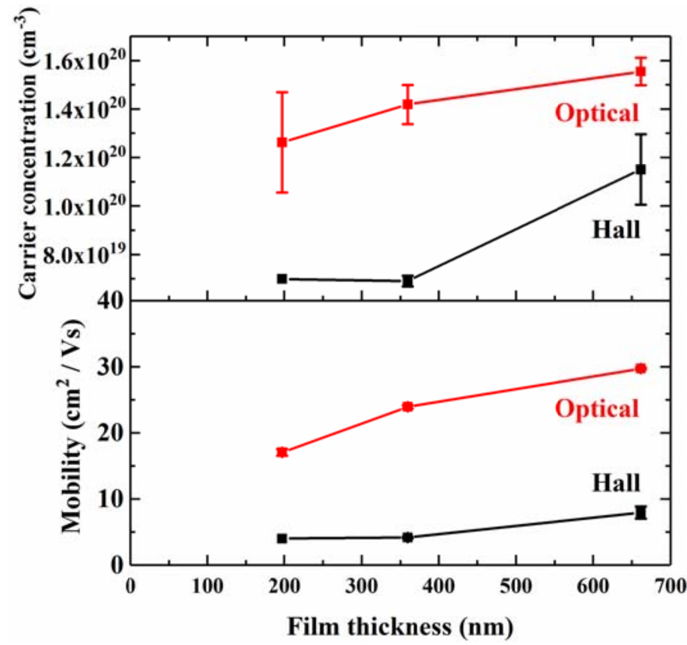

Figure A.37: Optical (red) and Hall (black) electrical properties of SiZO (0.6%) thin films of various thicknesses.

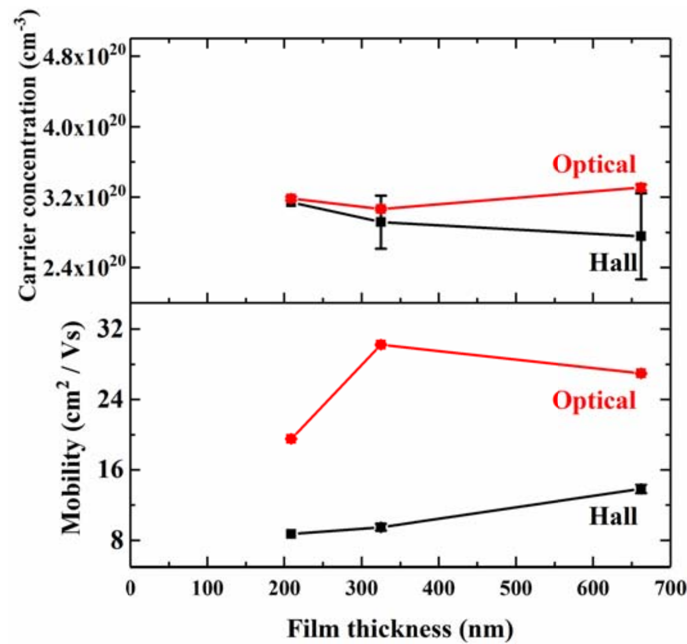

Figure A.38: Optical (red) and Hall (black) electrical properties of IZO (2%) thin films of various thicknesses.

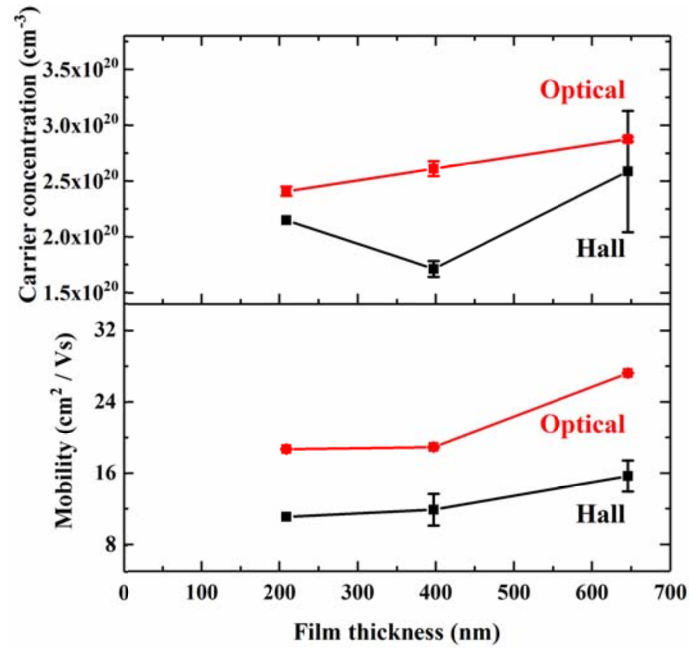

Figure A.39: Optical (red) and Hall (black) electrical properties of InSiZO (2% In-0.6% Si) thin films of various thicknesses.

References

[1] Manifacier, J. C., Gasiot, J. & Fillard, J. P. 1976. A Simple Method for the Determination of the Optical Constants n, k and the Thickness of a Weakly Absorbing Thin Film. *Journal of Physics E: Scientific Instruments,* 9**,** 1002.

[2] Swanepoel, R. 1983. Determination of the Thickness and Optical Constants of Amorphous Silicon. *Journal of Physics E: Scientific Instruments,* 16**,** 1214.

Publications

As of the time of writing, the following is a list of the publications. Additionally, several manuscripts are currently in preparation and ready for submission soon.

Vai, A. T., Rashidi, N., Fang, Y., Kuznetsov, V. L. & Edwards, P. P. 2016. Contrasting the Grain Boundary-Affected Performance of Zinc and Indium Oxide Transparent Conductors. *Journal of Physics: Condensed Matter,* 28, 224003.

Jie, X., Xiao, T., Yao, B., Gonzalez-Cortes, S., Wang, J., Fang, Y., Miller, N., AlMegren, H., Dilworth, J. R. & Edwards, P. P. 2018. On the Performance Optimisation of Fe Catalysts in the Microwave - Assisted H_2 Production by the Dehydrogenation of Hexadecane. *Catalysis Today,* 317, 29-35.

Jie, X., Gonzalez-Cortes, S., Xiao, T., Yao, B., Wang, J., Slocombe, D. R., Fang, Y., Miller, N., Al-Megren, H. A., Dilworth, J. R., Thomas, J. M. & Edwards, P. P. 2019. The Decarbonisation of Petroleum and Other Fossil Hydrocarbon Fuels for the Facile Production and Safe Storage of Hydrogen. *Energy & Environmental Science,* 12, 238-249.